ABSTRACT

Title of Document: AN INTEGRATED GAS SENSING SYSTEM BASED ON SURFACE-FUNCTIONALIZED GALLIUM NITRIDE NANOWIRES WITH EMBEDDED MICRO-HEATERS

Guannan Liu, Doctor of Philosophy, 2015

Directed By: Professor Martin Peckerar
Department of Electrical and Computer Engineering

In the last few decades, significant improvements have been made in gas sensor technologies. Metal-oxide sensors have been used for low-cost detection of combustible and toxic gases. However, hurdles relating to sensitivity, stability and selectivity still remain. Recently, nanotechnology has helped tremendously through the introduction of nano-engineered materials like nanowires and nanoclusters. Nanowire sensors have much better sensitivity as compared with thin-film devices due to the larger detecting surface-to-volume ratio. But clearly, improvements are still needed.

For real-world applications, selectivity between different classes of compounds, such as combustible and toxic gases, is highly desirable. An ideal chemical sensor should distinguish between the individual analytes from a single class of compounds. For example, in detection of benzene or toluene, a good sensor will not be disturbed by other aromatic compounds present in the environment. This is a huge challenge for semiconductor based

metal-oxide sensors, such as TiO_2, SnO_2, Fe_2O_3 and ZnO, which have inherent non-selective surface adsorption sites.

Recently, a new class of nanowire-nanocluster (NWNC) based gas sensors has gained interest. This type of sensor represents a new method of functionalizing the surface for selective adsorption and detection. The adjustable sensitivity can be achieved by tuning the density, size or composition of the nanoparticles that decorate the nanowires. These advantages make the NWNC sensors a good alternative to conventional thin-film sensors. So far, research into NWNC sensors has demonstrated the potential in sensing many important classes of compounds. However, most of these NWNC devices require elevated working temperatures. They also have long response/recovery times and must function in an inert atmosphere. All these limitation will be the obstacles in real-world usage for domestic, environmental or industrial applications. And finally, the sensors thus developed must be manufacturable. That is, they must be batch fabricated with high yield.

To remedy these problems, my thesis was divided into the following tasks,

1. Develop dry etching techniques to fabricate horizontally aligned GaN nanowires (NW), combining these techniques with wet etching treatment for surface damages removal. I call this a "top-down approach" using a subtractive process that fabricates NWs from thin-films and adding sensitive nanocrystals after the initial NW definition. This is to be compared to the additive "bottom-up" nanowire growth by MBE/HVPE/Sol-gel, in which NWs are grown, harvested from the growth surface and subsequently re-attached to a new surface. The top-down approach enhances the yield and homogeneity of the NW and it is mass-production oriented.

2. Study the metal-oxide nanoclusters (NCs) deposition method by physical vapor deposition (PVD) and rapid thermal annealing (RTA) for TiO_2, SnO_2, WO_3, Fe_2O_3, etc. Develop the metal nanoparticle deposition method by PVD for Au, Ag, Pt, Pd, etc.
3. Study the crystalline phases and gas adsorption sites formed by the method and establish a database connecting metal-oxide bonding sites with different target chemicals.
4. Utilize Si doped n-type and unintentionally doped GaN nanowires functionalized with different metal-oxide and metal-oxide/metal composite nanoclusters to create a series of highly selective and sensitive gas sensing nanostructure devices.
5. Develop a low-cost micro-heater (MH) for local high temperature generation with low power consumption. This allows the rapid chemical desorption cycles as we anticipate frequently re-use or reset of the sensor. It also enables the use of these NWs in high temperature sensor applications.
6. Integrate the NW, NCs and MH into one working sensor, and integrate multiple types of gas sensors on a single chip. The chip can simultaneously sense many types of gases without interference.

In this study, the potential of multicomponent NWNC based sensors for developing the next-generation of ultra-sensitive and highly selective chemical sensors was explored. We have achieved μA and nA levels of baseline detector current and we have shown that low UV illumination enhances sensitivity for some cases. These sensors have low power consumption making them suitable for portable devices.

AN INTEGRATED GAS SENSING SYSTEM BASED ON SURFACE-FUNCTIONALIZED GALLIUM NITRIDE NANOWIRES WITH EMBEDDED MICRO-HEATERS

By

Guannan Liu

Dissertation submitted to the Faculty of the Graduate School of the
University of Maryland, College Park, in partial fulfillment
of the requirements for the degree of
Doctor of Philosophy
2015

Advisory Committee:
Prof. Martin Peckerar, Chair
Dr. Abhishek Motayed, Co-advisor
Prof. John Melngailis
Prof. Romel Gomez
Dr. Albert Davydov
Prof. Lourdes G. Salamanca-Riba

© Copyright by
Guannan Liu
2015
Analog & Mixed Signal Systems Design Laboratory
Electrical and Computer Engineering
University of Maryland, College Park

Thin-Film and Nanostructure Processing Group
Material Metrology Laboratory
National Institute of Standard and Technology, Gaithersburg

Dedication

To my parents, Guiyou Liu and Ru Wang,

and

to my wife, Lin Tian,

for their love, endless support and encouragement.

I love you with all my heart

Acknowledgements

This dissertation would be incomplete without mentioning the significant contributions from my advisor, colleagues, friends and family. I am the most fortunate person who was surrounded by a great team of supervisors and mentors.

First and foremost, I would like to express my deepest gratitude to my advisor, Dr. Martin Peckerar, for his support, guidance, movitation, patience, enthusiasm, extensive knowledge and experiences that gave me the positive energy to move forward.

I would like to thank Dr. Abhishek Motayed, who helped me through the past four years with all his passionate ideas, through instructions and inspiring navagations. I would never have been able to finish my Ph.D. program without his invaluable advice when tasks seemed overwheling and never-ending.

I would like to acknowledge Dr. John Melngailis, Dr. Albert Davydov and Dr. Romel Gomez for their kindly help and guidance so that my research can fully utiliz laboratory facilities at both University of Maryland and National Institute of Standards and Technology. I benefited greatly from useful discussions with Dr. Sergey Krylyuk, Dr. Baomei Wen, Dr. Deepak Sharma, Dr. Feng Yi, and Dr. Ratan Debnath in many technical issues. My special thanks also go to N5 Sensors. Inc for their assistance in my gas sensor project, especially Ms. Nichole Sullivan and Mr. Audie Castillo, and to FlexEl, LLC for their support and help in my micro-heater project, especially Dr. Daniel Lowy and Mr. Amir Kahrim. I would like to thank Dr. Jong-Yong Ha and Dr. Filiz Yesilkoy for their help and patient “orientation” when I first joined the groups, and my other collegues for their help and inspiring discussions including Mr. Ting Xie, Mr. Po-Chun Huang, Dr. Rongyue

Wang, Mr. Scott Bauman, Dr. Chao Wang, Dr. Wei Zhao, Mr. Nick Kratzmeier and Ms. Jing Xia.

Finally, I want to thank my parents for their endless support and as always letting their only child travel half of the earth to pursuit his dreams from Changchun to Hong Kong, to Urbana-Champaign, to College Park. I would also like to acknowledge my wife, Lin Tian, who has always being with me with her whole hearted love and devotion through the years.

Last but not the least, I appriciate all the friends I met and worked with in the United States during this wonderful journey. I am luckly blessed to meet you in my life.

Table of Contents

List of Figures

List of Tables

List of Abbreviations

AFM	Atomic Force Microscopy
CNT	Carbon Nanotube
CVD	Chemical Vapor Deposition
EG	Ethylene Glycol
FIB	Focused Ion Beam
GaN	Gallium Nitride
ICP	Inductively Coupled Plasma
IPA	Isopropanol
IR	Infrared
KOH	Potassium Hydroxide
MH	Micro-heater
MHP	Micro-hot-plate
NC	nanocluster
NP	nanoparticle
NW	nanowire
NWNC	nanowire-nanocluster
MBE	Molecular Beam Epitaxy
MFC	Mass Flow Controller
PECVD	Plasma-Enhanced Chemical Vapor Deposition
PID	Photo-ionization Detector
ppb	parts per billion
ppm	parts per million
ppt	parts per trillion
PVD	Physical Vapor Deposition
RIE	Reactive-ion Etching
RTA	Rapid Thermal Anneal
SEM	Scanning Electron Microscopy
SnO_2	Tin Dioxide
TiO_2	Titanium Dioxide

UID	Unintentionally-doped
UV	Ultra Violet
VOC	Volatile Organic Compound
WO_3	Tungsten Trioxide
ZnO	Zinc Oxide

Chapter 1: Overview

1.1 Importance of Chemical/Gas Sensors

Electronics devices are widely used in our daily lives and the signals and information generated are recorded and stored in many new ways. Information desired from the environment is converted to electronic signals via a sensor. Sensors can register information including temperature, motion, gravity, pressure, sound, etc. More and more attention is currently paid to biological state (blood pressure, blood oxygenation, body temperature, pulse, etc.), chemical, environment, atmospheric pressure, humidity, and light sensing. For environmental and national security reasons, reliable and portable detectors must exhibit high sensitivity and selectivity for harmful environment conditions. In the last few decades, significant improvement has been made in gas sensor technologies.

A chemical sensor is a device that identifies a chemical species and quantifies the concentration of atoms, molecules, or ions in gases or liquids by producing a measureable signal [1]. Detection of chemical species in air such as industrial pollutants, poisonous gases, chemical fumes, and volatile organic compounds (VOCs) is vital for the health and safety of communities around the world [2]. Chemical and explosive detection systems constitute the front line of defense against chemical weapons and terrorist threats [3]. Gas sensors are widely developed in commercial and industrial applications like combustion engine monitoring, process control, and environmental monitoring [4]. Chemical sensors can also be used for food quality control, breathe analysis and disease detection [5]. Due to all these importance, applications extensive research is on-going in the sensor field, and

the advent of nanotechnology is continually influencing this development. The goal is to achieve both low cost, low power dissipation, and high performance in these devices.

1.2 Characteristics of a Gas Sensor

Generally, a sensor's performance can be characterized by the following set of parameters [6-8].

- Sensitivity: the change of measured signal (resistance, conductance) when sensor exposed to certain concentration of target analyte.
- Selectivity: the ability to discriminate between the components of a gas mixture and provide detection signal for the component of interest.
- Stability: the ability of a sensor to provide reproducible results for a certain period of time. This includes retaining the sensitivity, selectivity, response, and recovery time.
- Detection limit: the lowest concentration of the analyte that can be detected by the sensor under given conditions, particularly at a given temperature.
- Dynamic range: the analyte concentration range between the detection limit and the highest limit.
- Resolution: the lowest concentration difference that can be distinguished by sensor.
- Response time: the time required for sensor to respond to a step concentration change from zero to a certain concentration value.

- Recovery time: the time it takes for the sensor signal to return to its initial value after a step concentration change from a certain value to zero.
- Working temperature: the temperature at which the sensor operates.

An ideal chemical sensor should be able to operate at room temperature and possess high sensitivity, good selectivity, high stability, low detection limit, a wide dynamic range, good resolution, fast response and recovery times.

1.3 Current Sensor Technologies and Limitations

Due to the massive literature available on conventional and novel sensing techniques, I have reviewed a collection of papers focusing on portable gas sensing technologies only. These include the following:

1. Catalytic sensors: also known as pellistor, targeted for flammable, combustible gases using a heated wire via catalytic oxidation [9-11]. The target gas will be oxidized while releasing heat when comes into contact with the catalytic surface. The electrical resistance of the wire changes and is then converted into a readable display on the instrument. The catalytic combustion sensors typically use a lot of power to operate. They have selectivity issues and regularly require fresh or recharged batteries. These sensors require oxygen or air to work and their effective functioning is placement dependent [12].

2. Electrochemical sensors: Electrochemical sensors are typically available for a variety of toxic and flammable gases like carbon monoxide, hydrogen, nitrogen oxides hydrogen sulfide and chlorine. The target gas molecules diffuse into the membrane at the top of the sensor and then react with the chemicals on the sensing electrodes to generate electrical current [13-15]. A common problem is cross-sensitivity issues, for example alcohol vapors and unsaturated hydrocarbons can easily interact with the sensor electrode materials creating a common signal. Short life-time due to limited amount of unrecoverable base materials, and cannot be exposure to a high concentrations are the other disadvantages of these sensors.

3. Infrared sensors (IR sensors): IR sensors work via a system of transmitter beams from IR sources and detected by IR detectors. By sensing the light intensity change of transmitted IR light due to the presence of an absorbing target gas and comparing this intensity to a reference beam, we are able to detect combustible or noxious gases (specifically hydrocarbon vapors and carbon dioxide.) The altered state of the light beam determines the type of gases. The light absorption and intensity changes reveal the type and concentration of gases [16-18]. The main drawback to IR sensors is their high cost. IR sensors are more sophisticated and expensive, which need frequent calibration and routine maintenance. It is not suitable for use in wearable applications.

4. Photoionization detectors (PIDs): PID is a type of gas detector and typically measures volatile organic compounds (VOCs) from sub parts per billion (ppm) to 10000 ppm. Photoionization detectors rely on specific chemical properties of the VOCs. Instead of absorbing light, a PID uses high energy photons, normally UV light source, to ionize gas molecules into positively charged ions. Once the gas is ionized, it passes through two charged plates, which separate the gas ions and the free electrons. As the gas ions flow towards the plates, a current is generated between the two plates. The greater the concentration of the component, the more ions are produced and collected, and the greater the current [19, 20]. However, PID sensors cannot distinguish the type or species of the VOCs. They are non-selective, high-cost, sophisticated and require routine maintenance.

5. Metal-oxide thin-film sensors: They are used for detecting a range of gases including toxics and combustibles and work via a gas sensitive and porous film that is composed of titanium, tin, zinc or tungsten oxides [21, 22]. Materials are maintained at working temperature between 300 to 500 ℃ where thermal generated electron-hole pairs and high temperature enhanced the reactions at a sufficient rate. The mechanism of thin-film sensor is based on changing of the resistance of a thin-film upon adsorption of the gas molecules on the surface of a semiconductor. The gas-solid interactions affect the resistance of the film because of the amount of free carrier (electron for most cases) in the film were trapped and released by adsorption and desorption of target gases [23]. However, resistive metal-oxide gas sensors have serious drawbacks in terms of selectivity, long-term baseline drift, long-time recovery and high-temperatures required for high power operation, which limits their use in portable applications.

6. Field effect sensors: also known as FET sensor, MOSFET sensor and targeting for toxins, explosives and VOC's. The MOSFET sensor device is based on a field effect transistor with catalytic metal as the gate contact. The gas molecules modulate the conduction channel by effect the voltage to the gate of the transistor [24-27]. For the MOSFET sensor, gate and drain are shorted so the device functioning as a two-terminal device. Drawbacks are the low-sensitivity and limited selectivity. The metal gates in these FETs have to be thin and porous to achieve the required sensitivity, however this gate design will lead to many reliability issues during the real-time sensing.

Table 1.1 shows a summary of applications and limitations of 6 portable gas sensing technologies.

Sensor Device Type	Applications (Gas)	Limitations
Catalytic	Flammable Combustible	High power consumption, interference issues
Electrochemical	Toxic	Cross-sensitivity, short life-time
Infrared	Combustible Hydrocarbon Greenhouse	High cost, large size, high power consumption, need routine maintenance
Photoionization	Volatile organic compounds (VOCs)	Macro-scale, cross sensitivity, limited working range, short life-time
Metal-oxide thin film	Toxic Explosive	Cross-selectivity, baseline drift, require high temperature
Field effect	Toxic Explosive / VOCs	Reliability, limited selectivity and sensitivity due to gate quality

Table 1.1 Comparison of current technologies for portable sensing systems

1.4 Design of High Performance Gas Sensor

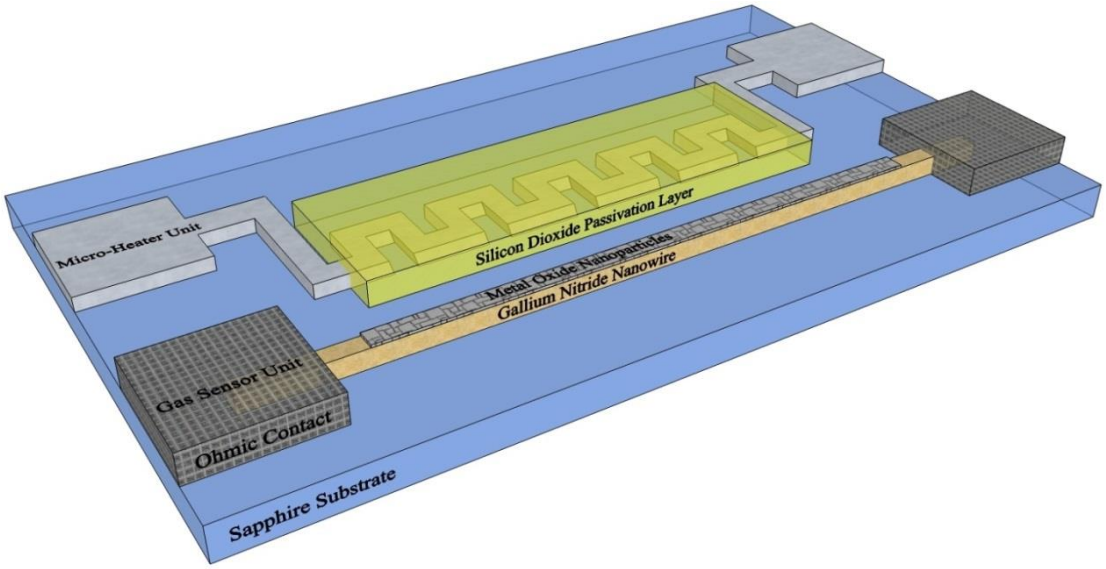

Fig. 1.1 High performance integrated solid-state gas sensor design diagram

Fig. 1.1 presents the schematic design of my highly sensitive and selective, reliable and robust, working at room-temperature, integrated solid state gas sensor. Each sensor module is made of two components in parallel: a gas sensor unit and a micro-heater unit. Gas sensor unit is nanowire-nanocluster structure, functioning as the main active sensing part and working at room-temperature. The micro-heater unit is a component part of the integrated system stays in idle mode most of the time. It only works at the time of cleaning adsorbents on chip surface because after some rare and extreme sensing conditions like very high concentration of target gases or unknown chemicals exposure and coverage, the system needs "reset" and desorb all the unwanted attached chemicals to maintain the sensor output results reliable and repeatable. The micro-heater can quickly engage and generate local heating that help the nanowire and surrounding areas desorbing unwanted gas phase chemical molecules attached. The heating assistance further improves the sensor system to be more reliable and robust.

1.4.1 Gas Sensor Unit

Modern semiconductor industry has grown through the fast development of nanotechnology. It is well known that the electrical and physical properties of nanoparticles (NPs) and nanowires (NWs) can change significantly with the environment. This is due to the nanostructure's high surface to volume ratio [28-30]. Solid state gas sensors can be designed basing on NWs and NPs, and fabricated using integrated solid state device techniques. For NPs, it is hard to directly make electrical contacts to the small structure. However, this small structure can be used as bonding and reaction center due to its fast respond to environmental changes. NWs are very suitable for current measurements. Current flow changes dramatically with the NW electrical properties (conductance/resistance, effective channel width modulation, interface carrier scattering/trapping, etc.) Research shows that NW detectors are sensitive, but not selective due to the single type of analyte binding site common to all analytes [31, 32]. To enhance the NW based sensor's selectivity, single or combined NPs of metal-oxides and metals are used to decorate the NW, creating different binding sites for different reactive chemicals. The NPs or nanoclusters (NCs) decoration can be single metal-oxide, metal or a mix with different combination with optimized ratios. This nanowire-nanocluster (NWNC) hybrid device can mitigate the problem of selectivity by fine tuning the combinations of metal and metal-oxide NCs supported by Gallium Nitride (GaN) NWs. This hybrid structure not only improve the sensitivity and selectivity, but also decrease the detection time and most importantly it will have the capability of tailoring selectivity to individual analytes by incorporating different NC materials.

The GaN NW with NCs decorations gas sensing structure has advantages as comparted to other structures (such as the GaN nanobelt, nanoribbon and thin-film) functionalized by the same NCs. The NW is a 1D material that leads to NC decoration of the top surface as well as sidewalls. Nanobelt, nanoribbon and thin-films are 2D materials for which the dimension of the sidewall is negligible compared to the dimension of the top surface. Thus, the NC decoration effect is mainly on the top surface only. Assuming the NCs on NW and 2D materials are identical, and the diameter of NW is the same with the thickness of 2D materials. The NWNC sensor structure can improve the sensitivity by involving sidewalls of 1D material beside top surface. The conductivity modulation will be enhanced by introducing more space charge area from sidewalls, and push more free carriers to the NW core. Moreover, 1D GaN NW has lower working current comparing to the 2D GaN. Device noise is proportional to the square root of the baseline current, the lower noise leads to a higher signal to noise ratio which enhance the detection limit of the sensor. From cost point of view, using NW structure can integrated more NWNC sensors on a single chip and produce more devices from each wafer as opposed to the limited throughput and low yield of 2D structure devices.

1.4.2 Micro-Heater Unit

Over the past decade, great interest has been shown in low cost, fast response, low-power micro-heaters for a variety of applications [33]. In particular, micro-heaters (MH) and micro-hot-plates (MHP) are integrated with chemical and gas sensors for cycles of releasing chemicals and maintain working temperature [34-40], humidity sensor [41, 42] and MEMS micro fluid pumps for ambient temperature setup [43]. They can also be used

in medical care, to deliver aerosol drugs and delivery through inhalation [44-46]. Moreover, they can be powered by high charge-capacity, light weight, flexible battery sources [47, 48]. Several early micro-heater designs had been reported using thin-films such as poly-Si to fit in CMOS process [49, 50]. Recently, platinum [41, 51] or Platinum wire pattern based metal combinations (Pt/Ti, Pt/Cr, Pt/Al_2O_3 or Pt/MgO) have been widely explored [34-37, 40]. However, for the low cost in this gas sensor system and for other possible applications, we choose nickel. It has 34% less electrical resistivity and 27% more thermal conductivity comparing to platinum, and is much cheaper. There is no report that I have found on nickel heater elements. The well controlled electroless Nickel plating method is another low cost process for depositing thick metal heater patterns. A low cost micro-heater for aerosol generation has been developed using thin-film deposition, electroless metal plating and selective wet etching technology. The heating element is fabricated by e-beam evaporation and solution based nickel plating. The metal pattern temperature reaches the boiling point of glycerol (290 ℃) and higher. This structure and the use of a plating bath and wet etch render the device remarkably low cost (less than 2 ¢ per device). This MH successfully integrated with gas sensors to assist desorption of unwanted checmicals. Other applications of the MH design in medical procedures, such as aerosol generation and drug inhalation therapy are also explored.

1.5 Contributions and Accomplishments

Gallium nitride (GaN) nanowires functionalized with titanium dioxide, platinum-titanium dioxide composites, tin dioxide, iron oxide and tungsten trioxide were investigated, optimized and developed to selectively detect hydrogen, nitrogen dioxide, aromatic compounds, and ammonia. These are integrated with a micro heater that uses low cost metal deposition method and wet etch process techniques for assistance in chemical release cycles. The micro heater can be used for medical drug inhalation and aerosol generation purposes as well. All the fabrication processes were designed and optimized to be capable of reliable wafer batch production and homogenous device performance. Processes developed include the top-down approach of single NW arrays, MH formation, NCs and NPs deposition. A comparison between mass-production orientated processes [52, 53] and individual-chip-alignment based processes [54-58] is listed in Table 1.2 and Table 1.3 for NW and NCs formation respectively. I summarize the efforts performed in completion of this thesis as follows:

1. I demonstrated a dry etched "top-down" fabricated structure showing features aligned in a horizontal plane parallel to the wafer surface, as shown in figures on the left side of Table 1.2. Previous technique use molecular beam epitaxy (MBE) to grow nanowires vertical up (perpendicular to) the wafer surface. Placement of these vertical structures is rather random across the surface, as shown in images on the right side of Table 1.2, These features must be released from the surface, and subsequently placed on another substrate (either individually or in bundles by dielectrophoresis.) Dielectrophoresis is an electromagnetic wave NW alignment

technology that applies a RF voltage bias on the sides of solution through electrodes. The solution has NWs dispersed in it. The "top-down" dry etching method developed here uses the stepper/scanner lithography system to define the nanowire patterns, followed by inductively coupled plasma (ICP) dry etch. By this method, the NWs are identical in arrays and sensor fabrication can be easily integrated and mass produced.

2. I developed methods for removing sidewall defects and roughness caused by ion bombardment during dry etching. The potassium hydroxide (KOH) and phosphoric acid (H_3PO_4) wet etch can remove the defects appearing as linear vertical texture along the NW sidewalls that inhibited previous attempts at creating dry etched NWs from succeeding.

3. I demonstrated a nanocluster formation method and I designed a fast characterization method using IV conductance measurement and ellipsometry techniques besides SEM imaging. Further optimization of titanium dioxide, tin dioxide, iron oxide, tungsten trioxide NCs was accomplished. Previous work on NCs rely on chemical formation of powders, the NCs formation method in this thesis used physical vapor deposition (PVD) followed by rapid thermal annealing (RTA) which can be fully integrated with modern CMOS processes. This PVD-RTA method has advantages in NCs coating uniformity and compatibility to dynamic structures as the comparison shown in Table 1.3. The characterization technique is fast, reliable and non-destructive compared to SEM imaging.

4. I did the design of experiments leading to the establishment of a gas sensing database starting with TiO_2, SnO_2, WO_3, Fe_2O_3, TiO_2-Pt, etc. Metal-oxide thin-film

sensors were fabricated and tested by being exposed to various target gases. Responsive and non-responsive materials were determined and were recorded in a database.

5. I developed an electroless nickel plating process to create thick Ni layers from a seed layer. This technique allows precise control of the final thickness of a film far thicker than would be allowed by lift-off. Moreover, the chemical solution bath is much lower cost comparing to high-vacuum equipment. This method was used in the micro-heater process that can be integrated with gas sensor and provide heat to augment the chemical release cycle. The inexpensive and easily fabricated micro-heater thus developed allows for easy mass productions. This heater can be used in aerosol generators and fabricated as a single device for drug inhalation therapy.

6. I developed a process integration scheme for including all three micro- and nano-structures into a single NWNC hybrid sensor device. Integration considerations including the process flows, RTA, multiple passivation layers, NW yield improvement, active opening windows, passivated control elements and ohmic contact improvement were studied in detail. The techniques for multiple sensors integration into a single sensor chip were first time reported. These enables the simultaneously multiple gas sensing capability of a single sensor chip. I developed a process integration methods for including multiple gas sensors in a single chip for simultaneously sensing of variety of gases.

7. I characterized the fully integrated nanowire-nanocluster hybrid gas sensor and micro-heater system. Most of the sensor units work at room temperature without the need of heating assistance which ensures low power consumption. The sensor's

fast response and recovery behavior maintained after many sensing cycles. This implies that the developed technology has several advantages like low power consumption, long life time reliability, high sensitivity and selectivity in sensing performance. The micro-heater allows for improved gas desorption and the use of high temperature sensors.

The NWNC gas sensor fabricated can achieve high selectivity and sensitivity. Integrated MH helps improve the reliability and the life-time of the sensor and assists desorption of absorbed chemicals. Table 1.4 lists the performance of GaN / TiO_2-Pt NWNC hydrogen sensor technology comparing to other novel hydrogen gas sensing devices currently under developing. The significant features and advantages of the integrated sensors are:

i. Room temperature sensing as well as high temperature thermal sensing is possible.

ii. Selective sensing of low gas concentrations.

iii. Reliable and repeatable sensing and an ability to recover back to the same baseline signal level as opposed to baseline drift and limited lifetime.

iv. Fast respond and short recovery time.

v. Capable of cheap mass production and integration with existing CMOS processes, as opposed to the individual nanowire pick-and-place fabrication. This improves throughput, reproducibility and yield.

vi. The MH utilizes a low cost micro fabrication process to achieve fast respond and a robust heating function. The MH can be integrated into sensor devices for gas sensing assistance as well as individually used in aerosol generation and medical inhalation applications.

Comparison Lists	Top-Down Fabrication (mass-production oriented)	Bottom-up Fabrication (individual-chip based)
NW Formation/Growth	Subtractive process from thin-film	MBE / HVPE / Sol-gel NW growth
Homogeneity Control: Length Diameter Orientation Shape flexibility	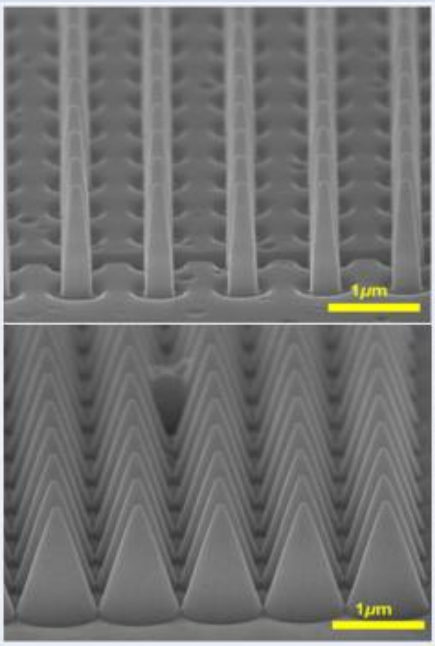	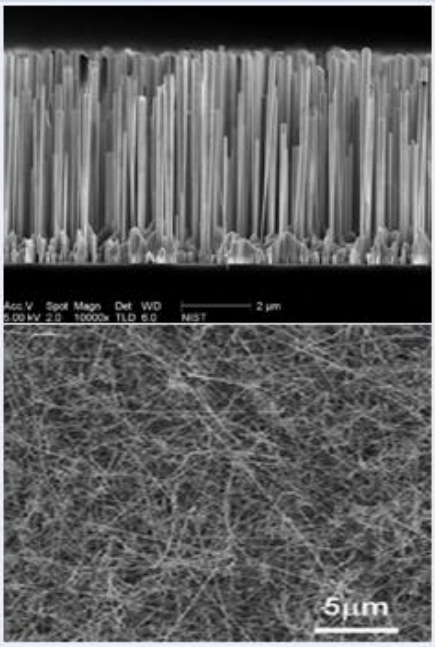
NW Alignment	Pattern-defined array Alignment-free	Up-detachment Individual-chip-alignment
Homogeneity Control: Yield Effective Length	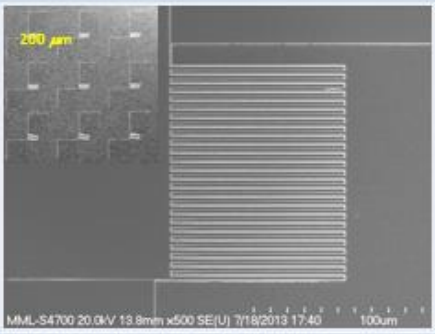	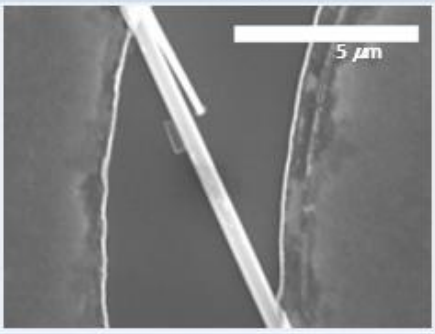
NW Contact	Planer contact Large effective contact area	High aspect ratio contact Small effective contact area
Homogeneity Control: Yield Contact Area Contact Resistance	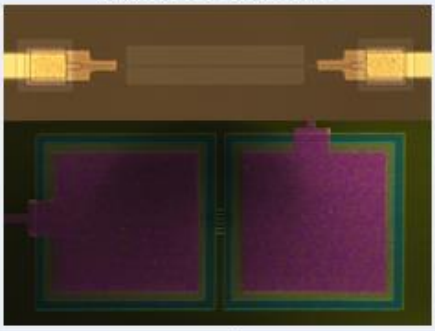	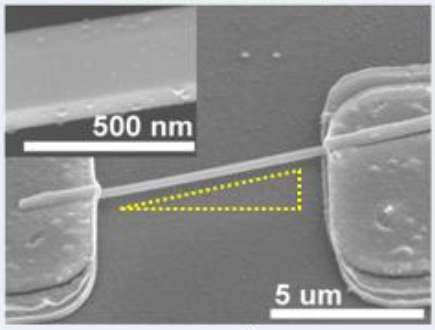
NW Summary	Less processing steps High compatibility and homogeneity Capable of wafer-level production	Grow-detach-align steps High chip-to-chip variation Single device process

Table 1.2 Mass-production orientated processes vs. individual chip based processes for NW

Comparison Lists	Deposition Fabrication (dynamic wafer structure oriented)	Spin-Coating Fabrication (Planer wafer based)
NCs Formation/Growth	Sputter and Rapid Thermal Anneal Process	NCs Dispensed Solution Spin-Coating Process
NCs Control: Size Conformity Surface Coverage Phase & Orientation	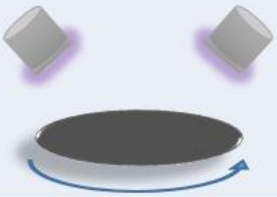	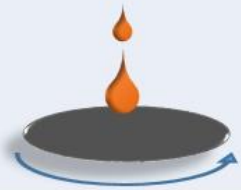
	 *Uniform coverage density along the wafer*	 *Decreasing density from center to edge*
	Conformal deposition over dynamic structure 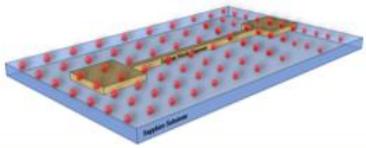	*NCs stack at the high aspect ratio structure* 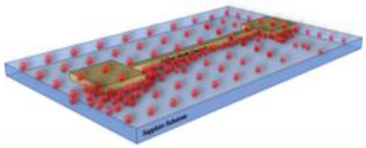
NCs Summary	Flexible NC size and phase control Uniform coverage regardless of wafer structure High cost for vacuum instruments (sputter)	Standard NC size and phase, no control Uniform coverage only on planer wafer Low cost for spinner and hot-plate

Table 1.3 Mass-production orientated processes vs. individual chip based processes for NCs

	Fabrication Method	Carrier Gas	Selectivity / Sensitivity	Detection Range	Working Temp.	Response / Recovery Time	Ref.
GaN NW / TiO_2-Pt NC	Top-down etched NW / PVD NCs	Breathing Air	High / 75% - 450%	500 ppm – 500,000 ppm (50%)	Room Temperature	30 s / 60s	This work
Pd doped WO_3 film	Sol-gel process	Breathing Air	Not mentioned / 1 -10,000	1000 ppm (0.1%)	100 ℃ – 300 ℃	100 s / 100 s at 300 ℃ to 10 s / 10 s at 100 ℃	[59]
Pt coated WO_3 film	Hydro-thermal grow	Dry Air / Pure N_2	Not mentioned / 5 -16	1000 ppm – 1%	Room Temperature	15 min / 15 min	[60]
Pt-WO_3 film	Co-sputter deposition	Breathing Air	Not mentioned / 3.8 - 26	50 ppm – 200 ppm	95 ℃ – 220 ℃	0.6 / 8.6 min at 220 ℃ to 4.5 / 30+ min at 95 ℃	[61]
Pt coated GaN NW	CVD growth	N_2	Not mentioned / 12%- 14%	10 ppm – 3000 ppm	150 ℃	2 min / 5 min	[62]
ZnO nanowire	MOCVD grow-detach-disperse-align	Ar	Low (H_2, O_2) / 90%	500 ppm – 4000 ppm	Room Temperature	55 s / cannot fully recover	[63]
TiO_2 nanotube	Hydro-thermal grow vertically	N_2	Low (H_2, O_2) / 10 - 20	100 ppm – 5,000 ppm	150 ℃	65 min / 65 min	[64]
Pd nanowire networks	Porous membrane mask	N_2	Not mentioned / 0.1% - 10%	100 ppm – 50,000 ppm (5%)	Room Temperature	10 s - 100 s / 10 s - 100 s	[65]
Pd coated graphene	CVD / Evaporation	N_2	Low (H_2, O_2)/ 1% - 33%	20 ppm – 1000 ppm	Room Temperature	1 - 5 min / 2 - 10 min	[66]
Pd coated SnO_2 nanofibers	Eletro-spinning and sintering	Breathing Air	ultralow (CH_4, CO, NH_3, H_2, C_2H_2, ethanol, toluene and acetone) / 1% - 30%	20 ppm – 1000 ppm	Room Temperature – 320 ℃	2 s – 13 s / 2 s- 7 s	[67]
Pd contact Si nanowire	CVD grown NW	Breathing Air	Low (H_2, NO_2, NH_3)/ 1% -33%	10 ppm – 50,000 ppm (5%)	Room Temperature	30 min / 60 min	[68]

Table 1.4 Comparison of the current state of the art hydrogen sensors

1.6 Organization of the Dissertation

This dissertation has been presented in eight chapters.

Chapter 1 (this chapter) gives a brief overview to readers about this whole dissertation. I start with the importance of chemical gas sensors and how to characterize a typical gas sensor, followed by a review of current gas sensor technologies with corresponding limitations and bottle necks. A proposal design for developing the high performance sensing device was discussed for each unit in brief. Contributions and accomplishments of this work have been highlighted towards the end of the chapter.

Chapter 2 gives the background reviews of current nanotechnology, develops in nanowire and nanoparticles. Semiconductor nanowire has been used widely in sensing application since the past decade. General properties of gallium nitride bulk and nanostructure materials are discussed in brief. Metal-oxide and thin-film sensors have been studied for more than three decades and the properties of metal-oxide nanoparticles are briefly reviewed. Some literature review of the nanowire-nanocluster hybrid sensors is presented and discussed.

Chapter 3 presents the formation of a single gallium nitride nanowire, from step-by-step fabrication details of the nanowire arrays to ohmic contact formation. The wet etch post treatment was discussed in detail to remove the surface damage caused by dry etching. The single-nanowire two-terminal device as a UV detector was presented.

Chapter 4 presents the formation of the metal-oxides nanoclusters and describes the surface morphology, structural, electrical and optical characterization effort for optimizing

and analyzing the nanoclusters. The same metal-oxide deposition methods are used to fabricate thin-film gas sensors and photodetectors.

Chapter 5 describes the micro-heater development process. The chapter also describes other disposable applications beyond heating assistance in gas sensing system. Four different types of low cost micro-heaters were presented. Nickel plating bath and wet etching techniques were briefly discussed.

Chapter 6 shows the overall process integration of the micro-heater unit and nanowire-nanocluster gas sensing unit. Extra protection layer and passivated designs are used. The fabricated device layout and packaging steps were presented. Methods to integrate multiple sensors on a single chip were covered.

Chapter 7 makes an attempt to present the gas sensing measurement set-up and the performance of the different gas sensors. This chapter also provides explanations of the sensing performance and proposes a sensing mechanism based on the current literature and observed trend on the devices fabricated in this work.

Chapter 8 summarizes this research and presents a path to future research efforts related to the work. Possible applications of this sensor technology and emphasis the importance of further understanding and which could be of interest of future research.

Chapter 2: Background

This chapter presents the background for understanding the key component, important concepts and materials, physical principals and chemical mechanisms behind the gas sensing with semiconductor nanowires and nanoclusters. The detailed literature reviews of sensing technology as well as the NWNC sensing technology are included here.

2.1 Nanomaterials, Nanowires and Nanoparticles

Nanomaterials and nanostructures are defined as having at least one critical dimension that is 10 nanometers or less. For the purpose of this thesis, a nano-metric device is one whose dimensions are conveniently expressed in nanometers. At the nanoscale level, the physical, chemical, and biological properties of materials differ very much from the properties of the bulk matter [69-71]. The different properties enable the development of high density and complex functional materials and systems, which in many ways can improve our daily lives.

Nanowires are one-dimensional structures that are cylindrical in shape, with length to diameter ratios often greater than 10 ³ Nanoparticles are zero-dimensional particles sized range from 1 nm to 100 nm. Nanowires and nanoparticles are highly functional structures with unique properties originate from their low dimensionalities [72-74]. Nanowires can be grown without any substrate, which result in no lattice mismatch and coefficient of thermal expansion (CTE) mismatch in these structures. So idea grow nanowires are free from strain, dislocations, and other structural defects. Due to their high surface to volume ratio property, nanowires are widely used in applications such as photodetector [75-77],

optical switch [78-80], ultraviolet nano-laser [81-83], biological sensor [84-86], chemical sensor [84, 87-89], solar cell [90-93], etc. In the cases of gas sensors, conduction through the nanowire is strongly affected by the chemical species adsorbed on the nanowire surface [94-97]. This property enables us to develop highly sensitivity chemical, gas and biological sensors as well as provide effective heat conduction and convection. As NWs can be dry-etched through top-down approach from thin-films defined patterns by lithographic methods, they have the capability of integration with any developed Si fabrication plant. This opens up the possibility of integrating III-V compound semiconducting nanowire devices with conventional CMOS microelectronics. Detailed advantages of this fabrication method are listed in Table 1.2. Reduced dimensionality enhances optical, electrical and chemical properties of the nanowires. Nanoparticles research raises intense studies in application in biomedical [98-101], optical [102, 103] and sensing field [104-106]. Nanoparticle is the material size in between bulk and atomic or molecular levels. At this level, the surface properties of a material become significant. The interesting and unexpected properties of a material in the nanoparticle from are largely due to the large surface area to volume ratio. There are many way to synthesis nanoparticles, including attrition [107, 108], pyrolysis [109-111], hydrothermal [112-114] and sol-gel [115-118]. The PVD-RTA synthesis method developed in this dissertation maintains the nanoparticle uniform and is compatible with modern CMOS microelectronic processing platforms. Detailed advantages of this fabrication method are listed in Table 1.3.

2.2 Semiconductor Nanowires for Gas Sensing

Molecular trapping on nanowire surface changes the electrical properties (conductivity/resistivity) of the nanowire. For gas sensors, current will change when exposed to target analytes. Sensing properties of nanowire formed by silicon [119, 120], metals [121, 122], metal-oxides [123, 124], and polymers [125, 126] have been studied and reported. All prior studies successfully demonstrated that the nanowire sensors show enhancement in superior sensitivity, response time and catalytic efficiency because of large surface to volume ratio improve the reaction speed and provide more bonding sites. However, due to surface interaction of bare nanowire and gas are limited and non-specific, similar to nanowires' bulk counterparts, bare nanowire exhibits the same lack of selectivity. Metal-oxide materials have good selectivity to certain type or group of chemical analytes. To maintain the high sensitivity and short respond time, nanoparticles and nanoclusters decoration on the nanowires structure are proposed to improve selectivity by the fine-tuned NPs and NCs surface bonding sites [127-129], these approaches will be discussed in later sections.

2.3 Properties of Gallium Nitride Nanowires

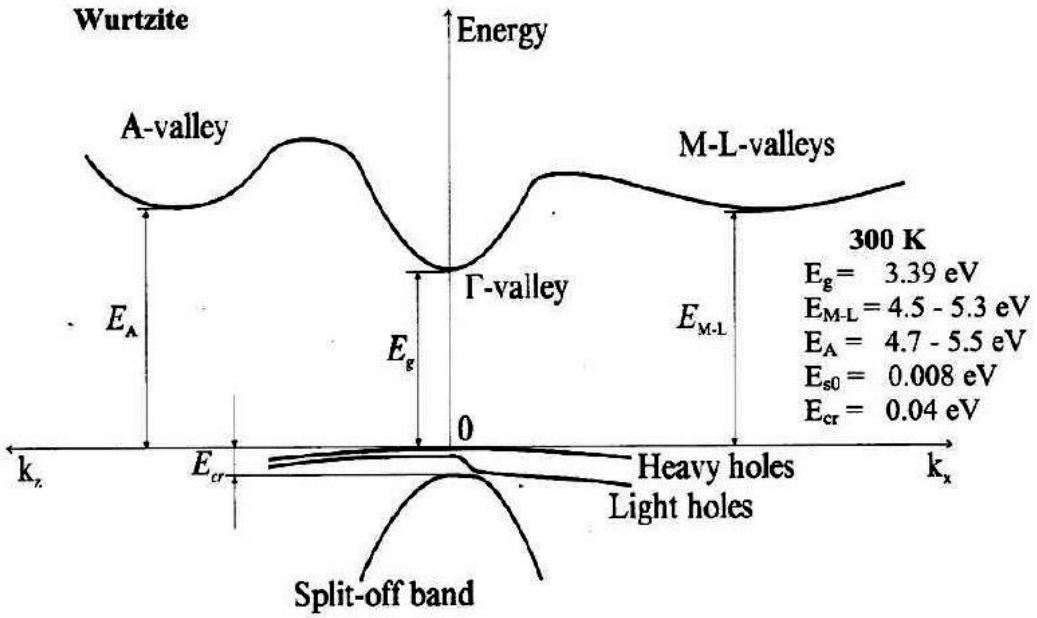

Fig. 2.1 Band Structure of wurtzite GaN

Gallium Nitride has direct band gap energy of 3.39eV at room temperature which is about 2 times higher than silicon or gallium arsenide (GaAs). Fig. 2.1 shows the band structure of wurtzite GaN [130, 131]. This wide band gap allows the GaN to work at high temperatures because the thermally driven electron-hole generation is low. The very strong gallium-nitrogen bond of GaN makes it robust and less vulnerable to corrosive chemicals and environment stress [132, 133]. GaN nanodevices are widely used in power electronics, space, and ultraviolet (UV) emission and high-temperature devices. GaN NWs of a range of bandgaps can be made by alloying and doping. This contrasts with carbon nanotubes with fixed bandgap. Also, carbon nanotubes still cannot be selective grown of semiconducting or metallic nanotubes [134, 135]. One of the advantages that GaN over

other III-V compound semiconductor is that (unlike GaAs or InP) GaN has a low density of surface states, which will not pin the surface Fermi-level at a characteristic value. So GaN will lead to have a low minority carrier surface recombination velocity. So depositing different metal catalysts will have different surface depletion effects, which in turn will enable us to personally tailor the selectivity to certain analyte.

To maximize the sensitivity of bare GaN nanowire sensors, the critical dimension of the nanowire (diameter) should have some dimensional restrictions. If were sensing changes in mobile charge density in accumulation layers, the sensor film thickness should be at most twice the extrinsic Debye length. The extrinsic Debye length, L_D, for a semiconductor is defined as:

$$L_D = \sqrt{\frac{\varepsilon K_B T}{q^2 N_d}}$$

Where ε is the dielectric constant, k_B is the Boltzmann's constant, T is the absolute temperature in kelvins, q is the elementary charge, and N_d is the density of dopants (either donors or acceptors).

Similarly, of we are sensing changes in depletion thickness, the sensor thickness should be on the order of the depletion depth. This is of course, a function of background doping concentration and surface charge induced bias.

The GaN nanowire produced in this dissertation is n-type with donor density of $10^{17} cm^{-3}$. At room temperature, the Debye length for the nanowire is approximately 10 nm. The GaN nanowires grown by molecular beam epitaxy (MBE) technique produce random nucleation creating a wide range of densities and diameters even within a single

growth process. Optimized growth provides diameters in the range of 200nm to 350nm [58, 136-138]. This dissertation uses an MOCVD method to grow GaN thin-films for the top-down dry-etching. The catalyst-induced growth technique is better than the catalyst-free approaches. Because the MBE grows GaN always end up with un-intentionally n-type doping due to the volatile nitrogen species that generate the nitrogen vacancies [139]. MBE requires ultrahigh vacuum conditions and the relatively low growth temperature which reduces the surface atom mobility, leading to an increased defect density in the GaN epi-layer [140]. MBE grown GaN will provide very limited sensitivity due to the heavily doped n-type background and defect densities. A top-down etched nanowire structure method from an ultra-low doped and high quality MOCVD GaN thin-film is proposed to overcome this lack of sensitivity.

2.4 Metal-Oxides Thin-Film for Gas Sensing

In the field of gas detection, the use of thin-film metal-oxides helps achieve low cost, low power consumption, acceptable sensitivity and stability [141-143]. A typical thin-film metal-oxide gas sensor and the sensing behavior is illustrated in Fig. 2.2 [144]. The sensor structure is simple and easy for fabrication with interdigitated electrodes (IDE) deposited on metal-oxide thin-film. The metal-oxide sensors detect gases by the modulation of bulk or surface conductivity. This is reflected in the current flowing through the device. Metal-oxide gas sensors cover a wide range of detection capabilities including oxygen, explosive and toxic gases. However, so far, even the state-of-art level of metal-oxide gas sensors cannot solve the sensitivity problem and most of them need heating

assistance and require elevated working temperature. Sensitivity of the metal-oxide sensors is controlled by many factors. The sensor works by gases interacting with the metal-oxide. Under standard conditions, thin-film sensors exposed to oxygen or other reactants, these species absorbed on surface become charged, and deplete the surface of mobile charges. This formed space charge region usually reduces the effective conduction thickness of film. When the sensor exposed to a target gas, the absorbed oxygen will react through this depletion mechanism and cause further depletion or removal of the oxygen from the surface. A change of the effective conducting thickness is reflected in a reduced or increased conductivity, detectable by monitoring the current flowing through the film. Previous studies conclude three independent factors that controlled the thin-film sensors sensitivity: receptor function, transducer function and output resistance change as illustrated in Fig. 2.3 [144]. From the above described sensing mechanism, several conclusions can be made to summarize the mechanism of metal-oxide gas sensing:

- The smaller crystalline size and thinner and more porous the metal-oxide films enhance the effect of conduction channel thickness modulation. This makes the device more sensitive.
- It is important that the concentration of native surface states be minimized for a sufficient band bending modulation when metal-oxide responds to an analyte.
- To achieve good sensing, the metal-oxide should be chosen so that the activation energy of chemisorption on the oxide surface is small and the energy of desorption should be high. This insures that there is a stable amount of gas absorbed during sensing period. So many oxides cannot work as a chemical-resistive sensor as they do not satisfy this simple rule.

- Decorating the oxide with nanoparticles catalyzes the chemisorption of analyte onto the surface which lead to increasing of sensitivity, improving of sensing performance and tuning the selectivity.
- Many other factors like crystalline facets, porosity of the material, dopants, surface defects can influence the sensor performance as well.
-

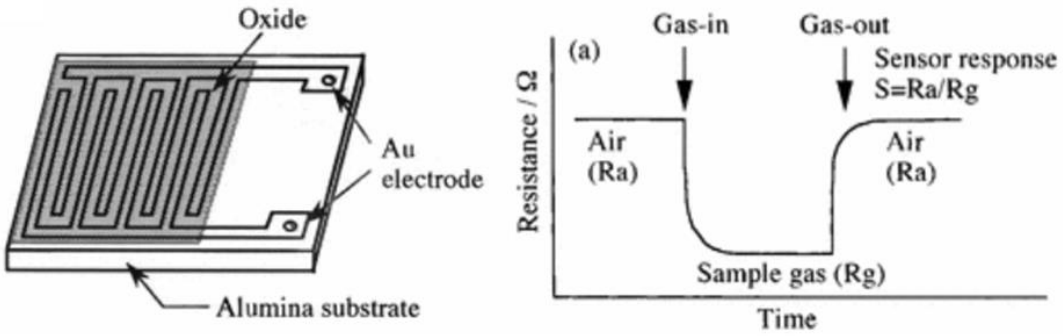

Fig. 2.2 Schematic diagram of a typical thin-film metal-oxide sensor and sensing behavior

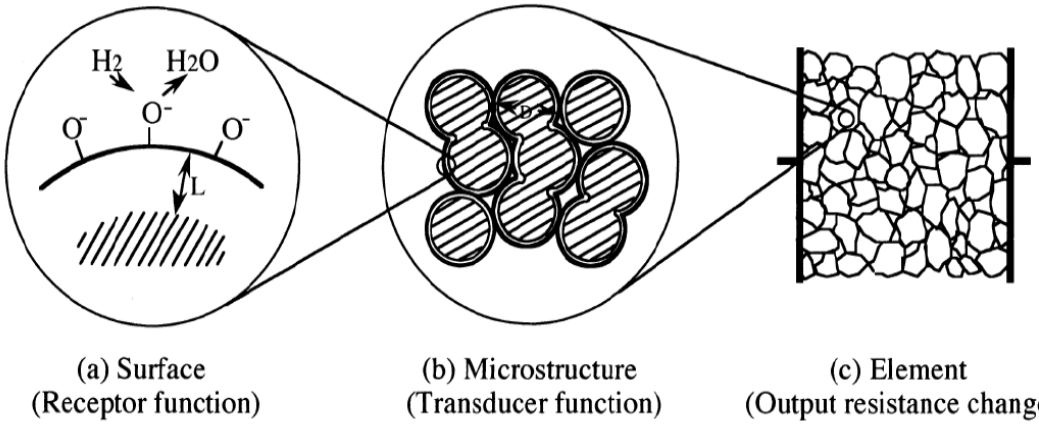

Fig. 2.3 Schematic diagram of the receptor, transducer and output resistance functions control the sensitivity of a thin-film metal-oxide gas sensor.

2.5 Properties of Metal-Oxide Nanoparticles

For the bulk semiconducting metal-oxide materials, the band gaps are normally wide and the material reactivity is low [145]. However, for nanoparticle (NP) sized metal-oxides, the band gaps changes with the decreasing of the material size and this band gap modulation affects the chemical reactivity [146-148]. Metal-oxide nanoparticles are small in size, have high surface to volume ratio and in high density of corner/edge surface sites which result in unique physical and chemical properties. Solid-gas reactions mostly occur at the surface, interface regimes and grain boundaries of the solid. For nanoscale metal-oxide, the unique structure and electronic surface properties result in a significant adsorption of analytes. Moreover, the presence of dominate phases, dangling bonds and oxygen vacancy sites in the oxide can enhance the chemical sensing selectivity of the system. One type of gas has different binding energies for different type of adsorption sites. The nanoparticle can achieve even higher and more efficient of conduction channel modulation than the thin-film nanostructure sensors. The presence of discrete atom-like electronic states also makes the nanostructure produces quantum confinement effects [149, 150].

2.6 Nanowire-Nanocluster hybrid sensing

For a bare nanowire (NW) two-terminal device, the sensitivity is limited by the wire diameter which is larger than Debye length and selectivity of the nanostructure is the same as bulk material. A nanowire-nanocluster (NWNC) hybrid sensor is made by decorating a NW surface with metal or metal-oxide nanoparticles (NPs) or nanoclusters (NCs). This enhances sensitivity and sharpens the selectivity. So, metal/metal-oxide NCs on a GaN NW will act as nanocatalysts, which will not only improve sensitivity and decrease the detection time, but also enable us to tailor the selectivity by using carefully selected metal/metal-oxide nanoparticles. Catalysts are used to lower the activation energy of corresponding reaction that produce ionized active radicals from the target absorbed analyte. And then the active radicals (e.g. H^+, O^-, OH^-) will spill-over to semiconductor surface with more effective charge carrier transfer. Spill-over and fermi-level control are the two very important effects when a catalyst put on a semiconductor surface [151-153]. Catalysts of metal deposited on the semiconductor surface will affect the Fermi-level of the material. A metal-semiconductor junction will form and the Fermi-level will be flat on the zero current state. The depletion region will be formed on the semiconductor, and the depletion width can be modulated by target gases molecules adsorbed on metal nanoparticles as long as the metal particle is small enough and the fermi-level of metal is sensitive to adsorbents. The current through NW will be modulated by the depletion region width [154-157]. Moreover, the NCs and NPs can create additional absorption sites on NW. By all means, NCs improve the sensitivity and tailor the selectivity of the NW sensing system. The NCs and NPs of metal-oxide can function as catalysts that lower the activation energy of a reaction, helping fast dissociate chemicals to active radicals and improve sensing respond time.

In recent years, many researches have reported hybrid gas sensing nano-structures utilizing metal or metal-oxide NCs and NPs and decorate NWs or nanotubes. Leghrib et al. reported gas sensors detect NO and CO by tin dioxide (SnO_2) NCs decorated on multiwall carbon nanotubes (CNTs) [158]. Duy et al. presented ethanol sensing at a working temperature of 250 ℃ utilizing mixed SnO_2 and TiO_2 clusters on single wall carbon nanotubes (SWCNTs) [159]. Balzsi et al. demonstrated NO_2 sensing with hybrid composites of hexagonal WO_3 powder and metal decorated CNTs at room temperature [160]. Kuang et al. reported an increase in the sensitivity to H_2S, CO, and CH_4 based on SnO_2 NW sensors by surface functionalization with ZnO and NiO NPs [161]. Zhang et al. utilized ZnO NWs decorated with Pt NPs to sense ethanol and got sensitivity three times higher than control group sensors that without Pt NPs decorations [162]. Chang et al. demonstrated ZnO NWs decorated with Au NPs to sense CO and got sensitivity enhanced significantly as well [127]. Dobrokhotov et al. designed GaN NWs decorated with Au NPs to sense N_2 and CH_4 [163]. Wright et al. fabricated Multiple GaN NWs decorated with Pd NPs for the detection of H_2 in N_2 carrier gas at room temperature [62].

All the above research indicates that the NWNC hybrid sensors are promising. However, there are still many challenges and barriers to overcome:

1. Most of the NWs are growing vertically by MBE/CVD methods, followed by sonication detachment and individually alignment to electrodes. These series of processes cannot maintain batch to batch uniformity. The yield issue and the non-repeatable device behavior are the bottle necks that hinder the gas sensor move to mass production.

2. Most experiments use high operation temperatures (more than 250 ℃). Only few reports show room temperature sensing, but the sensitivities reported are low and response time is long. Selectivity is limited to few numbers of chemicals.

3. Very few research groups use air as carrier gas. For most of cases, oxygen in air will affect sensing. However, ideally the sensor should detect target analytes in air.

Chapter 3: Gallium Nitride Nanowire

This chapter provides an overview of the proposed fabrication scheme for the single GaN NW array that subtractive processed by the top-down approach (dry / wet etching). Starting with a high-quality thin-film of GaN on sapphire wafer, followed by PECVD deposition of passivation layer, stepper lithography and ICP resistive metal mask deposition, ion milling and ICP dry etch. And KOH/H_3PO_4 wet etch post treatment was discussed in detail to remove the NW sidewall roughness and surface damage caused by former dry etching process. In the end, top contact metallization, bond pads deposition, packaging and wire bonding will be discussed for later characterization purpose. The single-nanowire two-terminal device has excellent UV detector behavior.

Gallium Nitride (GaN) is a versatile semiconductor used in optical devices (light-emitting diodes, laser diodes, UV sensors) and in power electronics (power switches, RF devices, and high power transistors) [164]. Due to its direct band gap and chemical and thermal stability, GaN nanowires (NWs) are gaining significant importance as chemical sensor elements [163, 165, 166].

To date, most of GaN NWs devices are fabricated using chemical vapor deposition growth with a follow up detachment from the substrate and individual on-chip alignment. Due to the variation in morphology, dimensions, doping, and crystal quality, it is hard to control the quality of NWs grown via the bottom-up methods [167]. Besides, variations from a multi-step pick-and-place fabrication process result in a low yield of functioning devices. Thus, such a process has poor wafer-level integration capabilities, rendering mass-manufacturing challenging. An alternative approach to overcome these drawbacks is “top-

down fabrication", in which NWs are patterned on a uniform thin-film using standard lithography and etching. Vertically-aligned semiconductor NWs (nanorods, nanopillars or nanocolumns) have been demonstrated by such top-down methods [53, 168-171]. The heights of these nanostructures are limited by the thickness of the starting thin-film material, and they often exhibit tapering as a result of etching. On the contrary, horizontally-aligned NWs can be fabricated without any length limitations. For photodetectors and photovoltaic devices, vertically-aligned nanowires represent a high efficiency platform, whereas for chemical sensors horizontally-aligned nanowires are the optimal choice [84, 172, 173]. Due to its inherent inertness to most wet chemical etches, GaN nanostructures are commonly produced using dry etch techniques. However, high-aspect ratio GaN structures achieved by plasma etching are often associated with extensive side wall damage, result in lower performance of the device [174].Therefore, producing damage-free nitride structures with a precisely-defined geometry over large area remains a challenge.

By combining deep-UV projection lithography and inductively-coupled plasma (ICP) etching, this thesis demonstrates horizontally-aligned NWs etched from a GaN thin-film grown on sapphire. Since the rough and tapered NW sidewalls due to dry etching create leakage current and limit NW performance [174], a post ICP potassium hydroxide (KOH) wet etching procedure was developed to smooth the NW walls. The KOH etching also allows us to control the final shape and dimensions of the NWs. The PL and current-voltage (I-V) results verify the improved performance resulting from the KOH treatment.

The top-down approach described here can potentially enable GaN NW and SMW to be integrated with LED, micro-pumps, and micro heaters for system-on-chip

development [55, 56, 175-178]. Different types of sensors such as chemical, gas and bio sensors can be fabricated using the top-down method.

3.1 Fabrication of GaN Nanowire

In modern nano-electronic and micro-electronic manufacture industry, a general fabrication technique should have the following desirable characteristics: availability to batch fabrication, compatibility with standard CMOS silicon process and suitability for a wide range of nanowire materials besides gallium nitride. So far, many literature reports on e-beam lithography, focused ion beam (FIB), atomic force microscopy (AFM) and Dielectrophoresis manipulation and alignment of NWs, however, all of them cannot well fulfill above properties. The stepper/scanner projection lithography followed by inductively coupled plasma (ICP) etch and KOH wet etch polishing can achieve the high yield and reproducibility on nanowire fabrication. The fabrication of well-defined and aligned NW by dry etching is shown in the process diagram Fig. 3.1 and Fig. 3.2. Fig. 3.1 is a lift-off process and Fig. 3.2 is the alternative etch-back process. The following section demonstrates a high-throughput fabrication method of gallium nitride (GaN) nanowire (NW) and sub-micron wire (SMW) arrays using a combination of projection lithography, plasma etching, and post-plasma wet etching techniques. Photoluminescence (PL), field emission scanning electron microscopy (FESEM), and I-V measurements were used to characterize the GaN NW/SMW devices. These NWs/SMWs can be used to create highly-sensitive and selective conductometric chemical/bio-sensors.

The length and width of the wires can be precisely customized. The length of the NW/SMW varied from 5 μm to 5 mm and the width ranges from 100 nm to 500 nm. Such comprehensive control in the geometry of a wire is difficult to achieve with other fabrication methods. The post-plasma KOH wet etching greatly reduces the surface roughness of the GaN NW/SMW as well as improves the performance of devices. Complementary metal–oxide–semiconductor (CMOS) and micro-electro-mechanical system (MEMS) devices can be incorporated with GaN NW/SMW arrays on a single chip using this top-down fabrication method.

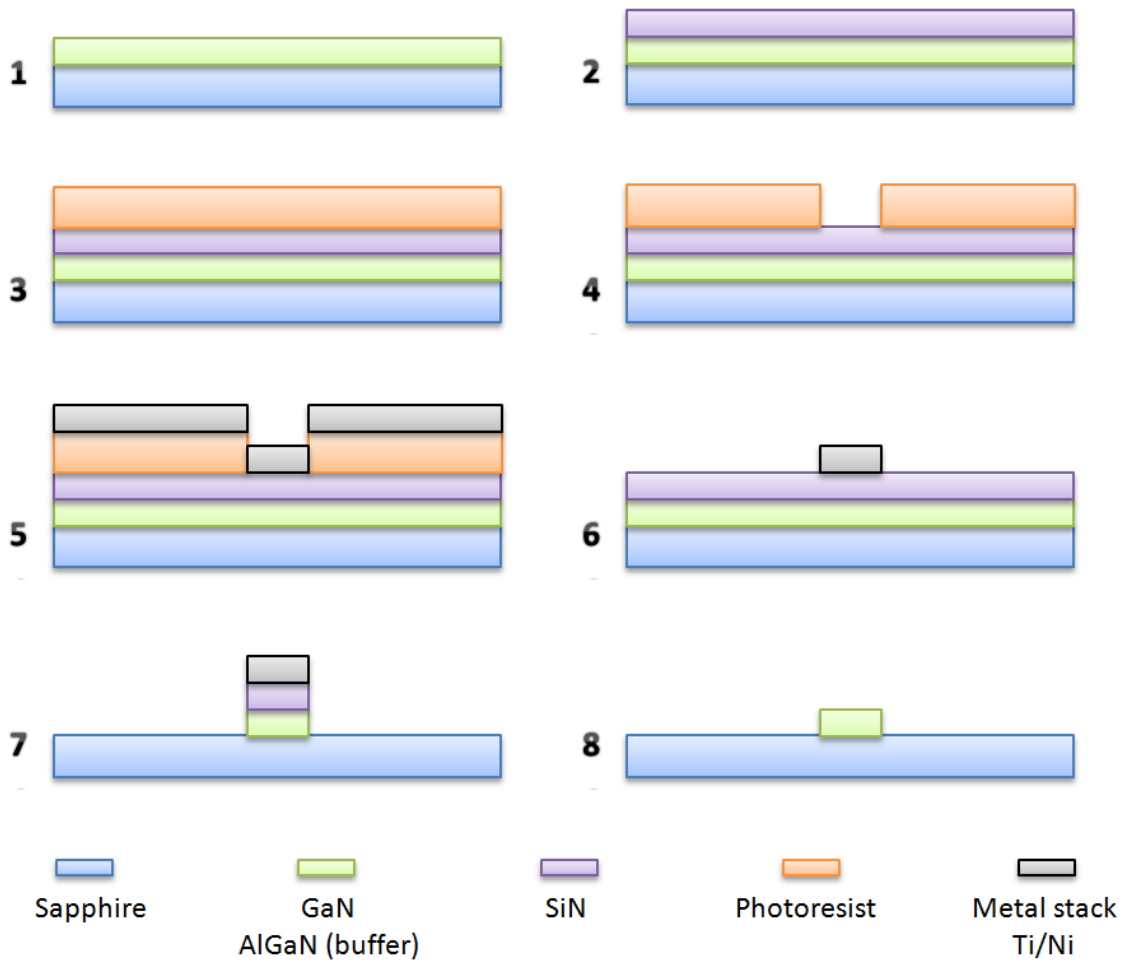

Fig. 3.1 Schematic representation of the nanowire fabrication (metal mask by lift-off) process flow: (1)RCA cleaning of GaN on sapphire wafer, (2) SiN etch-mask deposited using PECVD, (3) spin-coating of photo-resist stack of LOR3A and Ultra-i, (4) lithography use positive mask and development, (5) metal deposition by e-beam evaporator, (6) lift-off in 1165 photo-resist remover, (7) ICP etching to transfer the patter on GaN, (8) HF etching, RIE etching to remove metal and SiN etch masks, followed by subsequent KOH wet etch treatment.

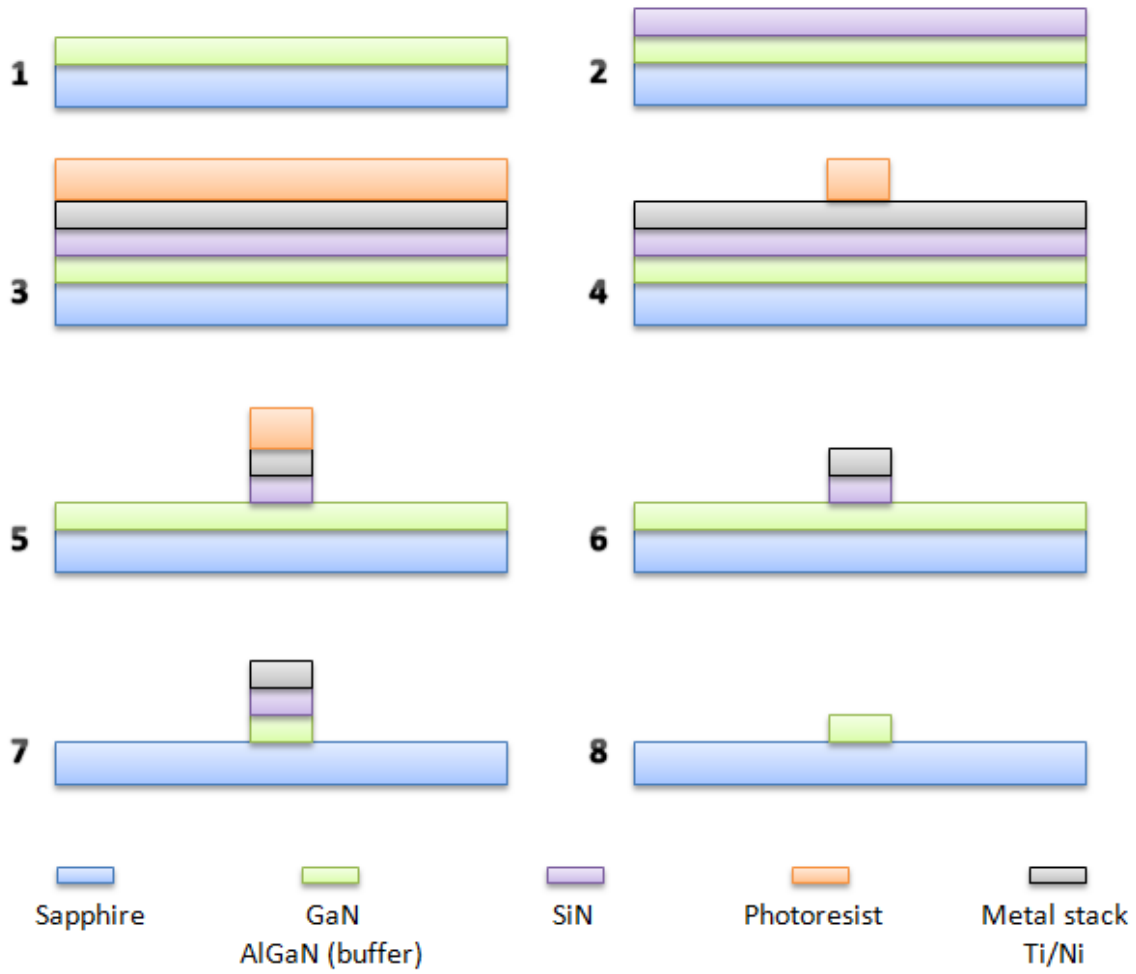

Fig. 3.2 Schematic representation of the nanowire fabrication (metal mask by etch-back, subtractive) process flow: (1)RCA cleaning of GaN on sapphire wafer, (2) SiN etch-mask deposited using PECVD, (3) metal deposition by e-beam evaporator, spin-coating of photo-resist stack of LOR3A and Ultra-i, (4) lithography use negative mask and development, (5) metal mask etching by ion-milling (6) remove photoresist by 1165 photo-resist remover, (7) ICP etching to transfer the patter on GaN, (8) HF etching, RIE etching to remove metal and SiN etch masks, followed by subsequent KOH wet etch treatment.

3.1.1 GaN Thin-Film Growth

The thin-film growth of the base gallium-nitride was carried out at NTT Advanced Technology Corporation, Japan. Two different thicknesses of commercial intrinsic GaN epitaxial layers (NTT Advanced Technology) grown on c-plane sapphire were used in this study: 3 μm thick GaN films were used for characterization of the etch rate of ICP dry etching, optimization of wet etching and measurements of PL spectra; 1 μm thick GaN films were used in the optimization of the wet etching process as well as in I-V characterization. AlGaN is a buffer layer widely used to compensate lattice mismatch and reduce stress in the growing film, and thereby improves the crystalline quality of GaN on sapphire. For photodetector device, the layer structure is conventional high quality undoped 1um GaN epitaxy growth on sapphire substrate with buffer layer of 500nm thick AlGaN. The composition of Al is 0.2 in AlGaN.

3.1.2 Wafer Preparation

The starting material is a two-inch wafer of unintentionally-doped (UID) GaN on sapphire substrate with a-plane orientation. The wafer is rinsed in Acetone, Methanol and then Isopropanol (IPA) with ultra sound sonication for 2 minutes each solvent. The samples are rinsed, removing any unwanted debris and now ready for standard RCA cleaning. This is a standard cleaning procedure in semiconductor manufacturing. The substrate preparation is as follows:

i. Immersion in RCA-1 solution formed with volume ratio of 5:1:1 H_2O (DI Water) + NH_4OH (Ammonium Hydroxide) + H_2O_2 (Hydrogen Peroxide) at 80℃ for 10 minutes to remove insoluble organic residues.

ii. A quick immersion into 50:1 solution of H_2O + HF for removing thin oxide layer formed in last RCA-1 step.

iii. Immersion in RCA-2 solution formed with volume ratio of 5:1:1 H_2O (DI Water) + HCl_2 (Hydrochloric Acid) + H_2O_2 (Hydrogen Peroxide) at 80 ℃ for 10 minutes to remove metallic residues.

In between each two steps, transfer wafer to DI water bath to clean surface solution residues.

3.1.3 PECVD Passivation Layer

After cleaning the wafer, a passivation layer of 50nm SiNx is deposited uniformly on the wafer by plasma enhanced chemical vapor deposition (PECVD, Plasma-Therm Versaline). PECVD is a common technique used in insulating and passivation purpose quality layers for SiNx, SiO_2, amorphous and polycrystalline silicon. PECVD is relatively cold process with normal deposition temperature of 100 ℃ to 300 ℃ and uses energetic electrons from the plasma to dissociate the precursor gases. In my process an even lower temperature of 80 ℃ is used to deliver a fast deposition rate of 2nm/s. Normally the leakage current in PECVD oxides is higher than other high temperature CVD processes. So the PECVD formed thin-films cannot be used as a functional oxide such as MOSFET gate oxide. However, this is not an issue in my design as the layer is merely a passivation for protection of the GaN surface from metal mask (Ti) penetration caused contamination. The layer of SiNx will eventually be removed after ICP dry etch. In our optimization, 50nm PECVD SiNx is good enough to prevent ICP high-energy ions penetrate with Ti into GaN

surface. The thickness of PECVD is double proofed by Nanospec Reflectometer (Nanometrics) and ellipsometry studies.

3.1.4 Stepper Lithography

Stepper lithography is a well-developed nano-scale patterning technique used in mass production. It is highly efficient and less sophisticated than e-beam lithography. An ASML i-Line stepper (PAS 5500/275) is used for this process. A resolution of 280nm can be achieved with this tool. Stepper lithography definition of the NW structure starting with spin photo-resist and the detailed processes are shown below:

i. Pre-bake wafer at 210 ℃ for 10 minutes to remove water and organic residues. Cool down wafer and nitrogen blow dry.

ii. A bi-layer stack of photoresists (MicroChem LOR3A and Ultra-i) were used to support a lift-off process for the metal shadow mask structure. Spin coating of LOR3A at 4000 rpm for 45 seconds followed by 5 minutes bake at 210 ℃ was used. After cool down, a spin coated Ultra-i (4000 rpm for 45 seconds followed by 90 seconds bake at 90 ℃) layer was installed.

iii. Stepper lithography with wafer bonding: bond a 2-inch wafer onto a carrier wafer, deep UV exposure with a 570 mJ/cm ^{2}of dose energy.

iv. Post-bake on 110 ℃ hot plate for 90 seconds, cool down and followed by develop in Microposit MF-26A for 60 seconds. Rinsed in DI water and after this step the windows for metal deposition are opened.

v. Reactive-ion Etching (RIE, Unaxis 790) and descum with a 30sccm flow rate of oxygen for 45 seconds to clean up the un-thoroughly developed resist residue.

3.1.5 Shadow Mask Metal Layer Deposition and Lift-Off

A bi-layer metal stack (50nm of titanium and 120nm of nickel) is used to form the shadow mask. Titanium is a good adhesive layer between GaN and nickel, and nickel is resistive under ICP chlorine etching. The Denton Infinity 22 E-beam Evaporator is used to deposit the metal. After deposition, wafers were immersed in 1165 or remover PG solvent with gentle Q-tip sweep for lift-off. Clean with acetone, methanol, IPA and DI water.

3.1.6 ICP Chlorine Dry Etch

An Oxford Plasmalab 100 is used in the ICP etching process, with a combination of 25 sccm of Chlorine, 5 sccm of Nitrogen and 1 sccm of Argon under condition of 40 ℃ temperature, 5 mTorr pressure, RF power of 300W and ICP power of 800W for 5 minutes. Several GaN layers (3 μm thickness) were ICP etched for different times to calibrate the etch rate. The etched thickness was measured by a profilometer and the data summary is shown in Fig. 3.3. Black dots show the original data, and the regression linearization analysis (green line) gives the dry etching rate of 428.9 nm/min. Based on this rate, an 3 min etching was performed on the 1 μm GaN/500 nm AlGaN films to fabricate the nanowire devices. The AlGaN etch rate is slightly slower than that of GaN, due to the sapphire is pretty resistive to chlorine etching, a little over etching estimation time was used. And in this ICP etch process, the SiNx un-covered by Ti/Ni layer is easily etched away at the beginning of the process. So, in consideration of these two reasons, the optimized etch time is set to 3 minutes.

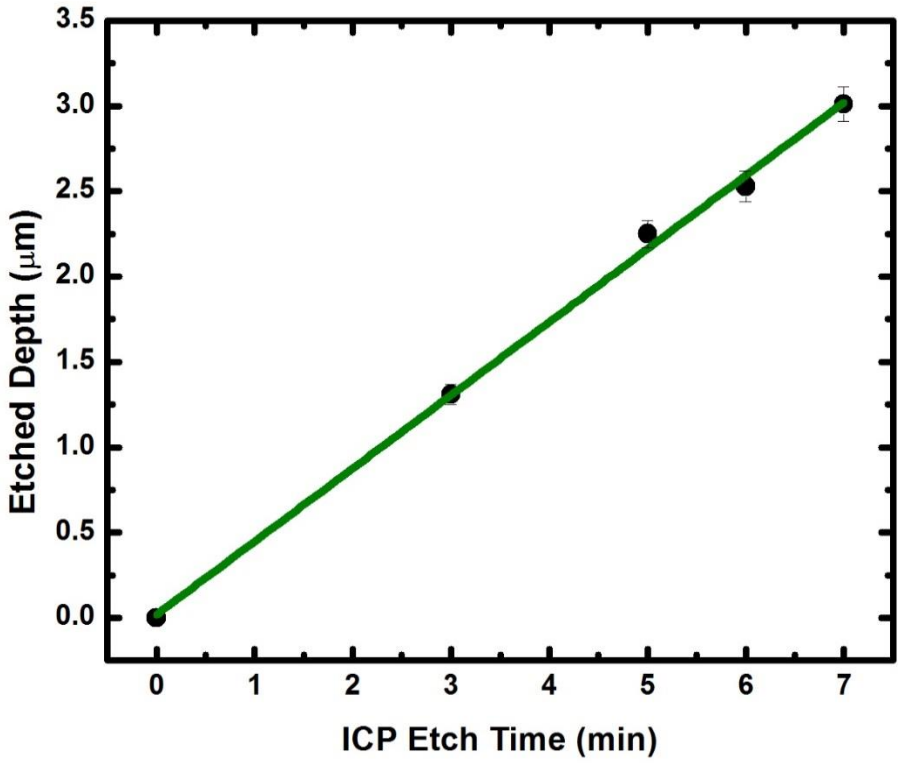

Fig. 3.3 ICP etch depth as a function of the etching time

(The original data are shown by black dots, and the linear fit presented by the green line)

3.1.7 Metal Mask and SiNx Removal

Part of the metal mask is etched during ICP, and the remaining portions can be removed by immersion in HF/HNO3/DIW (1:1:10) solution for 10 minutes. The SiNx layer can be removed by RIE SiNx etch for 5 minutes.

3.1.8 Potassium Hydroxide Surface Treatment

After ICP etch, the ideal cross section should be a rectangular shape. However, the actual shape is tapered as scanning electron microscopy (SEM) shows (see Fig. 3.4). Plasma etching creates a textured vertical lines structure on the NW, increasing surface roughness. This sidewall texture causes the formation of surface defects as the SEM image shows. These surface defects will generate surface states and effect sensor's sensitivity and selectivity. The top side is smooth due to the protection of the SiNx and Ti/Ni mask layer. To achieve ideal NW with smooth side walls, we can remove this roughness by adding an additional polishing step. This wet treatment step consists of a Potassium Hydroxide (KOH) etch. Wafer was immersed in 10% KOH in ethylene glycol (EG) solvent at 80 ℃ for 2 hours, the SEM image of smoothing, additive selection and optimization will be discussed in the next section.

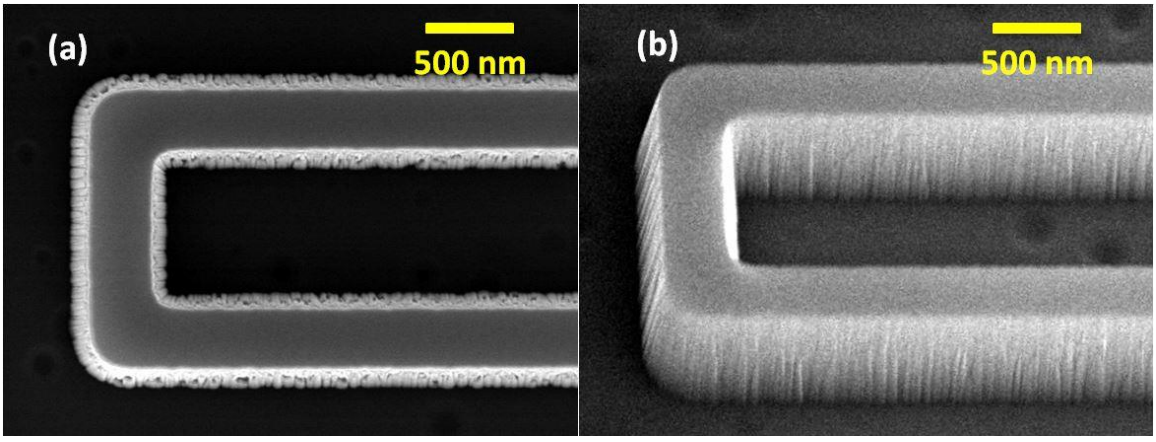

Fig. 3.4 SEM images of a nanowire section after ICP etch. (a) plan-view, (b) 45° tilted. The top surface appears smooth, however sidewall damage is evident.

3.2 Potassium Hydroxide Wet Etching

The vertical texture on the sidewalls formed by plasma bombardment is obvious and hard to remove in situ dry etching process. To remove the surface defects, KOH wet etching methods are explored with different etching temperatures, solvent compositions, additives and times.

3.2.1 Wet Etching Temperatures

The samples were etched for 10min in a 10% KOH in deionized water (DIW) solution at 40 ℃, 60 ℃ and 80 ℃. PL measurements were conducted before and after KOH etching as well as on the control sample (pristine GaN film). In Fig. 3.5, intensities are normalized with respect to peaks at impurity-related PL peak near 420 nm (Fig. 3.5a) and near-band edge (NBE) of 355 nm (Fig. 3.5b). Surface defects are created during the ICP etch, which are non-radiative recombination centers, results in the decreasing of the NBE emission compared to the impurity-related PL peaks at 420 nm and 600 nm. The subsequent KOH etch removes the ICP-damaged layers from the sidewall surfaces and remarkably reduces the surface non-radiative recombination centers density. After etching at 80 ℃, the overall shape of the PL spectrum of GaN NW surface resembles that of the pristine GaN film surface. Similar results also observed and reported on by Q. Li et al.[170].

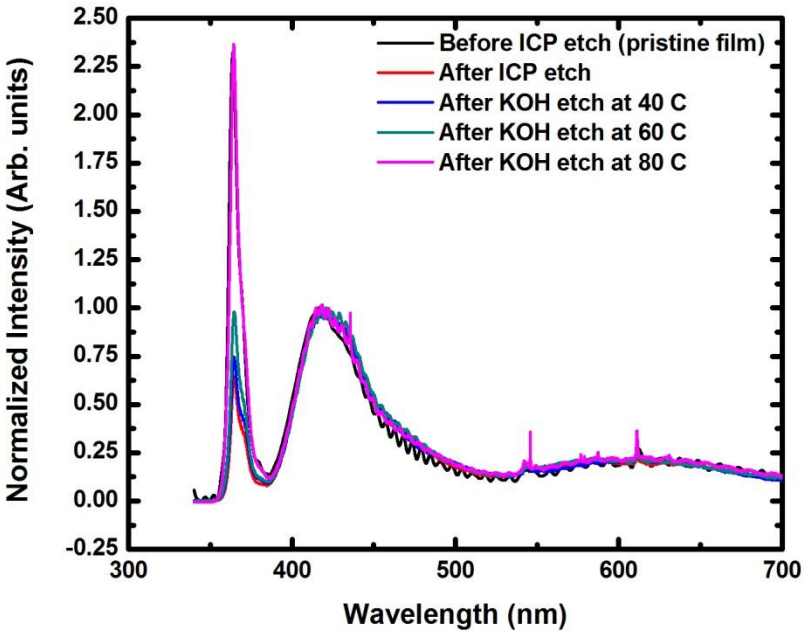

(a)

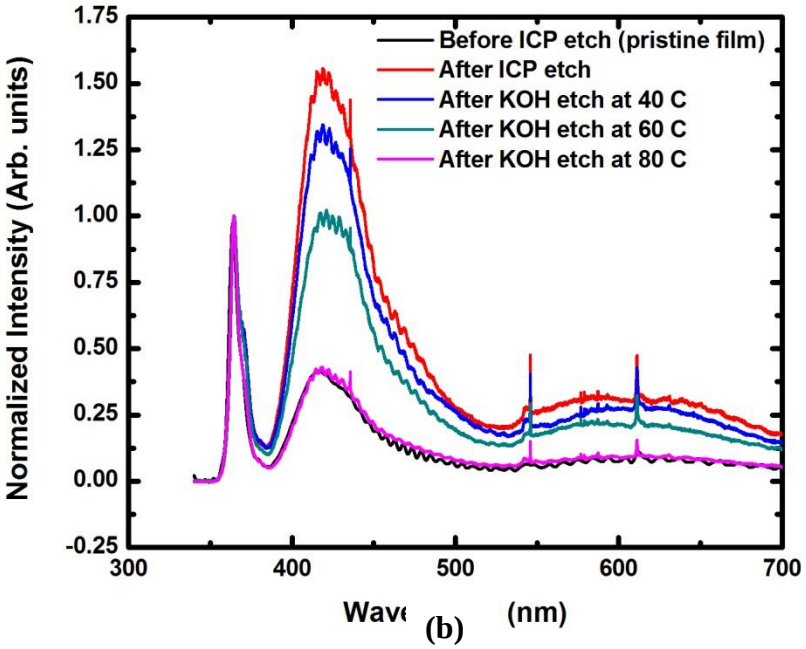

(b)

Fig. 3.5 Room-temperature PL measurements of GaN NWs. (a) Intensities are normalized with respect to impurity-related PL peak near 420 nm (b) Intensities are normalized with respect to the peaks at near-band edge (NBE) of 355 nm.

3.2.2 Wet Etching Solvents

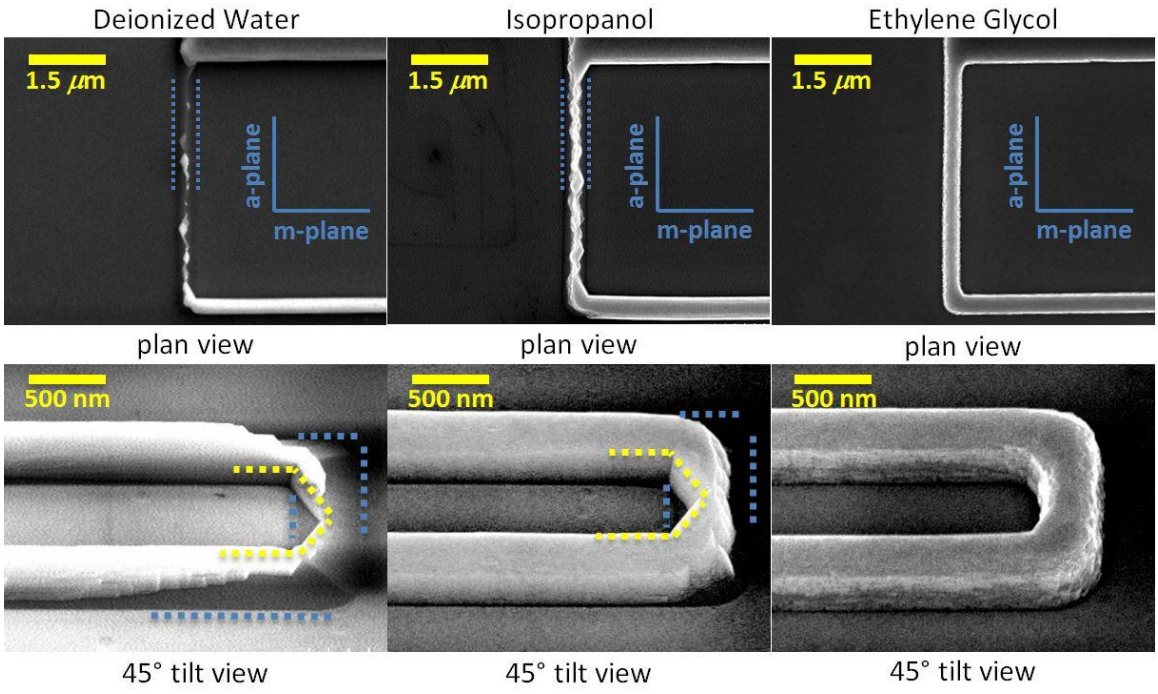

Fig. 3.6 SEM Images of NWs after KOH in different solvents. The first row indicates the a-plane and m-plane wires under study. The second row shows the conjoined parts. This is a short a-plane NW connects two m-plane NWs. For DIW and IPA solvents, a-plane NWs were over-etched and disconnected after treatment. Blue dash lines indicate the original NW sidewall positions before the treatment. Yellow dash lines indicate that the final sidewall positon after treatment. The m-planes replaced the original a-plane at the inner loop of the part because of a higher etch rate on the a-plane (in contrast to the m-plane.) For the EG solvent, NWs were not severely etched after the treatment. This result shows that the KOH in EG solvent is the best candidate for isotropic etching among the three explored.

The 10% KOH in DIW etchant used above shows the improvement of PL intensity at 80 ℃. However, the KOH in DIW shows aggressive etching of the a-plane of GaN, leading to an anisotropic etching profile as shown in the first column of Fig. 3.6. To address this issue, three different types of etch baths, namely 10% KOH in DIW, isopropanol (IPA)

and ethylene glycol (EG) , were studied in order to find a truly isotropic etch, one that is more controllable when used in batch fabrication.

All three groups were studied under the same conditions: 10 min etching at 80 ℃. PL measurements were conducted after treatment. These results are similar to those shown in Fig. 3.5 (purple line). SEM images (Fig. 3.6) reveal different etching rates of different facets: for the top surfaces (c-plane) of GaN NWs, etching was not observable for all three cases. The sidewalls of the NWs (a-plane and m-plane) were found to be more easily attacked by KOH.

Generally speaking, the a-plane is less stable than m-plane due to a higher surface energy [179, 180], so the etching rate is faster on a-plane than on the m-plan. SEM images (Fig. 3.6) show NWs disconnected at several points after etching with KOH in DIW, while m-plane NWs remain the same. Thus, we conclude KOH in DIW etches a-plane much faster than the other solutions. A high reaction rate is not favorable in achieving the smooth etched surfaces [181, 182]. An organic solvent addition, such as IPA or EG, slows down the a-plane etching process and making it comparable in rate to m-plane etching in order to achieve “isotropic” etching. The organic solvent contained in the solution plays an important role in the etching process. The organic molecules will selectively adhere to some crystallographic planes (a-plane in our case), thereby hindering the access of etching agent (KOH) and slowing down the corresponding plane’s etching rate. KOH in IPA etching shows an improvement in the isotropy of the etch process. IPA can slow down the etch rate of a-plane. However, it still etches faster than the m-plane. KOH in EG etching shows the most isotropic result since both a-plane and m-plane end up with the same NW width. Both the first and second column of Fig. 3.6 highlights the original NW sidewalls

before treatment by blue dashed lines. It is obvious that the a-plane etches faster than m-plane NWs in DIW and IPA. The high magnification image of the 90 ° bend parts proves this fact. The inner side of the NWs is etched to m-planes with 120 ° inter-planar angles between them. This is highlighted by the yellow dashed line in these figures. These results show that KOH in EG solvent is the best candidate for an isotropic etching for GaN.

3.2.3 Wet Etching Time

A series of studies of etching times from 10 min to 5 h based on the optimized condition of 10% KOH in EG at 80 ℃ were conducted. SEM images were taken to observe the NW sidewall surface roughness changes with the increasing etching time. Fig. 3.4 shows the control group without wet etching treatment. Sidewalls were rough created by plasma bombardment can be clearly seen. Fig. 3.7 shows a set of SEM images of NW sidewalls after wet etching of 10 min, 20 min, 2 h, and 3 h. The NWs had similar surface morphology with etching times greater than 3 h etching. Both 2 h and 3 h of etching show smooth sidewalls. Comparing Fig. 3.4 and Fig. 3.7 (a) we conclude KOH goes into the deep trenches to widening them and causing the vertical textures to become more pronounced at the beginning of the wet etching. After that, the horizontal textures and steps on the tapered sidewall become visible. The horizontal and vertical texture “cut” the sidewalls into “brick-like” blocks (Fig. 3.7 (b)). These convex block textures are attacked by KOH with further wet etching and decreases the size into smaller convex spots (Fig. 3.7 (c)). After 3 h of etching, the convex structures largely disappeared, ending up with smooth sidewalls (Fig. 3.7 (d)). In Fig. 3.7 (c), (d), the interface layer, highlighted with yellow dash

lines, of GaN and AlGaN are identified easily on the smooth sidewall. The original sidewall's position before wet etching can be determined by a KOH resistive nucleation layer as highlighted with blue dash lines.

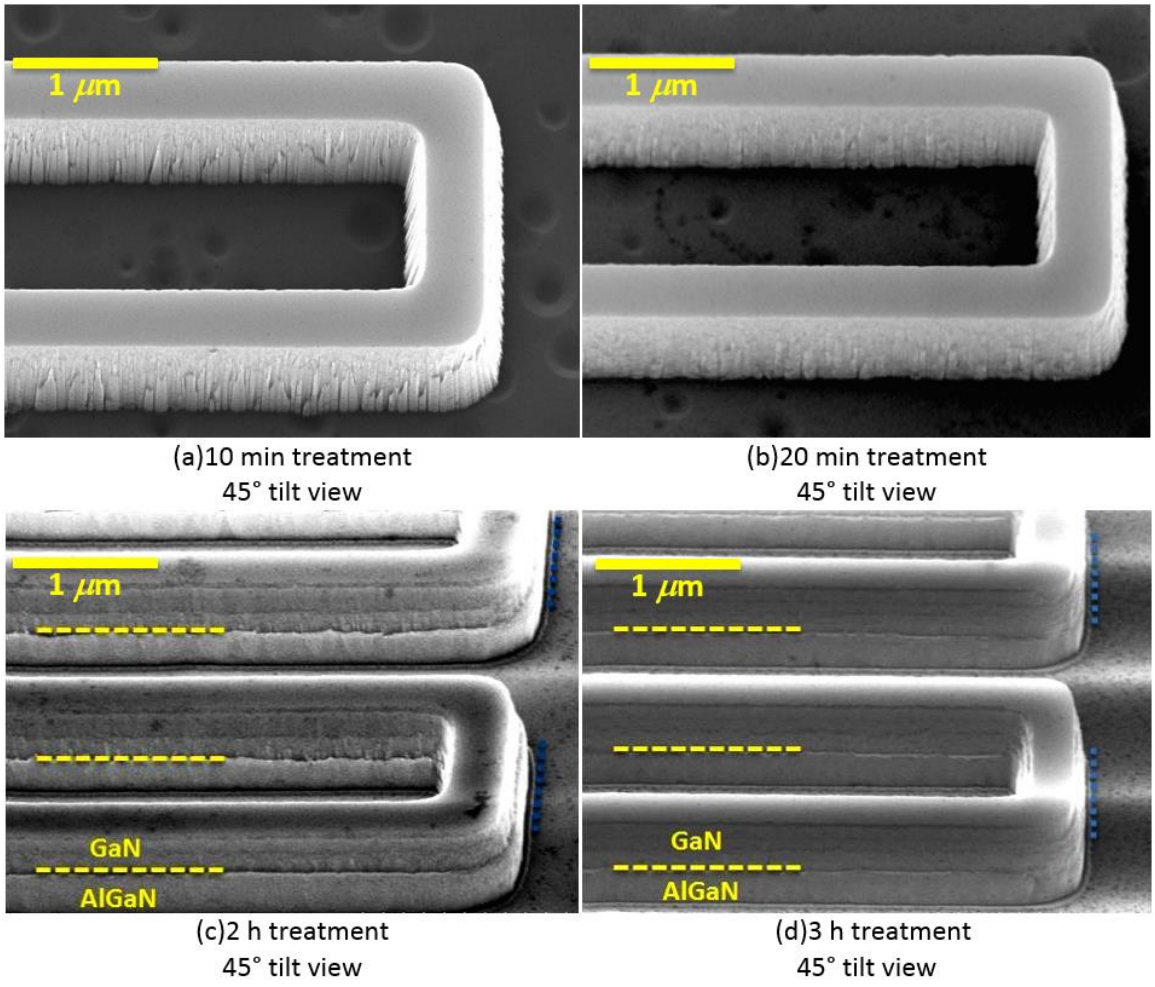

Fig. 3.7 (a)-(d) correspond to different etching times from 10 min to 3 h under condition of 10% KOH in EG at 80 ℃. Blue dash lines in (c) and (d) indicate the original NW sidewall position before the treatment. Yellow dash lines in (c) and (d) indicate the interface between GaN and AlGaN layers after treatment.

3.3 Electrical Characterization

3.3.1 Ohmic Contact Formation

3.3.1.1 Photolithography

Photolithography is a well-developed sub-micro and micro-structure tool in mass production industry, comparing to stepper, it is contact alignment and use UV. MA6 Front and Back Contact Aligner (Suss Microtec) is used for this process, resolution of sub-micro can be achieved. The fabrication process of photolithography definition of ohmic contact structure starting with spin photo-resist is detailed below:

i. Pre-bake wafer at 210 ℃ for 10 minutes to remove water and other organic residue. Cool down wafer and nitrogen blow.

ii. A bi-layer stack of photoresists (MicroChem LOR3A and Microposit S1813) were used to support a lift-off process for the ohmic contact metal. Spin coated LOR3A at 4000 rpm for 45 seconds was use as a first layer, followed by 5 minutes bake at 210 ℃. We next spin coated S1813 at 4000 rpm for 45 seconds followed by a 60 second bake at 115 ℃.

iii. UV exposure with 90 mJ/cm ^{2}dose energy.

iv. Post-bake on 115 ℃ hot plate for 60 seconds, cool down and followed by develop in Microposit MIF-319 for 60 seconds. Rinsed in DI water and after this step the windows for metal deposition are opened.

v. Reactive-ion Etching (RIE, Unaxis 790) was followed by a descum with 30sccm flow rate of oxygen for 30 seconds to clean up the remaining developed resist residue.

3.3.1.2 Ohmic Contact Metal Deposition and Lift-Off

A Ti/Al/Ti/Au metal stack has been reported by many researchers as a low-resistance ohmic contact to n-GaN [183-185]. In this process, even with undoped GaN, the Ti (40nm) /Al (100nm) /Ti (40nm) /Au (40nm) exhibit linear I-V characteristics. A Ti/Al/Ti/Au metal stack was deposited in the Denton Infinity 22 E-beam Evaporator.

Titanium and aluminum based metallization schemes have been successfully used to form ohmic contacts of GaN. For the Ti/Al/Ti/Au stack of layers, the first Ti layer aiming to have a good contact due to its high sticking coefficient to the semiconductor surface, so it is Titanium adhesive layer. In order to form a good ohmic contact, the work function of the contact metal has to be matched with the electron affinity of the semiconductor or near. Ti has a work function of 4.33eV which is very close to the electron affinity of GaN (4.1eV). GaN surfaces have a very high chemisorption affinity for oxygen. As a result, a thin native oxide layer will form on surface of GaN. This layer can insulate the GaN from the metal. However, Ti has the great advantage of reducing the GaN native surface oxide by alloying. Ti can dissolve small amounts of oxygen and still remain in a stable α-Ti phase. During high temperature annealing, N out-diffuses from GaN to form TiN and the nitrogen vacancies in GaN act as donors. In that case, the undoped GaN will become heavily doped at the metal semiconductor interface. This further improves the ohmic contact lowering resistance even further. Aluminum, as the second layer has a thickness of 100nm. This layer is aimed to insure an overall low resistance contact. Another layer of titanium is added

in between the aluminum and the gold layers to prevent or minimize metal diffusion under high temperature RTA process afterwards. Top layer of gold (Au) is noble metal and used to prevent oxidation and corrosion of the metal stacks.

After deposition, lift-off is accomplished by immersion in 1165 or remover PG solvent accompanied by a gentle Q-tip sweep. Finally, wafer was cleaned with acetone, methanol, IPA and DI water.

3.3.1.3 Rapid Thermal Annealing

Rapid Thermal Annealing (RTA) is employed for ohmic contact formation of metal stack and GaN. High performance ohmic contact is essential to operation of nanowire devices. In RTA, the wafer is placed inside a thin quartz chamber with halogen lamps surrounding it. The temperature rise is fast (as high as 25 ℃ per seconds). The rapid rise of temperature generates stress in the nanowire device leading to a structural breakdown and re-bonds. The wafer ambient is 6000 sccm of ultra-pure Ar. The RTA is performed at 700 ℃ for 30 seconds. The temperature ramp rate is set to 100 ℃ per minute. Slow rise rate is set to make sure the GaN, metal stack and metal-oxide are given enough time to reach equilibrium while keeping a low stress level. This RTA process generates a well-functioning, low resistance ohmic contact.

3.3.2 IV Characterization

The electrical properties of the no KOH treatment control group NWs and a 2 h KOH etched NWs with different lengths were studied. I-V measurements were conducted

under UV (355 nm wavelength, 48 μW/cm ² intensity) illumination. Due to the high resistivity of intrinsic GaN, dark currents measured in the pA range (from 10 pA to 100 pA). With UV excitation, resistances tend to increase with increasing NW length, shown in Fig. 3.8. The KOH treated NWs show lower resistance compared to those which not KOH treated and of the same length under UV excitation. This enhancement becomes more significant as the NW length decreases. This phenomenon can be explained either by the suppression of the non-irradiative recombination process due to surface improvement or the surface treatment may lead to a lower barrier resistance and form the ideal ohmic contacts.

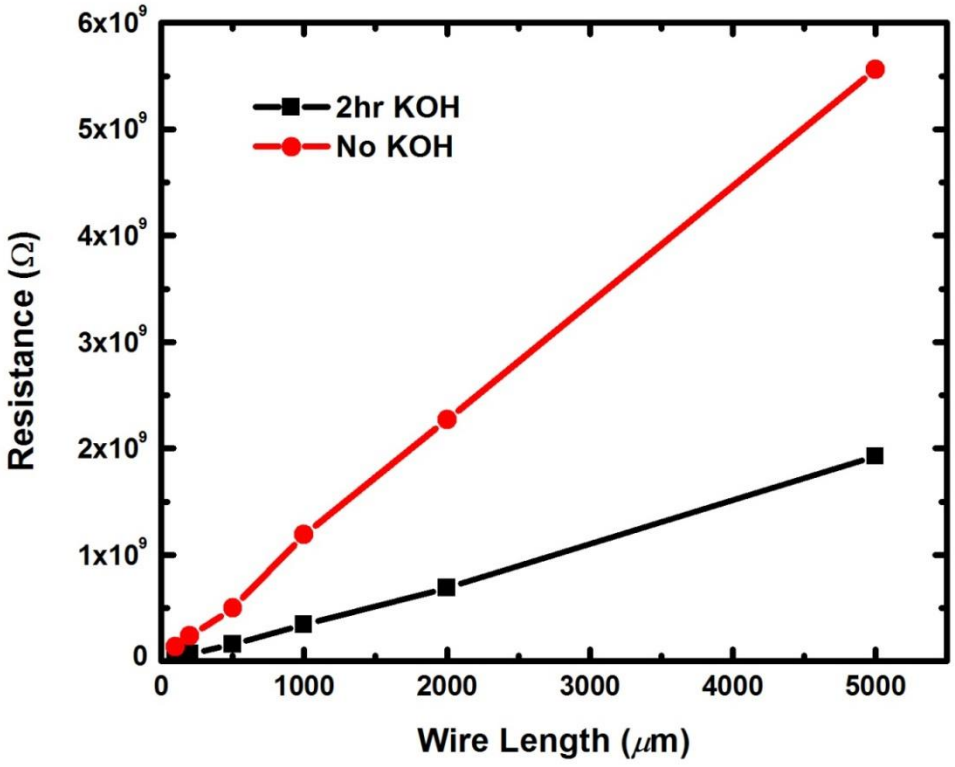

Fig. 3.8 Electrical behavior with UV assistance of NW before and after KOH treatment

3.3.3 UV Response

UV photocurrent measurements were conducted with 200 μm and 1000 μm NWs. For both lengths, NWs with and without KOH wet etching samples compared. The same UV source intensity and voltage biases were used for 5 cycles, 2 min for each cycle (1 min UV on and 1 min off). Fig. 3.9 shows the response of the NWs' conductance to this cycle. Note: the NW is almost insulating without UV exposure. For the same dimension, surface-treated NWs show almost 3 times higher current under UV exposure. Furthermore, the UV response is proven to be repeatable and reliable over multiple cycles.

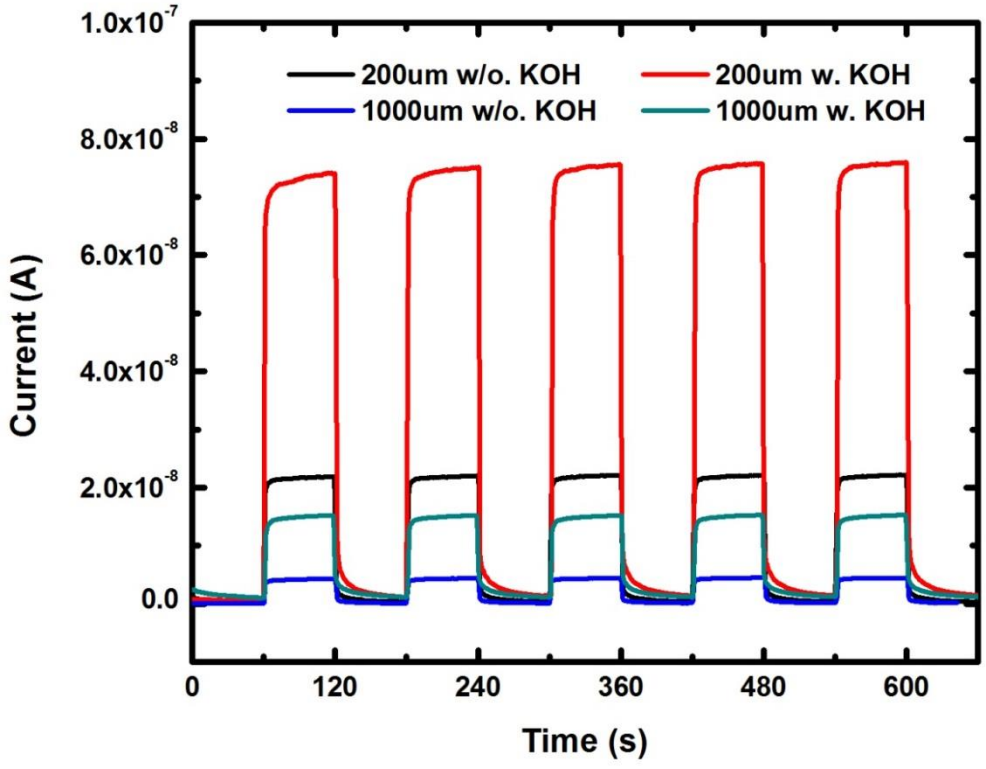

Fig. 3.9 UV photocurrent transient measurement of 200 μm and 1000 μm long NWs with and without KOH treatment.

3.4 Chapter Conclusion

In this study, methods and techniques to reliably and reproducibly fabricate different lengths of alignment-free, horizontal nanowire arrays for various applications were presented. Stepper lithography, ICP etching and KOH wet etching techniques were used to ensure mass production capability and competitive performance to conventional bottom-up nanowires. Different wet etching temperatures, solvents, and times were explored for surface improvement of NWs. PL, SEM and I-V characterization were used to show wet etching is necessary for optimal GaN NW devices. On the basis of our experimental results, this NW fabrication method shows promise, potentially enabling mass production of sensors, optical and power devices based on single NW structures. The top-down approach described here enables GaN NW and SMW to be integrated with LEDs, micro-pumps, micro heaters to provide useful sensor structures. Many sensors (chemical, gas and biology) using bottom-up GaN NWs can be benefit from the top-down approach. The study was published at the journal of Microelectronic Engineering[52].

Chapter 4: Metal-Oxide Nanoclusters and Thin-Films

This chapter describes the optical, electrical and structural characterization effort for analyzing the metal-oxide nanoclusters (MONCs) and the corresponding thin-films. Surface morphology and microstructure of the MONCs was characterized by scanning electron microscope (SEM) and atomic force microscope (AFM). The crystallinity and phase analysis was assessed by X-ray diffraction (XRD) and auger electron spectroscope (AES). The element composition of thin-film was studied by energy dispersive spectrometer (EDS) and X-ray photoelectron spectroscopy (XPS). Electrical characterization of the thin-film was performed by measuring the current-voltage (I-V) curves by Agilent B1500A and S4200 semiconductor parameter analyzer.

4.1 Fabrication of Metal-Oxide and Metal Nanoclusters

Deposition of NCs is a tricky part because on one hand, sufficient amount of fully functioning NCs and high surface coverage can provide high sensitivity; on the other hand, over deposition will cause isolated island of metal-oxide coalesce into a conducting film. Two methods are mainly considered, sputtering followed by RTA process of NCs and spin-coating of chemically synthesized NPs.

The Denton Vacuum Discovery 550 is used for sputtering each metal-oxide NCs. High purity metal-oxide targets were used and RF magnetron sputtering sources at different substrate temperatures with a wide range of Ar/O_2 flow rate and RF/DC power were optimized. For metal-oxides, rapid thermal annealing (RTA) after the deposition is necessary to achieve a dominating crystalline phase of NCs. The finalized recipes for many

types of metal-oxides and metals are shown in Table 4.1 and Table 4.2. The detailed optimization process will be covered in the following section. Take TiO2 for example, the TiO2 NCs were prepared by RF sputtering of a TiO2 target using Denton Vacuum Discovery 550 system. The base pressure was maintained below 2E-6 Torr. The substrate temperature was fixed at 325 ˚C to increase the mobility of arriving particles. Ar gas flow of 50 sccm and RF power of 100 W was used to yield a low deposition rate. The RTA process at 700 ˚C for 30 sec in Ar gas ambient was conducted right after the deposition. The RTA was set a ramp rate of 100 ˚C / min.

Metal-Oxide Materials	RF Power (W)	Deposit Temp. (˚C)	Deposit Time (s)	Ar Flow (sccm)	O_2 Flow (sccm)	RTA Temp. (˚C)	RTA Time (s)	RTA Ramp (˚C/min)
TiO_2	100	325	240	50	0	700	30	100
SnO_2	200	90	300	20	30	700	30	100
WO_3	30	325	180	50	0	700	30	100
Fe_2O_3	100	300	300	40	0	700	30	100
V_2O_5	80	90	300	36	4	300	30	100
ZnO	100	90	300	50	0	700	30	100

Table 4.1 List of metal-oxide NCs deposition recipes by sputtering method followed by RTA

Metal Materials	DC Power (W)	Deposit Temp. (˚C)	Deposit Time (s)	Ar Flow (sccm)	O2 Flow (sccm)
Pt	20	25	60	20	0
Pd	20	25	60	20	0
Au	20	25	60	20	0
Ag	20	25	60	20	0

Table 4.2 List of metal NCs deposition recipes by sputtering method

4.2 Process Optimization by I-V Characterization

The sputter deposition of a material from nothing on bare substrate to thin-film on substrates includes 4 phases. The deposition process start with forming small nucleation and isolated particles, the further deposition will bring more energized particles with certain level of mobility on the surface to adhere on early formed particles and form grains. Further deposition will make the grains grow and finally grain boundaries start merging and form amorphous thin-film. Considering the NCs have larger surface to volume ratio than continuous thin-film. And Isolated NPs have less deposition surface coverage percentage than NCs. Both of the case will decrease the surface sites density and ergo decrease the sensitivity of the sensor devices. The ideal NCs should be the deposition phase that in between the early isolated NPs phase and the final conductive thin-film phase.

It is challenging to precisely control the process because the threshold thickness of general metal-oxide forming thin-films from isolated NCs is around 1 to 4 nm (based on my optimization data). The crystal sensor that in situ detects the sputter deposition thickness is unreliable in this ultra-low thickness region. Optimization experiment with extremely low deposition rates were designed and run more multiple times to ensure the reproducibility and reliability.

4.2.1 I-V Measurement for Fast Optimization

A new method based on conductivity measurement was developed to shorten the optimization turnaround time. For the metal-oxide thin-film fabricated by sputtering the metal-oxide target with oxygen absent or deficient condition, the sputtered metal-oxide is conductive due to the oxide deficiency in the material. The oxide vacancy can be

considered as n-type dopant in metal-oxide semiconductor. Optimization experiments were run on prepared samples with pre-deposited electrodes instead of bare sapphire wafer or real NW samples. By applying a voltage bias on the electrode pair and measuring the current level, each sample can be told whether the used recipe forms NCs or thin-film right away. This approach is fast by avoiding huge amount of time in SEM imaging of the NCs on NW or substrate samples. Examples of TiO_2 and WO_3 optimization current-voltage plots are shown in Fig. 4.1 and Fig. 4.2.

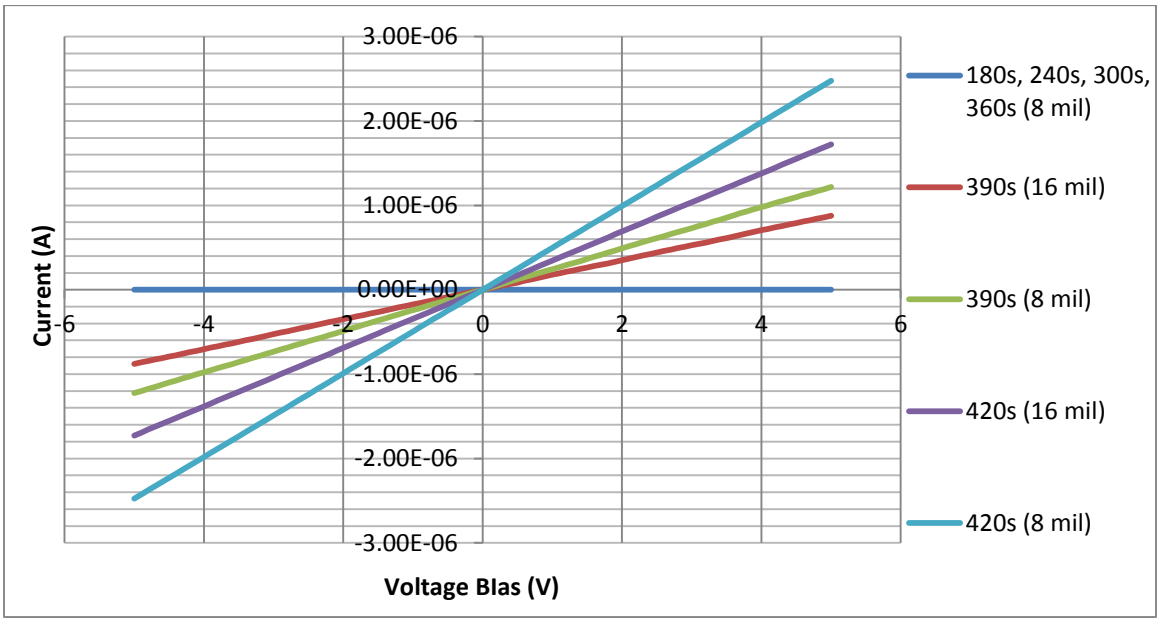

Fig. 4.1 I-V measurement of different thickness of TiO_2

(8 mil and 16 mil stands for electrode distances and are converted to 200 μm and 400 μm respectively)

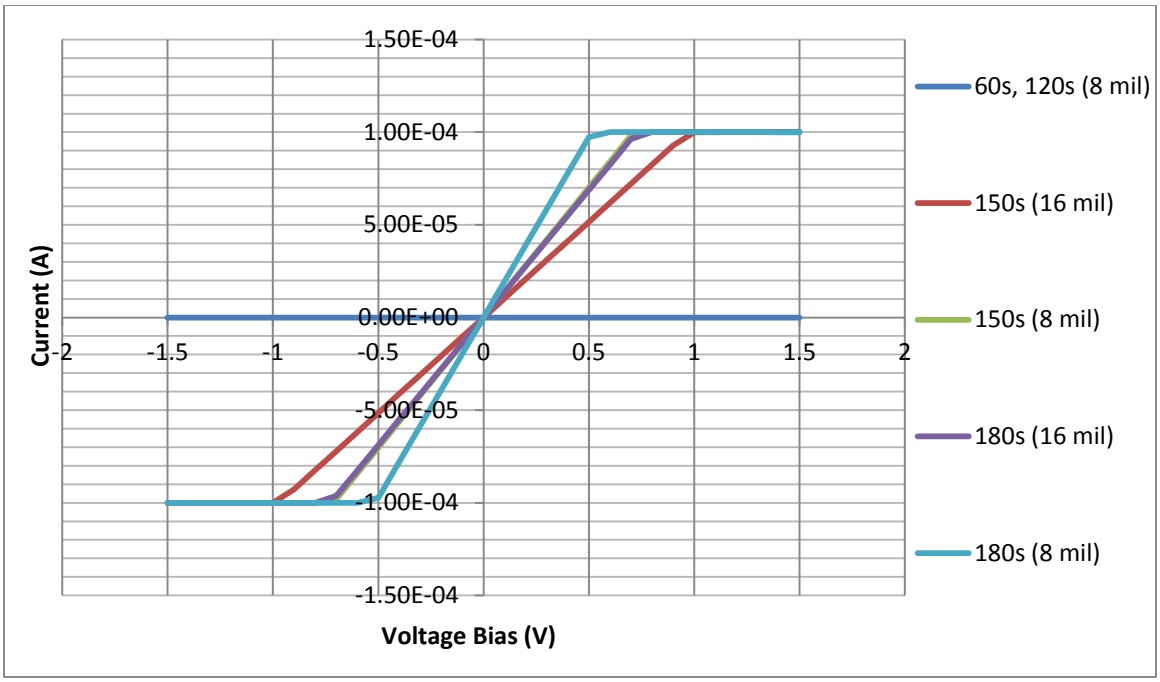

Fig. 4.2 I-V measurement of different thickness of WO_3

(8 mil and 16 mil stands for electrode distances and are converted to 200 μm and 400 μm respectively)

It is obvious that the threshold deposition time for TiO_2 and WO_3 are 360s and 120s. The corresponding thicknesses calculated from deposition rate are 6 nm and 3 nm respectively. The deposition rate is calibrated from thick film deposited for a long time.

4.2.2 Inspection of Optimized Nanoclusters

The finally NCs fabricated by the optimized recipes was inspected with SEM and AFM microscopy imaging. Fig.4.3 shows the AFM images of TiO_2 NCs deposition thickness of 1 nm and 3 nm. We used the AFM in tapping mode to sense atomic forces and

plot the surface morphology. The imaging technology can scan critical dimension down to nanometer range by height variation. But the technique cannot distinguish between different materials, especially when the different surfaces exhibit little height variations. SEM imaging can distinguish two different materials by their different atomic masses and by mass density changes. Fig. 4.4 shows the SEM images of SnO_2 NCs formed by the 5 nm deposition and the continuous SnO_2 film formed by the 7 nm deposition. Similar SEM images of WO_3 NCs (1 nm and 4 nm) on sapphire substrate are shown in Fig.4.5.

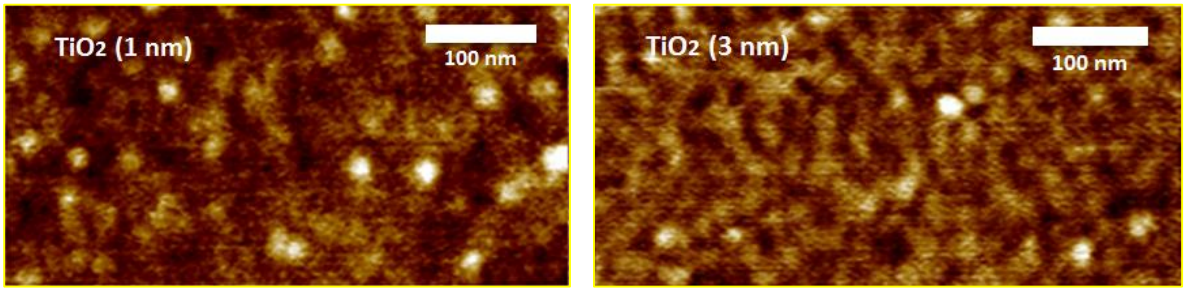

Fig. 4.3 AFM images of TiO2 NCs with low and high surface coverage percentage

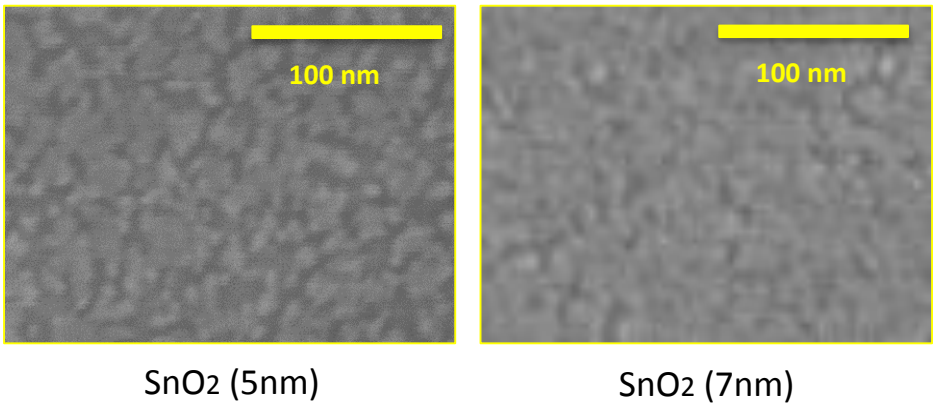

Fig. 4.4 SEM images of SnO_2 NCs and thin-film formed by 5 nm and 7 nm deposition

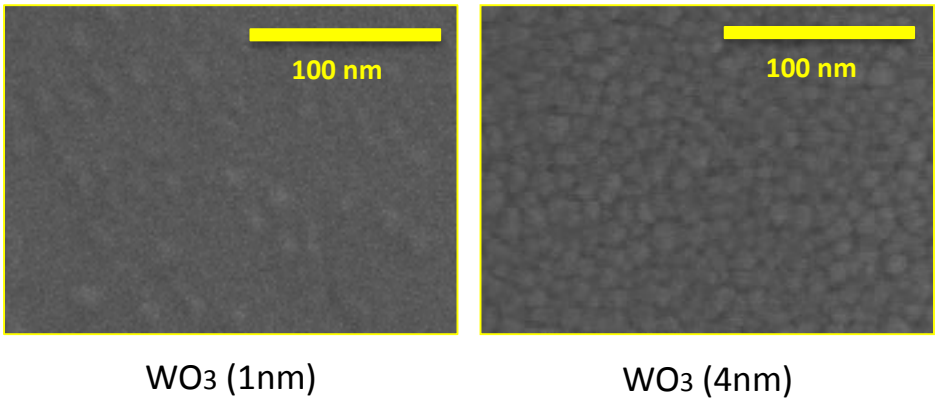

Fig. 4.5 SEM images of WO_3 NCs with low and high surface coverage percentage

4.3 Metal-Oxide Thin-Film Gas Sensors and Gas Sensing Database

Metal-oxides are well known for sensitive and active in surface bonding with chemical molecules. With the heat or photon assistances, the metal-oxide can split or activate the adsorbates to reactive ions or radicals and enhance the chemical reaction as catalysis. Water split with metal-oxide NPs to generate hydrogen and oxygen is one of the promising applications based on that theory [186-188]. Many synthesis uses metal-oxide for low temperature and selective purpose [189, 190]. Lots of toxic gases are decomposed by metal-oxide catalysts [191-193]. Different crystal orientation and phase of NCs surface will have different bonding sites for corresponding chemical gases. The ideal candidates for each metal-oxide surface would be the gases that have higher adsorption energies than desorption energies. In this case, there will be a net amount of adsorbed gases when statistic equilibrium reaches.

The properties of metal-oxide surfaces and the sensing capabilities were studied by characterizing the thin-film sensors and the thin-films. The thin-films were prepared exactly the same way with NCs but deposition for a longer time to ensure the deposition

thickness beyond the threshold which was calibrated in the last section. The thin-film samples were characterized by XRD and ellipsometer for the phase and band-gap properties. The thin-film sensors were put into the gas sensing chambers (details in chapter 7) and run multiple gases for sensing capability characterization. A small database was established base on the gas sensing results. The links between each metal-oxide material to all the sensitive gases were generated.

The thin-film sensing study illustrates an idea that highly selective sensors cannot rely on single metal-oxide NCs. Mixing of metal-oxides and metals is a clear path to fine tune the selectivity of a high performance gas sensor.

4.3.1 Thin-Film Sensor Preparation

The thin-film sensor structure of each sample is shown in Fig. 4.6. Metal-oxide thin-film was deposited onto a sapphire wafer using the recipe mentioned in NCs fabrication. A longer deposition time was used to ensure the formation of thin-film. Take TiO_2 thin-film sensor as an example, a 50 nm thickness was deposited. An extra dummy wafer for later thin-film characterization was deposited at the same time. After the RTA process, interdigitated electrodes (IDEs) were patterned on the metal oxide thin-films.

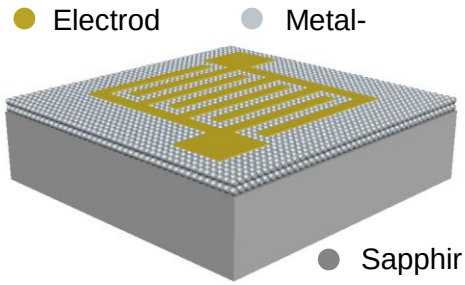

Fig. 4.6 Metal-oxide thin-film sensor structure

4.3.2 Thin-Film Characterization

XRD of different metal-oxide thin-films were studied. The study of thin-films can reveal the crystalline phase of NCs in a certain level. The XRD of TiO_2 thin-film revealed the anatase phase dominates. Fig. 4.7 shows XRD patterns of the 50 nm TiO_2 thin-film coated on silicon substrate, the diffraction peaks arising exclusively from anatase phase. The inset figure confirms the XRD pattern of peaks of silicon substrate.

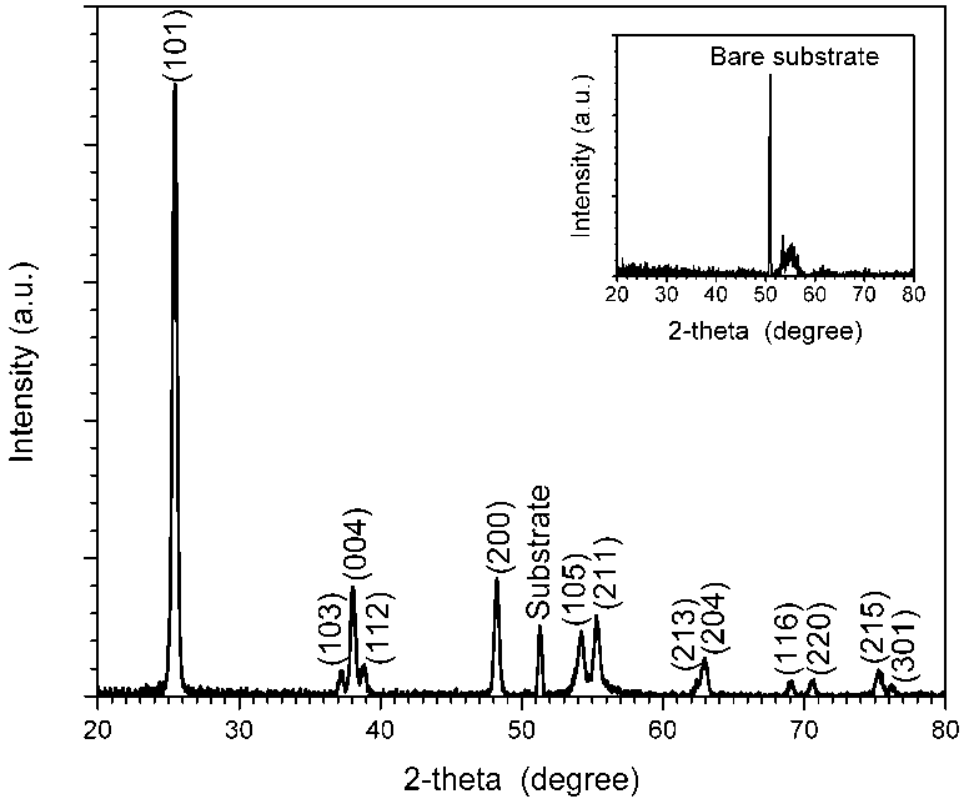

Fig. 4.7 XRD patterns of TiO_2 thin-film

4.3.3 Gas Sensing Database

Thin-Film Material	Sensitive Gas(es)	Non-Sensitive Gas(es)
TiO_2	Benzene, Toluene, Ethylbenzene, Xylene, NO_2, NH_3	CO, CO_2, HCN
WO_3	NH_3, NO_2	
SnO_2	NO_2, CO, Methanol, Ethanol, Isopropanol	
Fe_2O_3	CO	
CoO	NO, NO_2	
CuO	H_2S, HCN	CO, NH_3, Methanol, Ethanol, Xylene
TiO_2 / Pt	H_2	
TiO_2 / Pd	H_2	
TiO_2 / Fe	H_2S	
TiO_2 / Cu	CO, CO_2	
SnO_2 / Pd	H_2	
SnO_2 / Fe	H_2S	
SnO_2 / Cu	Cl_2, HCl, HCN	
SnO_2 / CuO_2	Cl_2, HCl	HCN

Table 4.3 Gas sensing database for metal-oxides

Table 4.3 shows the database that links each metal-oxide material to all the responsive target gases. It is clear that the thin-film sensor has the limitation in selectivity, single type of metal-oxide material generally responses to multiple gases. Take TiO_2 thin-

film sensor as an example. It shows response to nitrogen dioxide gas as well as organic gases (methanol, ethanol, and aromatic compound). Fig. 4.8 shows the TiO_2 thin-film sensor respond to 250 ppm NO_2 under UV exposure (wavelength 365 nm, intensity 468 $\mu W/cm^2$) and in dark. The sensor was introduced to 250 ppm NO_2 for 5 min of sensing period followed by 5 min of breathing air. It is obvious that NO_2 sensing behavior is enhanced by UV irradiation. Fig. 4.9 shows the TiO_2 thin-film sensor responses to different concentrations of NO_2 under UV irradiation.

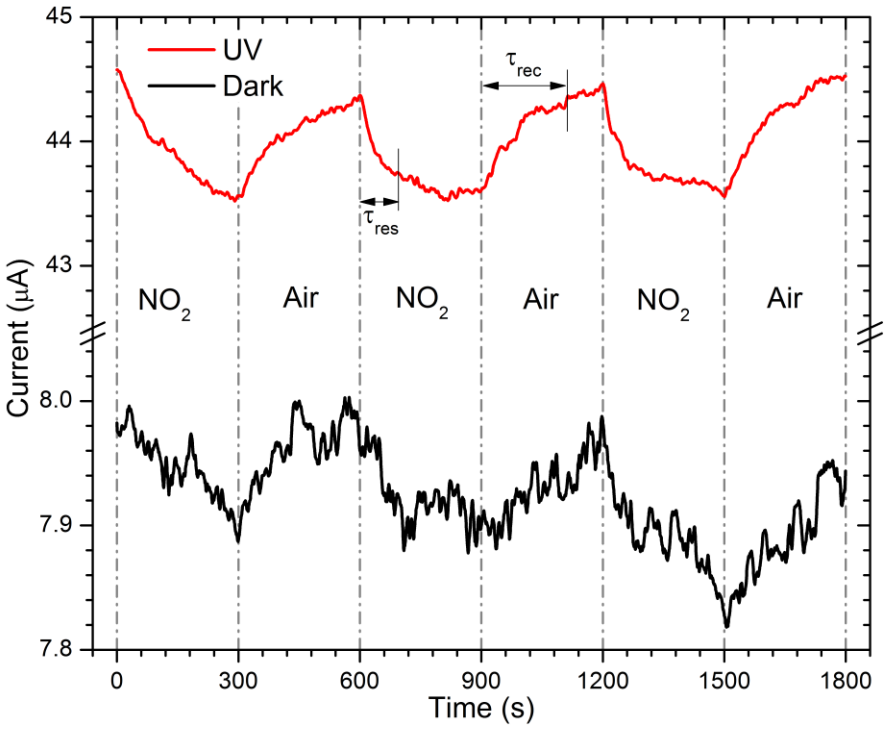

Fig. 4.8 TiO_2 thin-film dynamic response to 250 ppm NO_2

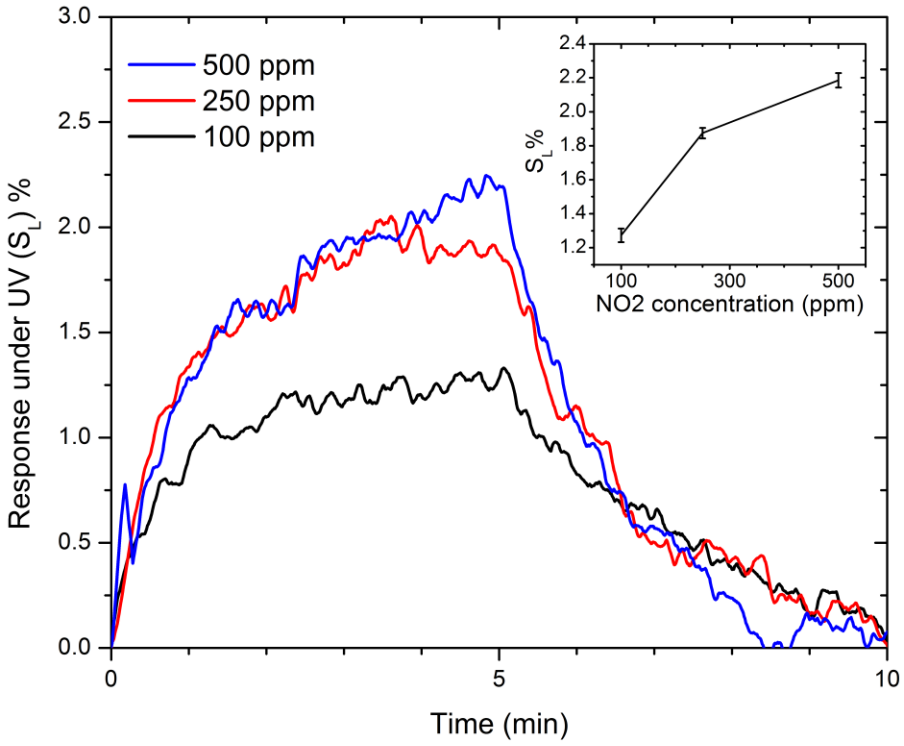

Fig. 4.9 TiO_2 thin-film response to 100 ppm, 250 ppm and 500 ppm NO_2

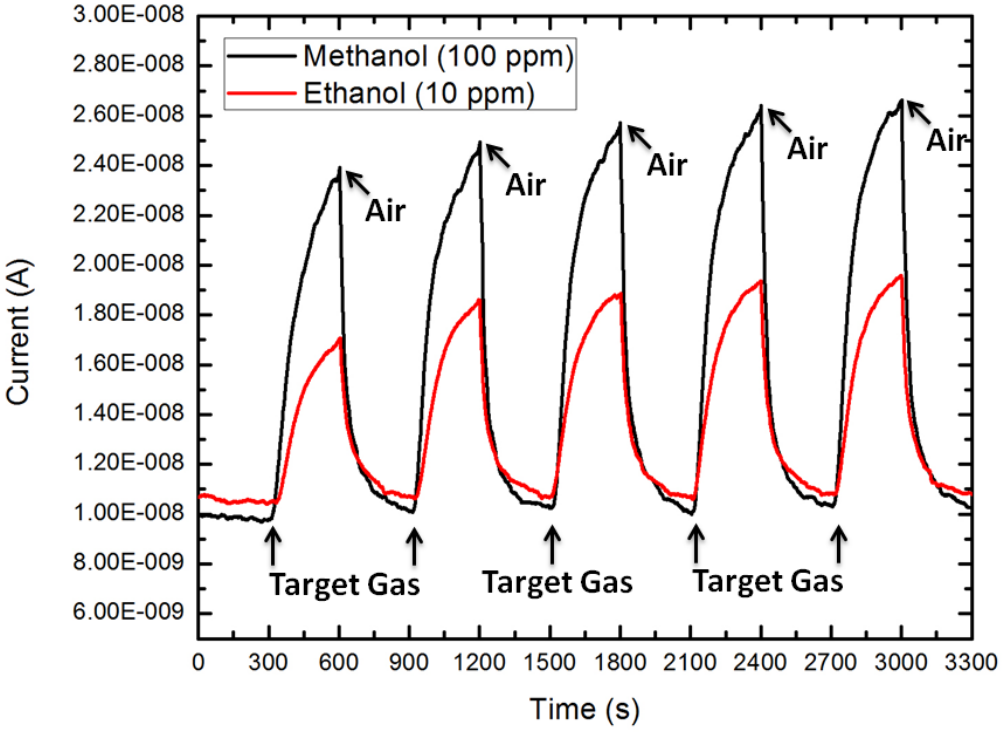

Fig. 4.10 TiO_2 thin-film sensor cross sensing with alcohol gases

Thin-film sensors have limitations in selectivity, generally a single type of metal-oxide thin-film responses to multiple gases. Fig. 4.10 shows the same TiO_2 thin-film sensor can response to low concentration alcohol gases with high sensitivity. The sensing signal never achieved steady state which a stable and saturated current when sensing even after a long time sensing exposure (30 min, Fig. 4.11). The TiO_2 thin-film sensor respond to Benzene, Toluene, Ethylbenzene and Xylene (BTEX) is shown in Fig. 4.12. A drifting baseline current is obvious in the figure, which further proof the thin-film sensors normally degrade sensing capability with the time. Similar baseline current drifting and sensitivity degradation was observed in WO_3 thin-film sensor for ammonia sensing (Fig. 4.13 and Fig. 4.14). Fig. 4.13 is the WO_3 thin-film on KOH treated GaN surface and Fig. 4.14 is on the H_3PO_4 treated GaN substrate.

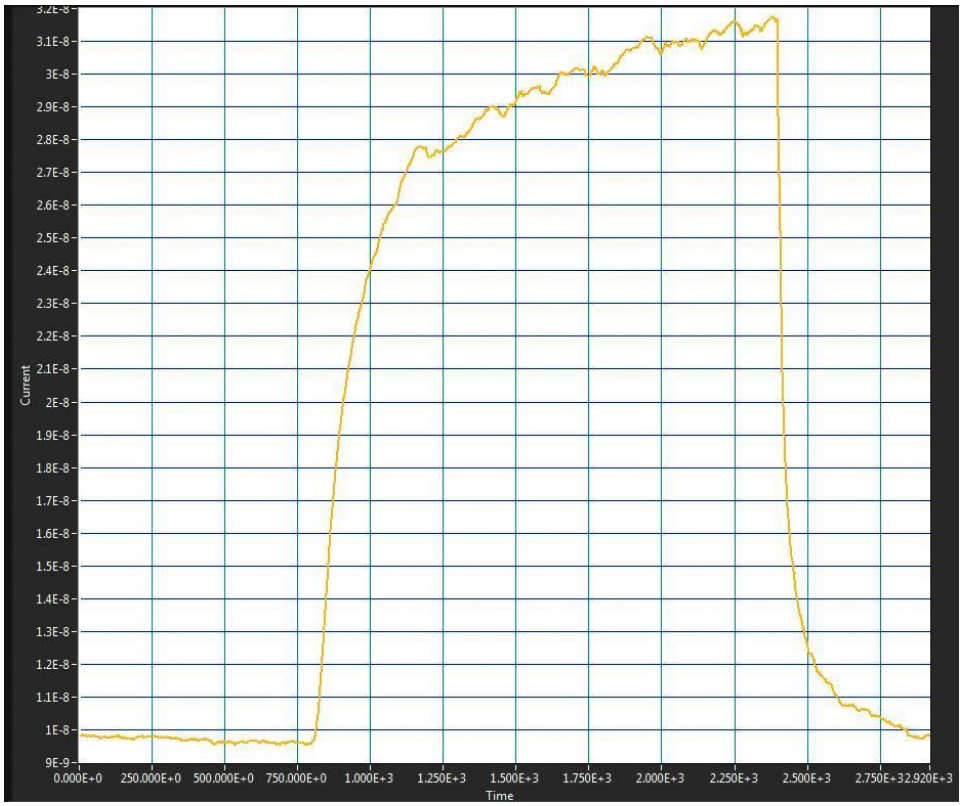

Fig. 4.11 TiO_2 thin-film sensor 30 min exposure to methanol

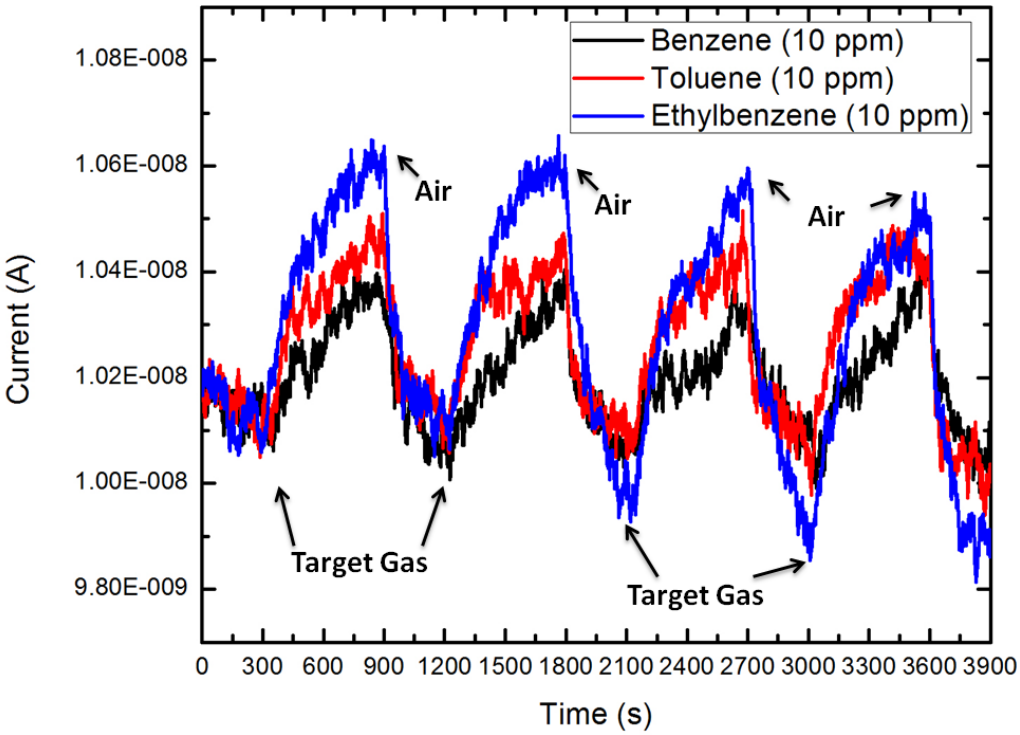

Fig. 4.12 TiO_2 thin-film sensor cross sensing with BTEX gases

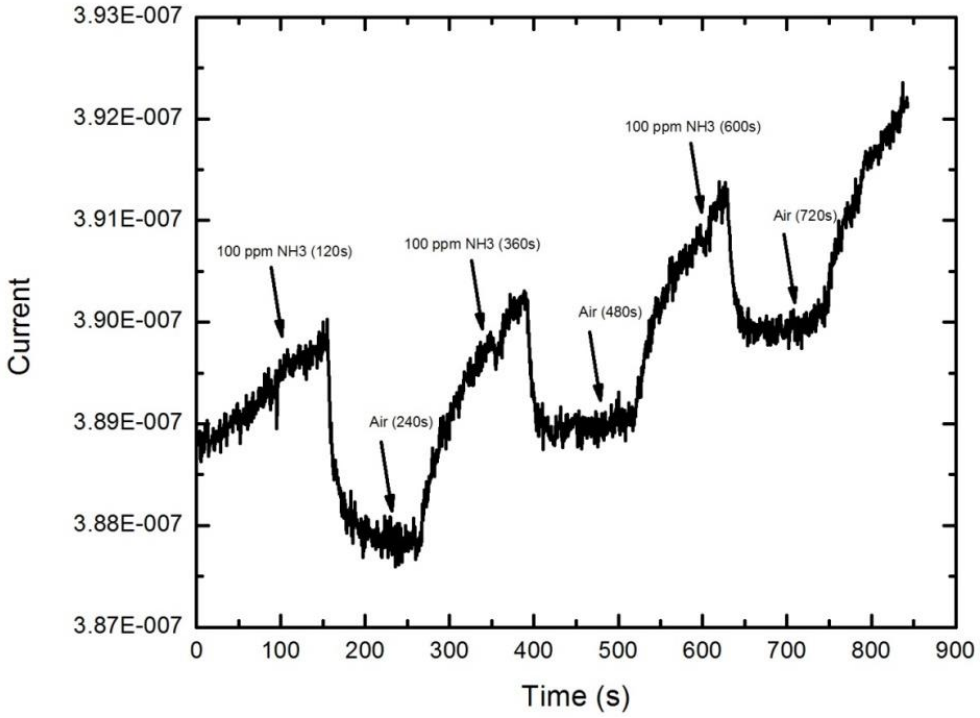

Fig. 4.13 WO_3 thin-film sensor response to ammonia (NH_3)

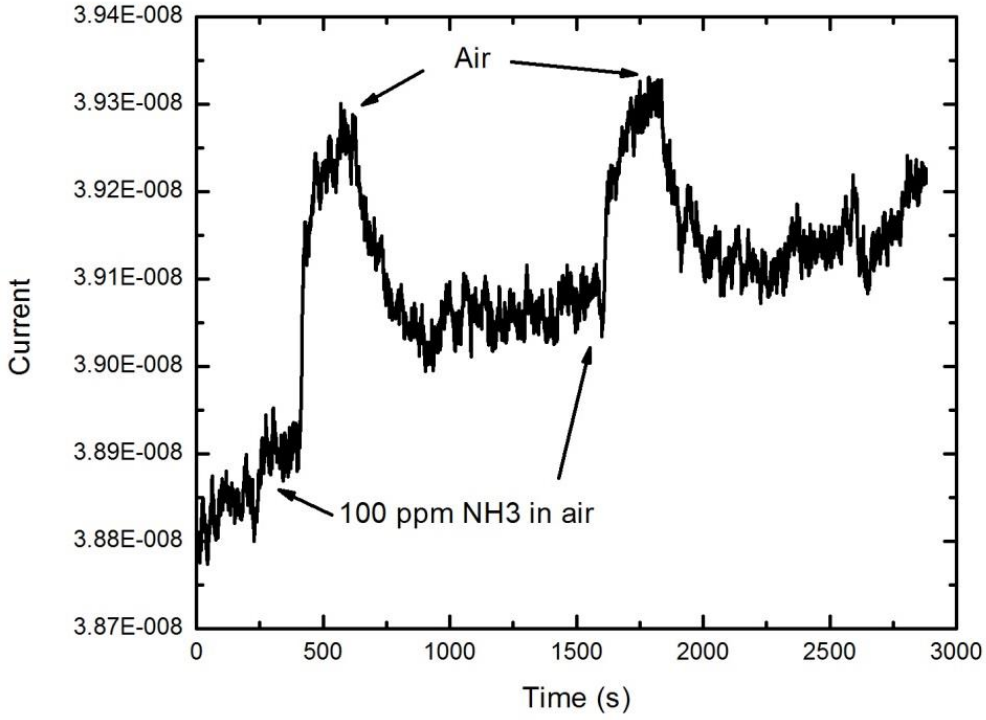

Fig. 4.14 WO_3 thin-film sensor response to ammonia (NH_3)

4.4 Thin-Film Photodiodes

A self-powered ultraviolet photodetector based on p-NiO and n-ZnO was fabricated using the sputtering technique on indium doped tin oxide (ITO) coated plastic polyethylene terephthalate (PET) substrates. The p-n junction showed photo response with quantum efficiency over 63% under UV illumination at an applied reverse bias of 1.2V. The engineered ultrathin Ti/Au top metal contacts and UV transparent PET/ITO substrates allowed the PDs to be illuminated through either frontside or backside. Morphology, structural, chemical and optical properties of sputtered NiO and ZnO films were also investigated.

As a representative II-VI group semiconductor, ZnO is intrinsically n-type with 3.3 eV direct bandgap, 60 mV exciton binding energy, and additionally high radiation and chemical resistance [194, 195]. For the UV PD applications, junctions that are composed of ZnO have been investigated extensively due to the excellent electrical and optical properties of ZnO [196-199]. Despite the advantage of simple fabrication process as well as low stray capacitance, high internal gain of ZnO based Schottky and metal-semiconductor-metal PDs, p-n junction structure appears to be more promising due to its stability, low or zero bias currents, high impedance, lower applied filed, and faster response [195, 200].

The PDs have been fabricated on PET substrates using the RF sputtering method and the deposited thin films/devices have been characterized. Fig. 4.15 shows the schematic of the device structure whereas Fig. 4.16 shows the optical image of the same, demonstrating its transparency and flexibility.

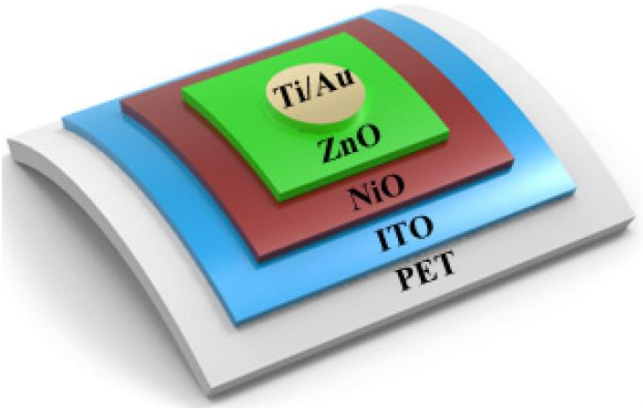

Fig. 4.15 Schematic of the p-NiO/n-ZnO PD on PET/ITO substrate

Fig. 4.16 The fabricated device exhibiting flexibility and transparency

In Fig. 4.17, grazing incidence X-ray diffraction (GIXRD) measurements of the fabricated device show all the diffraction peaks that can be assigned as cubic NiO (JCPDS-78-0643) or hexagonal wurtzite ZnO structure (JCPDS 36-1451), accordingly. Fig. 4.18 shows the bandgaps of the NiO and ZnO thin films with Tauc plots measured by UV-vis spectroscopy. The bandgaps are estimated by extrapolating the linear region of the Tauc plots of $(\alpha h\nu)^2$ versus $h\nu$ to $h\nu = 0$, where α is the absorption coefficient and $h\nu$ is the photon energy. The estimated bandgaps are 3.74 eV and 3.25 eV for NiO and ZnO, respectively. The wide bandgaps lead to the transparency of the prepared films in the visible spectrum

and will determine the rising and falling edges of the EQE patterns under various reverse bias voltages.

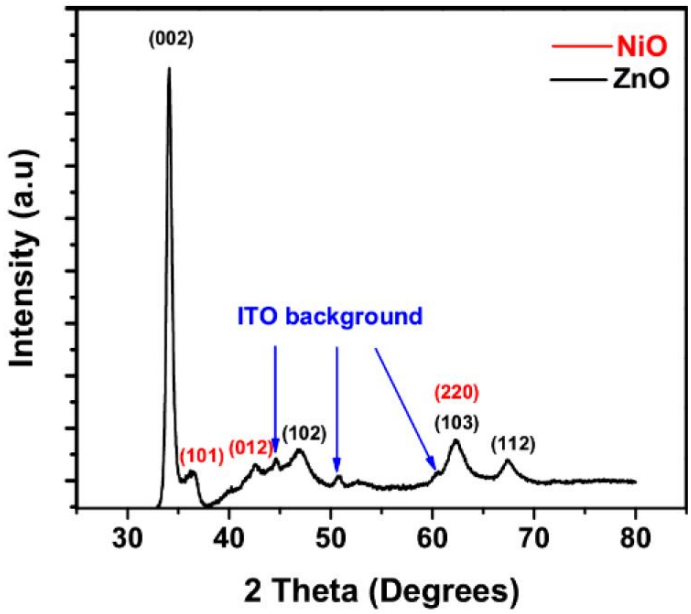

Fig. 4.17 ERD scans taken from the fabricated devices

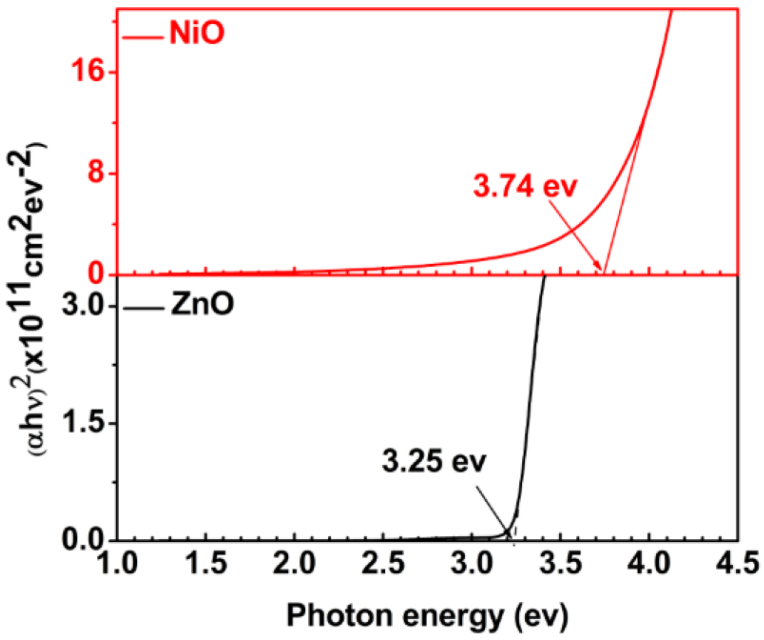

Fig. 4.18 Tauc plot for direct energy bandgap from absorption spectroscopy

The Fig. 4.19 illustrates the mechanism of the self-powered PDs through the band diagrams of the fabricated device. Under UV illumination, electron-hole pairs are generated in the depletion region of the device. At the interface of NiO and ZnO films, the built-in electric field across the depletion region separates the photo generated electron-hole pairs and drives them out of the depletion region. The drifted electrons then diffuse through the ZnO layer to be collected at the Ti/Au cathode. Similarly, the photo generated holes reach to the ITO anode through the NiO layer. Figure 4.20 shows the current-voltage (I-V) characteristics of p-NiO/n-ZnO heterojunction device in the dark and under UV illumination from the backside (PET/ITO) at room temperature. The applied voltage ranges from −1.2 V to 1.2 V, where the positive voltage means reversed bias. The diode shows an obvious rectifying behavior and a rectification ratio of ≈111 at ±1.2 V is calculated from the dark current.

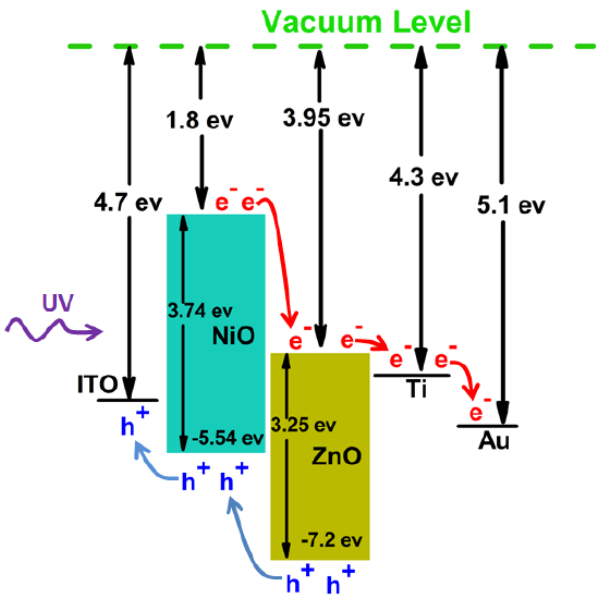

Fig. 4.19 Energy bandgap of the PD

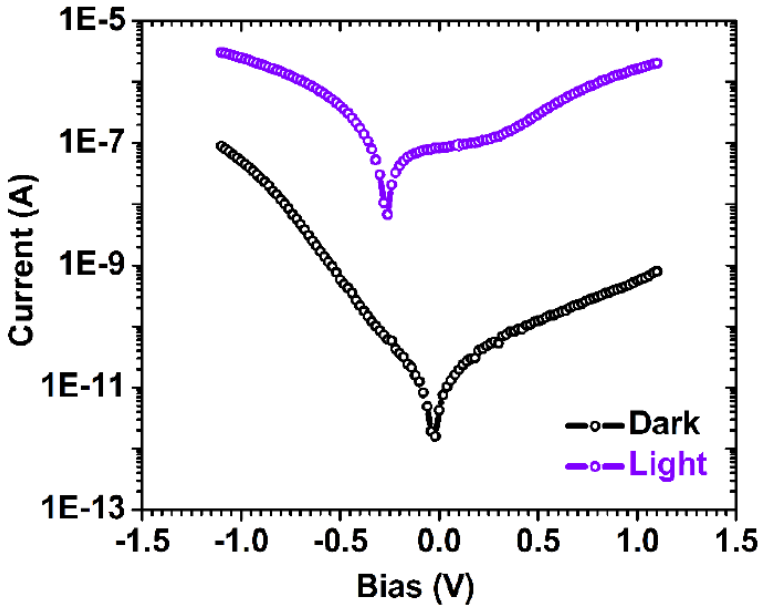

Fig. 4.20 Diode characteristic of the PD

Fig. 4.21 shows the temporal response of the fabricated photodetectors under illumination of 365 nm UV at room temperature. The photocurrent increases very rapidly upon exposure to UV radiation, stays essentially constant during the UV exposure, and decays much faster when UV is turned off. The rise time (tr) for the photocurrent to reach from 10% to 90% of its maximum value is ≈323 ms and the decay time (td) for the photocurrent to decrease from 90% to 10% of the peak value is ≈12 ms. The slow response of the PD is related to strong carrier trapping. These photoconductors exhibit comparable or better temporal response than other oxide based PDs [201, 202], indicating high quality engineered metal oxide heterojunction with excellent sensitivity.

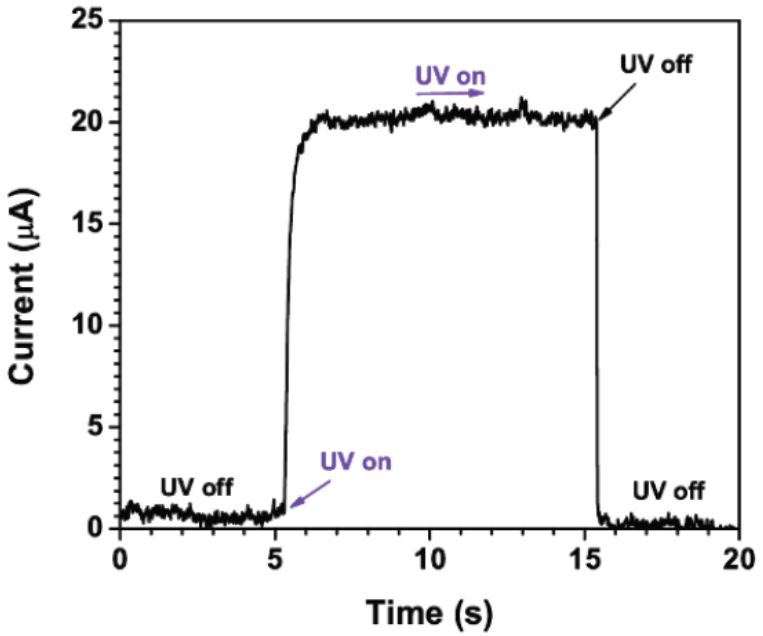

Fig. 4.21 Current-time plot of photocurrent response of the PD

4.5 Spin Coating of Nanoparticles and Solution-Processed Thin-Film Photodiodes

Both sputter deposition of NCs and spin-coating of NPs were studied. The final sensor process picked the sputter deposition over spin-coating chemical synthesized NPs even though NPs have smaller size and larger surface to volume ratio than NCs. The decision was made from process integration point of view. Spin-coating process doesn't have a conformal and uniform coverage of NPs on 3-D and high aspect ratio wafer structures like high-wall NWs and deep-trench windows. But the spin-coating method has advantage in low-cost, so that it can be used for thin-film and NPs deposition on plane wafer and low aspect ratio substrates. The solution-processed thin-films were explored and spin-coated on transparent glass substrate. The fabricated p-n junctions were proved novel photodiodes.

Solution-processed p−n heterojunction photodiodes have been fabricated based on transition-metal oxides in which NiO and ternary Zn1−xMgxO (x = 0−0.1) have been employed as p-type and n-type semiconductors, respectively. Composition-related structural, electrical, and optical properties are also investigated for all the films. We observed that the bandgap of $Zn_{1-x}Mg_xO$ films can be tuned between 3.24 and 3.49 eV by increasing Mg content. The fabricated highly visible-blind p−n junction photodiodes show an excellent rectification ratio along with good photo response and quantum efficiency under ultraviolet (UV) illumination. With an applied reverse bias of 1 V and depending on the value of x, the maximum responsivity of the devices varies between 0.22 and 0.4 A/W and the detectivity varies between 0.17×10^{12} and 2.2×10^{12} cm $(Hz)^{1/2}/W$. The photodetectors show an excellent UV-to-visible rejection ratio. Compositional non-uniformity has been observed locally in the alloyed films with x = 0.1, which is manifested

in photo response and X-ray analysis data. This paper demonstrates a simple solution process, low cost, band tunable photodiodes with excellent figures of merit operated under low bias.

Transition-metal oxide (TMO) UV PDs was fabricated by solution-process of p-NiO and n-$Zn_{1-x}Mg_xO$ (x = 0−0.1) layers on conductive fluorine-doped tin oxide (FTO) covered glass substrates. Sol−gel $Zn_{1-x}Mg_xO$ thin films show a hexagonal wurtzite type of crystalline structure and no significant change of grain morphology for all the films studied. The devices show prominent but tunable UV photo response with various Mg contents consistent with the bandgap of alloyed ZnO. For higher Mg content (x = 0.1), compositional non-uniformity has been observed over the film which is manifested in the device's optical properties.

4.5.1 Experiment Details

For NiO, nickel acetate tetrahydrate was dissolved in 2-methoxyethanol and monoethanolamine (MEA) in a glass vial. Similarly, $Zn_{1-x}Mg_xO$ precursor solution was prepared separately using zinc acetate tetrahydrate and magnesium acetate tetrahydrate in the same solvents. The molar ratio of Ni^{2+}:MEA or (Zn^{2+}+Mg^{2+}):MEA was maintained at 1:1 in the solution. The concentration of Mg^{2+} was adjusted to form $Zn_{1-x}Mg_xO$ thin films with x ranging from 0 to 0.1. Concentration of all metal ions was 0.4 M. The dissolved precursors were magnetically stirred at 60 ℃ for 2 h in a water bath and then filtered with a 0.45 μm filter.

The FTO/glass substrates were cleaned with acetone and isopropanol in an ultrasonic bath, rinsed with deionized water, and finally dried with N_2 gas. For thin-film

fabrication, NiO precursor was spin-coated on the substrates and the film was immediately dried at 300 ℃ for several minutes on a preheated hot plate in a fume hood. The procedure was repeated multiple times to achieve film thickness of 250 to 300 nm. The same procedure was repeated for $Zn_{1-x}Mg_xO$ to obtain ≈90−120 nm thick film. Finally, the films were annealed at 400 ℃ for 20 min in air. Ultrathin Ti (10 nm)/Au (3 nm) top contacts were deposited by electron-beam evaporation at a rate of about (0.5−1) Å/s through a metal mask having an array of circular openings of 3.8 mm. No process optimization was performed.

Surface morphology and cross-sectional structure of the PDs were examined using a Bruker Dimension FastScan atomic force microscopy (AFM) instrument and a Hitachi-4700 high-resolution scanning electron microscopy (SEM) instrument equipped with energy dispersive X-ray spectrometry (EDS). Cross-sectional images were taken from freshly cleaved samples after coating them with carbon to avoid charging effects (Fig. 4.23). Structural characterization of the oxide films was conducted using conventional X-ray diffraction (XRD) (Fig. 4.24). Vacuum ultraviolet variable angle ellipsometry (VUV-VASE) measurements were performed to determine the dielectric functions of the films from which optical band gaps were extracted by employing Tauc plots (Fig. 4.25).

4.5.2 Results Discussion

Fig. 4.22 shows the schematic of the PD with various components associated with the p−n junction photodiode. A cross-sectional SEM image of a representative device is depicted in Fig. 4.23. The SEM image clearly shows the multilayer structure of the PD for nominal Mg concentration of x = 0.05, showing various oxide layers on FTO/glass

substrates. The thicknesses of spin-coated NiO and $Zn_{0.95}Mg_{0.05}O$ have been estimated to be about 250 and 120 nm, respectively. The sharp interface between NiO and $Zn_{0.95}Mg_{0.05}O$ indicates smooth surfaces of fabricated films. Lifetime of photo generated carrier is a crucial factor in determining the performance of a PD. The photo generated minority carrier outside the depletion region (the interface) has a very short lifetime because of fast recombination with majority carriers. Hence, the sensitive region of a UV PD is the depletion region as is generally recognized. Meanwhile, defects in the interface will greatly reduce the lifetime of photo generated charge carriers in terms of enhanced possibility of scattering and functioning as recombination centers. Therefore, a sharp, high-quality interface ensures better performance of the PD.

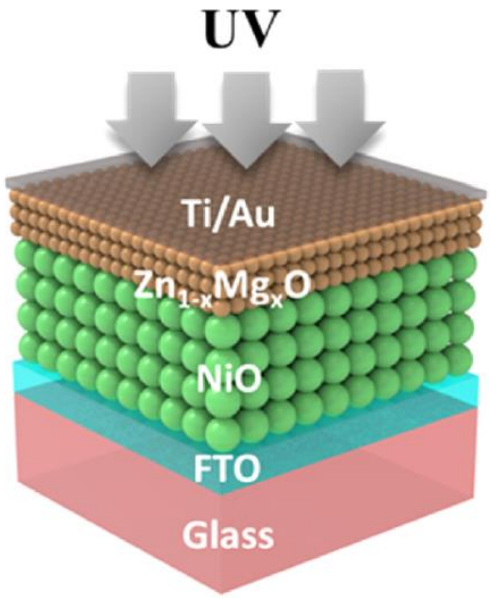

Fig. 4.22 Schematic of the device

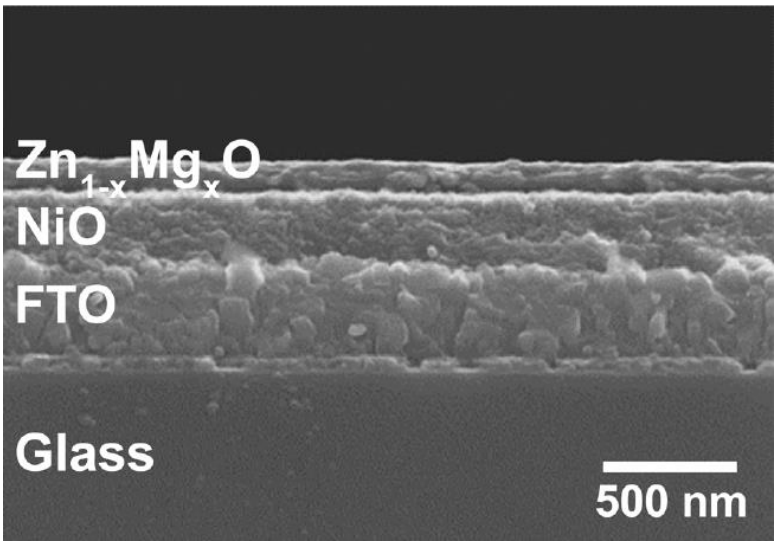

Fig. 4.23 Cross-sectional SEM image of PD with x=0.05

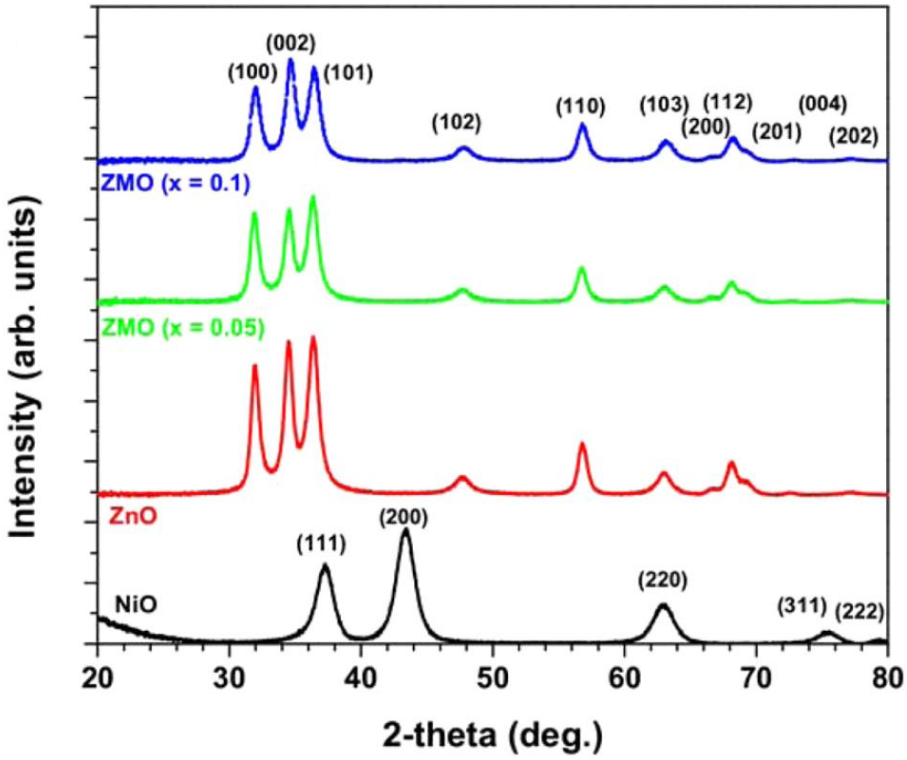

Fig. 4.24 XRD scans of diffraction peaks from cubic NiO and hexagonal $Zn_{1-x}Mg_xO$

Fig. 4.24 shows XRD patterns of prepared NiO and $Zn_{1-x}Mg_xO$ (x = 0, 0.05, 0.1) films. All the diffraction peaks can be identified as cubic NiO (JCPDS entry 78-0643) or

hexagonal wurtzite ZnO structure (JCPDS entry 36-1451), accordingly. These results imply that the fabricated ZMO films retain the ZnO hexagonal wurtzite crystal structure without any segregation of MgO phase. The broad diffraction peaks are in agreement with the polycrystalline nature and the small grain size of processed thin films. A subtle shifting of ZnO (002) toward higher diffraction angle from 34.51 °(x = 0) to 34.68 °(x = 0.1) with an increase in Mg content is identified in Fig. 4.19. This observation can be attributed to the slightly lower ionic radii of Mg2+, which decreases the grain size of ZMO in the c-axis.

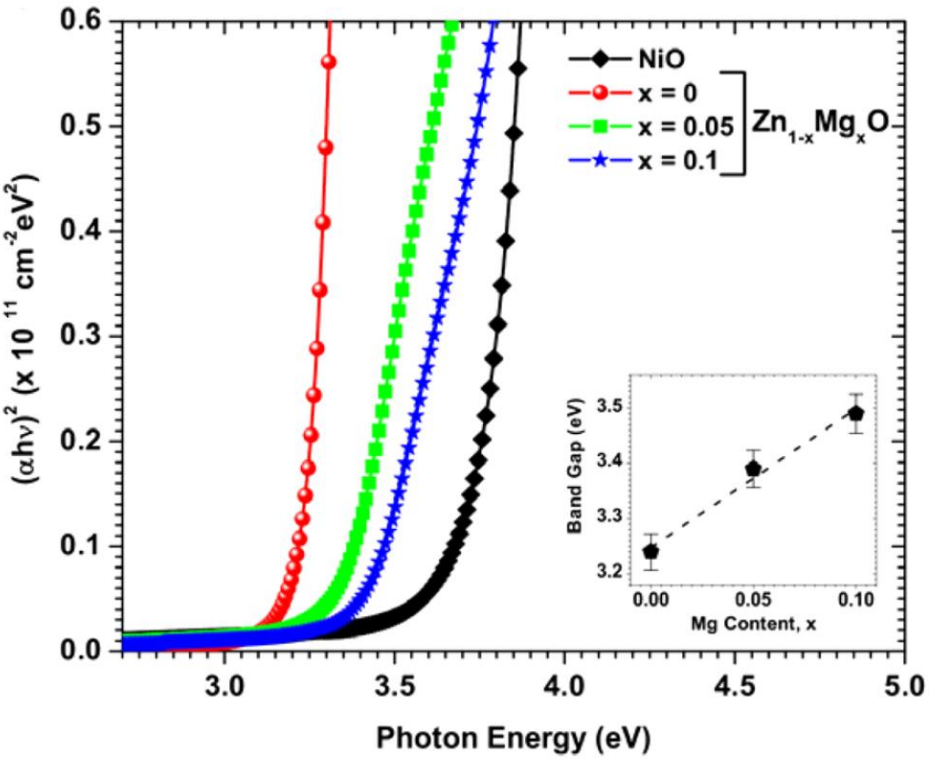

Fig. 4.25 Tauc plot estimation of the band gap by ellipsometry (inset shows the band gap linearly fit as a function of Mg content)

To understand the optical absorption and bandgap energy of NiO and $Zn_{1-x}Mg_xO$, absorption coefficients (α) are calculated from the pseudodielectric functions of the thin

films using ellipsometry. The optical band gap (Eg) is then derived from the Tauc plot, which is a linear relationship of $(\alpha h\upsilon)^2$ versus $h\upsilon$ where $h\upsilon$ is the photon energy (Fig. 4.25). Eg is deduced from a linear fit to the near band gap spectral region and is found to be ≈ 3.72 eV for NiO, which is an agreement with reported data [203].For $Zn_{1-x}Mg_xO$ films, there is a gradual blue shift of the fundamental absorption edges with the increase of Mg concentration. The value increases linearly from 3.24 eV for x = 0 to 3.49 eV for x =0.1, which can be fitted with the equation Eg = (3.248 + 2.51x) eV.

It must be noted here that for x = 0.1, the Tauc plot shows another linear regime at lower energy (below 3.7 eV) in addition to the one used for linear fitting, and this may indicate some composition variation across the sample as will be shown later. Although the ionic radius of Mg^{2+} ions (0.57 Å) is almost equal to that of Zn^{2+} ions (0.60 Å) [204], which might imply a wide range of solubility of Mg in ZnO, the thermodynamic solubility limit of Mg in ZnO is a mole fraction of only 4% [205]. However, solid solubility of MgO in ZnO has been reported to be mole fraction of 33% for thin films deposited by PLD [206] and 43% deposited by MBE[207]. The sol−gel method is based on equilibrium growth conditions. Thus, the solubility is influenced by the starting precursors, solvents, temperature, etc. as opposed to other non-equilibrium growths. The compositional fluctuations in solution-processed $Zn_{1-x}Mg_xO$ systems have also been reported for modest [208-210] to higher [211] Mg content, and our data also indicate some possible compositional variation for x = 0.1.

In any case, all the films are highly transparent in the visible range, which makes them suitable for UV PDs. Considering the limitation of this sol−gel technique, one can

utilize either PLD- or MBE-grown Zn1−xMgxO on NiO to avoid such compositional non-uniformity at higher Mg content.

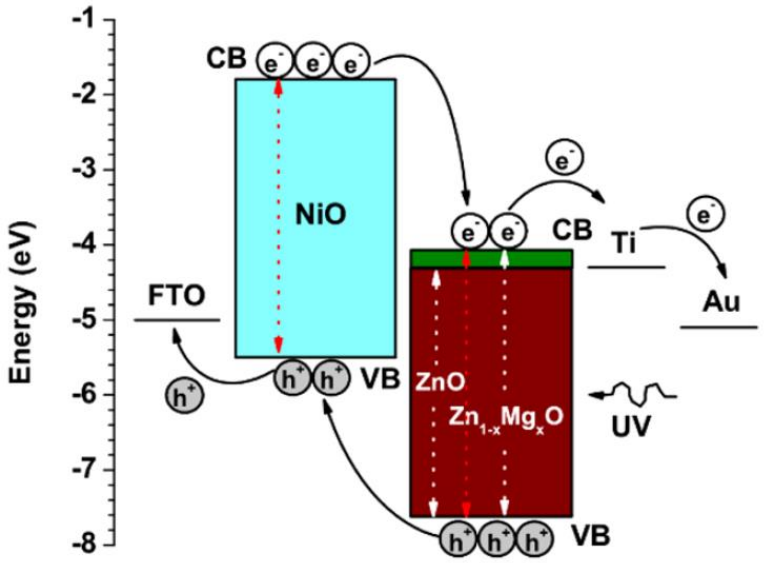

Fig. 4.26 Energy levels of various components in the PDs

The energy levels of various components of the PD are shown in Fig. 4.26, where Zn1−xMgxO is depicted as a tunable bandgap system because of different Mg content. On the basis of the reported data, incorporation of Mg^{2+} into ZnO leads to the modifications of conduction band (CB) edge of the ternary oxide whereas the valence band (VB) edge remains unchanged [212]. Thus, the CB edge changes within $\approx$ 0.25 eV as the corresponding bandgap of Zn1−xMgxO varies from 3.24 to 3.49 eV with an increase in Mg content (x = 0−0.1). Under UV illumination, the photogenerated electrons are transported through the Zn1−xMgxO layer to the Ti/Au cathode and the holes are transported from the NiO to the FTO anode. On the basis of the band-edge energy offsets, NiO/Zn1−xMgxO layers form a type-II heterojunction (Fig. 4.26). The built-in field as well as the energy gradient at the type-II interface enables spatial separation of electrons and

holes. The current−voltage characteristics of the heterojunction diodes reveal the anticipated rectifying behavior in the dark and exhibit an excellent rectification ratio of ≈ 18 500 at ±1 V (inset of Fig. 4.27). Under UV illumination, current enhancement is observed under forward and reverse bias because of the photo generated carriers. It is worthwhile to mention here that the current density of the devices decreases after Mg alloying because of the increase of resistivity. Undoped ZnO is an n-type material, and the higher carrier density is attributed to the interstitial zinc and/or oxygen vacancy [213]. When Mg is incorporated into ZnO, the oxygen vacancies are suppressed, which reduces the carrier density in the film [214]. Hence, dark current decreases from 100 to 18 nA at a reverse bias of 1 V when the Mg content increases from 0.05 to 0.1.

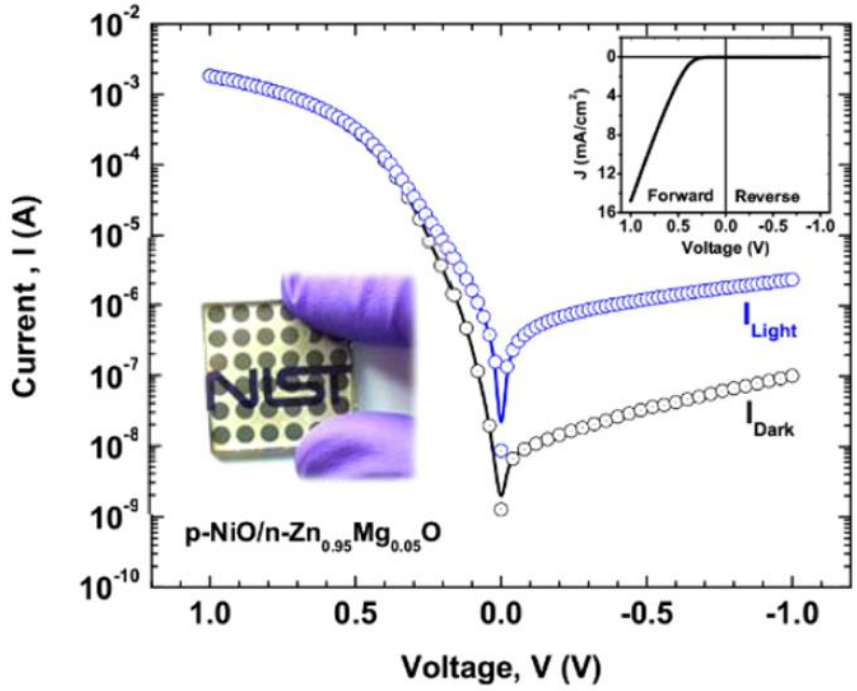

Fig. 4.27 Current-voltage plot of PD with x=0.05 in dark and UV illumination (335 nm wavelength and 1.2 μW power)

4.6 Chapter Conclusion

In this chapter, methods and techniques to fabricate metal-oxide thin-films, NPs and NCs were explored. The threshold thickness for NCs formation were characterized and revealed. The thin-film samples with the same NCs sputtering conditions were used for gas sensing database establishment. The thin-film sensors thus fabricated respond to a wide range of gases. I also show that metal oxide thin film sensors lack selectivity and it is hard to maintain a constant baseline current. Reliably and reproducibly fabricating thin-film stacks based on solution-processes for various applications were explored. The resulting fabricated thin-film p-n junctions can be used as photodiodes. XRD, AFM, and SEM techniques were used in characterization of the NCs and thin-films. On the basis of our experiments, the metal oxide NCs and thin-film fabrication methods show promise, potentially enabling mass production of sensors and optical devices based on single layer, stacked layers or integrated onto NWs. The top-down approach described here enables the NCs to be integrated with NWs and micro heaters to provide useful sensor structures. The process overcomes the barrier of the spin-coating process that exhibits the non-uniform coverage issue for 3-D or high aspect ratio wafer structures. Many sensors (chemical, gas and biology) using metal-oxide/ metal NCs can be benefit from the top-down approach and the sensing database. The study was published at the journal of alloy and compound [215], applied physics letter: material [216], and ACS advanced materials and interfaces [200].

Chapter 5: Micro-Heater

This chapter gives the fabrication details of the micro-heater devices: the embedded micro-heater that was integrated with gas sensors, other several low-cost designs that use a free-standing silicon membrane or Si_3N_4-memberane support for aerosol generation purpose. Low-cost metals deposition and wet etch process techniques were used to fabricate large batches of micro-heaters. Other applications were explored, such as medical drug aerosol generators for inhalation therapy.

Over the past decade, great interest has been shown in low cost, fast response, low-power micro-heaters for a variety of applications [33]. In particular, micro-heaters (MH) and micro-hot-plates (MHP) are integrated with chemical and gas sensors for cycles of releasing chemicals and maintain working temperature [34-40], humidity sensor [41, 42] and MEMS micro fluid pumps for ambient temperature setup [43]. They can also be used in medical care, to deliver aerosol drugs and delivery through inhalation [44-46]. Moreover, they can be powered by high charge-capacity, light weight, flexible battery sources [47, 48]. Several early micro-heater designs had been reported using thin-films such as poly-Si to fit in CMOS process [49, 50]. Recently, platinum [41, 51] or Platinum based metal combinations (Pt/Ti, Pt/Cr, Pt/Al_2O_3 or Pt/MgO) have been widely explored [34-37, 40]. However, for low cost, we choose nickel. Elemental nickel has 34% less electrical resistivity and 27% more thermal conductivity comparing to platinum, and is much cheaper. There is no report that I have found on nickel heater elements.

5.1 Embedded Micro-Heater for Gas Sensor

A robust micro-heater (MH) which is the same dimension in length as NW was studied to generate local heat assistant for NW. The gas sensor designed and fabricated can work properly at room temperature. The embedded MH is to enhance the sensing unit and enable the system to be more reliable and robust in real-time sensing situations. The local heating will increase the desorption rate of unwanted gases on NW and reset the sensor to the baseline. On the other hand, the MH enables the sensor unit with the capability to work at the extreme cold environment like north/south pole and space.

5.1.1 Design Considerations

Micro-heater, metal pattern in meander shape on wafer substrate and in parallel with nanowire, was designed and made. The length of the MHs are designed the same with the NWs (10, 50, 100 and 200 μm). The MH pattern is designed to a meander shape line that has width of 5 μm and lays 20 μm away from and in parallel with the NW. For each NW, a MH is aside for generating a local high temperature and assisting desorbing all the unwanted gases to reset the gas sensor unit. Fig. 5.1 shows the schematic of the MH alongside of the gas sensor unit.

To maintain the whole system low power consumption, the MH was designed carefully by considering three major factors: the MH size, the heat conduction efficiency of the chosen substrate material and NW material, the heat loss due to convection at the MH surface. Device size wise, the smaller the MH, the lower power consumption will be achieved. The width of MH is chosen to be 5 μm. For heat conduction control, the ideal

MH should only generate a high temperature island in a small area to maintain the total low power consumption. In this sense, I designed the MH metal pattern deposit on the AlGaN or sapphire substrate (this is defined by the NW dry etching, will discuss more and detail process integration in Chapter 6), and be parallel to and 20 um apart from the GaN NW. The thermal conductivity of GaN is 220 W/m ∙K at room temperature [217-222], $Al_{0.2}Ga_{0.8}N$ is only around 20 W/m ∙K [221-223] and sapphire is 27.21 W/m ∙K [224, 225] ($Al_{0.2}Ga_{0.8}N$ and sapphire are close). In this way, the generated heat will be confined within a small area due to the low thermal conductivity of AlGaN and sapphire substrate and will be uniformed distributed within the GaN NW due to its high thermal conductivity. A design of 300 nm thick SiO_2 passivation layer to cover the whole MH is an additional strategy to minimize the heat convection at the surface. Due to the thermal conductivity of SiO_2 is 1.4 W/m ∙K [226, 227], a magnitude lower than $Al_{0.2}Ga_{0.8}N$, sapphire substrate and nickel metal (90.0 W/m ∙K), the majority of the heat generated will be forced and conduct downward through the substrate to the NW.

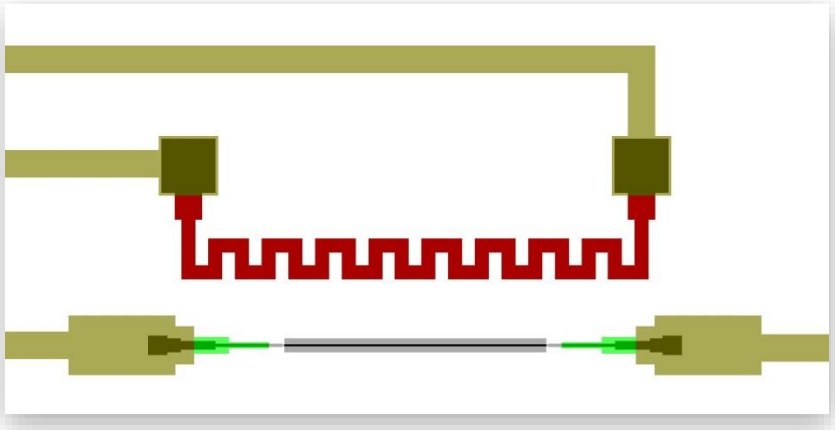

Fig. 5.1 Design schematic of the MH embedded to gas sensor

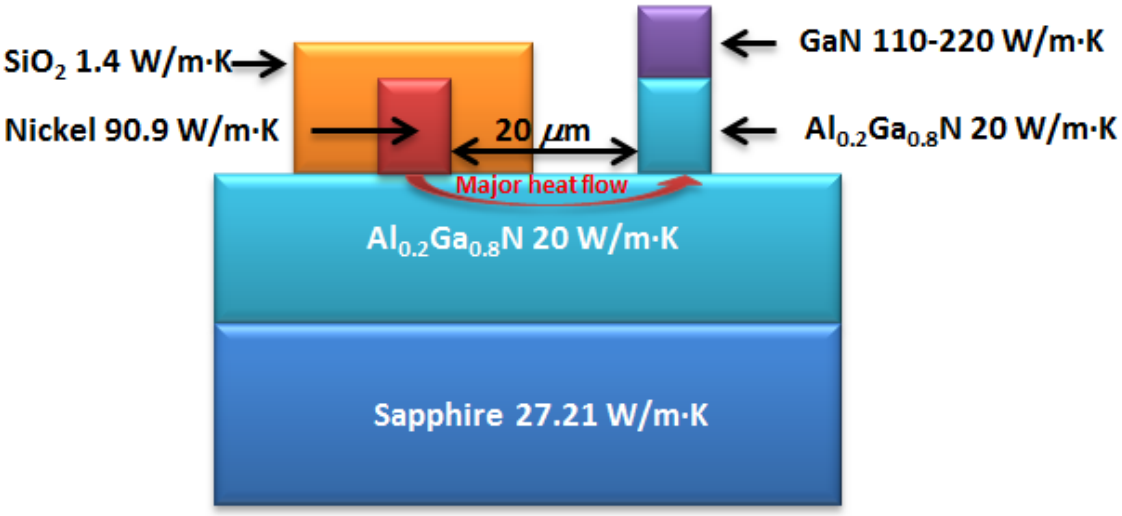

Fig. 5.2 Major heat flow and the thermal conductivity profile of materials

5.1.2 Fabrication

AlGaN thin-film on sapphire substrate was pre-baked at 210 ℃ for 10 minutes to remove water and other organic residue. A bi-layer stack of photoresists (MicroChem LOR3A and Microposit S1813) were used to support a lift-off process for the heater metal. Spin coated LOR3A at 4000 rpm for 45 seconds was use as a first layer, followed by 5 minutes bake at 210 ℃. We next spin coated S1813 at 4000 rpm for 45 seconds followed by a 60 second bake at 115 ℃. After UV exposure with 90 mJ/cm ^{2}dose energy, the MH wafer was post-baked on 115 ℃ hot plate for 60 seconds, cool down and followed by developing in Microposit MIF-319 for 60 seconds. reactive-ion etching (RIE, Unaxis 790) was followed by a descum run with 30sccm flow rate of oxygen for 30 seconds to clean up the remaining un-thoroughly developed resist residue.

A Ti/Ni (10 nm / 210 nm) metal stack was deposited in the Denton Infinity 22 E-beam Evaporator. The wafers were lifted-off in PG Remover or 1165, and rinsed clean in IPA and DI water. Rapid Thermal Annealing (RTA) is employed for stress release and enhances the reliability of the MH. In RTA, the wafer is placed inside a thin quartz chamber with halogen lamps surrounding it. The temperature rise is fast (as high as 25 ℃ per seconds). The wafer ambient is 6000 sccm of ultra-pure Ar. The RTA is performed at 700 ℃ for 30 seconds. The temperature ramp rate is set to 100 ℃ per minute. Slow rise rate is set to make sure the metal stack is given enough time to reach equilibrium while keeping a low stress level. A passivation layer of 300 nm SiO_2 was deposited uniformly on the wafer by plasma enhanced chemical vapor deposition (PECVD, Plasma-Therm Versaline) to seal the MHs from air, reduce the oxidation while heating, decrease the heat loss through surface convection and push heat conduct to the substrate direction.

5.1.3 Heating Performance

Infra-red (IR) camera was used to characterize the heater elements. Emissivity calibration was run at 50 ℃, 100 ℃, 150 ℃ and 200 ℃. The MH samples were put on a hot plate without engaging the MH, set the hot plate temperature to the calibration set point and wait for 10 min for an equilibrium state achieved. Tune emissivity value to match the IR camera readings with the hot plate set temperature. The emissivity values are 0.90, 0.93, 0.88 and 0.60 W/m ²at 50 ℃, 100 ℃, 150 ℃ and 200 ℃ respectively.

5, 10 and 15 V voltage biases were applied to each MH to see the heat generation efficiency. The current, power and steady state temperature are shown in Table 5.1.

Voltage Bias	5 Volts			10 Volts			15 Volts		
MH Length	I(A)	P(W)	T(˚C)	I(A)	P(W)	T(˚C)	I(A)	P(W)	T(˚C)
10 μm	0.05	0.25	60	0.078	0.78	150	NA	NA	NA
50 μm	0.041	0.205	55	0.072	0.72	100	0.078	1.17	170
100 μm	0.04	0.2	50	0.07	0.7	100	0.078	1.17	170
200 μm	0.026	0.13	40	0.054	0.54	80	0.065	0.975	150

Table 5.1 IV measurement and IR camera characterization of MHs

The temperature targets are 60 ˚C and 110 ˚C for removal of organic adhesion and humidity respectively. From the data in Table 5.1, it is obvious the power consumption for the shortest MH with smallest surface area is the most power efficient MH. Fig. 5.3 to Fig. 5.6 show the IR camera imaging of 10, 50, 100 and 200 μm MH at 5 and 10 V bias temperature distribution densities. Due to the MH is very small and the resolution of IR camera is 20 μm, each MH only occupies 4 pixels. The accurate temperature of MH cannot

be told, but the temperature of the local area and the temperature distribution can be read from the IR images.

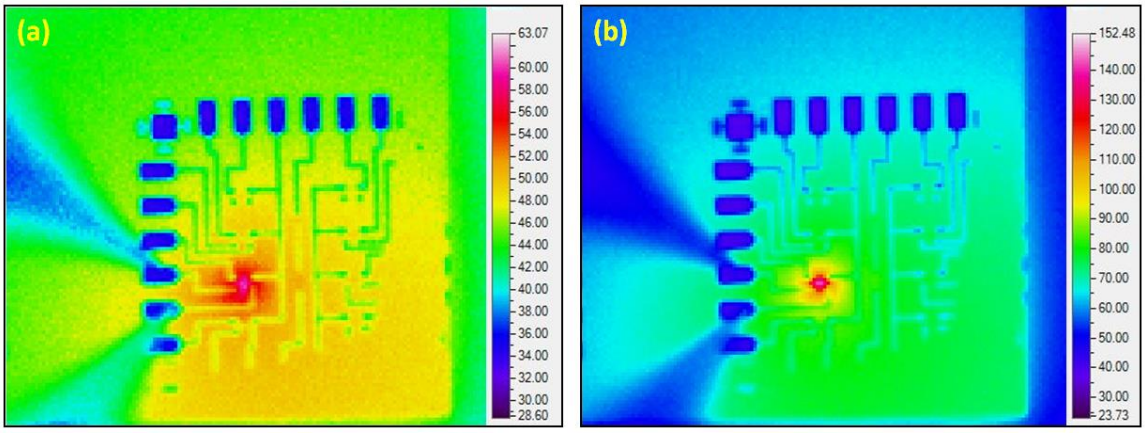

Fig. 5.3 IR Images of 10 μm MH with (a) 5 V bias and (b) 10 V bias

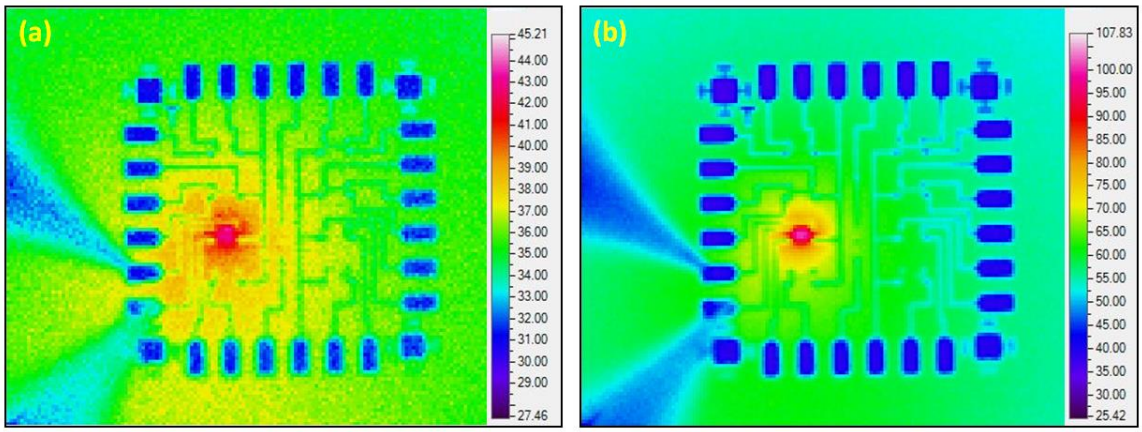

Fig. 5.4 IR Images of 50 μm MH with (a) 5 V bias and (b) 10 V bias

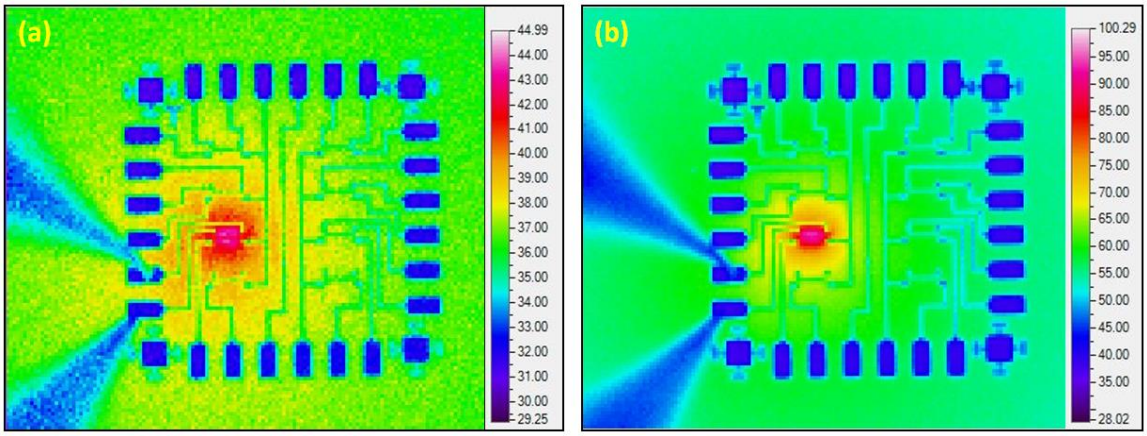

Fig. 5.5 IR Images of 100 μm MH with (a) 5 V bias and (b) 10 V bias

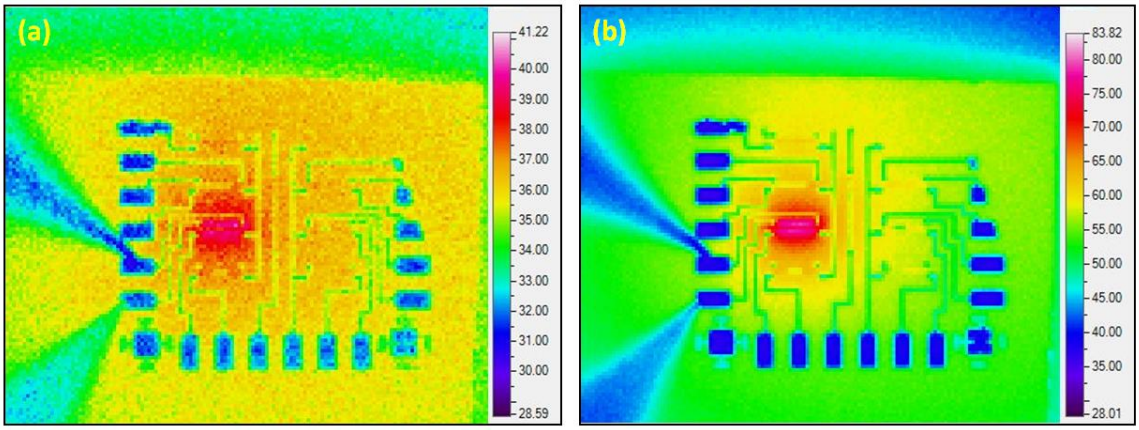

Fig. 5.6 IR Images of 200 μm MH with (a) 5 V bias and (b) 10 V bias

5.2 Low-Cost Micro-Heater for Aerosol Generation

The micro-heaters were further explored for low-cost and disposable applications. Using vacuum instruments, cleanroom facilities and metal deposition tools are the major factors keep the total cost high. The well controlled electroless nickel plating method is a good low-cost alternative process for depositing thick Ni heater patterns. It is fast (270nm/min) and low cost comparing to the waiting time of purging to high vacuum of PVD equipment. The thickness and growth rate are controllable at the same time. Thermal Evaporator has difficulty controlling deposition rate, and it is time consuming for thick metal deposition. Moreover, PVD cannot deposit metal thickness larger than the thickness of shadow mask or the limit of lift-off photo-resist, the subtraction process need more process steps and time-consuming dry etching back. The solution based nickel plating bath can grow metal as thick as 10 μm without peel-off issues.

The substrate of MH must conduct heat generated by micro-heater-coil and ideally achieve uniform temperature all over the local area. Different substrate materials were reported have acceptable performance, Si membrane is widely applied for MEMS designs due to their excellent thin-film electrical and mechanical properties [33, 35]. Reports also show heaters based on Si_3N_4/SiO_2 structures present high-thermal characteristics [34, 36, 40]. Other reports show Polyimide exhibits better mechanical and thermal properties in achieving free-standing membrane in high yield in fabrication, as compared to Si_3N_4 and SiO_2 membranes' fragile nature [39, 51]. In my work, both silicon and silicon nitride membranes are used to achieve different functions. Amorphous silicon is resistive to HF/HCl (10:1 volume ratio) etch. It can be used as good shadow protective layer when wet etching a trench and achieving free-standing membrane. While silicon nitride has slower

etching rate in HF/HCl acid and it can be used to form reservoirs for drugs store at side of MHs. HF/HCl is a fast etchant for glass slides, exhibiting an etch rate of 25um/min. For example, a 0.13mm-0.17mm micro-cover-glass, it takes 5 min to etch away and leave a free-standing membrane pre-deposited on top of the glass. Photo resist AZ4620 was tested and proved to be a good protection mask in HF/HCl acid for at least 8 min (from my research optimization run). It can be used to function as a shadow mask and define the reservoir.

General fabrication starts with a fast PECVD deposition of silicon nitride or amorphous silicon thin-film on normal micro cover glass, followed by Cr/Ni seed layer deposition, Ni plating, spin coating AZ4620 photoresist on sides, photo lithography and wet etch. The process discussed here is on purpose of low cost, fast fabrication and for disposable device applications. So the dimensions and structures are in hundreds micrometer level. Nanotechnologies can be implemented to further scale down the size to nano-devices and integrated with other nanostructures as mentioned in the former section.

There are 4 types of micro-heaters designed and fabricated to meet the requirement of different applications: MHs with no reservoir and MHs equipped with a side, bottom, or top reservoir. All 4 types can function as an aerosol generator. Shadow masks of both meander and double-spiral wires with different lengths were used for seed layer metal deposition. The nickel plating bath was made using a MacDermid nickel plating bath, at a plating temperature of 88 ℃ and magnetic stirring at 66 rpm, the output deposition rate is 270nm/min.

5.2.1 No-Reservoir Micro-Heaters

This type of micro-heater design is planar and suitable for integration with other devices. Fig. 5.6 shows the process steps of the device fabrication. An Oxford Plasma Lab plasma enhanced chemical vapor deposition (PECVD) system was used to deposit 1 μm of silicon nitride or 200 nm of amorphous silicon on top of 0.13-0.17mm or 0.17-0.25mm micro-cover-glass wafers as a MH supporting film (Fig. 5.6a). 10nm of Cr and 20nm of Ni were deposit by E-Beam evaporation using e-beam evaporator (Denton Infinity 22) with a stainless steel shadow mask to form the seed layer, Cr being used as an adhesion layer to avoid later thick Ni deposition peel-off issues.

The shadow masks were made by laser cutting and have 100 μm width wires in meander and double-spiral shapes (Fig. 5.6b). AZ4620 was spun with 1.5k rpm to yield thickness of 15 μm, followed by hard bake to protect heater patterns and the supporting film (Fig. 5.6c). The wafer was then flipped and spun with AZ4620 resist, followed by soft-bake. The photolithography was accomplished using an exposure dose of 365nm UV for 90 s and development in AZ400K/DIW (1:3 volume ratio) for 90 s, followed by hard bake (Fig. 5.6d). Wet etch in the HF/HCl (10:1 volume ratio) bath for 5 min (Fig. 5.6e). Photo-resist was stripped in heated Remover PG or 1165, and followed by a standard acetone-methanol-isopropanol-DI water sequence rinse, then drying by nitrogen gas blow (Fig. 5.6f).

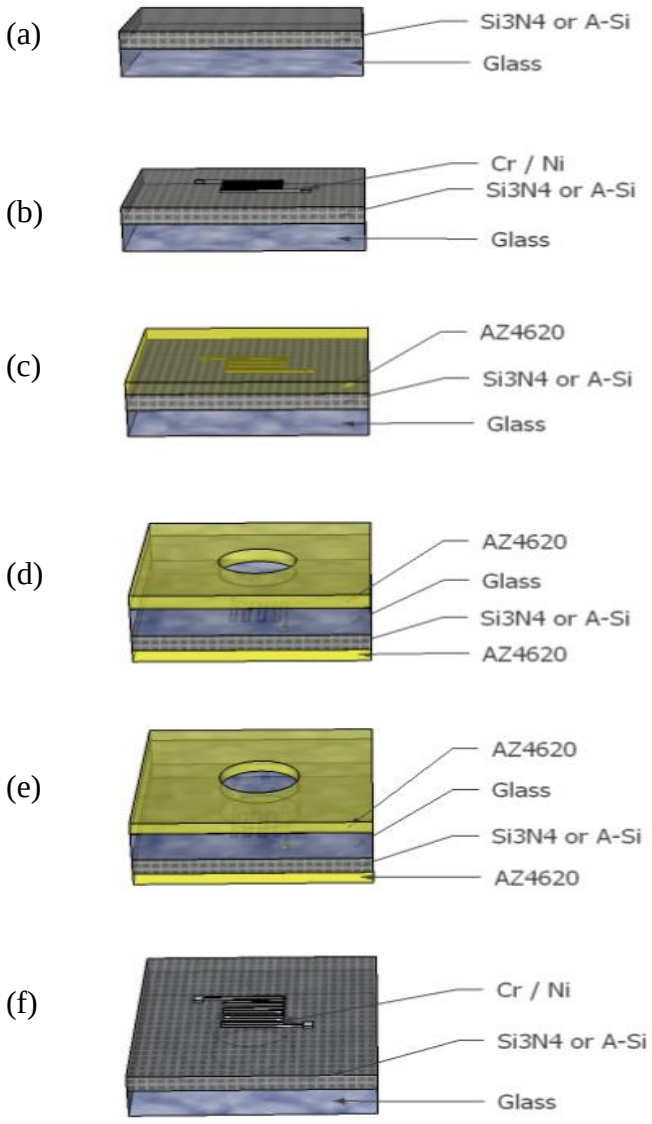

Fig. 5.6 Fabrication steps of the no-reservoir micro-heater with the ability to integrate other sensor devices. a) Micro-cover-glass with MH supporting film layer. b) Adhesion Cr layer and seed layer of Ni deposed and then thick Ni plated. c) Heater pattern covered and protected by photo-resist AZ4620 layer. d) Flip the sample over and spin photo-resist layer followed by photo-lithography to define the wet etch area. e) HF/HCl wet etch the glass. f) Remove photo-resist and flip over the sample.

5.2.2 Side-Trench Reservoir Micro-Heater

This type of micro-heater design is similar to the one described above, but the main goal here is aerosol generation rather than CMOS and MEMS compatibility. Inhaled drugs, initially in the liquid state, can be stored in the reservoir, and then transferred to the micro-hot-plate via a wicking fiber cloth (e.g., a filter paper) to evaporate, and generate an aerosol. Fig. 5.7 shows the process steps used. In order to form a trench, only a silicon nitride supporting film can be utilized, as it has a small etch rate in HF/HCl (Fig. 5.7a). Steps similar to those encountered in the no-reservoir design flow were used for step (b) to (f). Instead of hard baked AZ4620 to protect the metal, the side reservoir was defined by photolithography (Fig. 5.7c). At the end, the aerosol generator fluid was introduced in the top reservoir, and connected to the reservoir and micro-heat with a fiber cloth tissue (Fig. 5.7g).

5.2.3 Bottom-Sealed Reservoir Micro-Heater

This type of design aims to optimize medical drug aerosol generation. As compared to side reservoir micro-heaters, this design has a larger volume sealed reservoir storage space underneath the micro-heater. When the heater generates heat the liquid in the reservoir vaporizes and the higher pressure will pump up more fluids been driven and transferred through the fiber tissue to the MH. Fig. 5.8 presents the process steps of the device fabrication. In order to reduce the number of fabrication steps, only amorphous silicon membrane is used, which has a high chemical resistivity to HF/HCl acid etch. Otherwise, an extra photo-resist layer should be spun onto the surface, to protect the silicon nitride from being etched. The top part of the MH is made via the same process as the no-

reservoir MH component (Fig. 5.8a - Fig. 5.8f). The bottom part of the MH is formed by taking wafers from step (a) and flipping them over, spinning AZ4620, followed by soft-bake, photolithography exposing with a dose of 365nm UV for 90 s, and development in AZ400K/DIW (1:3 volume ratio) for 90 s. This defines the bottom reservoir (Fig. 5.8g). The components are wet etched in HF/HCl (10:1 volume ratio) for 5 min (Fig. 5.8h). After the photo-resist got removed in Remover PG with a gentle Q-tip swab, wafers were cleaned by a standard acetone-methanol-isopropanol sequence rinse, and then drying by nitrogen gas blow (Fig. 5.8i). Finally the top and bottom parts were combined with sealing glue (epoxy) or wafer bonding wax, use fiber tissue to connect the reservoir, and cover the metal pattern of MH (Fig. 5.8j).

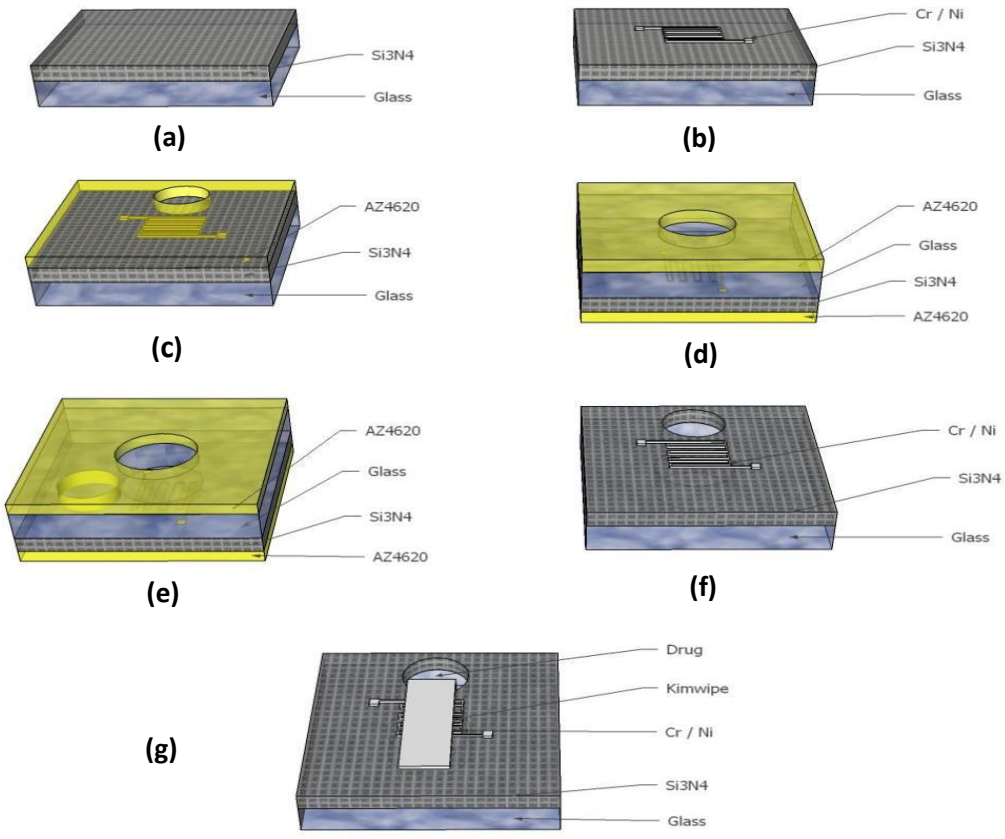

Fig. 5.7 Fabrication steps of the side reservoir micro-heater with the ability to store liquid state drugs. a) Micro-cover-glass with silicon nitride supporting film layer. b) Adhesion Cr layer and seed layer of Ni deposited and then thick plated with Ni. c) Spin photo-resist layer followed by photo-lithography to define the storage reservoir area. d) Flip the sample over and spin photo-resist layer followed by photo-lithography to define the wet etch area. e) HF/HCl wet etch both sides. f) Remove photo-resist and flip over the sample. g) Fill drug into the reservoir, stick a wicking fiber cloth on top, and connect to the reservoir

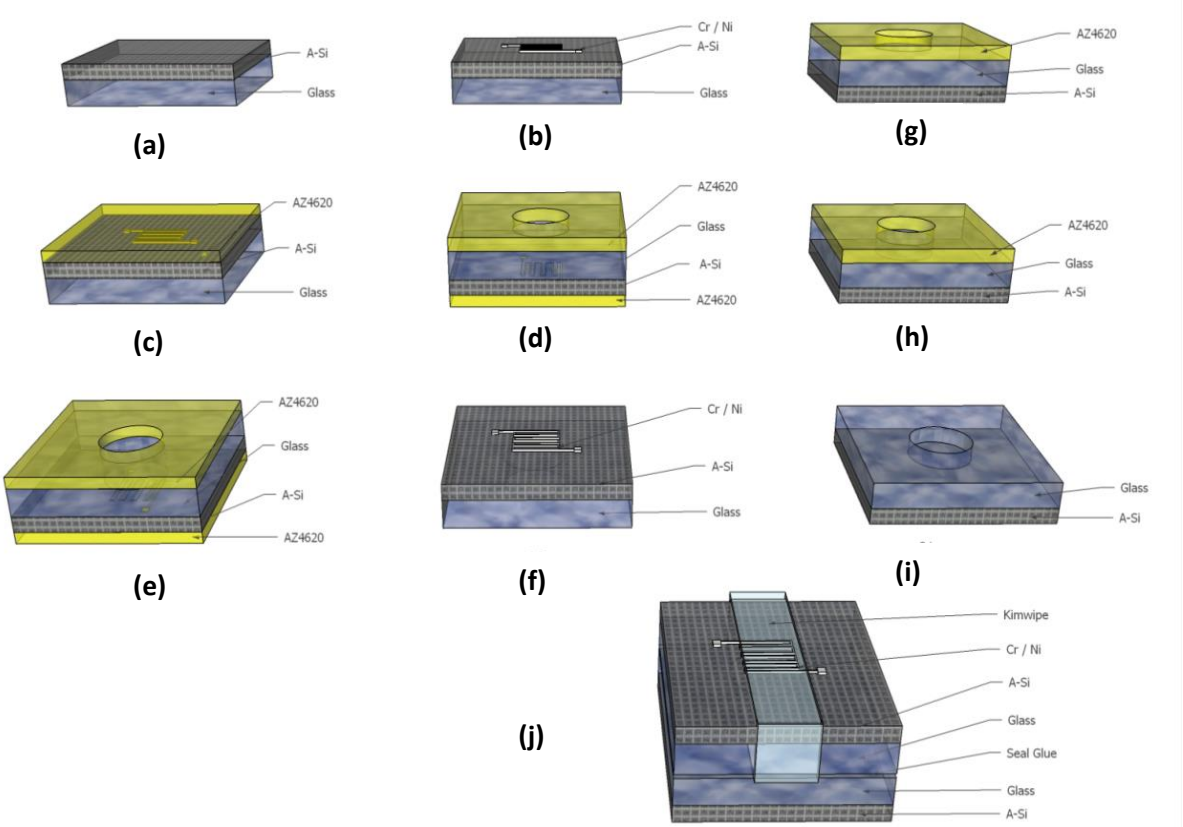

Fig. 5.8 Fabrication steps for the bottom reservoir micro-heater with the ability to store liquid state drugs in a sealed chamber. a) Micro-cover-glass with amorphous silicon layer. b) Adhesion Cr layer and seed layer of Ni deposed with thick Ni plated. c) Heater pattern covered and protected by photo-resist AZ4620 layer. d) Flip the sample over and spin photo-resist layer followed by photo-lithography to define the wet etch area. e) HF/HCl wet etch the glass. f) Remove photo-resist and flip over the sample; this becomes the top part of the micro-heater. g) Take samples from step a) and flip over, spin photo-resist layer, followed by photo-lithography to define the wet etch area for reservoir. h) HF/HCl wet etch the glass and form the bottom reservoir. i) Remove photo-resist, this

becomes the bottom part of the micro-heater. j) Seal the top and bottom part with seal glue, and use fiber cloth to connect reservoir, and then cover over the heater pattern.

5.2.4 Top Reservoir Micro-heater

This type of design is aimed at the medical drug aerosol generation process. Compared to the bottom reservoir MH, this design has larger volume for liquid storage, involves fewer fabrication steps, and even lower manufacturing cost owing to the mold made top part. Multiple MH units in parallel are used to vaporize a larger amount of liquid (or different liquids simultaneously), as shown in Fig. 5.9.

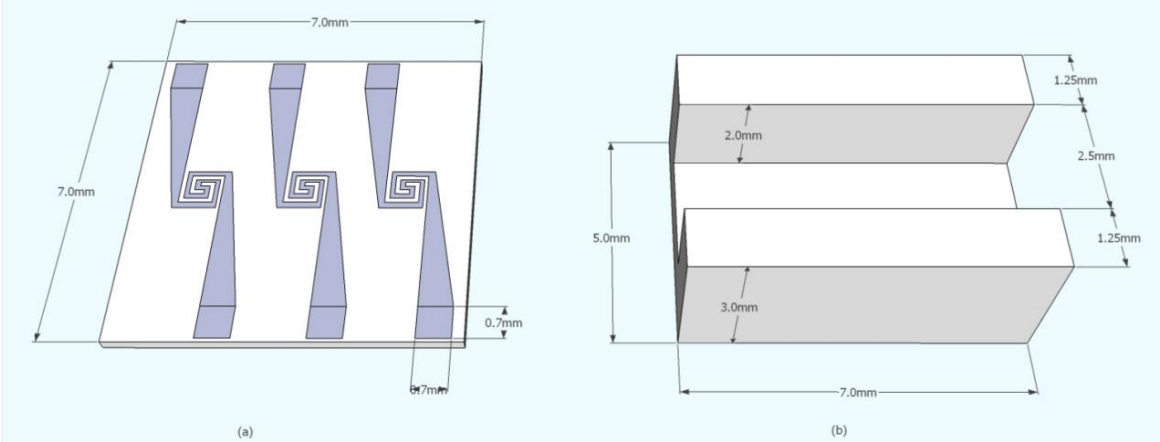

Fig. 5.9 Design of the top reservoir micro-heater: a) no-reservoir micro-heater with 3 double-spiral design in parallel. b) PVC mold made top reservoir with wick and solvent inside.

5.2.5 Fabrication Results

The Fig. 5.10 displays the fabricated devices: both silicon nitride and amorphous silicon supporting films are used. Four different length of meander shaper pattern (16mm, 18mm, 20mm, and 22mm, respectively) are processed to ascertain the best heating configuration.

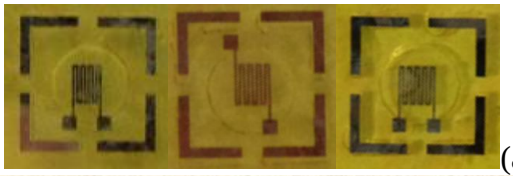
(a)
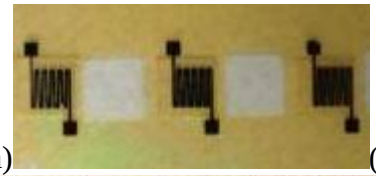
(b)
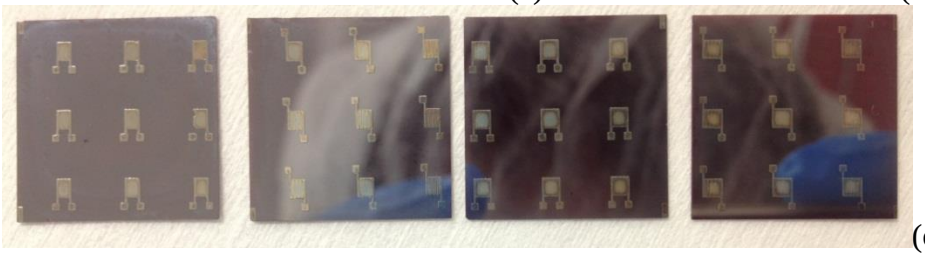
(c)

Fig. 5.10 Photographs of fabricated micro-heaters: a) no-reservoir MH with silicon nitride supporting film. b) Side reservoir MH with silicon nitride supporting film. c) No-reservoir MH with amorphous silicon supporting film (can be used as either top part of bottom reservoir MH or bottom part of top reservoir MH). Different lengths of metal pattern have been examined for optimization.

Thick plated metal patterns are used to achieve the low resistance and fast response of the MHs. The metal thickness and plating time are linearly proportional, and the resistance is inversely proportional to the plate thickness. Table 5.1 shows with the Ni plating time and pattern thickness doubled, resistances decrease by factor of 2. By adjusting plating times, we were able to achieve the targeted 8Ω, 9Ω, 10Ω, and 11Ω resistances required for the 16, 18, 20, and 22mm length patterns, respectively.

Process/Resistance	8 wires	11 wires
10nm Cr + 20nm Ni	5~6 kΩ	6~7 kΩ
Ni Plating 4 min (1 um)	75.3 Ω	100.4 Ω
Ni Plating 8 min (2 um)	37.8 Ω	50.3 Ω
Ni Plating 16 min (4 um)	16.1 Ω	23.1 Ω
Ni Plating 32 min (8 um)	8.1 Ω	10.9 Ω

Table 5.2 Pattern resistance with respect to different Ni plating times and thicknesses

In several cases, the total resistance would suddenly drop to 1~2Ω. This phenomenon is a consequence of the Ni-plating not only grows nickel on top of the wires, but also on the sidewalls. When this happens, the wires start merging with each other. This can be avoid by tight bonding the shadow mask and wafer, when depositing seed layers, or using photolithography and lift-off process when defining the seed layer.

5.2.6 Heating Performance

MHs temperature profile images were taken with an infrared camera (Optotherm Infrasight MI320). The results are shown in Fig. 5.11. The rectangular "block" structures in Fig. 5.11 are not directly obtained from the IR imager. But rather, the blocks are used to signify regions of different emissivities. One set of blocks (the upper set in Fig. 5.11) was set to account for the emissivity of the amorphous silicon film. The lower blocks were set to account for the nickel emissivity. In this way, quantitatively accurate temperature profiling of the MH surface was possible in light of emissivity differences. The inset in the upper left of the Fig. 5.11 shows the "raw" thermal image without emissivity correction at room temperature. The default emissivity for entire imaging area is 0.34. Nickel and amorphous silicon thermal emissivity were set to 0.13 and 0.75 correspondingly. These values were acquired through emissivity calibration at 100 ℃, 150 ℃, and 200 ℃.

Fig. 5.11 shows the temperature distribution under 1.7V bias. The Ni pattern can reach temperatures as high as 150 ℃. The silicon film is heated by the metal pattern and tends to be about 20 ℃ cooler than the metal itself. Different voltage bias levels, steady state temperatures and input powers are listed in Table 6.2. Operating temperatures of 150, 200, 250, and 350 ℃ are shown.

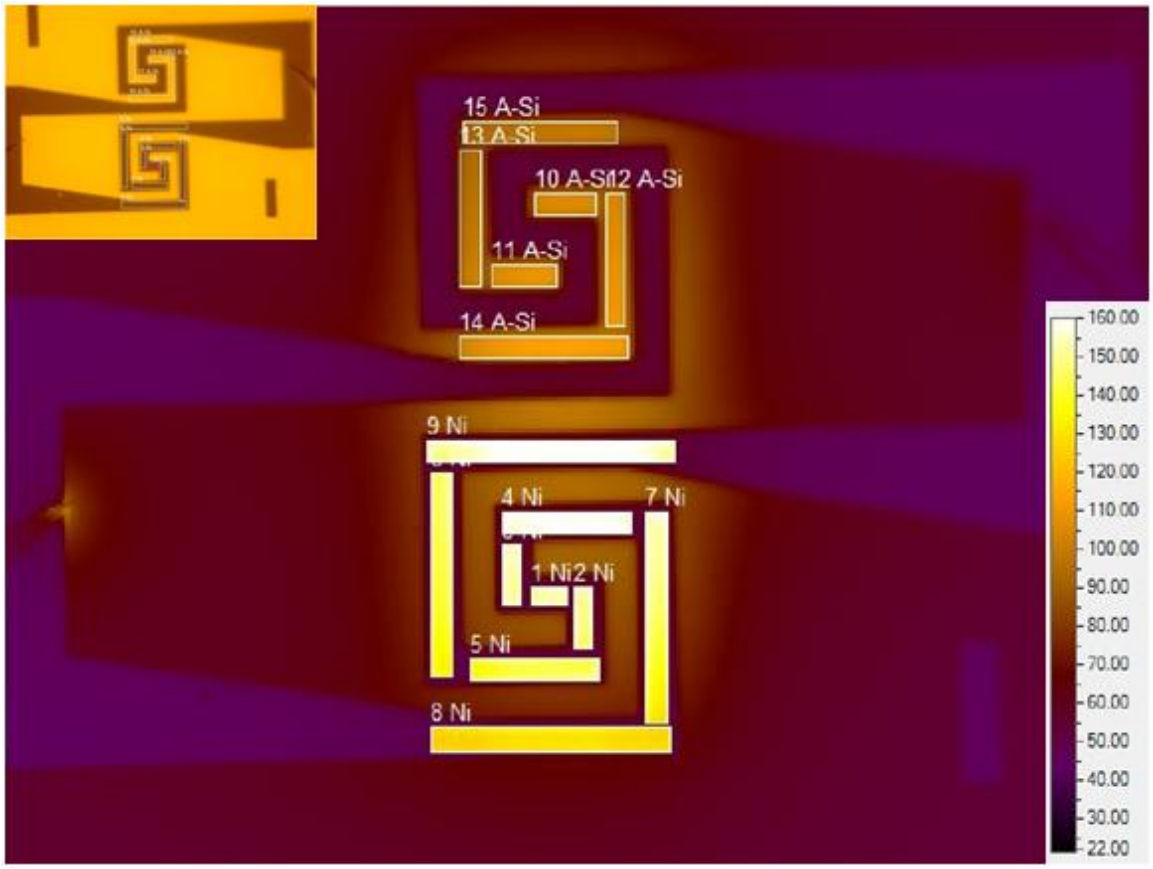

Fig. 5.11 IR image of 2 identical MHs in parallel for both A-Si and Ni areas temperature measurements with emissivity correction (Ni emissivity set to 0.13 and A-Si emissivity set to 0.75). Inset figure at upper left is room temperature IR image without emissivity correction before heat measurement, the default emissivity for entire imaging area is 0.34.

Input Voltage (V)	Power (W)	Temperature (℃)	Stabilized Time (s)
1.7	**0.846**	**150**	**Less than 1**
2	**1.016**	**200**	**Less than 1**
2.5	**1.600**	**250**	**Less than 1**
3	**2.394**	**350**	**Less than 2**

Table 5.3 Thermal measurement with respect to different input voltage bias

5.2.7 Aerosol Generation

Aerosol generation measurements were run with the setup as shown in Fig. 5.12.

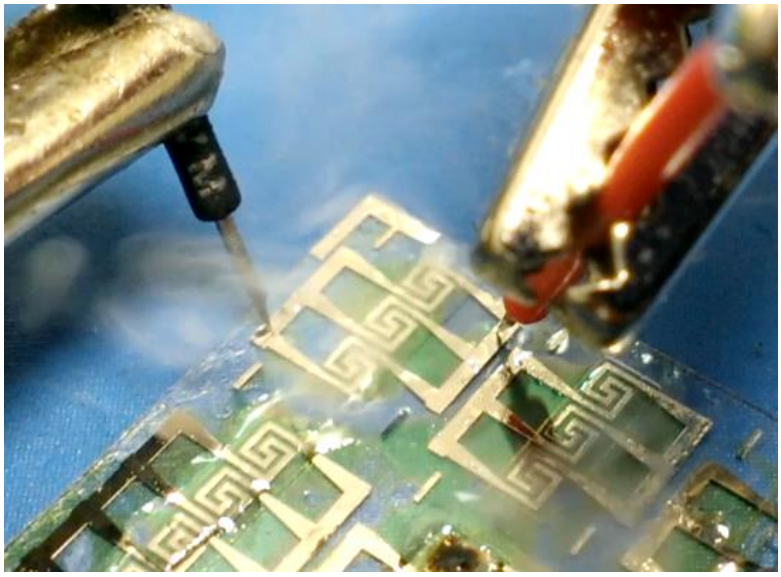

Fig. 5.12 Probe station setup for electrical and aerosol generation measurement.

In Fig.5.13, we demonstrate the correlation between the aerosol volume quantities versus the specific power needed by the MH to generate the respective density of aerosol. Given that in several tests we used MHs connected in parallel, the power usage had to be normalized; this is why the units are W per MH. As shown in the graph, a single MH can generate abundant amounts of aerosol at low power (0.8-1.0 W) with 1.7V voltage bias. For multiple MHs in parallel, the power requirement increased by ca. 50%. However, there was a gain in the kinetics of aerosol generation, as the aerosol was generated faster.

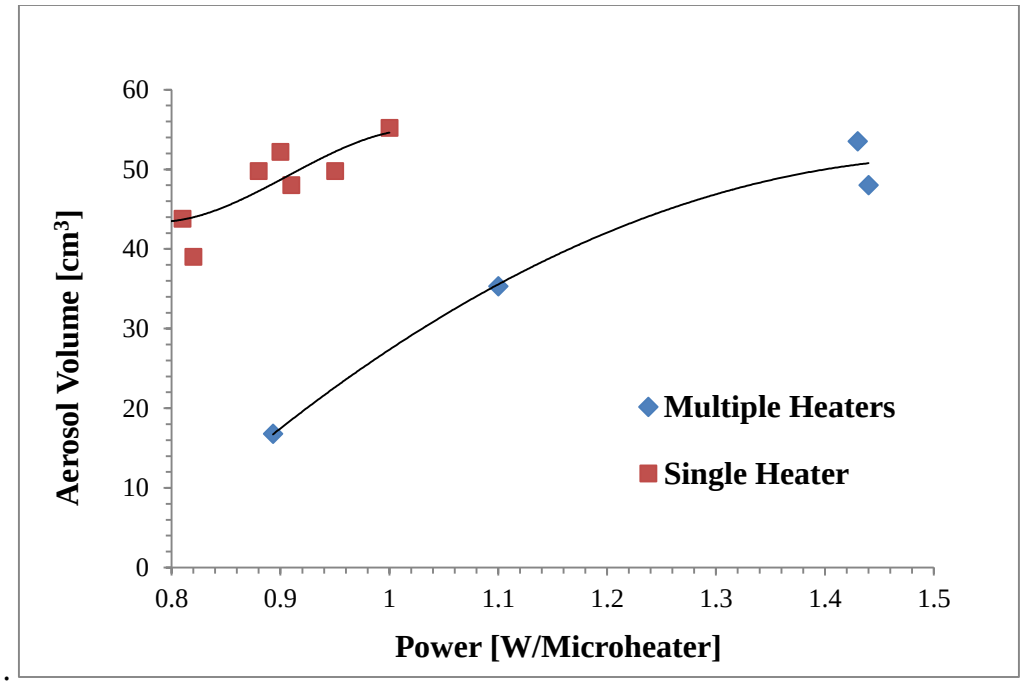

Fig. 5.13 Aerosol volume quantity relative to specific power required for its aerosol generation

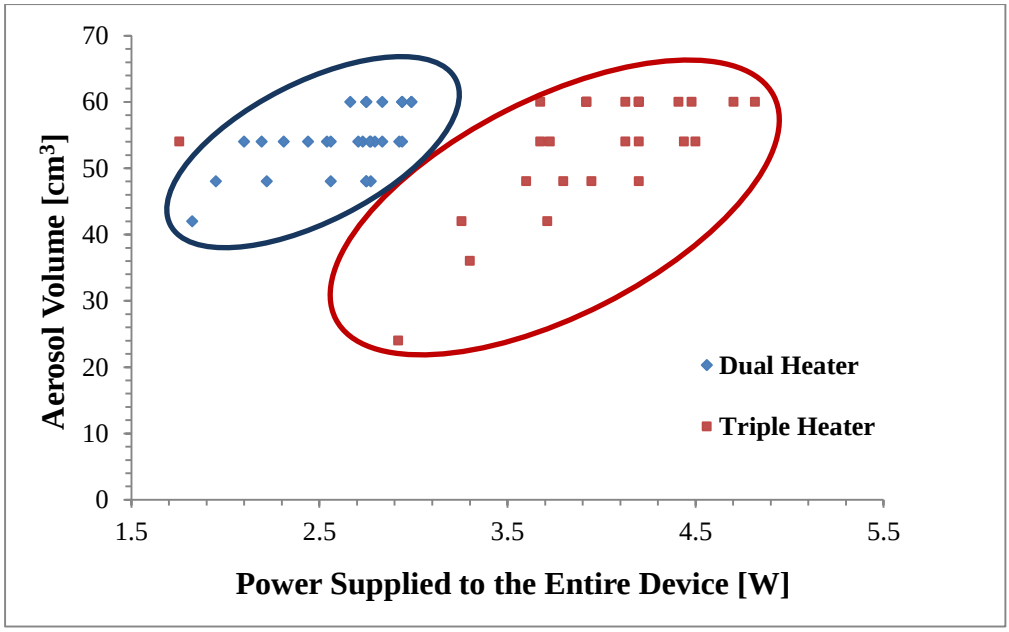

Fig. 5.14 Aerosol volume quantity relative to the total power needed by a device consisting of 2 MHs (blue data points) and 3 MHs (red data points), respectively.

In a series of tests, we have generated aerosol by means of the parallel designed dual and triple MHs. Results summarized in the graph displayed in Fig. 5.14 reveal a total power need of 2.05 ± 0.15 W for the dual MHs and of 2.35 ± 0.15 W for the triple MH systems, respectively.

In a series of 205 aerosol generating experiments, we obtained aerosol volumes in the range of 48.8 ±7.9 cm ³. A volume of 60 cm ³is the maximum volume that can be inhaled by a patient at one breath. In several cases we found that the total resistance of the MH would suddenly drop to 1~2 Ω and reduce the yield and repeatability. This phenomenon is a consequence of the Ni-plating not only growing nickel on top of the pattern, but also on the sidewalls. When this happens, the pattern wires start merging with each other. This can be avoided by tightly bonding the shadow mask and wafer when depositing seed layers, or by using photolithography and lift-off processes for defining the seed layer.

All the single, dual and triple MH systems generated consistently abundant amounts of dense aerosol. In a few instances, if one of MH of the dual systems burned out, the other one will continue operating with the remaining one. Similarly, the triple device was able to generate vapors with one remaining MH out of the initial three. In each scenario, the total quantity of aerosol was not affected, which enables the maintenance of smooth medical drug delivery, which remains constant over time. For our device, we set the voltage bias to 1.7 V to reach 150 ℃ for drug delivery purposes. Higher voltage bias (up to 3 V) and higher temperatures (up to 350 ℃) can be applied for other forms of aerosol.

5.2.8 Detailed Cost Analysis

To perform a unit item cost analysis we must break the process flow into unit operations. The most significant unit operations for the micro-heater process are broken out in the Table 6.3 below and unit operation costs are listed.

OPERATION	Cost of MH without Reservoir	Cost of MH with Reservoir
TOPSIDE BARRIER FILM DEPOSITION (PECVD)	$200.00	$200.00
SHADOW MASK PLATING SEED (E-BEAM)	$400.00	$400.00
ELECTROLESS UP-PLATE	$50.00	$50.00
TOPSIDE PROTECT (PHOTORESIST SPIN)	$50.00	$50.00
SHADOW MASK DEPOSITION FOR RESERVOIR	$0.00	$400.00
WET-ETCH RESERVOIR	$50.00	$50.00
STRIP TOPSIDE PROTECT	$50.00	$50.00
“SCRIBE AND DICE” INDIVIDUAL HEATERS	$200.00	$200.00
TOTAL	$1000.00	$1400.00

Table 5.4 MH Process Cost break down to each significant step

Material costs for the unit operation are included in the unit operation cost. We can easily process 10 “sheets” of material, 10cm x 10cm = 100cm2. Material costs are estimated to be $10/”sheet” of starting material 10 sheets of starting material will cost $100. Thus the processing/material cost per run would be $1500.00.

Next, we must assess the number of heaters that can be fabricated. We assume each heater image (taking “saw street’ space into account) will be 0.5cm x 0.5cm = 0.25cm2. Ten 100cm2 sheets contain 1000cm2, yielding 8333 devices. Thus, the current unit cost is 18¢.

It must be emphasized, that these are premium prices, paid to an external service "vendor." In this case, our vendor is the University of Maryland clean-room facility. Unit process costs role in university overheads that will not be incurred in an in-house operation. A fair fraction of the overhead is in clean-room maintenance. Our "in-house" operation will not require the stringent "class 10" clean-room specifications necessitating the use of HEPA filters, laminar air flow and other expensive measures.

The most expensive operation (and the operation that limits the number of simultaneously processed substrates) is the shadow mask evaporation process. We will certainly be able to increase the number of simultaneously processed substrates with specially designed equipment. This alone could increase process throughput by an order of magnitude. We feel confident that in-house process costs will be less than 2¢ per part.

5.2.9 Section Conclusion

We were able to fabricate different types of low cost, fast responding micro-heaters for various applications. Nickel plating and wet etching baths were used to reduce costs and increase the speed of the process. The devices exhibited the desired heating characteristics. Both double spiral shaped and meander shaped heaters were investigated. While both geometries operated well, no significant differences in heat or aerosol generation were noted from one micro-heater design to another. On the basis of our experimental results, this device shows promise as an aerosol generator for drug delivery. Owing to their low cost (<18¢ per part), such micro-heaters can be used as disposable aerosol dispensers, although multiple other uses are also enabled.

5.3 Chapter Conclusion

In this study, methods and techniques to fabricate embedded MHs and low-cost MHs and its applications were explored. The substrate, active element and passivation layer materials were carefully designed. The heating performance was characterized with IR camera. The MH for NW sensors can achieve 60 ℃ under 5V bias. And the MH for aerosol generation can easily reach temperature up to 350 ℃. Reliably and reproducibly fabrication of low-cost MH on solution-processes for nickel plating was optimized. On the basis of our experimental results, this low-cost fabrication method shows promise, potentially enabling mass production of disposable heating devices. The process overcomes the barrier of metal plating thickness limitation generally in chip scale devices. The embedded MH design has the capability of integration with CMOS, MEMS and other novel devices standardized process. Many sensors (chemical, gas and biology) using the MH can be benefit from the low-cost, compatibility and robust performance. This study was published at the journal of Microelectronic Engineering [178].

Chapter 6: Process Integration for Gas Sensors

This chapter gives the process integration details of the nanowire-nanocluster (NWNC) gas sensors. The former chapters have covered component design, process optimization and fabrication of nanowire, nanoclusters and micro-heaters. Process integration of all three micro- and nano-structures into a single NWNC hybrid sensor device will be revealed in this chapter. A gas sensor unit will be assembled by decorating the NW surfaces with NCs, and a MH will be put aside each NWNC sensor unit. Integration considerations included the process flows, RTA, multiple passivation layers, NW yield improvement, active opening windows, passivated control elements, ohmic contact improvement and the methods to integrate multiple sensors into a single sensor chip. The single type of NWNC gas sensor is a basic platform. The whole fabrication process of the platform contains more than 40 planer-process steps and 6 lithography masks. Methods to integrate multiple gas sensors into a single chip were explored and covered in this chapter to realize simultaneously multiple gas sensing capabilities. To approach this goal, NWs are designed and dry etched into arrays, and methods of depositing different NCs on to each assigned NW are designed. Every new type of sensor adding onto the original wafer needs the corresponding NCs deposited onto an assigned NW that hasn't been occupied and each takes extra 10 planer-process steps and 2 lithography masks. The whole process integration design was aiming to establish a platform. The platform technology has great advantage in product flexibility and has the capability of customized design. It enables all kinds of combinations of gas sensing capabilities and the possibility of fitting all possible real-time sensing scenarios and conditions.

6.1 Process Flow Design and Considerations

6.1.1 Integration of GaN NW

The GaN NW needs to exhibit high carrier mobility to maintain a high signal to noise ratio when sensing at sub-micro amp range. The as deposited material by PVD techniques will end up with huge amount of defects that significantly degrade the carrier mobility and limit NW sensitivity. Due to the strict requirement of high quality GaN, a MOCVD of GaN thin-film on the wafer is necessary. NW fabrication needs a subtractive process such as dry etching of a thin-film of GaN. This dictates that the first step of the whole process should be the NW formation. The GaN on sapphire generally needs a buffer layer of AlGaN to minimize crystal defects. An AlGaN buffer layer with thickness 600 nm will be sufficient enough to reduce the epitaxy of defects penetrating into the upper layers. The AlGaN was carbon doped to make the substrate non-conductive. During the AlGaN deposition, the CVD chamber will have a carbon tail in layer profile after turn off the MFC for carbon precursors. Therefore an extra intrinsic AlGaN (i-AlGaN) of 400 nm was deposited over the carbon doped AlGaN (c-AlGaN). Finally, a layer of high quality GaN with Si doping (1E17/cm^3) was grown on top. Si doped GaN is an n-type semiconductor material. Due to the resolution of the stepper lithography tool used is 300 nm, the thickness of the GaN film was designed to 300 nm, so that after the dry etching, the GaN NW has the cross section of a square size of 300 nm. The wafer layer profile before dry etching is shown in Fig. 6.1a. The NW after the dry etching cross-section profile is shown in Fig. 6.1b. The dry etching of NW arrays etched the wafer down to c-AlGaN layer instead of stopping at i-AlGaN layer. This design is to ensure the substrate of the final device will have no leakage current. On the other hand, the high aspect ratio of the fabricated NWs

will increase the failure rate of contact metallization on the 3D structures as shown in Fig. 6.2 and Fig. 6.3. Unless a thick metal contact deposited (1 μm), the high aspect ratio of NW is hard to form reliable contact. The metal lift-off process can only allow metal thickness below 280 nm to be processes. It is unreasonable to run 3-4 time lithography and metallization with a same mask. A SiO_2 buffer step layer of 300 nm is used to avoid thick metal depositions and this layer will be discussed in detail later in MH integration designs because it also served as the passivation layer for MHs, which is more important.

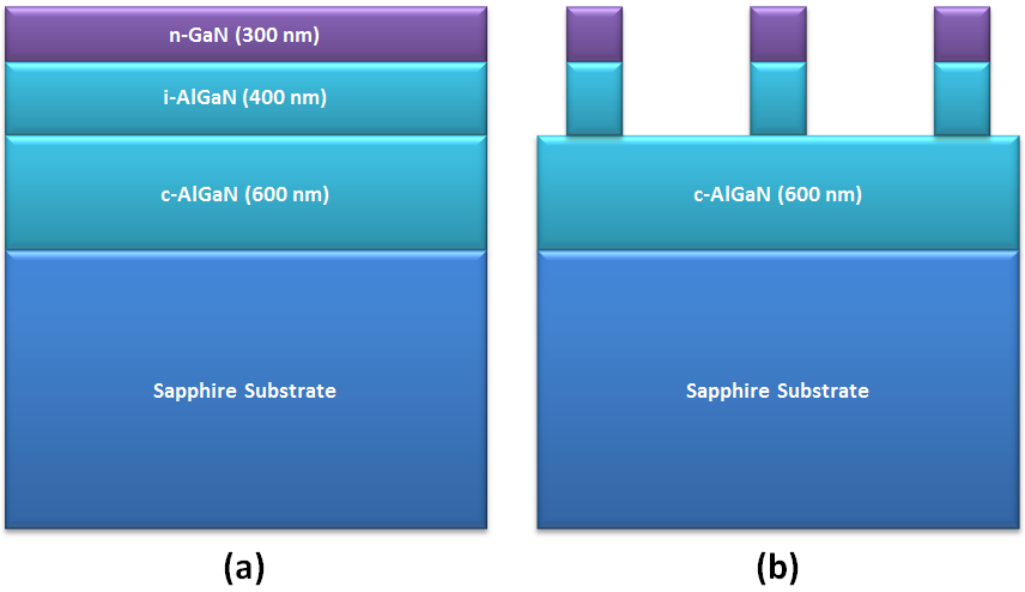

Fig. 6.1 (a) Wafer profile of GaN, AlGaN buffer layers on sapphire substrate (b) Wafer profile after dry etching of the NW arrays

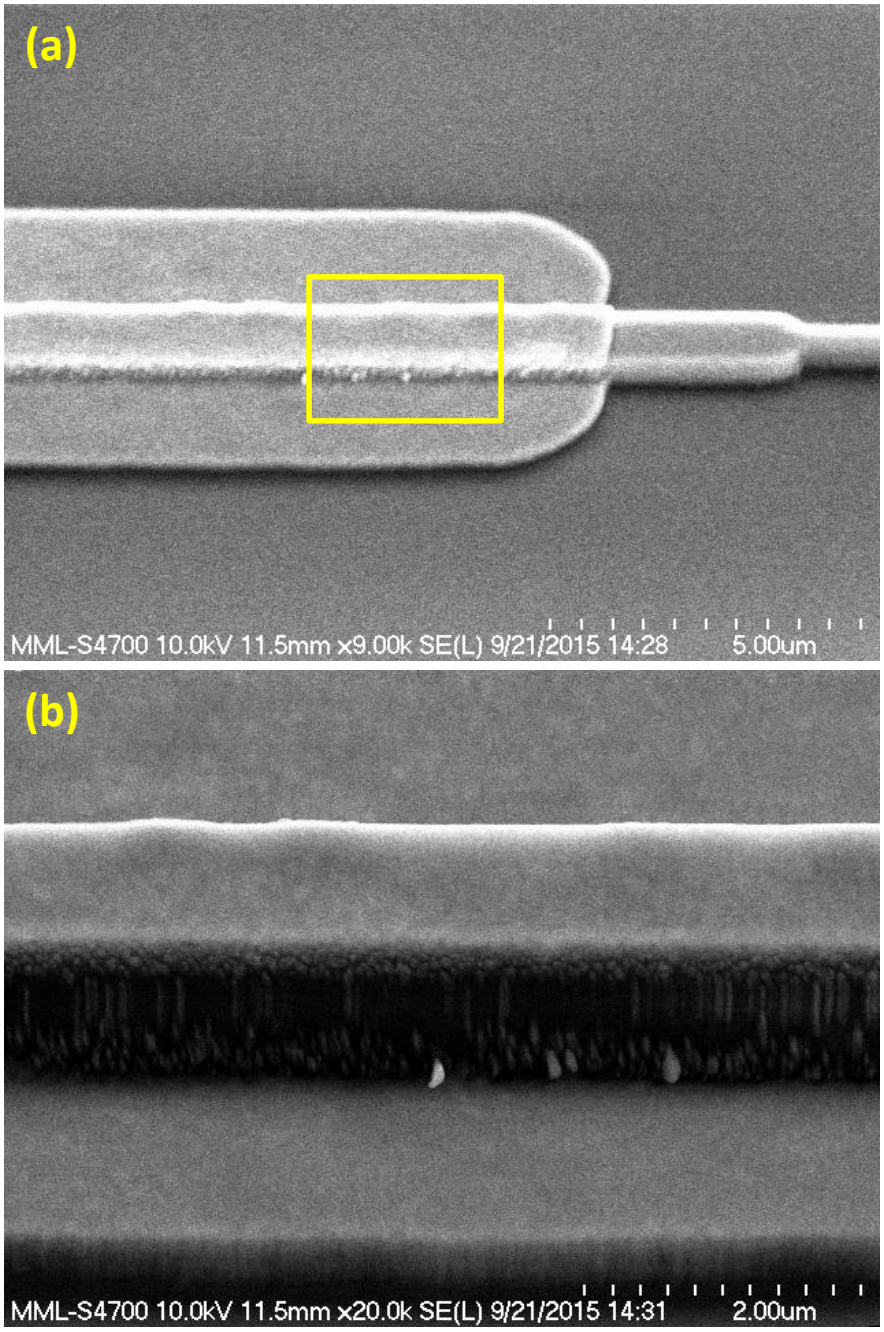

Fig. 6.2 SEM image of metal contact failure due to high aspect ratio of NW (a) NW terminal contact (b) high magnification image of highlighted area

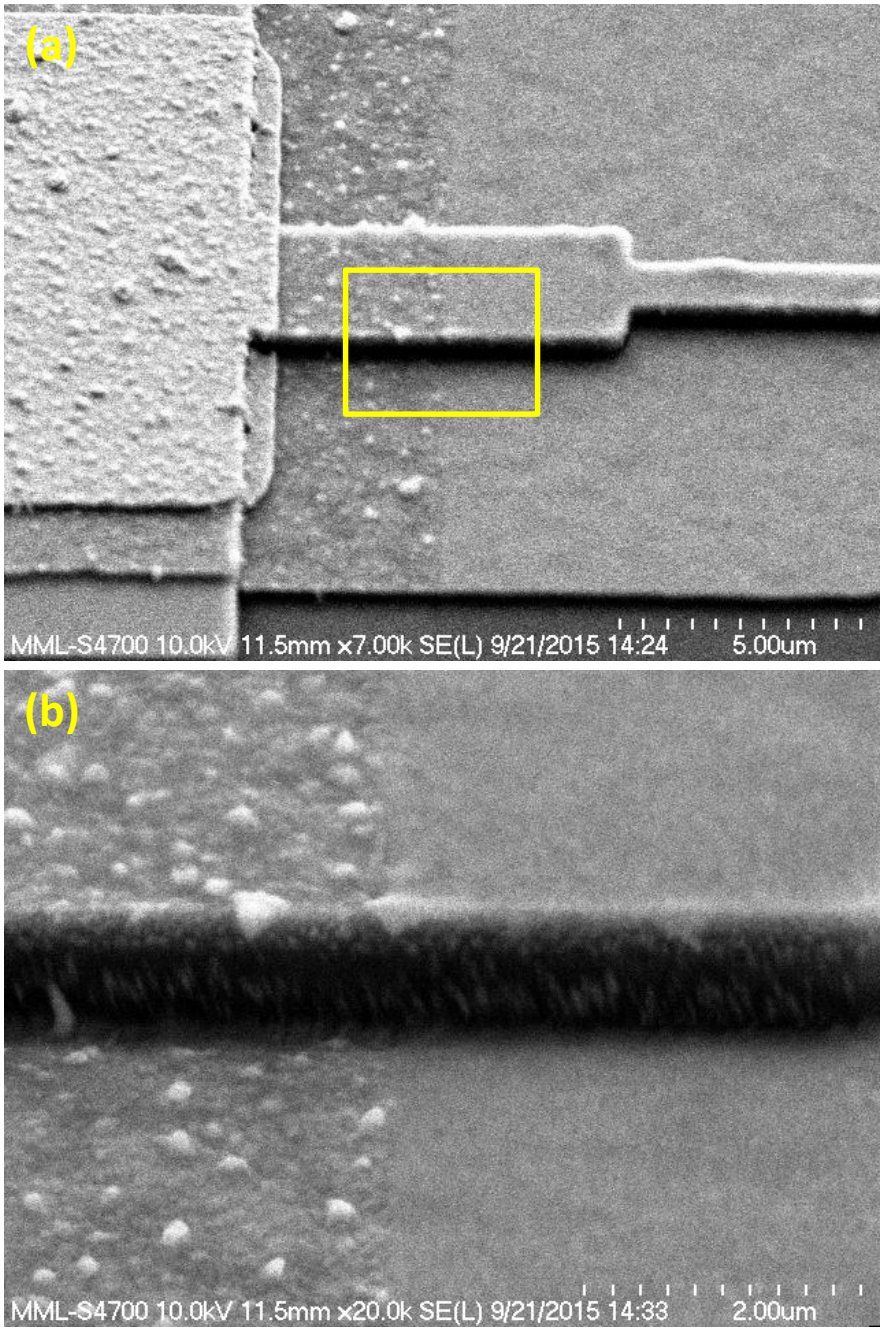

Fig. 6.3 SEM image of metal contact failure due to high aspect ratio of NW (a) NW terminal contact (b) high magnification image of highlighted area

6.1.2 Integration of Metal-Oxide NCs

Metal-oxide and metal NCs are the major sensing functional materials that once formed should avoid any further exposure to high temperature, moisture, photon dose, acid or basic chemicals that could trigger the phase changing from the chemical reactive to inert phases. Therefore, NCs were considered to be deposited at the end, right before bond pads metallization and packaging.

The NCs deposition using sputtering is a planer process that deposit NCs uniformly over the wafer. The active NCs for target gas molecules at the surface of NW are more favorable. Because only the gas molecules bonded with NCs on the NW surface will modulate the NW resistivity. However, the actual amount of NCs on NW is a very small percentage among all the NCs on wafer. NCs have huge surface to volume ratio, this will ends up lots of target gases bonding on sites that cannot be sensed by NW. And the massive amount of target gas got adsorbed on un-sensible NCs will hinge the detection limit to an even lower concentration. What worse is the large amount of adsorbed gas molecules on un-favorable bonding sites will increase the recovery time in desorption cycle. The ideal case is NCs only got deposited on NW surface. Therefore, the design of SiO_2 passivation layer is confirmed to be repositioned and patterned a trench open as an active window on top of each NW before NCs deposition. In that case, NCs will be deposited onto each NW inside the window and SiO_2 surface outside the window. The un-favorable NCs outside the window can be removed by SiO_2 etching process or deposit an extra thin SiO_2 passivation layer that bury all the un-favorable NCs to prevent them from exposure to environment. For basic platform, single type of gas sensing device, SiO_2 etching is used, it saves process steps comparing to additional passivation layers as shown in Fig. 6.4. For

multiple type of gas sensors integrated together, additional passivation layer will be used. Fig. 6.4 and Fig. 6.5 show the difference of subtractive and additive processes for active window openings. The detail process flow will be revealed in next sections.

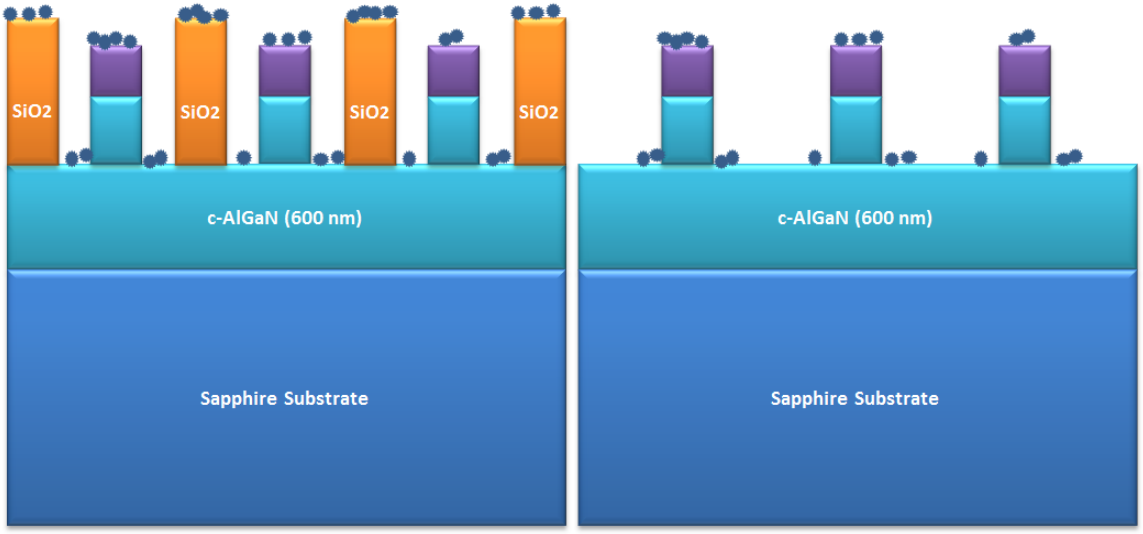

Fig. 6.4 Active window opening process for single type gas sensor

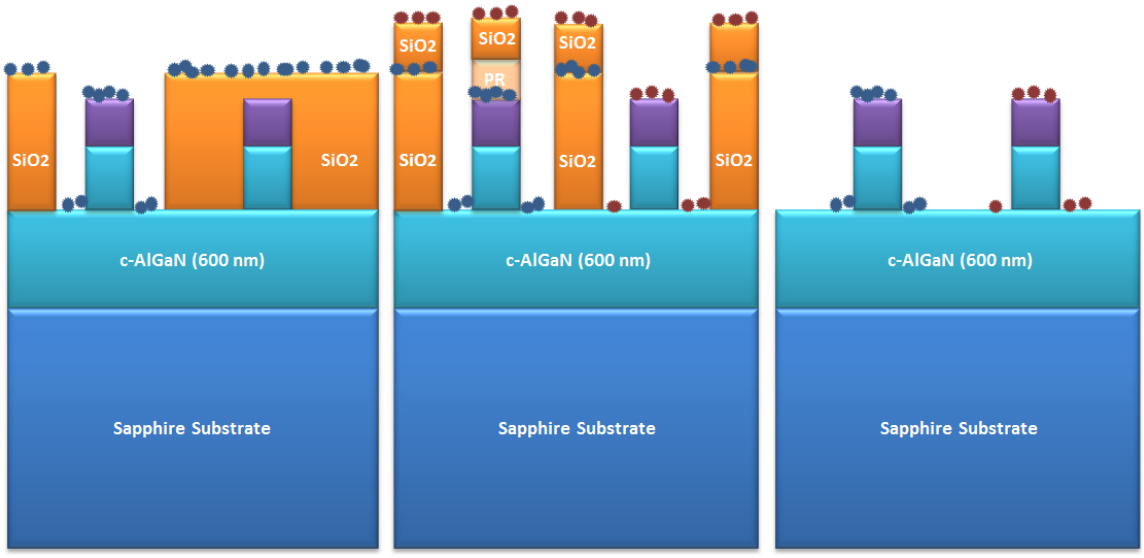

Fig. 6.5 Active window opening process for multiple types of gas sensor on single chip

6.1.3 Integration of MHs

The MH process is robust and the most flexible, which can be fitted into any stage of process, in this case it will be assigned right after the NW forms and before NCs deposited. Considering the heated metal wire can cause chemical sensing and reaction on the surface, a thick passivation layer of SiO_2 was implemented to isolate the MH metals and the target gases. The choosing of SiO_2 is due to its extremely low thermal conductivity as mentioned in Chapter 5. Major heat conduction will go through the substrate instead of convection loss on the surface. Moreover, this SiO_2 layer has multiple usages. It is important for active NW window opening in NC integration step as discusses in the former section. More importantly, this passivation layer can improve yield and eliminate final bonding pad metallization failure due to the non-conformity of metal PVD techniques. The SiO_2 layer with thickness of 300 nm will buffer the large aspect ratio as an additional step. Therefore the metal lines will go over two steps (300 nm and then 400 nm) instead of a big step of 700 nm. This is important for lift-off metal process because the lift-off thickness cannot larger than 400 nm. At least twice metal deposition and lift-off will be needed if there were no SiO_2 passivation layers.

6.2 Basic Platform: Single Type of Gas Sensor Process Flow

6.2.1 GaN NW Formation

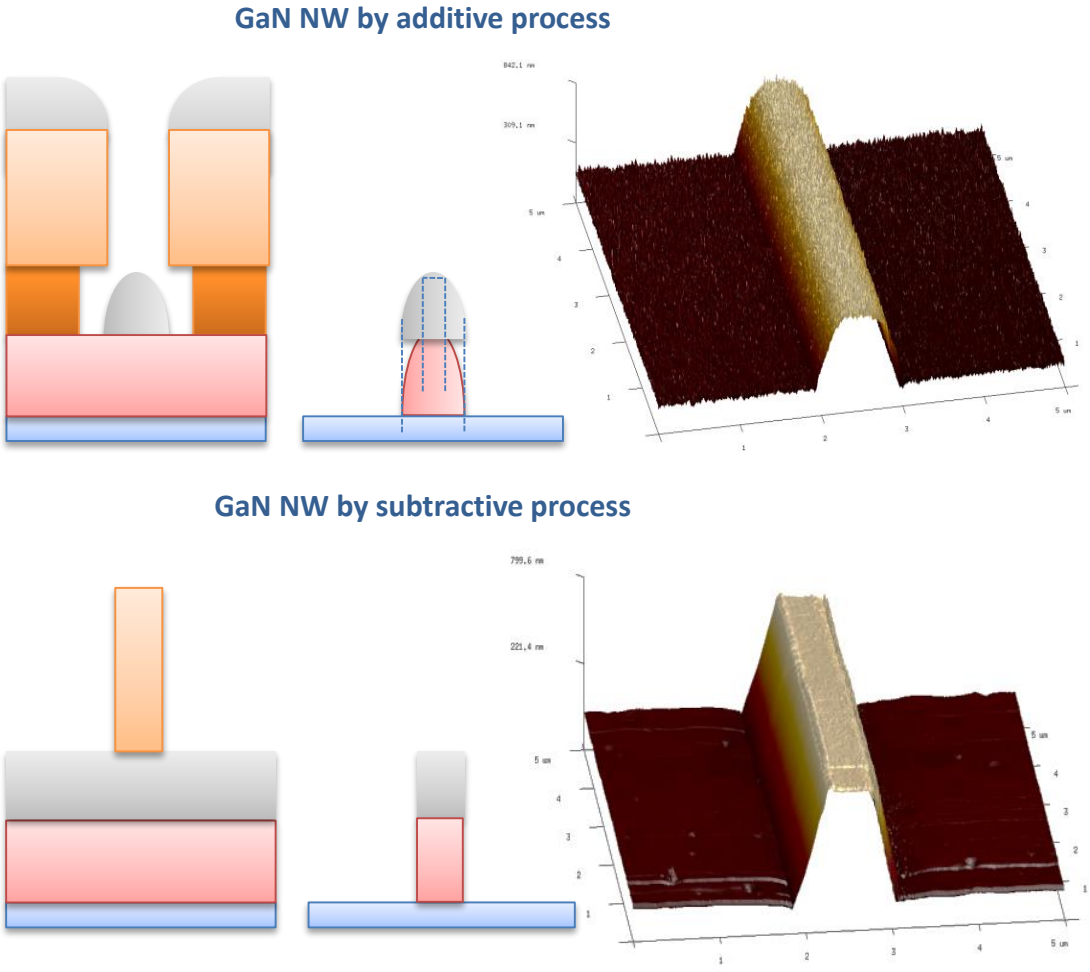

Fig. 6.6 Comparison of lift-off (additive) and etch-back (subtractive) processes of NW formation in theory and results from AFM imaging

A two inch wafer of GaN and AlGaN buffer layer on sapphire substrate was dry etched and wet polished to form single NW arrays, the detailed fabrication process is covered in Chapter 3. Learning the high aspect ratio of the NW will generate contact metal gaps and non-linear contact as shown in Fig. 6.2 and Fig. 6.3, the NW dry etch stops at the

AlGaN layer instead of etching all the way down to the sapphire substrate. Subtracting process instead of lift-off process for metal shadow mask was used for the better NW shape control and yield enhancement. The comparison of lift-off process NW and subtractive process was show in Fig. 6.6. Fig. 6.7 shows the wafer after all the NW process covered in Chapter3. The GaN etching pattern includes GaN NW, big contact pad of GaN and tapered buffer bridges. The large area contact pad in planer will improve the contact quality and yield.

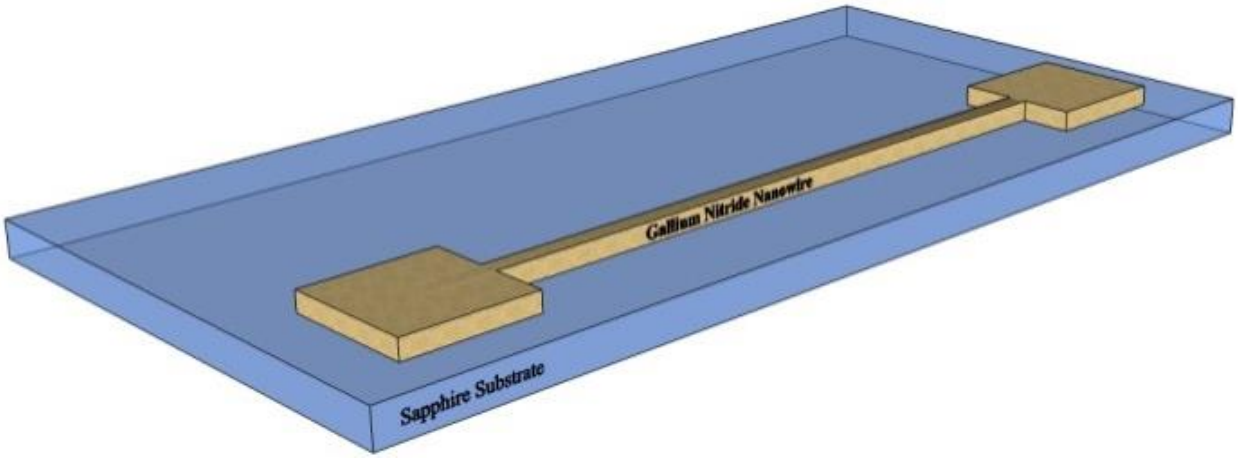

Fig. 6.7 Gas sensor process diagram after GaN NW formation

6.2.2 MH Implementation

After NW formation, A MH was patterned aside the NW by photolithography (Suss Microtec MA6 Front and Back Contact Aligner) and metal deposition of Ti/Ni (10 nm / 210 nm). The detail fabrication process was covered in Chapter 5. The distance between NW and MH is 20 μm. The MH and NW are shown in Fig. 6.8. The dimension of MH keeps the same with NW (10, 50, 100 and 200 μm). An extra MH in the center of the die not associate to any NW is designed and patterned as well. This MH can be used to heat up the whole sensor die or functioning as a thermal couple for future temperature monitoring purpose.

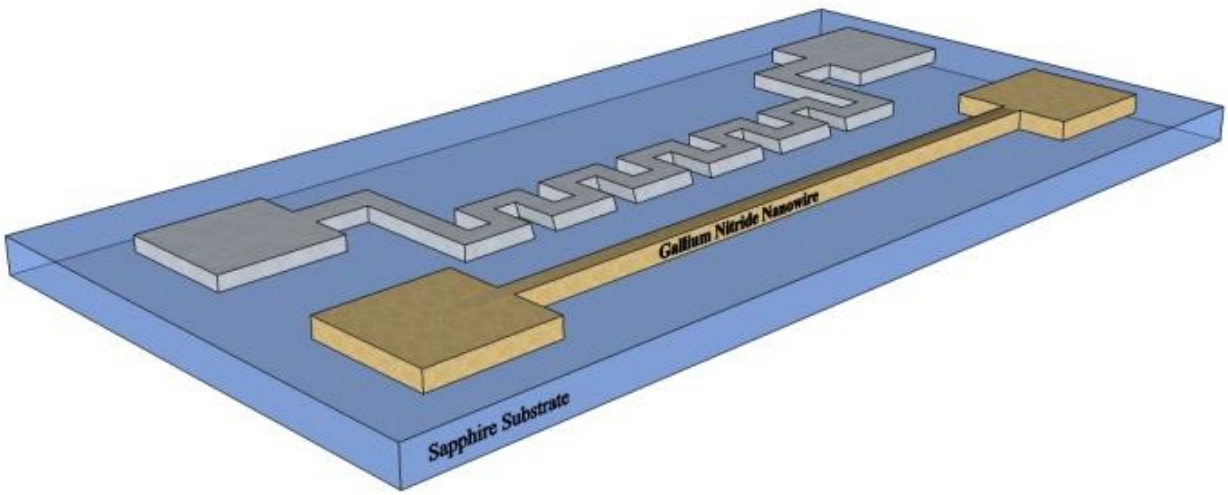

Fig. 6.8 Gas sensor process diagram after GaN NW and Ti/Ni MH assembled in parallel

6.2.3 Ohmic Contact Formation

MA6 Front and Back Contact Aligner (Suss Microtec) is used for ohmic contact patterning. Fabrication details were mentioned in Chapter 3. A bi-layer stack of photoresists (MicroChem LOR3A and Microposit S1813) were used to support a lift-off process for the ohmic contact metal. After UV exposure with 90 mJ/cm ²dose energy, post-bake and develop in Microposit MIF-319 for 60 seconds, reactive-ion etching (RIE, Unaxis 790) was used for a descum process with 30sccm flow rate of oxygen for 30 seconds to clean up the remaining un-thoroughly developed resist residue. Fig. 6.9 shows the gas sensor after a Ti/Al/Ti/Au metal stack was deposited in the Denton Infinity 22 E-beam Evaporator for ohmic contact.

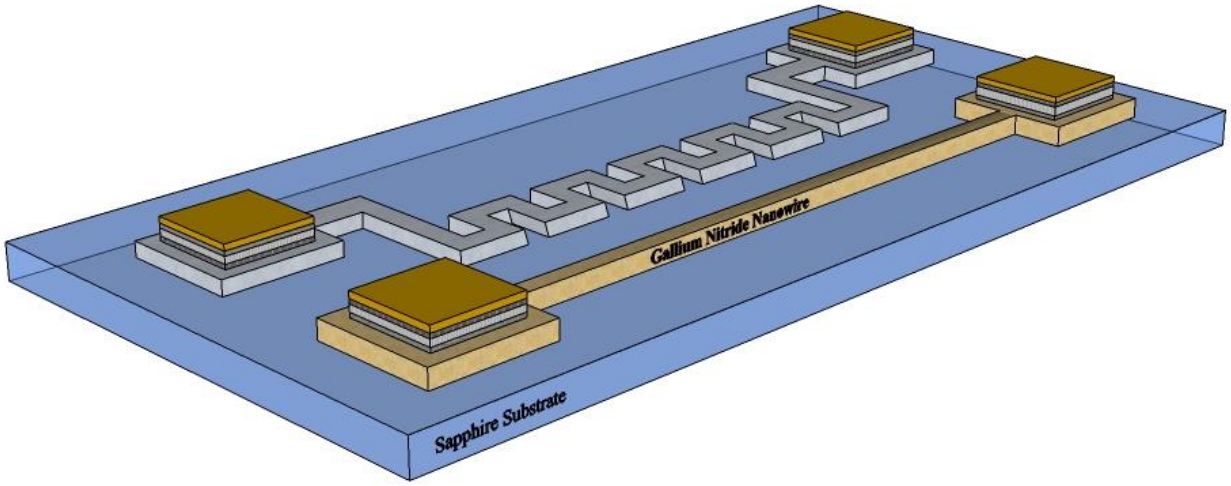

Fig. 6.9 Gas sensor process diagram after ohmic contact metallization

6.2.4 Active Window Patterning on Passivation Layer

After the ohmic contact metallization process, a passivation layer of 300 nm SiO_2 was deposited uniformly on the wafer by plasma enhanced chemical vapor deposition (PECVD, Plasma-Therm Versaline). PECVD is a common technique used in insulating and passivation purpose quality layers for SiN_x, SiO_2, amorphous and polycrystalline silicon. PECVD is relatively cold process with normal deposition temperature of 80 ℃ to 300 ℃ and uses energetic electrons from the plasma to dissociate the precursor gases. In my process an even lower temperature of 180 ℃ is used to deliver a fast deposition rate of 2nm/s and high quality of the film. Later process step will employ 80 ℃ to avoid high temperature induced process variation and phase changing of NCs. Normally the leakage current in PECVD oxides is higher than other high temperature CVD processes. So the PECVD formed thin-films cannot be used as a functional oxide such as MOSFET gate oxide. However, this is not an issue in my design as the layer is merely a passivation for protection of the MH surface from environment. The layer of SiO_2 will eventually be removed or covered with other oxide films. In my optimization, 300 nm PECVD SiNx is good enough to have a good coverage of MH. The thickness of PECVD deposited oxide film was double proofed by Nanospec Reflectometer (Nanometrics) and ellipsometry studies. Fig. 6.10 shows the wafer covered by SiO_2 passivation layer.

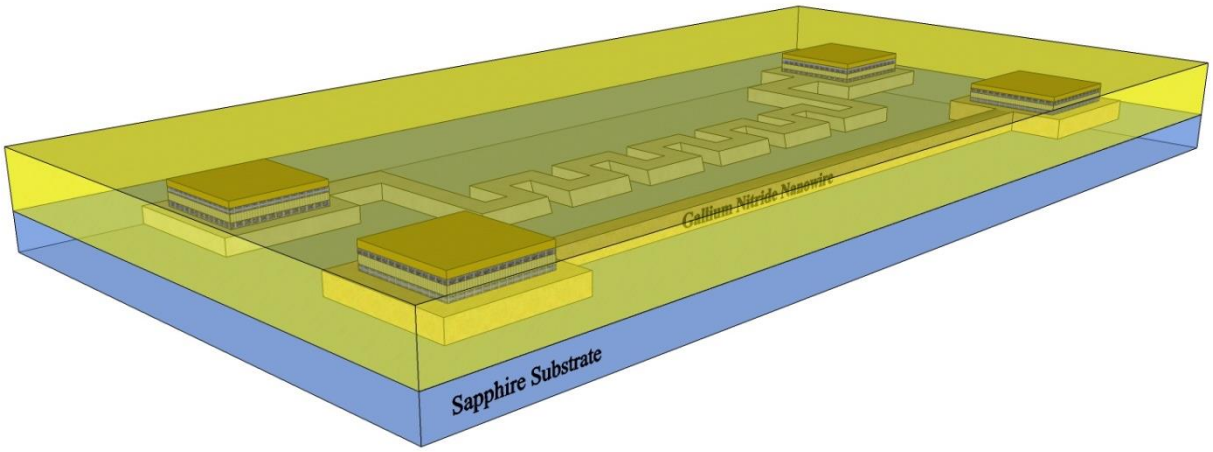

Fig. 6.10 Gas sensor process diagram after deposition of passivation layer of SiO_2

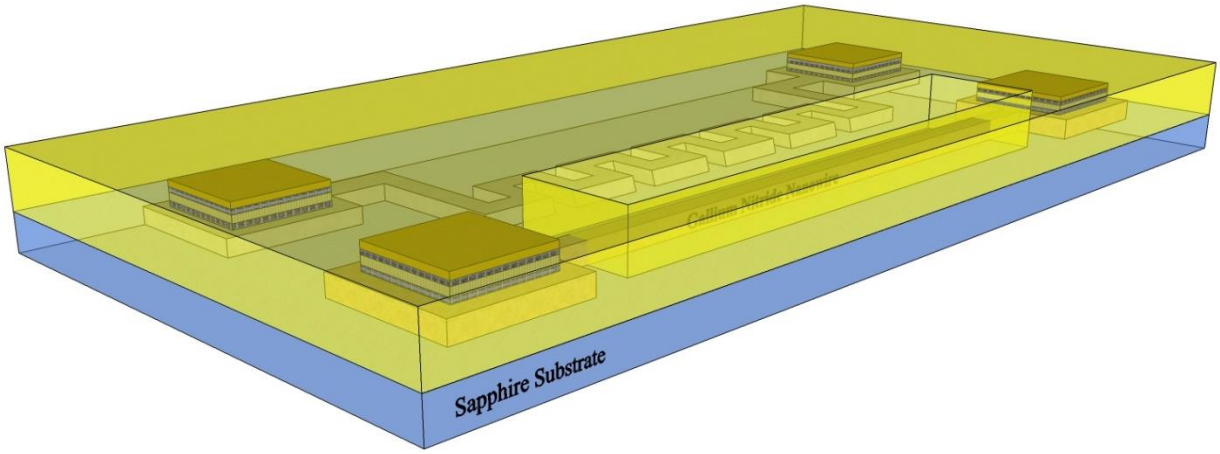

Fig. 6.11 Gas sensor process diagram after active NW open window patterning

Fig. 6.11 show the process diagram of gas sensor opened a window on top of NW and etched the SiO_2. MA6 Front and Back Contact Aligner (Suss Microtec) is used for NW open window patterning. Lithography and photoresist coating methods are the same with former mentioned MH and ohmic contact patterning. A bi-layer stack of photoresists (MicroChem LOR3A and Microposit S1813) were used, due to the adhesion issue of S1813 with SiO_2, either LOR3A or HMDS can be used for adhesion layer. The spin coating recipe

for LOR3A and HMDS is the same. After UV exposure with 90 mJ/cm ²dose energy, post-bake and develop in Microposit MIF-319 for 60 seconds, reactive-ion etching (RIE, Unaxis 790) was used for a descum process with 30sccm flow rate of oxygen for 30 seconds to clean up the remaining un-thoroughly developed resist residue. Dry etching with the same RIE or BOE wet etching is the last step to remove the SiO_2 in the window. For RIE dry etching, 10 min is sufficient enough to remove 300 nm SiO_2. For BOE (1:6) wet etchings, ideally 90 sec of BOE etch can remove 300 nm SiO_2. However, wet etching is hard to control and the HF have a higher chance cracking the photoresist when etch for a longer time. HF vaper etching is more controllable and repeatable comparing to BOE solution.

6.2.5 NCs Deposition and RTA

Metal oxide NCs were deposited by RF magnetron sputtering (Denton Vacuum Discovery 550) as shown in Fig. 6.12. Metal-oxide NCs phases were controlled by many parameters like substrate temperatures, chamber pressure, rf power and gas Ar/O_2 flow rate. The detail metal oxide NCs deposition methods and recipes for metal NCs as well were revealed in Chapter 4.

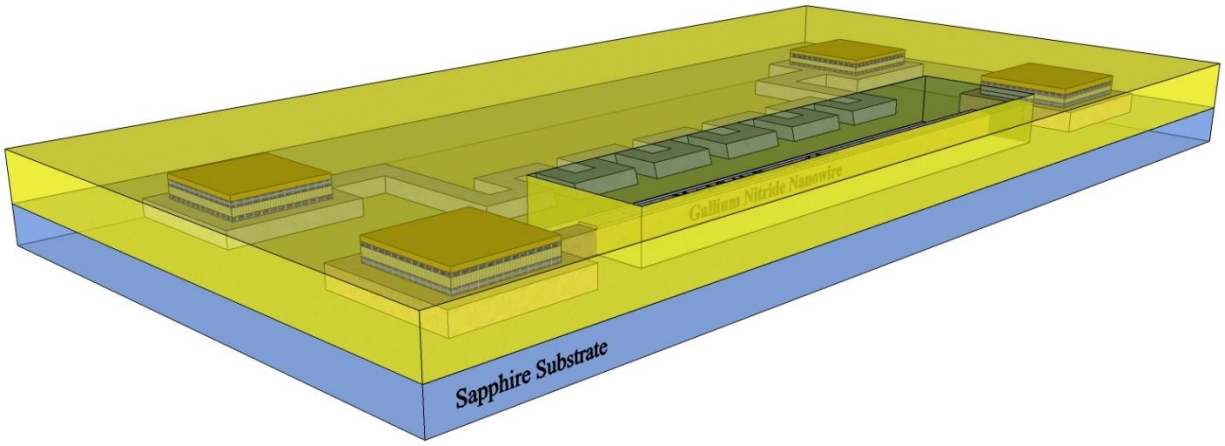

Fig. 6.12 Gas sensor process diagram after NCs sputter deposition

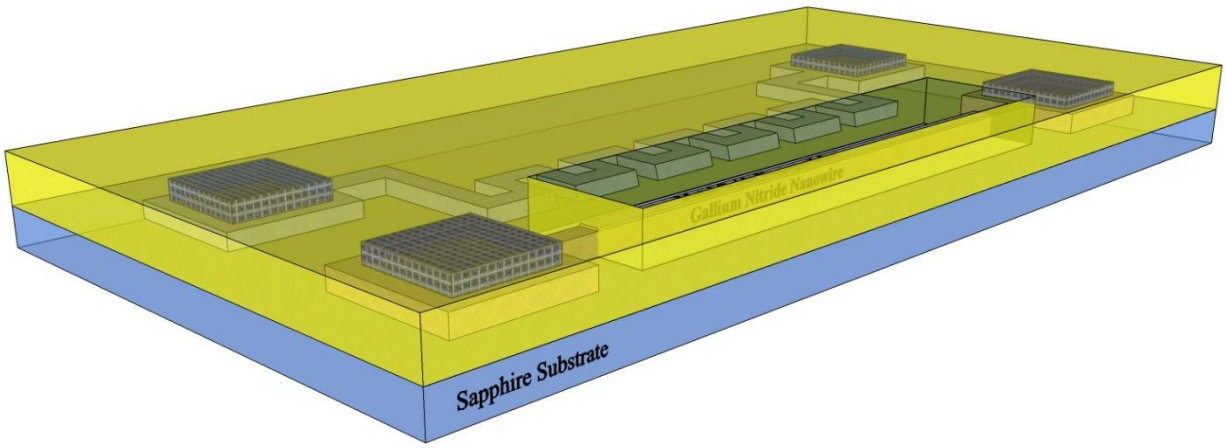

Fig. 6.13 Gas sensor process diagram after RTA

Rapid Thermal Annealing (RTA) is employed for MH, ohmic contact and NCs. High performance ohmic contact is essential to operation of sensor devices. Besides forming ohmic contacts, the RTA will help bonding of the metal-oxide sputtered on the surface of the GaN. It also passivates the surface states composed of dangling bonds. In RTA, the wafer is placed inside a thin quartz chamber with halogen lamps surrounding it. The temperature rise is fast (as high as 25 ℃ per seconds). The rapid rise of temperature generates stress in the nanowire device leading to a structural breakdown and re-bonds. The wafer ambient is 6000 sccm of ultra-pure Ar. The RTA is performed at 700 ℃ for 30 seconds. The temperature ramp rate is set to 100 ℃ per minute. Slow rise rate is set to make sure the GaN, metal stack and metal-oxide NCs are given enough time to reach equilibrium while keeping a low stress level. This RTA process generates a well-functioning, low resistance ohmic contact and recrystallizes the metal-oxide NCs. Both ohmic contact and NCs are supposed to anneal only once. That is why there is not RTA process right after ohmic contact metallization. Twice annealing will largely affect the contact performance. The ohmic contact annealing under the SiO_2 passivation layer can protect contact alloy from any contaminations from annealing chamber and NCs. Moreover, the annealing process will improve the MH's reliability and reproducibility. Fig. 6.13 shows the diagram of process after annealing, four metals forms ohmic contact alloy.

Some of the NWNC sensor needs both metal-oxide and metal NCs, like TiO2-Pt. The metal NCs is not necessary to be annealed. For the sensors need extra sputter deposition of metal NCs, the process of sputtering is assigned right after the RTA.

6.2.6 Passivation Etching and Vias Formation

The NCs sputter disposition is a planer process that uniformly coating the whole wafer surface with NCs, both on top of the NW and on passivation SiO_2 surface. The NCs on passivation layer is un-favorable because they will absorb target gases as well in real sensing. The existence of un-favorable NCs will affect the detect concentration and recovery time. An extra layer of photoresist was spin-coated and lithography patterned that protect the NW, MH and contact areas are developed. All the other unprotected areas will be etched later in the SiO_2 etching process, the un-favorable NCs will be removed together with etched SiO_2. To maintain low cost and minimized the number of process steps, the device terminal contact vias were patterned at the same time and a trench will be etched in that area in the SiO_2 etching process as well. Fig. 6.14 shows the photoresist after development and the pattern for vias and protection for MH, NW and contact areas. MA6 Front and Back Contact Aligner (Suss Microtec) was used for lithography patterning. Lithography and photoresist coating methods are the same with former mentioned MH, ohmic contact and active window patterning. A bi-layer stack of photoresists (MicroChem LOR3A and Microposit S1813) were used, due to the adhesion issue of S1813 with SiO_2, either LOR3A or HMDS can be used for adhesion layer. The spin coating recipe for LOR3A and HMDS is the same. After UV exposure with 90 mJ/cm^2 dose energy, post-bake and develop in Microposit MIF-319 for 60 seconds, reactive-ion etching (RIE, Unaxis 790) was used for a descum process with 30sccm flow rate of oxygen for 30 seconds to clean up the remaining developed resist residue.

SiO_2 Dry etching with the same RIE chamber or BOE wet etching is the last step to remove the SiO_2 in vias. The detail process recipes were revealed in section 6.2.4 when

discussing the active window etching. Fig. 6.15 show the process diagram of gas sensor opened vias on top of contacts and etched the SiO_2.

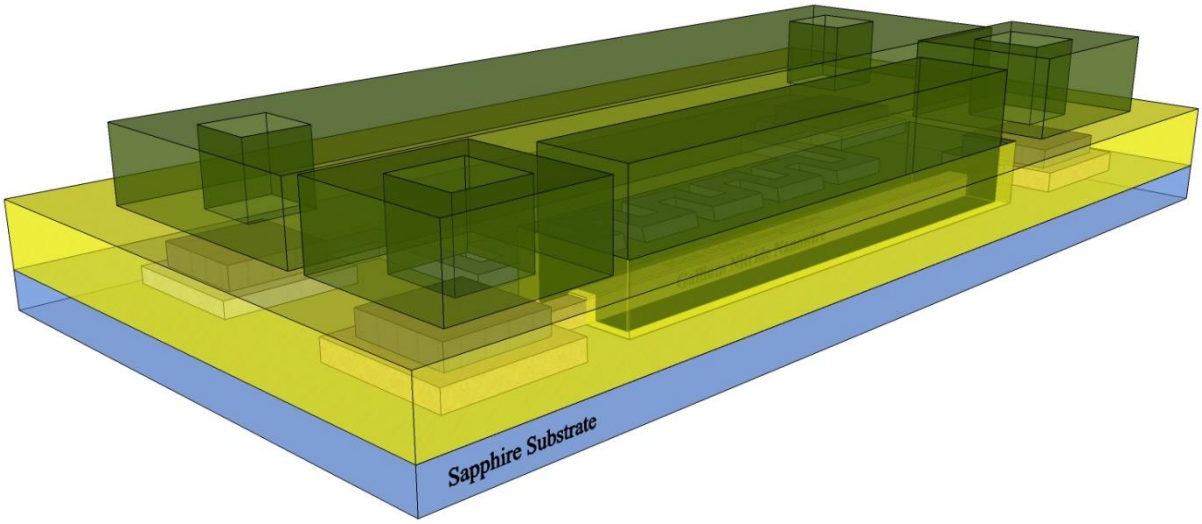

Fig. 6.14 Sensor process diagram after photolithography patterning

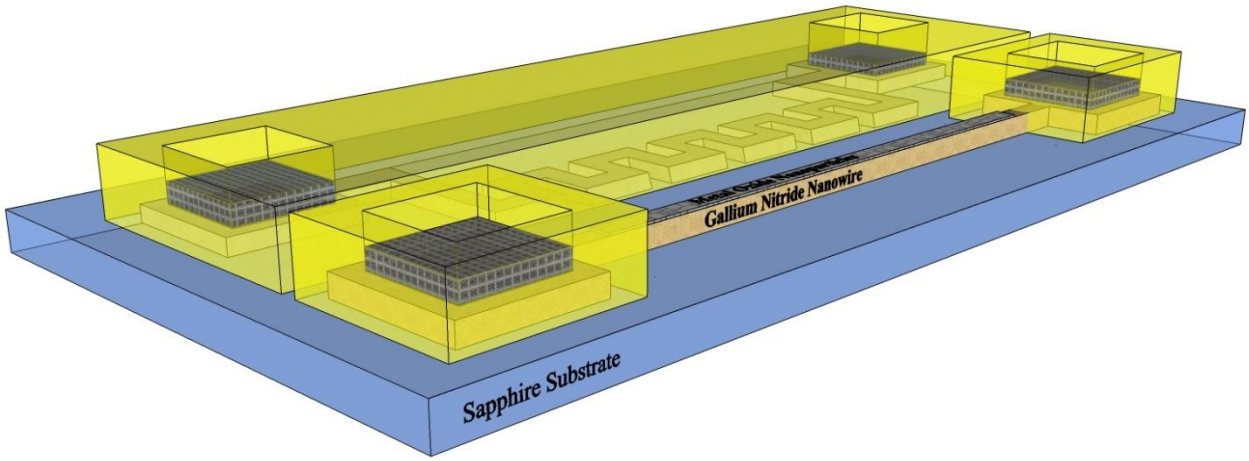

Fig. 6.15 Sensor process diagram after SiO_2 etching and vias formation

6.2.7 Bond Pad Patterning and Metallization

The on chip ohmic contacts are too small (20 μm x 20 μm) for wire bonding and after annealing the alloy of Ti/Al/Au is not suitable for forming a reliable bonding connection. An ideal bonding pad for wedge bonding should have soft and thick gold, aluminum or platinum layer at lease 100 nm. A bi-layer stack of photoresists (MicroChem LOR3A and Microposit S1813) were used to support a lift-off process for the bond pad contact metallization. Contact Aligner (Suss Microtec MA6) was used for bond pad contact patterning. After UV exposure with 90 mJ/cm ^{2}dose energy, post-baked and developed in Microposit MIF-319 for 60 seconds, reactive-ion etching (RIE, Unaxis 790) was used for a descum process with 30sccm flow rate of oxygen for 30 seconds to clean up the remaining un-thoroughly developed resist residue. Fig. 6.16 shows the gas sensor after the RIE descum processes and ready for bond pad contact metallization. Ti/Au (40 nm / 180 nm) bi-metal stack was deposited in the Denton Infinity 22 E-beam Evaporator with deposition rate of 1 Å/sec and lifted-off in PG remover or 1165. The deposition rate was monitored by a quartz crystal sensor. After acetone, methanol, isopropanol and de-ionized water cleaning, the final sensor chip before packaging is shown in Fig. 6.17. Reliable contacts were formed at the NW and MH terminals, and linked to 100 μm x 300 μm bonding pads at the edge of each die.

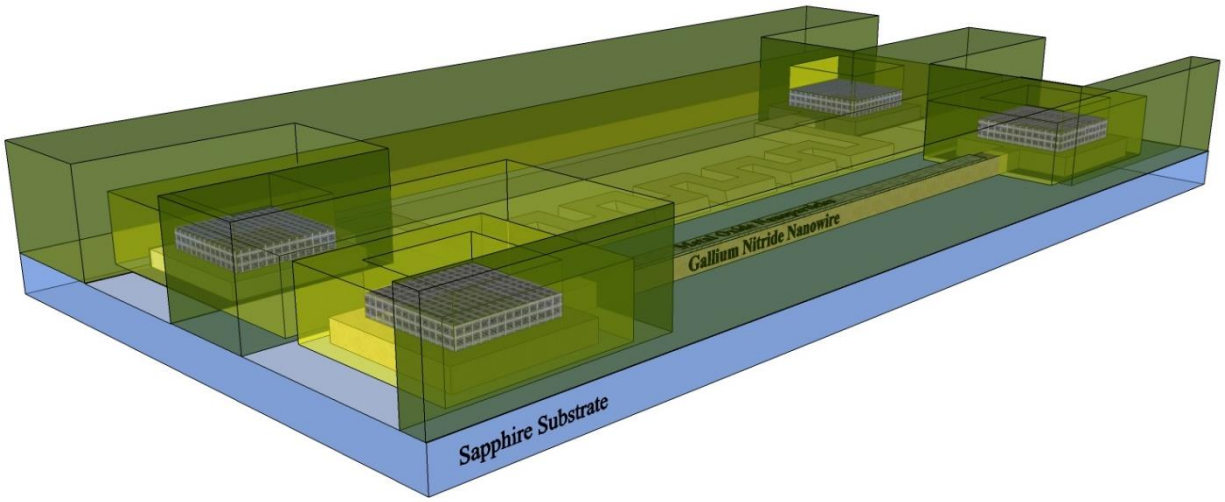

Fig. 6.16 Sensor process diagram after bond pad photolithography patterning

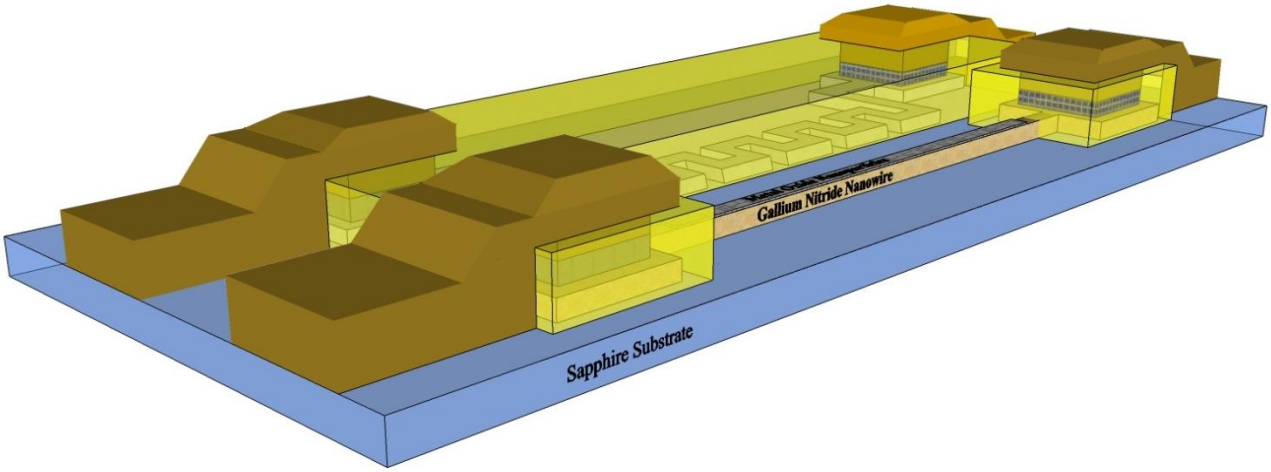

Fig. 6.17 Sensor process diagram after bond pad metallization

6.3 Simultaneous Sensing: Multiple Types of Gas Sensors on a Single Chip

Multiple types of sensors can be integrated onto a single die. From the basic platform mentioned in section 6.2, extra 10 planer process steps and 2 lithography masks will be needed for each additional type of NCs deposited on assigned NW. The additional process steps were added before RTA process, after the first NCs deposited in section 6.2.5.

6.3.1 Photoresist Protection Layer Patterning

Fig. 6.18 shows two of NWs and MHs arrays after the first NCs deposited, before the RTA process. Fig. 6.19 shows the photoresist after development and the pattern for protection of the former deposited NCs active window. MA6 Front and Back Contact Aligner (Suss Microtec) was used for lithography patterning. Lithography and photoresist coating methods are the same with former mentioned MH, ohmic contact and active window patterning. A bi-layer stack of photoresists (MicroChem LOR3A and Microposit S1813) were used. Due to the adhesion issue of S1813 with SiO_2, either LOR3A or HMDS can be used for adhesion layer. The spin coating recipe for LOR3A and HMDS is the same. After UV exposure with 90 mJ/cm ^{2}dose energy, post-bake and develop in Microposit MIF-319 for 60 seconds, reactive-ion etching (RIE, Unaxis 790) was used for a descum process with 30sccm flow rate of oxygen for 30 seconds to clean up the remaining developed resist residue.

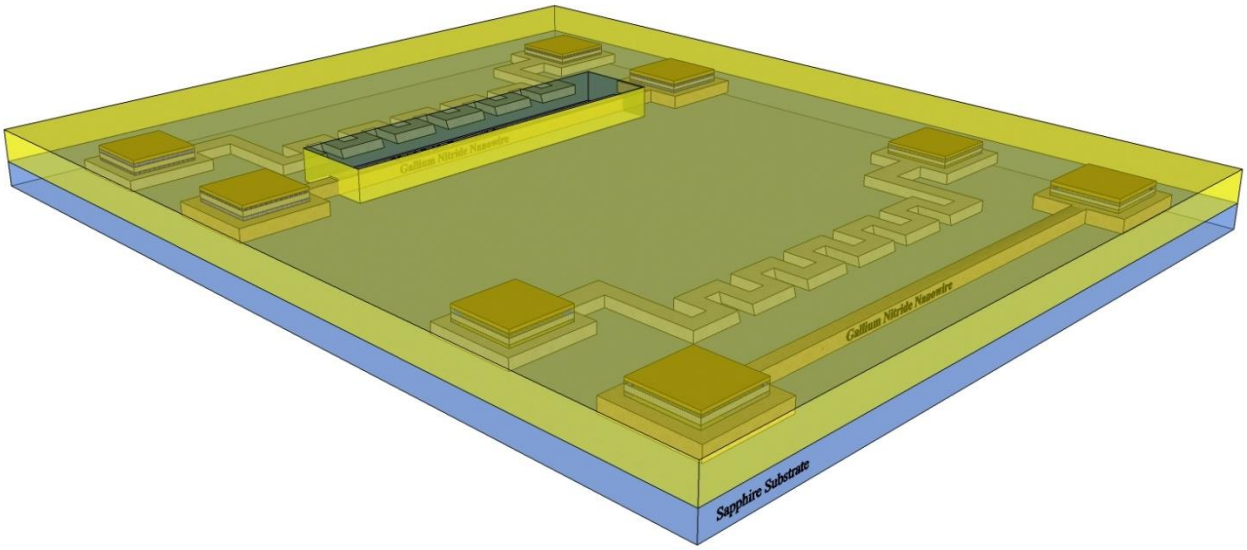

Fig. 6.18 Multiple sensors process diagram after the first NCs deposited

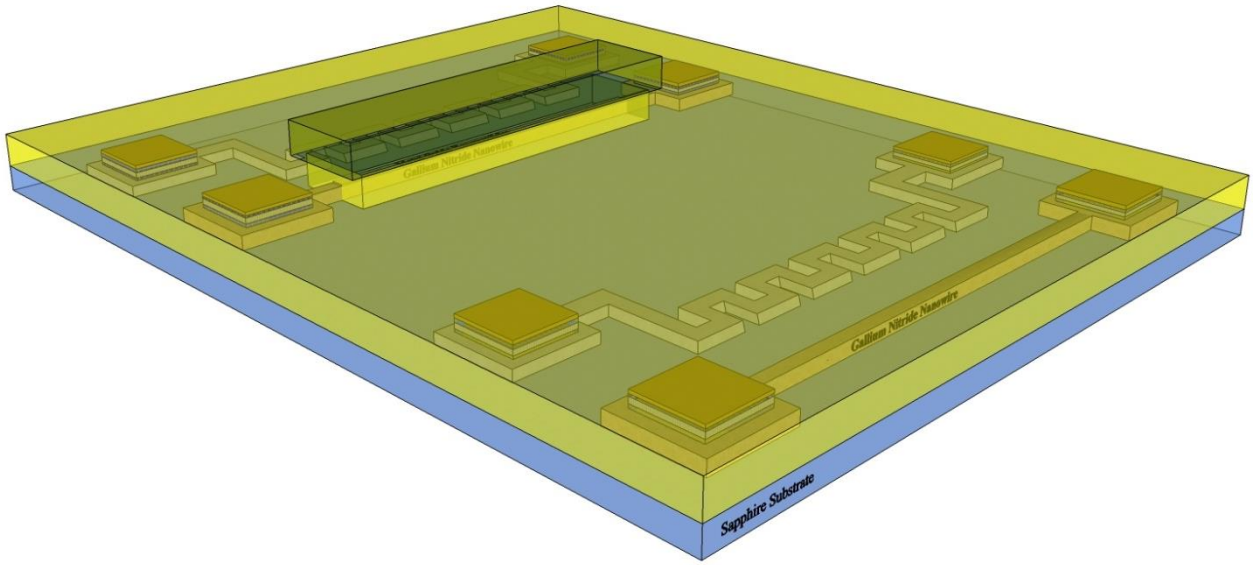

Fig. 6.19 Multiple sensors process diagram after photoresist protection layer patterned

6.3.2 Active Window Patterning on Passivation Layer

After the deposited NCs were protected by photoresist, a passivation layer of 50 nm SiO_2 was deposited uniformly on the wafer by PVD tools. PVD with sputtering or evaporating are both room temperature processes comparing to CVD technique which will ensure the photoresist maintain stable during the process. Another reason is CVD generally deposit conformal thin-films on all surfaces. SiO_2 growth on sidewall of photoresist will make the photoresist very hard to be removed later. The 50 nm SiO_2 is good enough to cover all the former deposited NCs on 300 nm SiO_2, and protect the new sputtered NCs from being contaminated by former NCs. The thickness of PVD deposited oxide film was double proofed by Nanospec Reflectometer (Nanometrics) and ellipsometry studies. Fig. 6.20 shows the wafer covered by SiO_2 passivation layer.

Fig. 6.21 shows the process diagram of gas sensor opened a new window on top of an undecorated NW and etched the SiO_2. MA6 Front and Back Contact Aligner (Suss Microtec) is used for NW open window patterning. Lithography and photoresist coating methods are the same with former mentioned MH and ohmic contact patterning. A bi-layer stack of photoresists (MicroChem LOR3A and Microposit S1813) were used. After UV exposure with 90 mJ/cm ^{2}dose energy, post-baked and developed in Microposit MIF-319 for 60 seconds, reactive-ion etching (RIE, Unaxis 790) was used for a descum process with 30sccm flow rate of oxygen for 30 seconds to clean up the remaining un-thoroughly developed resist residue. Dry etching with the same RIE or BOE wet etching is the last step to remove the SiO_2 in the window. For RIE dry etching, 12 min is sufficient enough to remove 350 nm SiO_2. For BOE (1:6) wet etchings, ideally 105 sec of BOE etch can remove 350 nm SiO_2. However, wet etching is hard to control and the HF have a higher chance

cracking the photoresist when etch for a long time. HF vaper etching is more controllable and repeatable comparing to BOE solution.

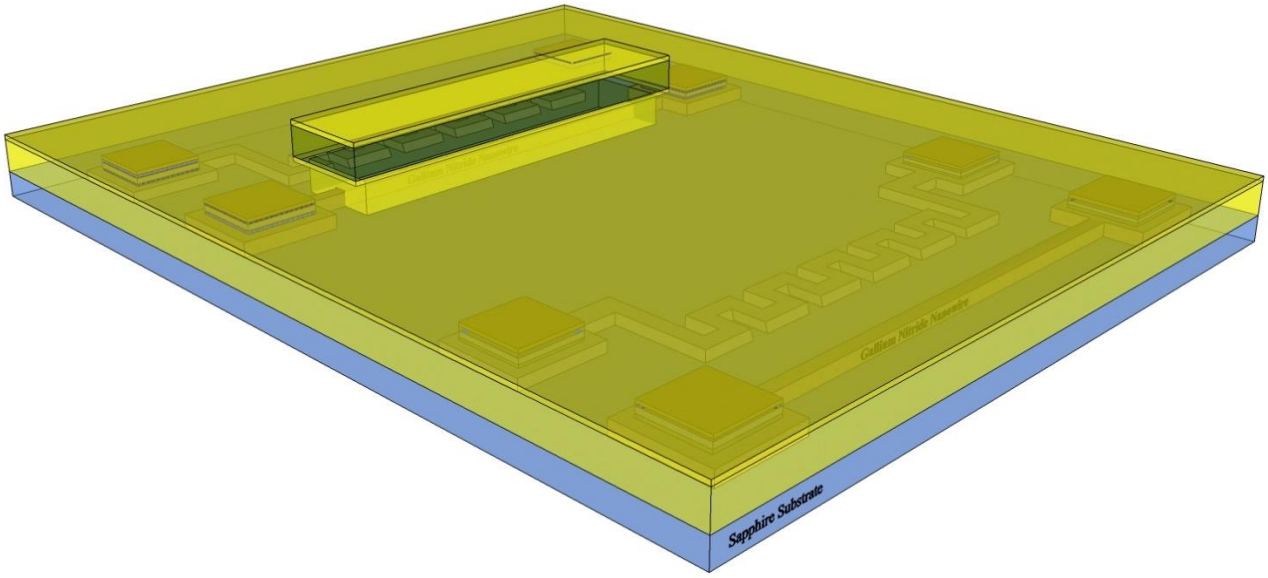

Fig. 6.20 Multiple sensors process diagram after deposition of passivation layer of SiO2

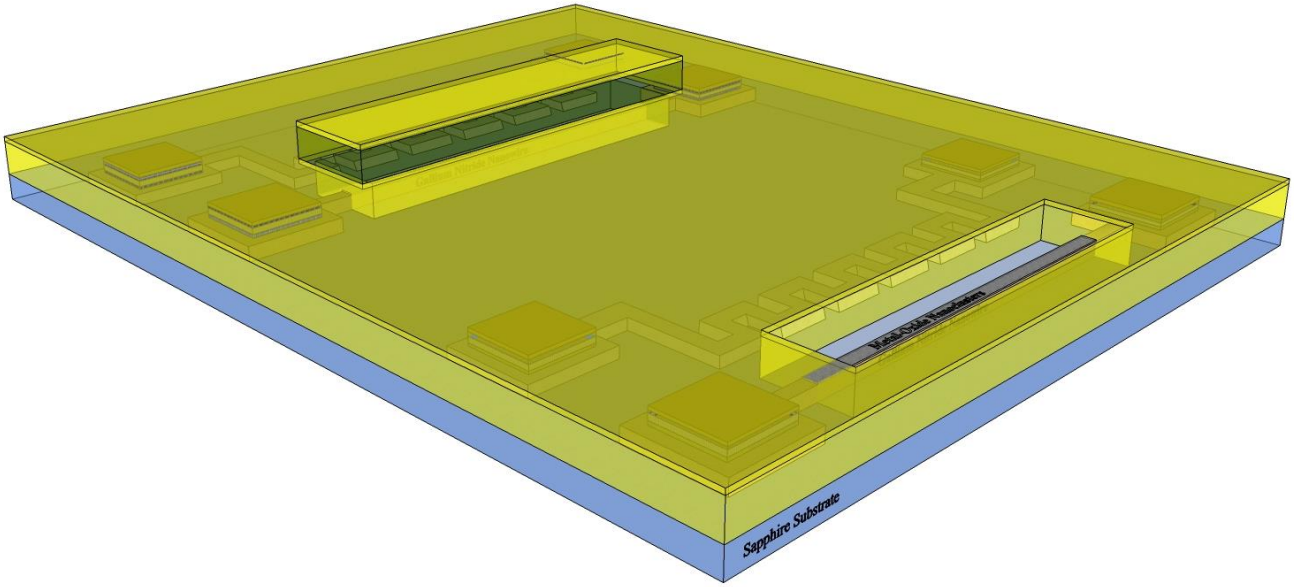

Fig. 6.21 Multiple sensors process diagram after 2nd active NW open window patterning

6.3.3 Photoresist Removal and RTA

After annealing, the wafer was rinsed in PG remover or 1165 to remove the photoresist, followed by acetone, methanol, isopropanol and de-ionized water cleaning. Fig. 6.22 shows the two different NCs each deposited on the assigned NW. The same process can be employed for the third, fourth and any additional NCs on new NWs, and the goal is multiple sensors on a single chip.

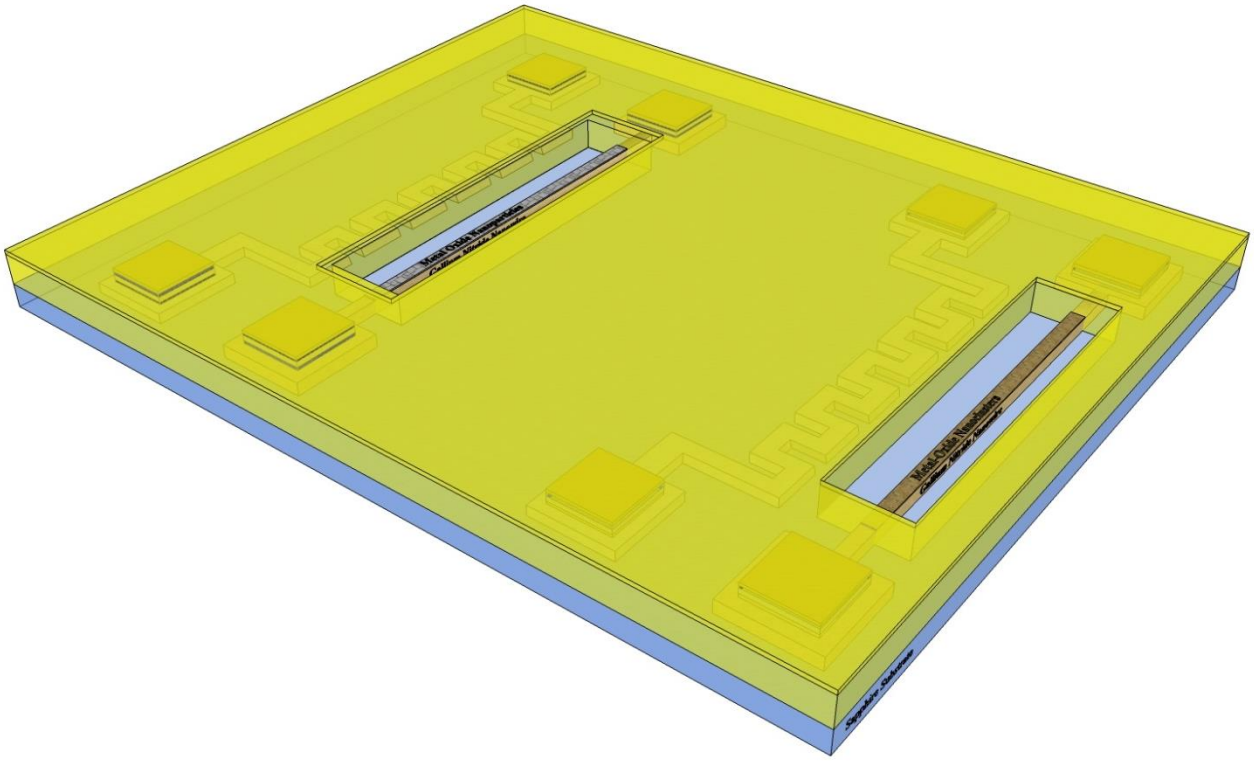

Fig. 6.22 Two types of sensor integrated on a single die

6.4 Device Packaging

The packaging process includes photoresist coating, dicing, die bonding and wire bonding. The wafer after the whole process was shown in Fig. 6.23(a). Each die (highlighted by red block) is 2.6 mm x 2.6 mm size and the detailed pattern is shown in Fig. 6.23(b). On each die, there are 8 NWs, top 6 NWs are active sensing elements and the bottom 2 NWs are passivated by thick SiO_2 layer. The passivated elements were designed as control groups for calibration of NW baseline current. The 6 active NWs can be decorated with same or different NCs, each NW has its own MH for desorption assistance purpose. The large and long MH in the middle of the die can be engaged and heat up the whole chip instead of each small local area around NW.

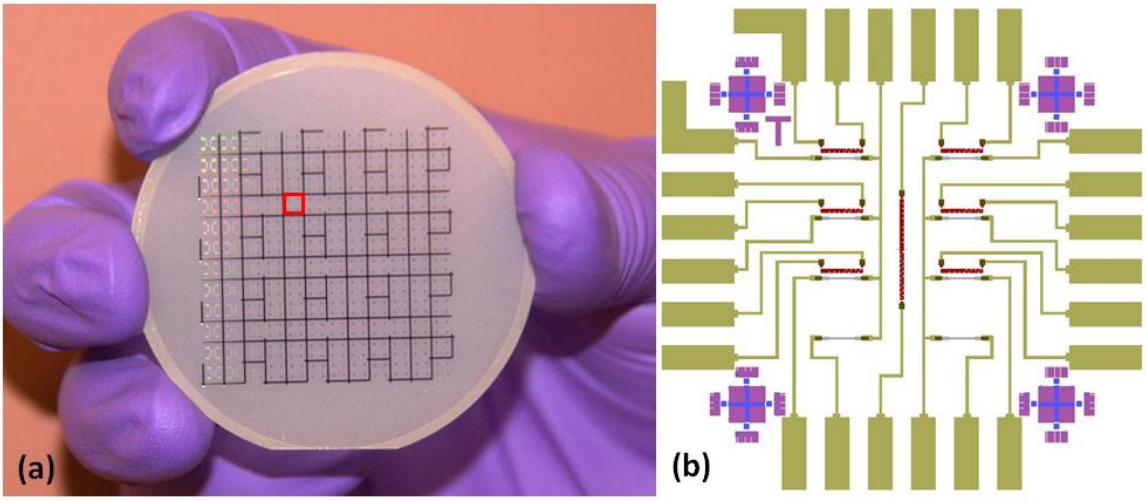

Fig. 6.23 (a) Final wafer before packaging (b) each die pattern

6.4.1 Photoresist Coating

A layer of photoresist was coated on wafer to protect the surface and device from damaging during the dicing process. Microposit S1813 was spun coated at 4000 rpm for 45 seconds followed by 60 sec bake at 115 ℃.

6.4.2 Dicing

The wafer was mounted on Microautomation Dicing Saw (Disco 341 Wafer Dicing Saw) and got diced into 2.6 mm x 2.6 mm size. After the dicing process, each die was immersed in the heated 1165 or remover PG solvent followed by cleaning with acetone, methanol and IPA with ultra sound sonication. Finally dies were rinsed in DI water and blow dried but nitrogen gas.

6.4.3 Die Bonding

Each die was individually mounted onto an open top side-brazed 24-pin dual in-line ceramic package with HD3007 (HD MicroSystems Polyimide Adhesive). The ceramic package was hot-baked at 110 ℃ for 5 min to dehydrate the surface. HD3007 was applied on ceramic package and hot-baked at 220 ℃ for 2 min to ensure it fully degassed. Die was put on top of the ceramic package and hot-baked at 350 ℃ for 5 min to let the HD3007 getting hard. Wait until the package fully cooled down to room temperature and transfer the chips to Au wire bonder.

6.4.4 Wire Bonding

The bonding pads of each die will be connected to ceramic package though Au wire wedge bonding. The wire bonder (Kulicke and Soffa Model 4526) was used. The packaged sensor chip which is ready for characterization and gas sensing measurement is shown in Fig. 6.24.

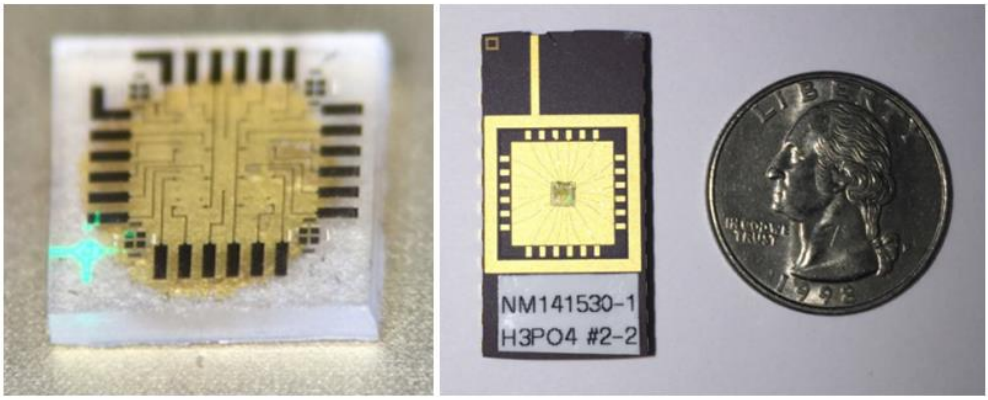

Fig. 6.24 Images of wire bonded gas sensor chips

6.5 Chapter Conclusion

This chapter reveals the process integration details of the nanowire-nanocluster (NWNC) gas sensors. Process integration of all three micro- and nano-structures into a single NWNC hybrid sensor device was discussed. Integration considerations including the process flows, RTA, multiple passivation layers, NW yield improvement, active opening windows, passivated control elements and ohmic contact improvement were explained in detail. The techniques for multiple sensors integration into a single sensor chip were first time reported. These enables the simultaneously multiple gas sensing capability of a single sensor chip.

The whole fabrication process of a single type of gas sensor contains more than 40 planer-process steps and 6 lithography masks. Every new type of gas sensor adding onto the original wafer needs the corresponding NCs deposited onto an assigned NW that hasn't been occupied. Each new NCs deposition will need extra 10 planer-process steps and 2 lithography masks. The whole process integration design was aim at establishment of a platform technology, which has great advantage in product flexibility and has the capability of customized design. It enables all kinds of combinations of gas sensing capabilities and the possibility of fitting all possible real-time sensing scenarios and conditions.

Chapter 7: Gas Sensing

In this chapter, the gas sensing measurement station for characterization of the NWNC sensor devices will be described. The set-up, including bubbler, pressure controller, gas mixing chamber and digital mass flow controllers (MFC) will be discussed. Several organic solvents can be mixed with ambient air and delivered to sensing chamber. Sensing results for TiO_2-Pt NCs / GaN NW sensor will be highlighted. Other nanoclusters alternatives and sensors, TiO_2-Pd NCs / GaN NW and SnO_2 NCs / GaN NW, will be explored.

7.1 Sensing Measurement Set-up

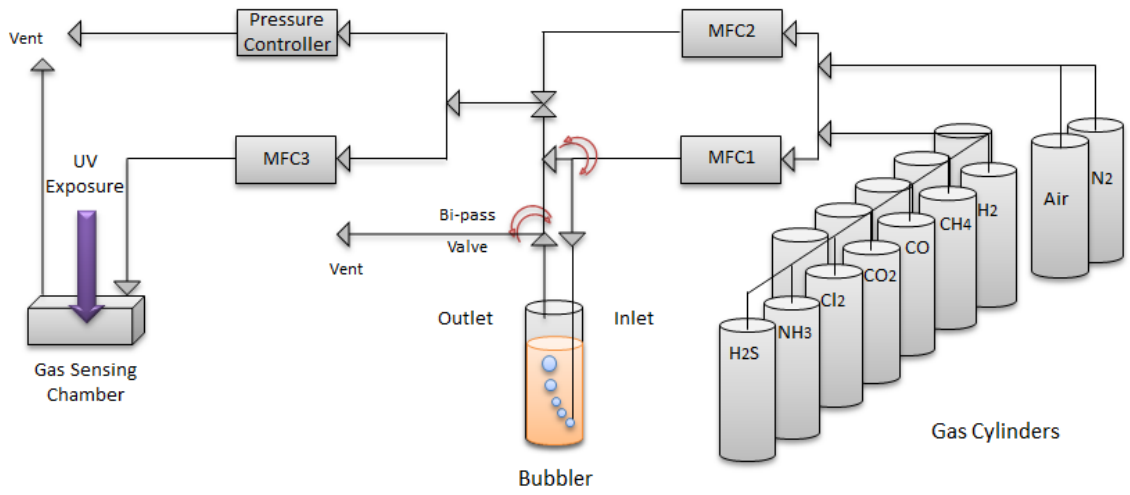

Fig. 7.1 Block Diagram of Gas Sensing Station Set-up

The schematic drawing of gas sensing station is shown in Fig. 7.1, gas tank cylinder with compressed breathing quality air (<9 ppm water vapor) is used as carrier gas for the whole system, N_2 carrier gas is an option for other experiments. The bubbler is filled with

high performance liquid analyte to be carried for organic sensors. For other gases, a high concentration cylinder can be connected directly to MFC1 and by-pass the bubbler. MFC1 has flow rate in between 0.2 sccm to 10 sccm to adjust the gas flow into bubbler. The small amount of analyte in its carrier gas is fully mixed with the carrier gas flow from MFC2. MFC2 has flow rate in the range of 200 sccm to 10,000 sccm (0.2 slm to 10 slm). The density of analyte in carrier gas can be manipulated by adjusting the MFC1 and MFC2 as well as the vapor pressure of the analytes. The analyte vapor picked up by the carrier gas and its concentration at the outlet of the bubbler depends on the vapor pressure of the analyte at the pre-set bubbler temperature. The bubbler is immersed in a temperature controller with a range of -15 ℃ to 75 ℃. The flow of the analyte at the outlet of bubbler is given by the equation 7.1,

$$F_{analyte\ out} = \frac{F_{carrier\ in} \times P_{vapor}}{P_{atmospheric} - P_{vapor}} \qquad (7.1)$$

where $F_{analyte\ out}$ is the flow rate of the analyte vapor at the bubbler outlet, $F_{carrier\ in} = F_{MFC1}$ is the flow rate of the carrier gas at the bubbler inlet, controlled by MFC1. P_{vapor} is the vapor pressure of the analyte in bubbler at the set temperature and $P_{atmospheric}$ is the atmospheric pressure which under normal condition is 760 mmHg. This equation is only valid for an ambient pressure larger than the vapor pressure. A bi-pass valve installed at the outlet of the bubbler is used to control the mixture (on and off) into the sensing chamber. MFC2 has much higher flow rate than MFC1 to dilute the analyte concentration with the carried gas. To maintain a constant pressure at the mixing chamber, a pressure controller is used to vent out extra gases. MFC3 is used to set gas flow rate into the sensing chamber with range from 2 sccm to 100 sccm.

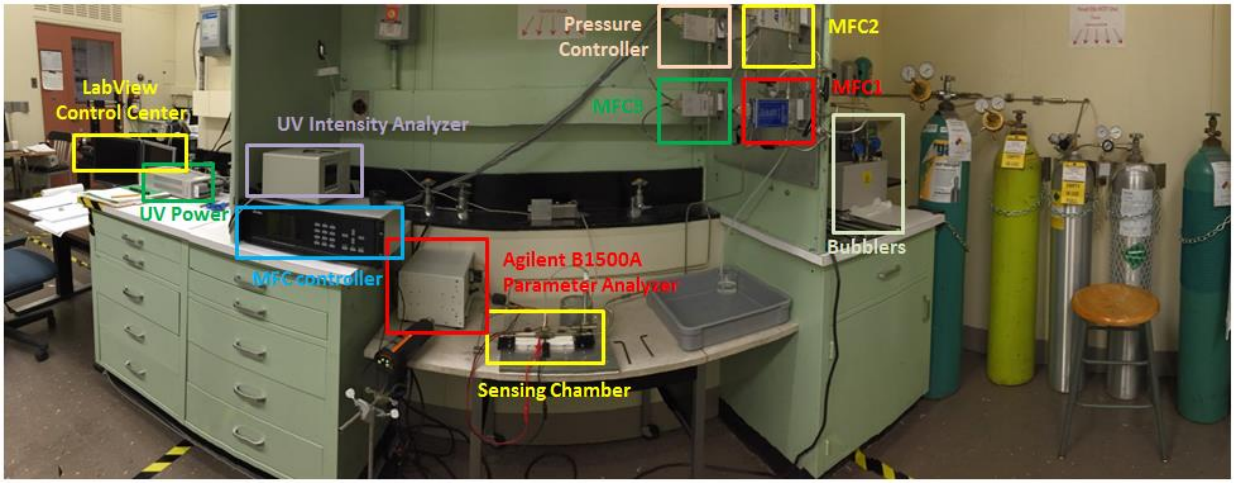

Fig. 7.2 Gas sensing measurement station

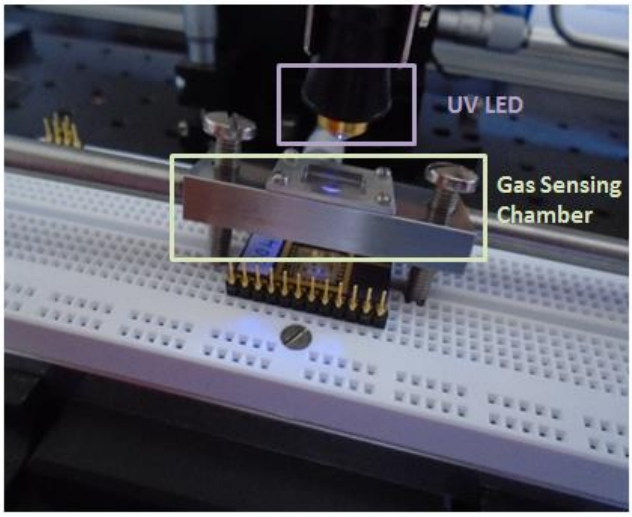

Fig. 7.3 Detailed assembly of UV LED, sensing chamber and sensor chips

For sensor device characterization, each sensor chip is placed in a customized stainless steel chamber with a quartz window on the top for UV exposure. The chamber volume is 0.73 mL. Electrical measurements were performed using an Agilent B1500A semiconductor parameter analyzer. The UV source works in the wavelength range from

215 nm to 400 nm, after optimization. The 355 nm wavelength filter is used and the deliver power of illumination is 50 μW/cm ^{2}through the quartz window. An alternate 355 nm UV LED can be used for higher intensity up to 496 μW/cm ^{2}. Fig. 7.2 shows the image of the real gas sensing station set-ups. Fig. 7.3 shows the detail assembly of UV LED, sensing chamber and the sensor chip.

7.1.1 Analyte Vapor Pressure Control

Vapor pressure of the analyte inside the bubbler can be controlled by bath temperature. The bubbler is immersed in a heat/cool tank filled with ethylene glycol and water. Adding ethylene glycol in water can decrease the freezing point of solution below 0 ℃ and increase the boiling point larger than 100 ℃. For weight percentage of 30% of ethylene glycol in water solution in heat/cool tank can achieve a wide bubbler temperature range from -15 ℃ to 104 ℃.

7.1.2 Mass Flow Controller

MFC1, MFC2 and MFC3 are MKS ALTA metal sealed type 1480A mass flow controller, at normal operating range, the pressure differential should be at least 10 psid for 10 to 5000 sccm flows and 15 psid for 10000 to 30000 sccm flows. The pressure differential should not exceed 40 psid. That means that for MFC1 (0.2 - 10 sccm) and MFC3 (2 - 100 sccm), the difference of pressure between inlet and outlet should be at least 10 psid. And for MFC2 (200 - 10000 sccm), the pressure at inlet and outlet were set to 15 psid.

7.1.3 Pressure Controller

The pressure Controller is an MSK electronic pressure controller 641A type. The controller is used to maintain constant pressure at the gas mixing chamber as well as to ensure the inlet working pressure for MFC3. The set pressure controller maintains a pressure difference of one atmosphere pressure (760 mmHg, 14.5 psid).

The pressure in the mixing chamber is twice the atmosphere pressure (29 psia), this maintains MFC1 and MFC2 working in the reliable conditions, and will not damage the MFCs when the mixing chamber suffering from short time pressure loss. The gas tank carrier gas pressure at the inlet was set to 45 psia by a regulator connected to gas cylinder.

7.1.4 UV Intensity Calibration

UV exposure is provided by a Newport Monochromator Illuminator 7340 series, controlled by LabView for wavelength optimization experiment. The best UV response for the NWs appears at the wave length of 355 nm. In the gas sensing experiments, the Newport UV source can be replaced by a commercial LED with the same wavelength. The Newport UV source is a series set-up and must be precisely tuned and well maintained prior to any measurements. However, LED is more portable and not necessary for any scheduled maintenance. Moreover, the GaN LED enables the sensor's capability of integrating illumination UV sources on-chip.

7.2 Sensor Characterization Parameters

7.2.1 Analyte Concentration

Analyte concentration is defined in units of ppm (parts per million), ppb (parts per billion) or ppt (parts per trillion) for low concentrations. Percentage representations were used to high concentration gases, 1% = 10,000 ppm. Concentration depends on the flow rates of MFC1, MFC2 and the vapor pressure of the analyte in bubbler. If a bubbler is used as the analyte source, from equation 7.1, concentration can be expressed by $F_{analyte\ out}$ as shown in equation 7.2.

$$Concentration\ (ppm) = \frac{F_{analyte\ out}}{F_{MFC1} + F_{MFC2}} \times 10^6$$

$$= \frac{F_{MFC1} \times P_{vapor}}{(P_{atmospheric} - P_{vapor})(F_{MFC1} + F_{MFC2})} \times 10^6 \qquad (7.2)$$

Where $F_{MFC1}$and F_{MFC2} are the flow rate through MFC1 and MFC2 correspondingly. For units of ppb and ppt, $\times 10^9$ and $\times 10^{12}$ will be applied respectively. During the sensing measurement, we try to achieve the lowest minimum detectable analyte concentration possible, so $F_{MFC1} \ll F_{MFC2}$. The equation 7.2 can be approximated as shown in equation 7.3.

$$Concentration\ (ppm) = \frac{P_{vapor}}{P_{atmospheric} - P_{vapor}} \times \frac{F_{MFC1}}{F_{MFC2}} \times 10^6 \qquad (7.3)$$

If a bubbler is not used, the concertation of analyte is only controlled by MFC1 and MFC2, equation 7.2 is simplified to equation 7.4. The approximated form for $F_{MFC1} \ll F_{MFC2}$, is shown in equation 7.5.

$$Concentration\ (ppm) = \frac{F_{MFC1}}{F_{MFC1} + F_{MFC2}} \times Con_{Analyte}(\%) \times 10^6 \qquad (7.4)$$

$$Concentration\ (ppm) = \frac{F_{MFC1}}{F_{MFC2}} \times Con_{Analyte}(\%) \times 10^6 \qquad (7.5)$$

Where $Con_{Analyte}$ is the analyte concentration from analyte source cylinder and represented in percentage format.

7.2.2 Response Time

Response time was defined as the time needed by sensor to reach 90% of the total response change after the exposure to analyte. If *Ib* (baseline current) is the current level without the analyte, and *Is* (sensing current) is the steady current under analyte exposure. The time needed for current change from *Ib* to *Ib* + 90% (*Is*-*Ib*) is defined as the response time.

7.2.3 Recovery Time

Recovery time was defined as the time needed by sensor output to recover back to 30% of the total respond after the start of the recovering cycle. If *Ib* (baseline current) is the current level without the analyte, and *Is* (sensing current) is the steady current under

analyte exposure. The time needed for current change from Is to Ib + 30% (Is-Ib) is the recovery time.

7.2.4 Sensitivity

There is some ambiguity in the literature on the definitions of sensitivity, resolution and response. In the gas sensing field, sensitivity is the change of measured signal (resistance, conductance) when the sensor is exposed to a certain concentration of target analyte [6, 7]. In general, though, (e.g. for temperature or radiation sensors), this is defined as response, and the slope of the response to the sensed quantity (temperature and radiation intensity in this case) is defined as sensitivity. However, in the gas sensor field, this quantity is defined as resolution. In this work, we opt to use "common gas sensor parlance" and define sensitivity as the change of resistance before and after gas sensing. We use the term "resolution" to define the slope of sensitivity (response) with respect to analyte concentration. The mathematical expression for sensitivity used here is shown in equation 7.6.

$$Sensitivity\ (differential) = \frac{R_{gas} - R_{air}}{R_{air}} \qquad (7.6)$$

Where R_{gas} and R_{air} are resistances of NWNC two terminal device exposed to target gas and air respectively. During the experiments, current was measured with a fixed voltage, so the sensitivity also can be expressed by current of device exposed to target gas and air, I_{gas} and I_{air} respectively, as shown in equation 7.7.

$$Sensitivity\ (differential) = \frac{I_{air} - I_{gas}}{I_{gas}} \qquad (7.7)$$

In open literature, there are another common ways to express highly sensitive device by taking ratio of resistances before and after exposure to target analytes, as shown in equation 7.8.

$$Sensitivity\ (ratio) = \frac{R_{gas}}{R_{air}} = \frac{I_{air}}{I_{gas}} \qquad (7.8)$$

7.2.5 Selectivity

Selectivity is the ability to discriminate between the components of a gas mixture and provide detection signal for the component of interest [6-8]. In this work, I defined the selectivity of my gas sensor by exposure it to all possible target gases individually and list all the gases that shown detectable response. If a sensor shows response to one type of gas only and shows no responds to other gases, then this sensor is defined as highly selective. For example the GaN / TiO_2-Pt sensor in section 7.3 only shows response to H_2 gas and no response to all other gases. If a sensor shows response to a group of gases and shows no responds to other gases, then this sensor is defined as good selectivity. For example, the NO_x sensor based on GaN / SnO_2 in section 7.4 only shows response to NO and NO_2 and shows no response to other gases. Selectivity can be quantified by a factor as the ratio of the response to the target analyte to the response to the interference species as shown in equation 7.9.

$$Selectivity\ Factor = \frac{Target\ Response}{Interference\ Species\ Response} \qquad (7.9)$$

7.3 Sensing Characteristics of the GaN / TiO_2-Pt NWNC Sensors

The nanowire arrays were patterned and dry etched by inductive coupled plasma (ICP) chlorine etcher followed by KOH wet etching. TiO_2-Pt composite NCs were deposited with magnetron sputter. NCs deposition recipes and process flows were explained in detail in the former chapters.

The GaN / TiO_2-Pt hybrid sensor shows high sensitivity and selectivity for H_2. In this study, the hydrogen sensor in different types of environments was compared. The proposed hybrid sensor is both sensitive and exhibits a reversible response. In fact as shown in Table 1.4, it shows higher sensitivity and shorter respond/recovery time than other reported sensors. By field emission scanning electron microscopy (FESEM) and atomic force microscopy (AFM) measurements, we were able to reveal the metal oxides surface morphology displayed in Chapter 4. Through X-ray diffraction (XRD) and X-ray photoelectron spectroscopy (XPS) we characterized the phase and composition of the material. The conductance measurements were applied to nanoclusters on a metal-dot-array pre-patterned substrate and I got further proof of the isolation property. Breathing air with and without UV illumination for 12 hours with negligible baseline drift and no decrease in sensitivity were observed. The sensors were selective for hydrogen and did not exhibit any response to VOCs, CO, CO_2, NH_3, NO_2, NO, SO_2, H_2S, and the response to alcohols shows magnitudes lower sensitivity when compared to H_2.

The gas sensing performance of the fabricated sensor was investigated at room-temperature in a custom-built apparatus. A gaseous mixture of target analyte and breathing air was introduced into the sensing apparatus. Mass flow controllers independently tuned the flow rate of each mixing component, target analyte and carrier gases, determining the

final composition of the mixed gas. The sensors were biased with a constant 5 V supply and currents were measured by a National Instrument PCI DAQ system. A 355 nm light emitting diode provided the UV illumination to the sensor. A detailed description of the experimental set-up and conditions can be found in the former sections.

7.3.1 Current-Voltage (IV) Characteristics

IV measurements were performed from -5 V to 5 V with UV off. The IV curve of the GaN/TiO_2-Pt hybrid sensors was nonlinear and asymmetric especially in between voltage bias of -2V and 2V, while the IV curve of the SiO_2 passivated control sensors was linear with relatively higher current as shown in Fig. 7.4. The nonlinear characteristic of the TiO_2-Pt sensor is not due to the contact resistance since the control NWs IVs are linear. The nonlinearity is likely due to the band bending effects at the GaN / (TiO_2-Pt) junction. The band bending forms depletion depth largely decreases the cross-sectional area for carrier transportation, which result in higher resistivity and lower current under the same voltage bias. 5V of voltage bias was use for gas sensing measurement since the IV curve near 5 V is in a linear range.

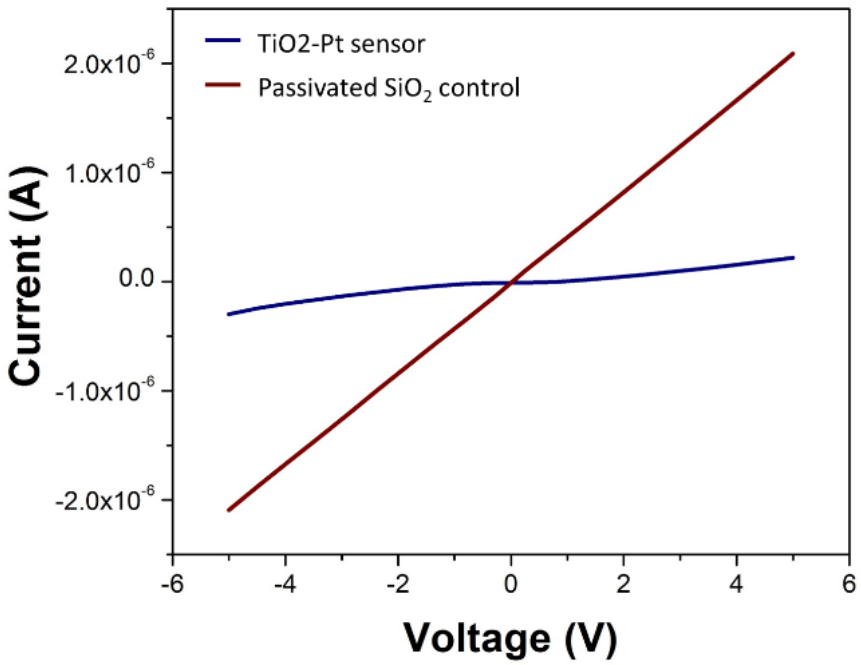

Fig. 7.4 IV characteristics of the active GaN/TiO_2-Pt and control sensors

Table 7.1 lists the sensor currents as measured under four conditions: in breathing air and N_2 ambient both with and without UV illumination. Surface adsorbed oxygen is a critical determinate in metal oxide reactivity and resistivity. Factors effecting the concentration of surface adsorbed oxygen on TiO_2 include the ambient atmosphere O_2 concentration and UV illumination. The oxygen adsorbed on TiO_2 NCs significantly affects the current conduct through the NW by depleting the electron near the GaN surface and increase the depletion depth. The current increase to 7 times when the device exposure in oxygen free ambient. Under UV illumination, large amount electron-hole pairs generated, holes diffuse to surface and electrons remain in the core of the NW. Excess amount of holes carrier enhances desorption rate of oxygen. Therefore, with UV exposure, current increases significantly due to photo generated electron-hole pairs increase the carrier concentration. Because the oxygen adsorption is low, sensors in N_2 and air show similar current magnitude.

Conditions		Current (A)
UV off	N_2	6.0×10^{-7}
UV off	Breathing Air	1.0×10^{-7}
UV on	N_2	1.2×10^{-6}
UV on	Breathing Air	1.0×10^{-6}

Table 7.1 GaN / TiO_2-Pt sensor baseline current measurements

7.3.2 H_2 Sensing Performance of GaN / TiO_2-Pt Sensors

The sensor resistance is on the order of 10 MΩ, to accurately test the current through the sensor without introducing new current path, a small resistor 100 kΩ was connected with gas sensor in series. A constant voltage of 5 V was applied to maintain the voltage of gas sensor around the linear range. A voltage meter was used to measure the voltage drop on two sides of resistor. The gas sensing measurement circuit layout is shown in Fig. 7.5(d). Fig. 7.5(a)-(c) show the 10% H_2 sensing results of the GaN / TiO_2-Pt sensor under three different conditions: (a) carrier gas is breathing air and no UV illumination during the test, (b) carrier gas is breathing air and use UV illumination during test the and (c) carrier gas is nitrogen and no UV illumination during the test. The current increased upon exposure to hydrogen in all three cases. That means the exposure to H_2 will decrease the resistivity of gas sensor. Comparing Fig. 7.5(a) and Fig. 7.5(b), the current increase is due to the UV illumination that generate electron-hole pairs that increase the carrier concentration. Comparing Fig. 7.5(a) and Fig. 7.5(c) reveals that N_2 ambient will decrease the device resistivity by reducing surface O_2 absorption amount. Both results fit with the IV characterization. Fig. 7.5(b) and Fig. 7.5(c) shows higher noise magnitude comparing to Fig. 7.5(a), that is because the increased current comes from the increased conduction channel cross-sectional area. There are lots TiO_2/ GaN interface near the GaN surface. The larger the carrier transport area, the closer the mobile charge comes to the TiO_2/GaN interface, the more likely it will be scattered and the effective mobility of the charge will be reduced. In the case of (b) and (c), the interface defects trap and release the mobile charges that generate majority of the noise. For the case of Fig. 7.5(a), carrier transport

area is narrowed down to the core of NW where carrier mobility is the highest due to the high quality of GaN.

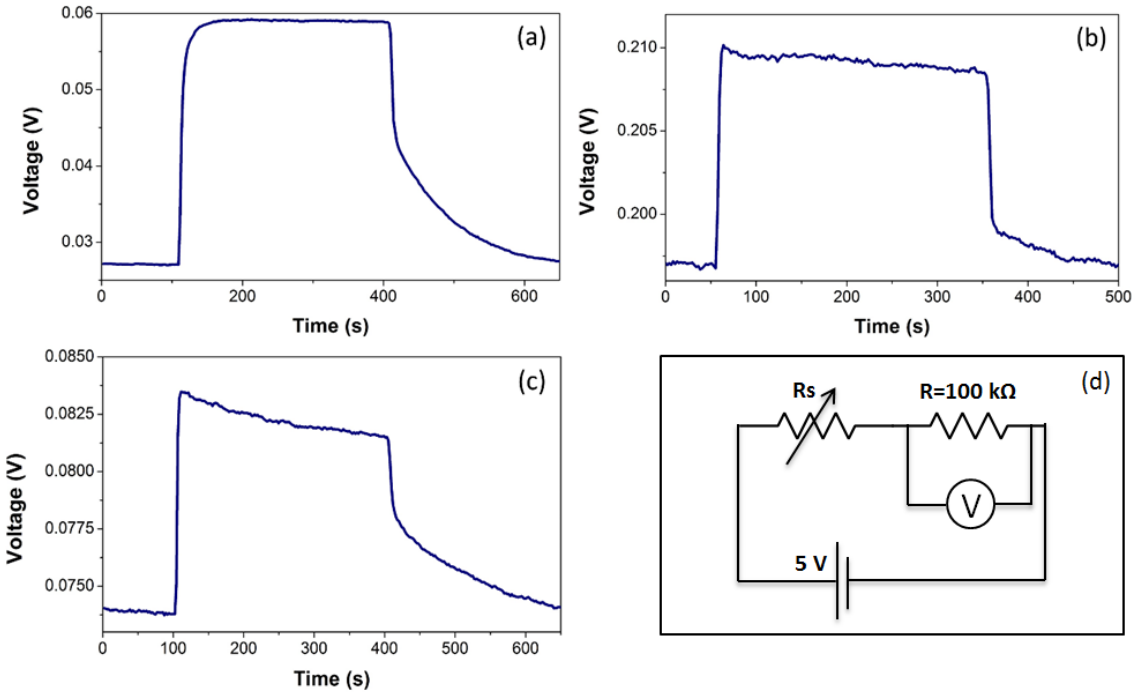

Fig. 7.5 Response of GaN / TiO_2-Pt to 10% H_2 for 300 sec. (a) breathing air carrier gas without UV illumination (b) breathing air carrier gas with UV illumination (c) nitrogen carrier gas without UV illumination (d) gas sensing measurement circuit layout

The device sensitivity was 25 times greater without the presence of UV light than in the presence of UV light and 15 times more sensitive in breathing air than N_2 without UV illumination as shown in Table 7.2. Sensitivity is defined as (Rgas – Rair) / Rair where Rgas and Rair are the resistances of the sensors in the presence of the analyte and in the presence of carrier gas only, respectively.

Conditions		H_2 Sensitivity
UV on	Breathing Air	6%
UV off	Breathing Air	150%
UV off	N_2	10%

Table 7.2 Comparison of the H_2 sensitivity in percentage with and without 365 nm UV illumination in breathing air and in nitrogen

The GaN / TiO_2-Pt can detect H_2 concentration down to 100 ppm and up to 100%. It can fully recover even after sensing extremely high concentrations. The H_2 sensitivity to different concentrations from 500 ppm to 40% can be linearly fitted to a logarithmically proportional increase in current as shown in Fig. 7.6. This sensor is the widest detection range for H_2 as compared to other alternatives from open literatures in Table 1.4. The responses to concentration below 100 ppm and above 40% were not distinguishable and they were observed similar to 500 ppm and 100% exposures respectively. A linear fit was applied to scattered data and the variance was 0.9921. The sensor was tested cyclically for 12 continuous hours with forty times of 5-minute-exposure to 10% H_2 followed by 5-minute-recovery, the sensing result is shown in Fig. 7.7. Negligible baseline drift occurred along with no degradation in sensitivity during the 12 hours testing.

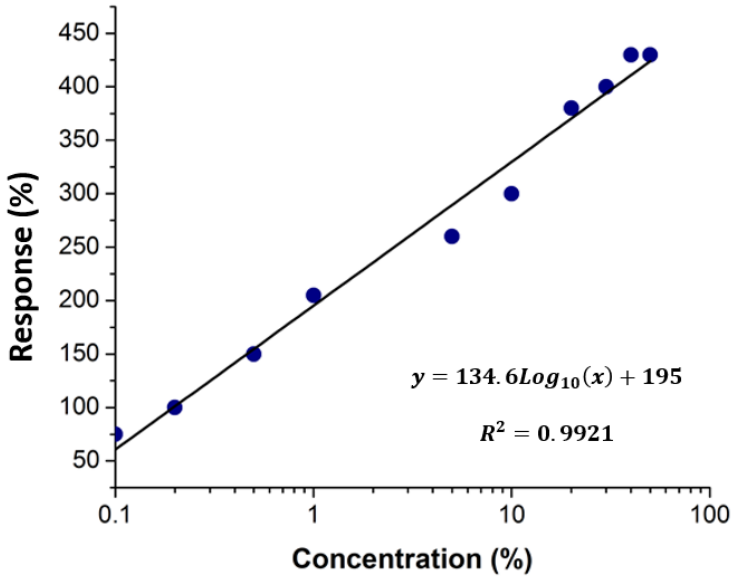

Fig. 7.6 Semi-logarithmic plot of sensitivity (response) to hydrogen gas concentration from 1000 ppm to 40% in breathing air

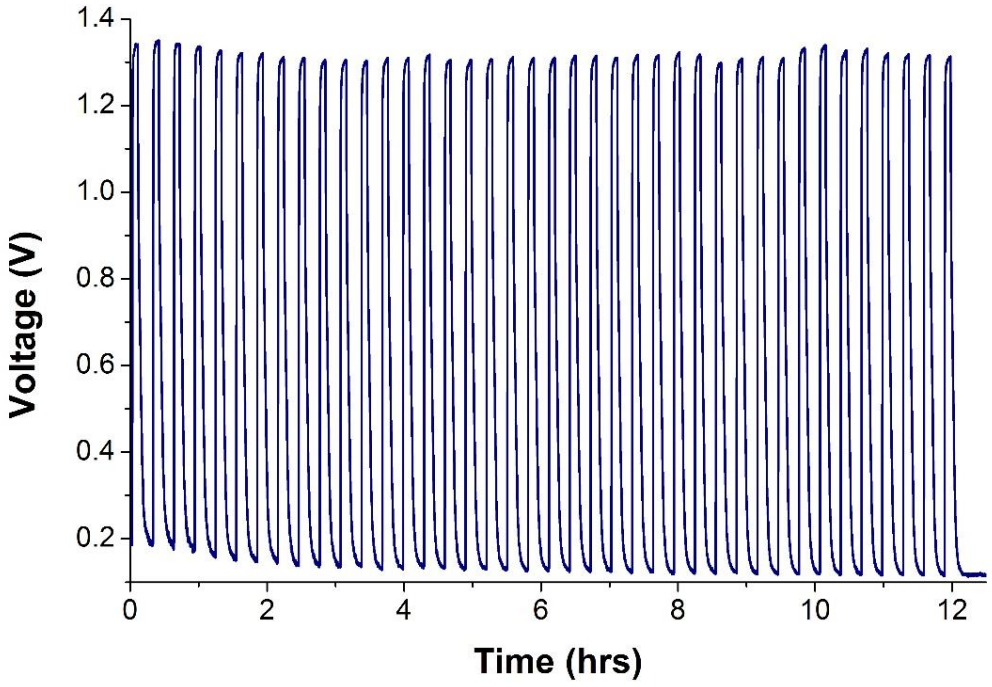

Fig. 7.7 Cyclic response of the GaN / TiO_2-Pt hybrid sensor exposed to 10% H_2 in breathing air with no UV illumination.

7.3.3 Selectivity of the GaN / TiO_2-Pt Sensor

The response of the GaN / TiO_2-Pt sensor in the presence of other analytes or interfering compounds/molecules with hydrogen was tested with 5-minute-exposures to 500 ppm of H_2S, SO_2, CO, CO_2, NH_3, NO_2, NO, SO_2, methanol, and benzene. The UV photocurrent did not change after these exposures and the device continued to respond to H_2 without showing any interference effects. The highly selectivity can be explained by the TiO_2-Pt NC composition. Detail mechanisms will be discussed in next section.

7.3.4 H_2 Sensing Mechanism for the GaN / TiO_2-Pt Sensor

The hydrogen sensing mechanism in these hybrid sensors is complex and depends on many factors including the metal-semiconductor junction, the analyte-NC interactions, NC adsorbates, and how these electronic interactions modulate the GaN NW current. The physical mechanism creating this conductivity change has remained ambiguous. Qualitative mechanisms are proposed, aimed at elucidating the physical basis of these observations.

Consider a GaN nanowire of arbitrary length (10, 50, 100 or 200 μm). The width and height of this wire is fixed at 300 nm. When exposed to various gases (O_2, CO, CO_2, alcohols of various types, benzene, methane, ethane, etc.), these wires by themselves exhibit little change in conductivity. However, when TiO_2 NC or thin-film was sputter deposited on these wires, the wires exhibit larger response in conductivity when they were exposed to the same gases. Sputter deposition of a small amount of platinum NPs enhances this effect and the sensor became selective to H_2 gas only. In the paragraphs below, we outline some further explanations of these observations. The base structure (with platinum inclusions) is shown in Fig. 7.8.

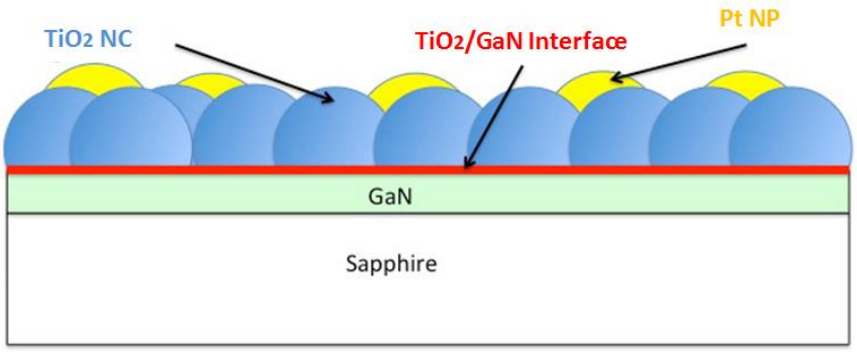

Fig. 7.8 Structure diagram of GaN / TiO_2-Pt NWNC gas sensor device

Both TiO_2 and GaN are wide band-gap semiconductors with E_g greater than 3.2 eV. Due to its intrinsic defect structure and oxygen deficiency, TiO_2 is n-type semiconductor with fairly conductivity and it is electron rich. The GaN wire is doped n-type by silicon addition and exhibits a mobile electron background of about 1E17/cm ? There is a difference in electron affinities between the TiO_2 and the GaN material. The electron affinity of the TiO_2 is about 1 eV larger than that of GaN. Thus, the conduction band edge of the TiO_2 is lower than the conduction band edge of GaN by about 1 eV. As the TiO_2 is heavily doped and GaN is intentionally doped, we assume that the Fermi levels of the two materials, when separate, are quite close to their respective conduction band edges. We can assume that the Fermi level of both materials is similarly close to its conduction band edge.

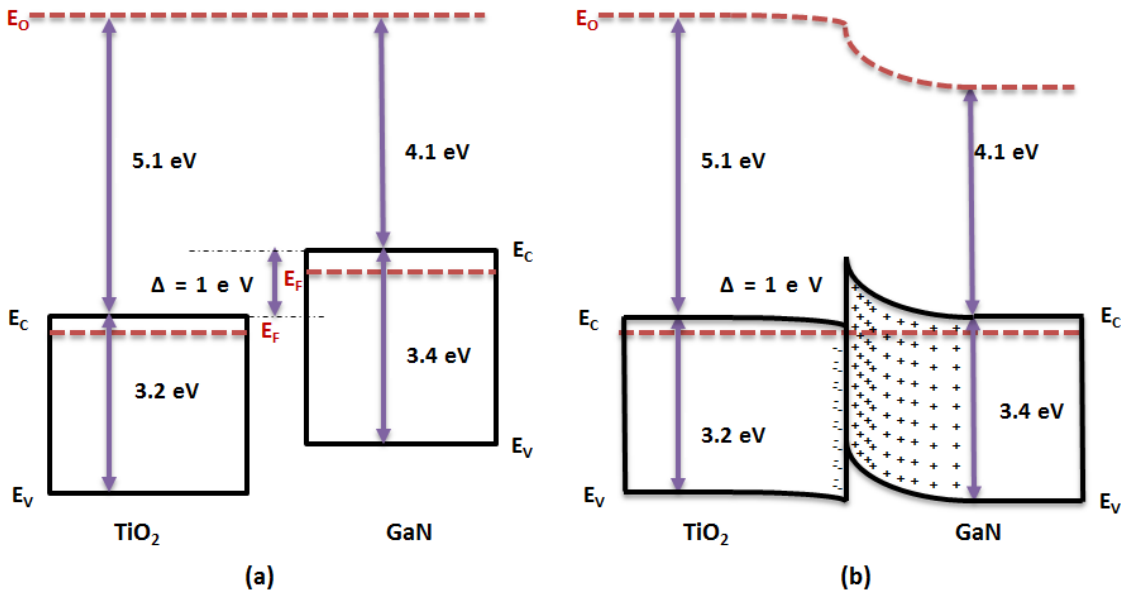

Fig. 7.9 The electronic structure of the TiO_2 / GaN system (a) before the materials are brought into contact (b) after the materials are bought into contact and a space charge layer formed

If the above assumptions hold, there can be a spill-over of mobile electron charge from the GaN into the TiO_2, leading to a thin depletion layer in the nitride. We now estimate that the Fermi level difference between the two materials is 1 eV, the TiO_2 is electron rich to the point that it cannot sustain a space charge and the whole space charge extends into the GaN. In that case we can estimate the depletion depth of extending into the nitride is about 100 nm. This thickness is determined by the background doping in the nitride (1E17 /cm ^{3}) and by the estimated a volt Fermi level offset between the TiO_2 and the GaN. The depletion width is 99 nm and 104 nm for carrier concentration in TiO_2 is 1E19 /cm ^{3}and 1E18 /cm ^{3}respectively. The dielectric constant for GaN is reported in between 8.9 and 9.5, 8.9 is used in this space charge estimation [228]. While this leads to a significant area reduction of the conductive channel, if we consider a three-dimension nanowire whose top surface and sidewalls are covered by TiO_2 NCs. That explains why the TiO_2 decorated NW shows much lower current than the SiO_2 passivated NWs in Fig. 7.4. The band diagrams are shown in Fig. 7.9.

The large amount of photo-generated charges “photodope" the GaN NW and shrink the depletion to a negligible thickness. As the UV incident flux is large (469 μW/cm ^{2}), the back-ground carrier concentration substantially increases, shrinking the space charge to a negligible thickness. The current boost was the result of both increased carrier concentration and widened transport channels.

Comparing Fig. 7.5(a) and Fig. 7.5(b) the experiment shows that under UV exposure, the sensor still has the capability of channel modulation and the sensor responds to hydrogen. Ideally, the total number of photo generated carriers in the wire will be unchanged by the space charge and adsorbed gas molecules. The space charge would

simply push those photo generated electrons to the core of the wire and they would still available for transport. Thus, the photocurrent should in no way be affected by the depletion narrowing of the transport channel. The result of Fig. 7.5(b) can be explained by the large photo-absorption of UV light by TiO_2 NCs shielding the GaN underneath from optical exposure. So under UV exposure, the channel modulation capability was weakened and the sensitivity decreased to 6% comparing to the 150% sensitivity without UV assistance.

With UV illumination, the number of carriers available for transport through the cross sectional area of the wire remains the same and is largely determined by the number of photo generated mobile carriers. All that changes is within a small space charge range near the TiO_2 / GaN interfaces. The closer the mobile charge comes to the TiO_2 / GaN interface, the more likely it will be scattered and the effective mobility of the charge will be reduced. This explains why in Fig. 7.5(a) and Fig. 7.5(b) sensing with UV illumination shows higher noise magnitude than sensing measurements without UV illumination. It is also possible that charged interface traps play some role. While the traps at the TiO_2 / GaN interface will not be affected directly by molecules attached to the TiO_2 NCs, the NCs charge can affect band bending and change the occupancy of interface traps. If the interface traps discharge, they will be less effective in creating scattering and mobility degradation. Or, if the traps become negatively charged, they will force the mobile channel charge more deeply into the channel, away from the scattering interface. This will, in turn, increase conductivity. In any event, with UV illumination, the charge state of the TiO_2 NCs and of the TiO_2 / GaN interface will dominate in defining conduction. In summary, when the sensor were illuminated by UV, photo-doping leads to shrinkage of the space charge

allowing mobile charge to move closer to the TiO_2 / GaN interface. There, the carriers are strongly scattered, trapped and recombined before collection. This generates noise and lower sensitivity.

Without UV illumination, the curvature of the bands does push the mobile charge away from the scattering centers and from possible interface recombination sites, some interaction with the interface is expected.

In summary, if the sensor is exposed to high intensity UV radiation. Photo exciting both TiO_2 NCs and GaN NW, any chemical adsorption on the TiO_2 that leaves a statistic net positive charge on the NCs will pull the electrons in the GaN closer to the interface, generation noises, reducing space charge and increasing conductivity. Also, those carriers incident on the interface may be trapped and recombine before collection. Statistic negative charge on the NCs has the opposite effect. Mobile charge will be forced to the center of the wire, away from the scattering interface, reducing noises, which slightly increasing the space charge area, decreasing the current.

On the contrary, if the sensor is measured in the dark and there are no photo generated carriers in either TiO_2 NCs or GaN NWs, then any chemical adsorption on the TiO_2 that leaves a statistic net positive charge on the NCs will reduce the space charge thickness in the GaN, widening the cross sectional area of channel and increasing conductivity by large. Negative charge on the NCs has the opposite effect. Mobile electrons will be further depleted and forced to the center of the wire. This narrows the transportation channel, thereby decreasing the current. The space charge for both conditions is large enough that carriers are far away from TiO_2 / GaN interfaces and producing the minimum noises.

The space charge is much smaller under UV illumination comparing to the space charge in dark (100 nm). Therefore, the conduction channel width modulation under UV exposure is substantially smaller than in dark. The same device shows lower sensitivity under UV illumination as compared to the sensitivity in dark, as shown in Fig. 7.5(a) and Fig. 7.5(b).

So now we must turn to surface chemistry to address the issue of how gas/NCs interactions lead to statistic surface net charge and space charge modulation. As an n-type semiconductor, TiO_2 depletion width increases in the presence of electron trapping adsorbates, such as O_2. To understand the O_2 adsorption on TiO_2 and its effect on GaN depletion width, the sensor current with two different concentrations of surface adsorbed O_2 on TiO_2 was examined by desorbing some of the surface O_2 in a N_2 atmosphere (Table 7.1). The sensor current was 6 times lower in air than in nitrogen implying a more negative charged TiO_2 surface leads to an increased depletion layer of GaN and a lower NW current. The effect a metal has on the semiconductor depletion layer is directly dependent on the work-function of the metal and the electron affinity of the semiconductor. The work function of Pt (6.35 eV) is higher than the electron affinity of TiO_2 (5.1 eV). TiO_2 will lose electrons to the Pt when in contact. Pt essentially acts in the same manner as in surface-adsorbed O_2, which enhances the negative TiO_2 surface charge and increases the space charge in GaN NW in dark. Table 7.3 lists the summary of how ambient oxygen concentration and the adsorption on TiO_2 NCs forms O_2^- affect the NW conductivity in dark. When ambient O_2 concentration increases, the number of O_2 molecules adsorbed on NCs increases as well. The electrons were depleted by absorbed O_2, and formed O_2^-, which accumulating the statistic negative charge by increasing the electron carrier life-time. The

net negative charge at the surface of TiO_2 depletes the GaN NW, pushes electrons to the core and decreases the conductive channel width. The conductivity will decrease as the result. Lower O_2 concentration has the opposite effect.

Mechanism of O_2 Adsorption on GaN / TiO_2-Pt Sensor		
Ambient O_2 Concentration	↑	↓
Number of O_2 Adsorbed on TiO_2 NCs	↑	↓
Number of O_2^- on TiO_2 NCs Surface	↑	↓
Statistic Net Negative Charge	↑	↓
GaN Space Charge Width	↑	↓
GaN NW Conductivity	↓	↑

Table 7.3 Mechanism of surface adsorption of O_2 on TiO_2 NCs modulate the NW conductivity without UV assistance (in dark)

The GaN / TiO_2-Pt sensor is highly selective to H_2. This was believed due to the introduction of Pt NPs on TiO_2 NCs. The heat of adsorption of H_2 on Pt is 100 kJ/mol [229] while on TiO_2 the number is negligible [230]. Upon exposure to H_2, the sensor current significantly increased implying that both the TiO_2 NCs depletion layer and the GaN NW space charge widths decreased. Introducing H_2 will decrease the O_2 concentration in the chamber, desorption O_2 from TiO_2 surface can increase the conductivity of NW (Table 7.3). The TiO_2 rapidly desorbs most of the O_2 on its surface and maintains a very low net absorption rate at equilibrium and decreasing its depletion layer [231-233]. However this O_2 concentration based mechanism is not the dominate driver of current boost, because

gases other than O_2 were tried and only H_2 shown a significant sensing response while other gas responses were negligible and barely observed.

The dominating sensing mechanism is illustrated in Fig. 7.10. The sensor in the air ambient absorbs O_2 at the oxygen vacancy sites of TiO_2 NCs. The attached O_2 depleted the electron carriers in TiO_2 and forms O_2^-. There is a net negative charge at the TiO_2 surface and a space charge formed in GaN NW surface. Once H_2 introduced into the system, this space charge depth shrinks due to the H_2 on a Pt NPs surface lose electron and dissociates at room temperature. There is a net transfer of electrons from H_2 to O_2^- on TiO_2 NCs and desorb the O_2. The H^+ trap holes and neutral the net negative charge on TiO_2 NCs surface, further accumulation H^+ can make the surface positive charged. The space charge in the GaN NW decreases, widening the conduction channel in the NW enhances the conductivity of the sensor. The dissociated H^+ can also spillover, migrate and reduce the O_2 adsorbed on TiO_2 NCs surface by producing water, which then desorbs [234]. New H_2 and O_2 molecules will adsorb on Pt and TiO_2 respectively. The pathway of chemical reactions is shown in equation 7.10 and 7.11.

$$H_2 + Pt \leftrightarrow Pt + 2H^+ + 2e^- \qquad (7.10)$$

$$4H^+ + O_2\,(ads) + TiO_2 + 4e^- \rightarrow TiO_2 + 2H_2O \qquad (7.11)$$

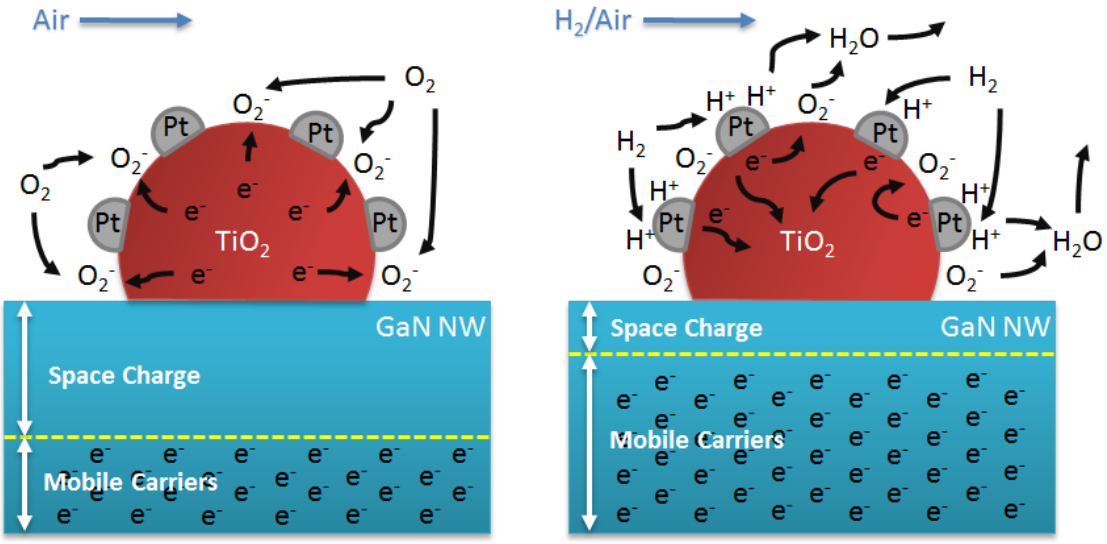

Fig. 7.10 H_2 sensing mechanism of GaN /TiO_2-Pt sensor in dark (without UV assistance)

7.4 Sensing Characteristics of the GaN / SnO_2 NWNC Sensors

The nanowire arrays were patterned and dry etched by inductive coupled plasma (ICP) chlorine etcher followed by KOH wet etching. SnO_2 NCs were deposited with magnetron sputter. NCs deposition recipes and sensor process flows were explained in detail in the former chapters.

The GaN / SnO_2 hybrid sensor shows high sensitivity and selectivity for NO_x, especially NO_2. The sensor was designed to work at room temperature with a UV assistant. It can sense NO_2 pollutants in breathing air at concentration lower than 100 ppm. The proposed hybrid sensor is both sensitive and exhibits a reversible response, higher sensitivity and shorter respond/recovery time than other reported sensors. By field emission scanning electron microscopy (FESEM) and atomic force microscopy (AFM) measurements, we were able to reveal the metal oxides surface morphology displayed in Chapter 4. Through X-ray diffraction (XRD) and X-ray photoelectron spectroscopy (XPS) we characterized the phase and composition of the material. The conductance measurements were applied to nanoclusters on a metal-dot-array pre-patterned substrate and I got further proof of the isolation property. As compared to the thin-film case, we believe the SnO_2 nanoclusters have larger surface area and larger numbers of surface adsorption sites. And so, with SnO_2-GaN heterojunction, the adsorption of NO_2 molecules enhances the effective channel modulation capability of the GaN nanowire.

The gas sensing performance of the fabricated sensor was investigated at room-temperature in a custom-built apparatus. A gaseous mixture of target analyte and breathing air was introduced into the sensing apparatus. Mass flow controllers independently tuned the flow rate of each mixing component, target analyte and carrier gases, determining the

final composition of the mixed gas. The sensors were biased with a constant 5 V supply and currents were measured by a National Instrument PCI DAQ system. A 355 nm light emitting diode provided the UV illumination to the sensor. A detailed description of the experimental set-up and conditions can be found in the former sections.

7.4.1 Current-Voltage (IV) Characteristics

IV measurements were performed from -5 V to 5 V with UV off and on. The IV curve of the GaN / SnO_2 hybrid sensors were linear and asymmetric due to the high quality ohmic contact formed, while the IV curve of the SiO_2 passivated control sensors was linear with relatively higher current for both UV on and off cases as shown in Fig. 7.11. The similar IV behavior observed for GaN / SnO_2-Pt sensors and passivation NWs. Surface adsorbed oxygen is a critical determinate in metal oxide reactivity and resistivity. Factors effecting the concentration of surface adsorbed oxygen on SnO_2 include the ambient atmosphere O_2 concentration and UV illumination. The oxygen adsorbed on SnO_2 NCs significantly affects the current conducted through the NW by depleting the electrons near the GaN surface and increase the depletion depth. Without UV illumination, the current increases up to 33% when the device exposure in oxygen free ambient (covered by SiO_2 passivation layer). Under UV illumination, a large amount electron-hole pairs are generated. Holes diffuse to surface and electrons remain in the core of the NW. An excess amount of hole carriers enhances the desorption rate of oxygen. Therefore, with UV exposure, current increases significantly due to photo generated electron-hole pairs. Because the oxygen adsorption effect is still operating, the passivated control NWs show 30% higher current than gas sensors. 5V of voltage bias was use for gas sensing measurement since the IV curve near 5 V is in a linear range.

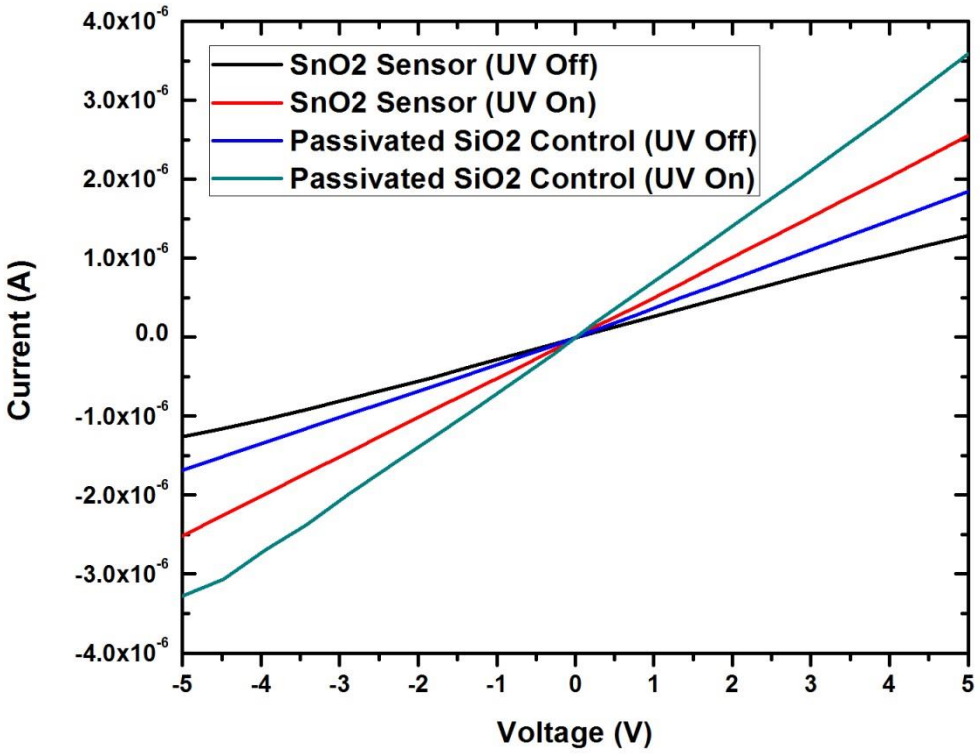

Fig. 7.11 IV characteristics of the active GaN / SnO_2 and control sensors

7.4.2 NO_x Sensing Performance of GaN / SnO_2 Sensors

With UV assistance, a constant voltage of 5 V was applied to the gas sensor and current was monitored. Fig. 7.12 shows the 500 ppm NO_2 sensing results of the GaN / SnO_2 sensor and the passivated control elements. The current decreased upon exposure to NO_2 for active sensors and the current remained in baseline for the control group. The sensitivity is 2.4% at 500 ppm of NO_2. The larger baseline current is due to the GaN NW surface being passivated from oxygen adsorption, as explained in last section. That means the exposure to NO_2 will increase the resistivity of gas sensor. Both results fit with the IV characterization. There is no sensing response without UV assistance. The adsorption of NO_2 molecules needs the photon energy and the oxidation is a UV catalysis process.

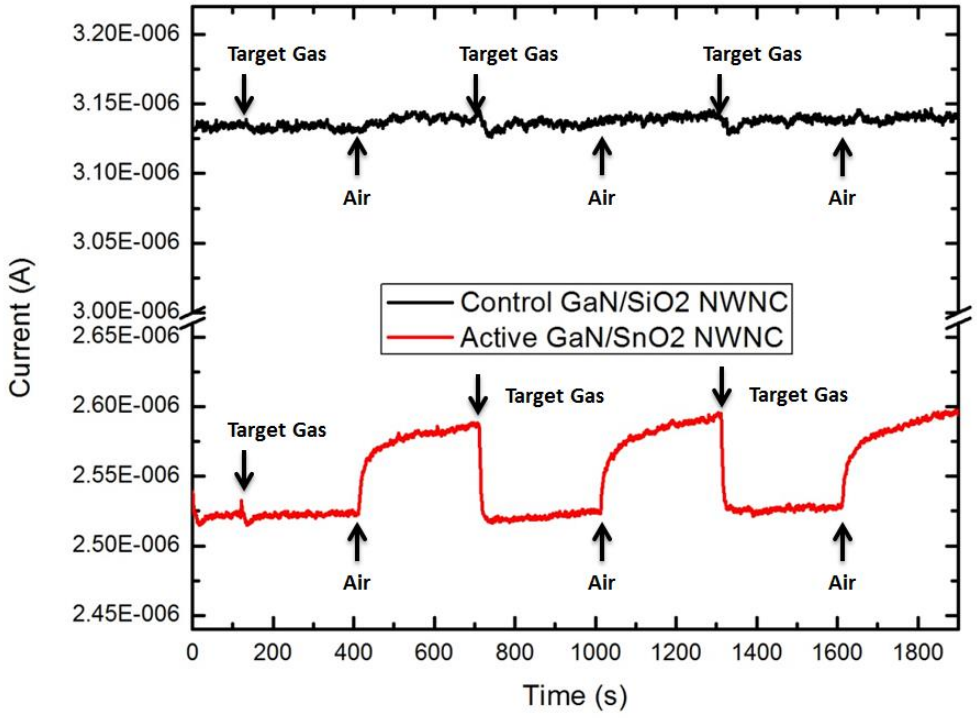

Fig. 7.12 NO_2 sensing of active sensor and passivated control elements

7.4.3 Selectivity of the GaN / SnO_2 Sensor

Response of the GaN / SnO_2 sensor in presence of other analytes or interfering compounds/molecules with hydrogen was tested with 5-minute-exposures to 500 ppm of CH_4, CO, CO_2, NH_3, NO_2 and NO as shown in Fig. 7.13. The UV photocurrent did not change after these exposures but NO_2 and NO, and the device continued to respond to NO_x without showing any interference. The high selectivity can be explained by SnO_2 NCs composition. Detail mechanisms will be discussed in next section.

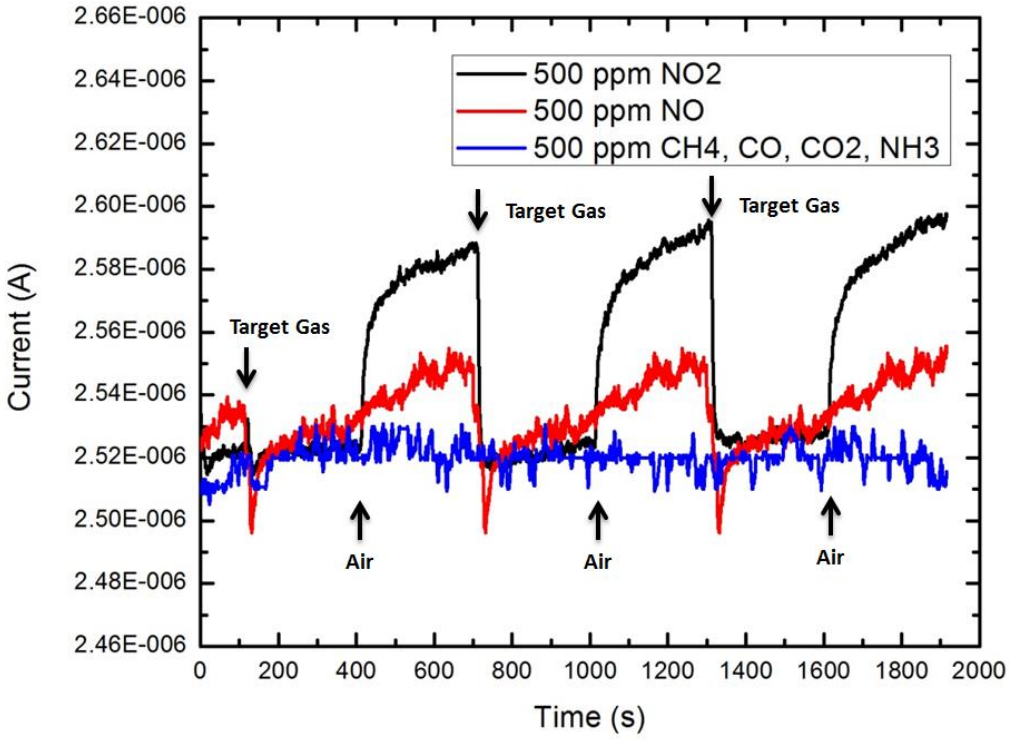

Fig. 7.13 Selectivity and gas sensor respond to multiple gases

7.4.4 NO_x Sensing Mechanism for the GaN / SnO_2 Sensor

The NO_x sensing mechanism in these hybrid sensors is complex and dependent on many factors including the formation of a semiconductor-semiconductor heterojunction, the analyte-NC interactions, NC adsorbates, and how these electronic interactions modulate the GaN NW current. The physical mechanism creating this conductivity change has remained ambiguous. Qualitative mechanisms are proposed aimed at elucidating the physical basis of these observations.

Consider a GaN nanowire of arbitrary length (10, 50, 100 or 200 μm). The width and height of this wire is fixed at 300 nm. When exposed to various gases (NO, NO_2, CO, CO_2, CH_4, NH_3, etc.), these wires by themselves exhibit little change in conductivity. However, when SnO_2 NCs or thin-film was sputter deposited on these wires, the wires exhibit larger response in conductivity when they were exposed to the same gases. In the paragraphs below, we outline some potential explanations of these observations.

Both SnO_2 and GaN are wide band-gap semiconductors with E_g greater than 3.4 eV. Due to intrinsic defect structure and oxygen deficiency, SnO_2 is n-type semiconductor with fairly conductivity and it is electron rich. The GaN wire is doped n-type by silicon addition and exhibits a mobile electron background of about 1E17/cm^3. There is a difference in electron affinities between the SnO_2 and the GaN material. The electron affinity of the SnO_2 is about 0.8 eV larger than that of GaN. Thus, the conduction band edge of the SnO_2 is lower than the conduction band edge of GaN by about 0.8 eV. As the SnO_2 is heavily doped and GaN is intentionally lighted doped, we assume that the Fermi levels of the two materials, when separate, are quite close to their respective conduction

band edges. We can assume that the Fermi level of both materials is similarly close to its conduction band edge.

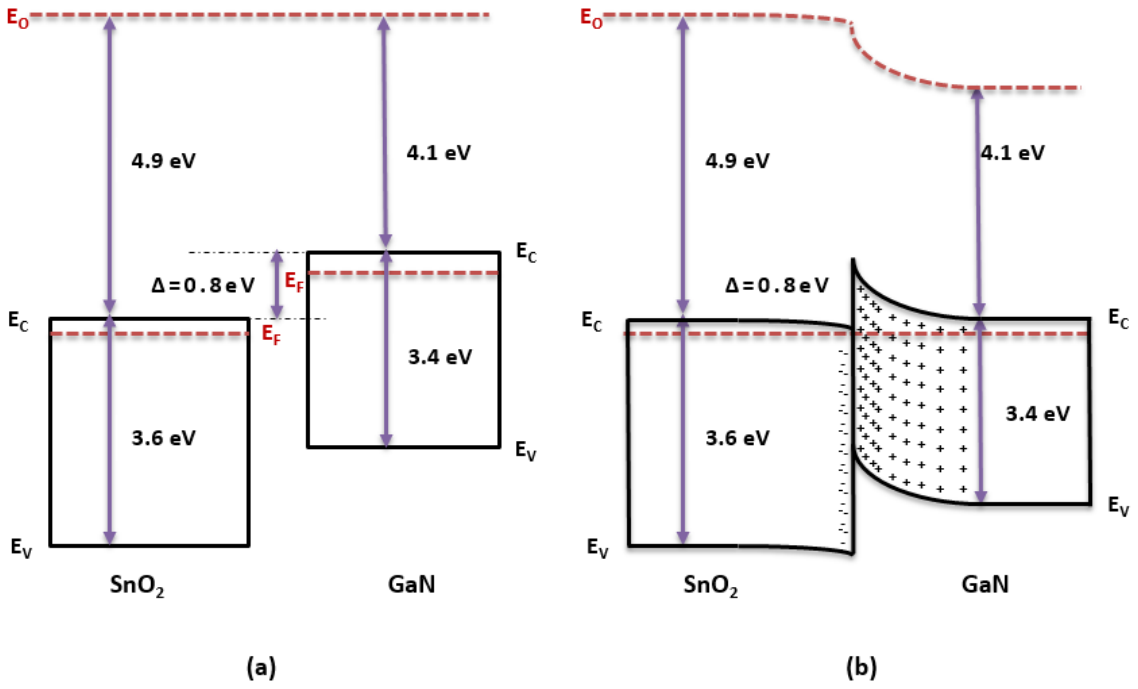

Fig. 7.14 The electronic structure of the SnO_2 / GaN system (a) before the materials are brought into contact (b) after the materials are bought into contact and a space charge layer formed

If the above assumptions hold, there can be a spill-over of mobile electron charge from the GaN into the SnO_2, leading to a thin depletion layer in the nitride. We now estimate that the Fermi level difference between the two materials is 0.8 eV, the SnO_2 is electron rich to the point that it cannot sustain a space charge and the whole space charge extends into the GaN. In that case we can estimate the depletion depth of extending into the nitride is about 90 nm. This thickness is determined by the background doping in the nitride (1E17 /cm ^{3}) and by the estimated a 0.8 volt Fermi level offset between the SnO_2

and the GaN. The depletion width is 89 nm and 93 nm for carrier concentration in SnO_2 is 1E19 /cm ^{3} and 1E18 /cm ^{3} respectively. The dielectric constant for GaN is reported in between 8.9 and 9.5, 8.9 is used in this space charge estimation [228]. While this leads to a significant area reduction of the conductive channel if consider a three-dimension nanowire that both top surface and sidewalls are covered by SnO_2 NCs. That explains why the SnO_2 decorated NW shown a 30% lower current than the SiO_2 passivated NWs in the IV characterization (Fig. 7.11). The band diagrams of two materials are shown in Fig. 7.14.

The large amount of photo-generated charges “photodope" the GaN NW and shrinks the depletion to a negligible thickness. As the UV incident flux is large (469 μW/cm ^{2}), the back-ground carrier concentration substantially increases, shrinking the space charge to a negligible thickness. The current boost was the result of both increased carrier concentration and widened transport channels.

With UV illumination, the number of carriers available for transport through the cross sectional area of the wire remains the same and is largely determined by the number of photo generated mobile carriers. All that changes is within a small space charge range near the SnO_2 / GaN interfaces. The closer the mobile charge comes to the SnO_2 / GaN interface, the more likely it will be scattered and the effective mobility of the charge will be reduced. This explains why in Fig. 7.12 and Fig. 7.13 sensing with UV illumination shows high noises. It is also possible that charged interface traps play some role. While the traps at the SnO_2 / GaN interface will not be affected directly by molecules attached to the SnO_2 NCs, the NCs charge can affect band bending and change the occupancy of interface traps. If the interface traps discharge, they will be less effective in creating scattering and mobility degradation. Or, if the traps become negatively charged, they will force the mobile

channel charge more deeply into the channel, away from the scattering interface. This will, in turn, increase conductivity. In any event, with UV illumination, the charge state of the SnO_2 NCs and of the SnO_2 / GaN interface will dominate in defining conduction. In summary, when the sensor were illuminated by UV, photo-doping leads to shrinkage of the space charge and allowing mobile charge to move closer to the SnO_2 / GaN interface. There, the carriers are strongly scattered, trapped and recombined before collection. This generates noise and lower sensitivity.

Without UV illumination, the curvature of the bands does push the mobile charge away from the scattering centers and from possible interface recombination sites, some interaction with the interface is expected.

In summary, if the sensor is exposed to high intensity UV radiation. Photo exciting both SnO_2 NCs and GaN NW, any chemical adsorption on the SnO_2 that leaves a statistic net positive charge on the NCs will pull the electrons in the GaN closer to the interface, generation noises, reducing space charge and increasing conductivity. Also, those carriers incident on the interface may be trapped and recombine before collection. Statistic negative charge on the NCs has the opposite effect. Mobile charge will be forced to the center of the wire, away from the scattering interface, reducing noises, which slightly increasing the space charge area, decreasing the current.

The space charge is much smaller under UV illumination comparing to the space charge in dark (90 nm). Therefore, the conduction channel width modulation under UV exposure is substantially smaller than in dark. If there were NO_2 response in dark, the sensitivity in dark should be higher than that under UV illumination.

So now we must turn to surface chemistry to address the issue of how NO_x / SnO_2 NCs interactions lead to statistic surface net charge and space charge modulation. As an n-type semiconductor, SnO_2 depletion width increases in the presence of electron trapping adsorbates, such as O_2. Table 7.4 lists the summary of how ambient oxygen concentration and the adsorption on SnO_2 NCs forms O_2^- affect the NW conductivity under UV illumination. When ambient O_2 concentration increases, the number of O_2 molecules adsorbed on NCs increases as well. The electrons were depleted by absorbed O_2, and formed O_2^-, which accumulating the statistic negative charge by increasing the electron carrier life-time. The net negative charge at the surface of SnO_2 depletes the GaN NW, pushes electrons to the core and decreases the conductive channel width. The conductivity will decrease as the result. Lower O_2 concentration has the opposite effect.

Mechanism of O_2 Adsorption on GaN / SnO_2 Sensor		
Ambient O_2 Concentration	↑	↓
Number of O_2 Adsorbed on SnO_2 NCs	↑	↓
Number of O_2^- on SnO_2 NCs Surface	↑	↓
Statistic Net Negative Charge	↑	↓
GaN Space Charge Width	↑	↓
GaN NW Conductivity	↓	↑

Table 7.4 Mechanism of surface adsorption of O_2 on SnO_2 NCs modulate the NW conductivity with UV assistance (under illumination)

The binding energy and net charge transfer of O_2, NO_2 and CO to SnO_2 surface sites were listed in Table 7.5 [235]. Upon exposure to NO_2, the sensor current significantly decreased implying a more negative charge accumulated on NCs surface and GaN NW space charge widths increased. First, introducing NO_2 will enhance the surface oxygen vacancy occupation therefore more electrons will transfer to the NO_2 and O_2. The accumulated negative charge increased the nitride space charge and push electron carriers away from SnO_2 / GaN interfaces. Less interface related electron trapping and scattering result in the low noise. The increased space charge width results in reduced conductivity. Gases other than NO_2 were tried and sensing responses were negligible and barely observed. The selectivity of sensor to NO_x can be explained by the binding energy of other gases is comparably low as CO shown in Table 7.5.

Gas Type	Binding Energy (kcal/mol)	Net Charge Transfer (el)
O_2	38.5	-0.88
NO_2	41.4	-0.51
CO	6.1	-0.10

Table 7.5 List of binding energy and net charge transfer

The pathway of a chemical reaction of NO oxidation to NO_2 in air at room temperature is shown in equation 7.11. The chemical reaction will be enhanced by UV illumination. Moreover, the SnO_2 under UV illumination generate electron-hole pairs. The electron rich layer was depleted by O_2 absorption on vacancy sites, forming an active

oxygen O_2^- species. The O_2^- species trap electron and increase their life-time. A statistic net negative charge is accumulated at the surface of SnO_2 NCs. Both NO and NO_2 can be actively oxidized by the active oxygen species as shown in equation 7.12 and 7.13, while the SnO_2 acts as a photo catalysis. When sensing with NO_2, only equation 7.13 applies. The adsorption of NO_2 will deplete more electrons from SnO_2 and enhance the negative charge at the surface of SnO_2, pushing electron carriers away from NW/NCs interfaces and decreasing the space charge, conductivity decreases slightly. When sensing with NO, all three equations (7.12 to 7.14) applies, but equation 7.13 and 7.14 are dominate and proceed with certain orders. The combined chemical reaction shown in equation 7.15 is believed the reaction is slow and needs multiple stages. The photo catalysis oxidation of NO_x was observed and reported in other type of wide band-gap metal-oxide materials [236, 237]. The dominating sensing mechanism is illustrated in Fig. 7.15. With UV illumination, large amount of electron-hole pairs were generated in both SnO_2 NCs and GaN NW. The sensor in the air ambient absorbs O_2 at the oxygen vacancy sites of SnO_2 NCs. The attached O_2 attracts electron carriers in SnO_2, and maintain a negative charge at the SnO_2 surface. The space charge layer at the SnO_2 / GaN interface increase but still maintain thin since the system is under UV illumination. Once NO_2 introduced into the system, this space charge depth further increase because more electrons got trapped, enhancing the net negative charge in statistic. The increased space charge depth pushed more mobile carriers far from the SnO_2 / GaN interfaces, further decreasing the conductivity.

$$2NO + O_2 \rightarrow 2NO_2 \qquad (7.12)$$

$$2NO\ (ads) + O_2^-\ (ads) \rightarrow 2NO_2\ (ads) + e^- \qquad \text{(on surface of } SnO_2 \text{ with UV)} \qquad (7.13)$$

$$2NO_2\ (ads) + O_2^-\ (ads) + e^- \rightarrow 2NO_3^-\ (ads) \qquad \text{(on surface of } SnO_2 \text{ with UV)} \qquad (7.14)$$

$$NO\ (ads) + O_2^-\ (ads) \rightarrow 2NO_3^-\ (ads) \qquad \text{(on surface of } SnO_2 \text{ with UV)} \qquad (7.15)$$

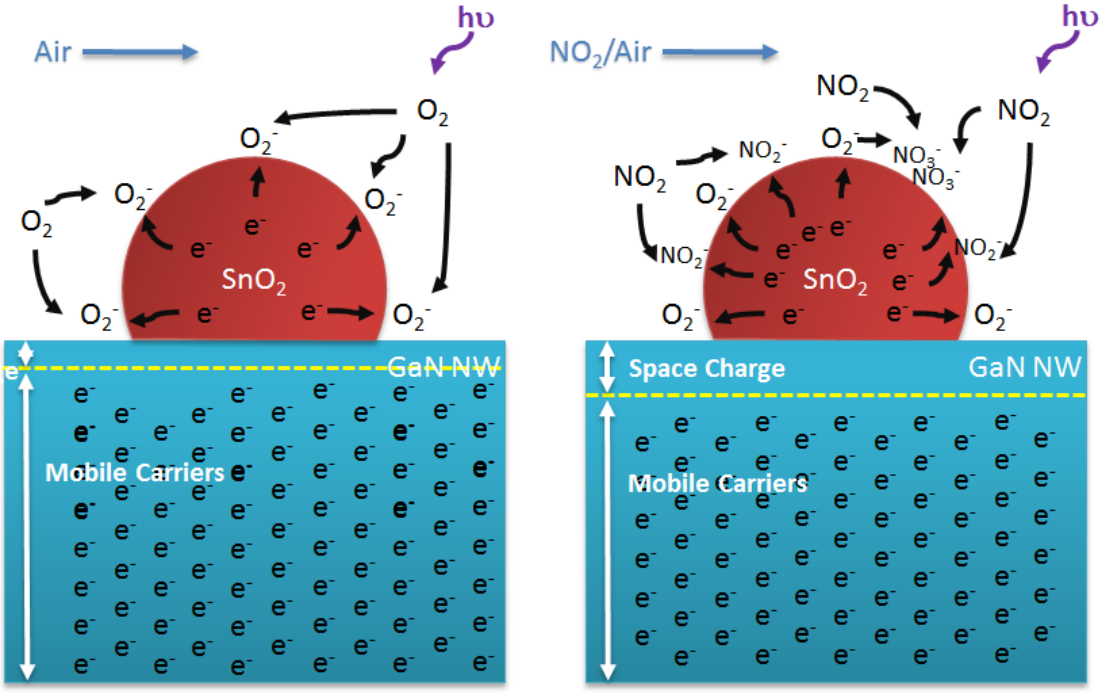

Fig. 7.15 NO_2 sensing mechanism of GaN /SnO_2 sensor in photon illumination (with UV assistance)

7.5 Chapter Conclusion

This chapter describes the gas sensing measurement set-up and summarizes the performance of the different gas sensors developed in this thesis. The set-up, including bubbler, pressure controller, gas mixing chamber and digital mass flow controllers (MFC) has been reviewed in depth. This chapter also explains the mechanism of sensing response based on the current literature and on the observed trend of the devices fabricated in this work. Sensing performance details of the nanowire-nanocluster (NWNC) gas sensors were tabulated and discussed here.

Sensing results for TiO_2-Pt NCs / GaN NW sensor were highlighted. It was discussed in detail to reveal the sensing mechanisms of the NWNC hybrid sensor. SnO_2 NCs / GaN NW were studied for NO_x sensing and the mechanisms were proposed. Other nanoclusters alternatives and sensors, TiO_2-Pd NCs / GaN NW will be explored.

Chapter 8: Conclusions and Future Work

7.1 Conclusions

For the first time, this thesis demonstrated a highly integrated top-down gallium nitride (GaN) nanowires (NWs) fabrication process. The NWs were functionalized with titanium dioxide, platinum-titanium dioxide composites, tin dioxide, iron oxide and tungsten trioxide. The results for these fabrication processes were presented. The goal was to design for reliable wafer production and to achieve homogenous device performance. NWNC hybrid gas sensors were investigated, optimized and developed to selectively detect hydrogen, nitride dioxide, aromatic compounds, and ammonia at room temperature. We integrated these sensors with a micro heater that using low cost metals deposition method and wet chemical process techniques for assistance in chemical release cycles. The micro heater can be used in medical drug inhalation and aerosol generation purposes as well. I summarize the efforts performed in completion of this thesis:

8. I demonstrated a dry etched "top-down" fabricated structure showing features aligned in a horizontal plane parallel to the wafer surface, as shown in figures on the left side of Table 1.2. Previous technique use molecular beam epitaxy (MBE) to grow nanowires vertical up (perpendicular to) the wafer surface. Placement of these vertical structures is rather random across the surface, as shown in images on the right side of Table 1.2, These features must be released from the surface, and subsequently placed on another substrate (either individually or in bundles by dielectrophoresis.) Dielectrophoresis is an electromagnetic wave NW alignment

technology that applies a RF voltage bias on the sides of solution through electrodes. The solution has NWs dispersed in it. The "top-down" dry etching method developed here uses the stepper/scanner lithography system to define the nanowire patterns, followed by inductively coupled plasma (ICP) dry etch. By this method, the NWs are identical in arrays and sensor fabrication can be easily integrated and mass produced.

9. I developed methods for removing sidewall defects and roughness caused by ion bombardment during dry etching. The potassium hydroxide (KOH) and phosphoric acid (H_3PO_4) wet etch can remove the defects appearing as linear vertical texture along the NW sidewalls that inhibited previous attempts at creating dry etched NWs from succeeding.

10. I demonstrated a nanocluster formation method and I designed a fast characterization method using IV conductance measurement and ellipsometry techniques besides SEM imaging. Further optimization of titanium dioxide, tin dioxide, iron oxide, tungsten trioxide NCs was accomplished. Previous work on NCs rely on chemical formation of powders, the NCs formation method in this thesis used physical vapor deposition (PVD) followed by rapid thermal annealing (RTA) which can be fully integrated with modern CMOS processes. This PVD-RTA method has advantages in NCs coating uniformity and compatibility to dynamic structures as the comparison shown in Table 1.3. The characterization technique is fast, reliable and non-destructive compared to SEM imaging.

11. I did the design of experiments leading to the establishment of a gas sensing database starting with TiO_2, SnO_2, WO_3, Fe_2O_3, TiO_2-Pt, etc. Metal-oxide thin-film

sensors were fabricated and tested by being exposed to various target gases. Responsive and non-responsive materials were determined and were recorded in a database.

12. I developed an electroless nickel plating process to create thick Ni layers from a seed layer. This technique allows precise control of the final thickness of a film far thicker than would be allowed by lift-off. Moreover, the chemical solution bath is much lower cost comparing to high-vacuum equipment. This method was used in the micro-heater process that can be integrated with gas sensor and provide heat to augment the chemical release cycle. The inexpensive and easily fabricated micro-heater thus developed allows for easy mass productions. This heater can be used in aerosol generators and fabricated as a single device for drug inhalation therapy.

13. I developed a process integration scheme for including all three micro- and nano-structures into a single NWNC hybrid sensor device. Integration considerations including the process flows, RTA, multiple passivation layers, NW yield improvement, active opening windows, passivated control elements and ohmic contact improvement were studied in detail. The techniques for multiple sensors integration into a single sensor chip were first time reported. These enables the simultaneously multiple gas sensing capability of a single sensor chip. I developed a process integration methods for including multiple gas sensors in a single chip for simultaneously sensing of variety of gases.

14. I characterized the fully integrated nanowire-nanocluster hybrid gas sensor and micro-heater system. Most of the sensor units work at room temperature without the need of heating assistance which ensures low power consumption. The sensor's

fast response and recovery behavior maintained after many sensing cycles. This implies that the developed technology has several advantages like low power consumption, long life time reliability, high sensitivity and selectivity in sensing performance. The micro-heater allows for improved gas desorption and the use of high temperature sensors.

The NWNC gas sensor fabricated can achieve high selectivity and sensitivity. Integrated MH helps improve the reliability and the life-time of the sensor and assists desorption of absorbed chemicals. Table 1.4 lists the performance of GaN / TiO_2-Pt NWNC hydrogen sensor technology comparing to other novel hydrogen gas sensing devices currently under developing. The significant features and advantages of the integrated sensors are:

vii. Room temperature sensing as well as high temperature thermal sensing is possible.

viii. Selective sensing of low gas concentrations.

ix. Reliable and repeatable sensing and an ability to recover back to the same baseline signal level as opposed to baseline drift and limited lifetime.

x. Fast respond and short recovery time.

xi. Capable of cheap mass production and integration with existing CMOS processes, as opposed to the individual nanowire pick-and-place fabrication. This improves throughput, reproducibility and yield.

xii. The MH utilizes a low cost micro fabrication process to achieve fast respond and a robust heating function. The MH can be integrated into sensor devices for gas sensing assistance as well as individually used in aerosol generation and medical inhalation applications.

7.2 Applications

The NWNC gas sensors can be used for:

- Indoor Environmental Monitoring: some specific places such as laboratories, hospitals, schools, and in the home (sensing natural gas leaks or CO). The indoor air quality will directly affect the people inside.
- Industrial Monitoring: many manufactory works generates waste gases or have potential leakage of gases can be first time detected. This can also installed on petroleum transmission pipeline and nature gas pipeline to real time monitoring leakages, spills or thefts.
- Hazard Detection and Avoidance: Security check at airport, train station, embassies can use the explosive compound sensor to improve screening efficiency and accuracy.
- Defense: Instead of heat detection and infrared decoy projectile, explosive detection can be used to missile tracking that increase the target accuracy and hit rate by sensing larger volume of explosive compounds.

The NCs deposition method, besides decorating gas sensor NWs, it can be used to deposit high quality thin-film for photodetector, photodiode, solar cell, etc.

The MH, besides assistant gas sensors, it can be used low cost aerosol generation applications such as nasal inhale drug delivery and disposable e-cigarette puff generation refills.

7.3 Future Work

There is a scope for improvement in some of the performance of the sensor devices presented in this work. At the same time, the database for gas sensing presented in this work need to be further investigated and verified. Important aspects to be considered in the future work on these sensor devices include:

• Room temperature operation of sensors requires greater attention to operation under humidity. Although some measurements for the response of the sensor towards water have been performed, a more reasonable study will be to do measurements under different humidity conditions.

• Though extensive studies have been performed indicating the selectivity of the sensor technology, it should be validated by performing exhaustive analysis in a mixture of possible interfering compounds.

• Effect of UV light intensity on the sensitivity of the alcohol sensors needs to be investigated for a broader intensity range. The current set up limited the maximum intensity to 469 μW/cm^2. In the given range, the sensitivity increases with increasing intensity. However the optimal intensity needs to be evaluated as the sensor response is likely to saturate or decrease if the intensity is increased beyond the optimal value.

• Investigation of the effect of oxide quality on sensing behavior could be a useful study to perform. Oxygen deficient vs. oxygen rich oxide, dense vs. sparse deposition of

oxide nanoparticles could be important control parameters for the sensor response characteristics.

Chapter 9: Bibliography

[1] T. C. Pearce, S. S. Schiffman, H. T. Nagle, and J. W. Gardner, *Handbook of machine olfaction: electronic nose technology*: John Wiley & Sons, 2006.

[2] J. Watson and K. Ihokura, "Gas-sensing materials," *MRS Bulletin*, vol. 24, pp. 14-17, 1999.

[3] L. A. Pinnaduwage, H.-F. Ji, and T. Thundat, "Moore's law in homeland defense: an integrated sensor platform based on silicon microcantilevers," *Sensors Journal, IEEE*, vol. 5, pp. 774-785, 2005.

[4] Y. Shimizu and M. Egashira, "Basic aspects and challenges of semiconductor gas sensors," *Mrs Bulletin*, vol. 24, pp. 18-24, 1999.

[5] I. A. Casalinuovo, D. Di Pierro, M. Coletta, and P. Di Francesco, "Application of electronic noses for disease diagnosis and food spoilage detection," *Sensors*, vol. 6, pp. 1428-1439, 2006.

[6] K. Arshak, E. Moore, G. Lyons, J. Harris, and S. Clifford, "A review of gas sensors employed in electronic nose applications," *Sensor review*, vol. 24, pp. 181-198, 2004.

[7] J. Watson, "The tin oxide gas sensor and its applications," *Sensors and Actuators*, vol. 5, pp. 29-42, 1984.

[8] S. R. Morrison, "Selectivity in semiconductor gas sensors," *Sensors and actuators*, vol. 12, pp. 425-440, 1987.

[9] D. Dabill, S. Gentry, and P. Walsh, "A fast-response catalytic sensor for flammable gases," *Sensors and actuators*, vol. 11, pp. 135-143, 1987.

[10] A. A. Poli, "Combustible gas detector having catalytic sensor stabilizing network," ed: Google Patents, 1989.

[11] E. Jones, "The pellistor catalytic gas detector," *Techniques and mechanism in gas sensing*, pp. 17-31, 1987.

[12] P. Moseley, "Solid state gas sensors," *Measurement Science and technology*, vol. 8, pp. 223-237, 1997.

[13] E. Bakker, "Electrochemical sensors," *Analytical chemistry*, vol. 76, pp. 3285-3298, 2004.

[14] E. Bakker and Y. Qin, "Electrochemical sensors," *Analytical Chemistry*, vol. 78, pp. 3965-3984, 2006.

[15] E. Bakker and M. Telting-Diaz, "Electrochemical sensors," *Analytical Chemistry*, vol. 74, pp. 2781-2800, 2002.

[16] D. Richter, D. Lancaster, R. Curl, W. Neu, and F. Tittel, "Compact mid-infrared trace gas sensor based on difference-frequency generation of two diode lasers in

periodically poled LiNbO3," *Applied Physics B: Lasers and Optics*, vol. 67, pp. 347-350, 1998.
[17] S. Lenaerts, J. Roggen, and G. Maes, "FT-IR characterization of tin dioxide gas sensor materials under working conditions," *Spectrochimica Acta Part A: Molecular and Biomolecular Spectroscopy*, vol. 51, pp. 883-894, 1995.
[18] B. Mizaikoff, R. Göbel, R. Krska, K. Taga, R. Kellner, M. Tacke, *et al.*, "Infrared fiber-optical chemical sensors with reactive surface coatings," *Sensors and Actuators B: Chemical*, vol. 29, pp. 58-63, 1995.
[19] J. N. Driscoll, "Evaluation of a new photoionization detector for organic compounds," *Journal of Chromatography A*, vol. 134, pp. 49-55, 1977.
[20] J. Lovelock, "A photoionization detector for gases and vapours," 1960.
[21] G. Sberveglieri, "Recent developments in semiconducting thin-film gas sensors," *Sensors and Actuators B: Chemical*, vol. 23, pp. 103-109, 1995.
[22] H. Meixner, J. Gerblinger, U. Lampe, and M. Fleischer, "Thin-film gas sensors based on semiconducting metal oxides," *Sensors and Actuators B: Chemical*, vol. 23, pp. 119-125, 1995.
[23] S. Capone, A. Forleo, L. Francioso, R. Rella, P. Siciliano, J. Spadavecchia, *et al.*, "Solid state gas sensors: state of the art and future activities," *Journal of Optoelectronics and Advanced Materials*, vol. 5, pp. 1335-1348, 2003.
[24] G. Eranna, B. Joshi, D. Runthala, and R. Gupta, "Oxide materials for development of integrated gas sensors—a comprehensive review," *Critical Reviews in Solid State and Materials Sciences*, vol. 29, pp. 111-188, 2004.
[25] D. James, S. M. Scott, Z. Ali, and W. T. O'hare, "Chemical sensors for electronic nose systems," *Microchimica Acta*, vol. 149, pp. 1-17, 2005.
[26] I. Eisele, T. Doll, and M. Burgmair, "Low power gas detection with FET sensors," *Sensors and Actuators B: Chemical*, vol. 78, pp. 19-25, 2001.
[27] J. Covington, J. Gardner, D. Briand, and N. De Rooij, "A polymer gate FET sensor array for detecting organic vapours," *Sensors and Actuators B: Chemical*, vol. 77, pp. 155-162, 2001.
[28] D. Zhang, Z. Liu, C. Li, T. Tang, X. Liu, S. Han, *et al.*, "Detection of NO2 down to ppb levels using individual and multiple In2O3 nanowire devices," *Nano letters*, vol. 4, pp. 1919-1924, 2004.
[29] P. V. Kamat, "Photophysical, photochemical and photocatalytic aspects of metal nanoparticles," *The Journal of Physical Chemistry B*, vol. 106, pp. 7729-7744, 2002.
[30] Y. Cui and C. M. Lieber, "Functional nanoscale electronic devices assembled using silicon nanowire building blocks," *Science*, vol. 291, pp. 851-853, 2001.
[31] K. J. Choi and H. W. Jang, "One-dimensional oxide nanostructures as gas-sensing materials: review and issues," *Sensors*, vol. 10, pp. 4083-4099, 2010.
[32] U. Yogeswaran and S.-M. Chen, "A review on the electrochemical sensors and biosensors composed of nanowires as sensing material," *Sensors*, vol. 8, pp. 290-313, 2008.
[33] G.-S. Chung, "Fabrication and characterization of micro-heaters with low-power consumption using SOI membrane and trench structures," *Sensors and Actuators A: Physical*, vol. 112, pp. 55-60, 2004.

[34] Y. Mo, Y. Okawa, K. Inoue, and K. Natukawa, "Low-voltage and low-power optimization of micro-heater and its on-chip drive circuitry for gas sensor array," *Sensors and Actuators A: Physical,* vol. 100, pp. 94-101, 2002.
[35] M. Casaletto, S. Kaciulis, G. Mattogno, L. Pandolfi, G. Scavia, L. Dori, *et al.*, "Surface study of thin film gas sensors on a Si micro-machined substrate," *Applied surface science,* vol. 189, pp. 39-52, 2002.
[36] U. Hoefer, G. Kühner, W. Schweizer, G. Sulz, and K. Steiner, "CO and CO 2 thin-film SnO 2 gas sensors on Si substrates," *Sensors and Actuators B: Chemical,* vol. 22, pp. 115-119, 1994.
[37] U. Dibbern, "A substrate for thin-film gas sensors in microelectronic technology," *Sensors and Actuators B: Chemical,* vol. 2, pp. 63-70, 1990.
[38] Y. Mo, Y. Okawa, M. Tajima, T. Nakai, N. Yoshiike, and K. Natukawa, "Micro-machined gas sensor array based on metal film micro-heater," *Sensors and Actuators B: Chemical,* vol. 79, pp. 175-181, 2001.
[39] M. Aslam, C. Gregory, and J. Hatfield, "Polyimide membrane for micro-heated gas sensor array," *Sensors and Actuators B: Chemical,* vol. 103, pp. 153-157, 2004.
[40] J. Gardner, A. Pike, N. De Rooij, M. Koudelka-Hep, P. Clerc, A. Hierlemann, *et al.*, "Integrated array sensor for detecting organic solvents," *Sensors and Actuators B: Chemical,* vol. 26, pp. 135-139, 1995.
[41] C.-L. Dai, M.-C. Liu, F.-S. Chen, C.-C. Wu, and M.-W. Chang, "A nanowire WO 3 humidity sensor integrated with micro-heater and inverting amplifier circuit on chip manufactured using CMOS-MEMS technique," *Sensors and Actuators B: Chemical,* vol. 123, pp. 896-901, 2007.
[42] C.-L. Dai, "A capacitive humidity sensor integrated with micro heater and ring oscillator circuit fabricated by CMOS–MEMS technique," *Sensors and Actuators B: Chemical,* vol. 122, pp. 375-380, 2007.
[43] W. Y. Sim, H. J. Yoon, O. C. Jeong, and S. S. Yang, "A phase-change type micropump with aluminum flap valves," *Journal of Micromechanics and Microengineering,* vol. 13, p. 286, 2003.
[44] G. Liu, D. A. Lowy, A. Kahrim, C. Wang, Z. Dilli, N. Kratzmeier, *et al.*, "A Low Cost Micro-Heater for Aerosol Generation Applications," *Microelectronic Engineering,* vol. 129, pp. 46-52, 2014.
[45] A. R. Bhashyam, M. T. Wolf, A. L. Marcinkowski, A. Saville, K. Thomas, J. A. Carcillo, *et al.*, "Aerosol delivery through nasal cannulas: an in vitro study," *Journal of aerosol medicine and pulmonary drug delivery,* vol. 21, pp. 181-188, 2008.
[46] P. W. Longest, B. M. Spence, L. T. Holbrook, K. M. Mossi, Y.-J. Son, and M. Hindle, "Production of inhalable submicrometer aerosols from conventional mesh nebulizers for improved respiratory drug delivery," *Journal of aerosol science,* vol. 51, pp. 66-80, 2012.
[47] M. Peckerar, Z. Dilli, M. Dornajafi, N. Goldsman, Y. Ngu, R. B. Proctor, *et al.*, "A novel high energy density flexible galvanic cell," *Energy & Environmental Science,* vol. 4, pp. 1807-1812, 2011.
[48] M. Peckerar, M. Dornajafi, Z. Dilli, N. Goldsman, Y. Ngu, B. Boerger, *et al.*, "Fabrication of flexible ultracapacitor/galvanic cell hybrids using advanced

nanoparticle coating technology," *Journal of Vacuum Science & Technology B,* vol. 29, p. 011008, 2011.
[49] M. Parameswaran, A. M. Robinson, D. L. Blackburn, M. Gaitan, and J. Geist, "Micromachined thermal radiation emitter from a commercial CMOS process," *Electron Device Letters, IEEE,* vol. 12, pp. 57-59, 1991.
[50] E. Yoon and K. D. Wise, "An integrated mass flow sensor with on-chip CMOS interface circuitry," *Electron Devices, IEEE Transactions on,* vol. 39, pp. 1376-1386, 1992.
[51] J.-s. Han, Z.-y. Tan, K. Sato, and M. Shikida, "Thermal characterization of micro heater arrays on a polyimide film substrate for fingerprint sensing applications," *Journal of Micromechanics and Microengineering,* vol. 15, p. 282, 2005.
[52] G. Liu, B. Wen, T. Xie, A. Castillo, J.-Y. Ha, N. Sullivan, *et al.,* "Top–down fabrication of horizontally-aligned gallium nitride nanowire arrays for sensor development," *Microelectronic Engineering,* vol. 142, pp. 58-63, 2015.
[53] D. Paramanik, A. Motayed, G. S. Aluri, J.-Y. Ha, S. Krylyuk, A. V. Davydov, *et al.,* "Formation of large-area GaN nanostructures with controlled geometry and morphology using top-down fabrication scheme," *Journal of Vacuum Science & Technology B,* vol. 30, p. 052202, 2012.
[54] R. Bajpai, A. Motayed, A. V. Davydov, V. P. Oleshko, G. S. Aluri, K. A. Bertness, *et al.,* "UV-assisted alcohol sensing using SnO 2 functionalized GaN nanowire devices," *Sensors and Actuators B: Chemical,* vol. 171, pp. 499-507, 2012.
[55] G. S. Aluri, A. Motayed, A. V. Davydov, V. P. Oleshko, K. A. Bertness, N. A. Sanford, *et al.,* "Highly selective GaN-nanowire/TiO2-nanocluster hybrid sensors for detection of benzene and related environment pollutants," *Nanotechnology,* vol. 22, p. 295503, 2011.
[56] G. S. Aluri, A. Motayed, A. V. Davydov, V. P. Oleshko, K. A. Bertness, N. A. Sanford, *et al.,* "Methanol, ethanol and hydrogen sensing using metal oxide and metal (TiO2–Pt) composite nanoclusters on GaN nanowires: a new route towards tailoring the selectivity of nanowire/nanocluster chemical sensors," *Nanotechnology,* vol. 23, p. 175501, 2012.
[57] Z. Wu, M. G. Hahm, Y. J. Jung, and L. Menon, "Epitaxially grown GaN nanowire networks," *Journal of Materials Chemistry,* vol. 19, pp. 463-467, 2009.
[58] K. Bertness, A. Roshko, L. Mansfield, T. Harvey, and N. Sanford, "Mechanism for spontaneous growth of GaN nanowires with molecular beam epitaxy," *Journal of Crystal Growth,* vol. 310, pp. 3154-3158, 2008.
[59] S. Fardindoost, F. Rahimi, and R. Ghasempour, "Pd doped WO 3 films prepared by sol–gel process for hydrogen sensing," *International Journal of Hydrogen Energy,* vol. 35, pp. 854-860, 2010.
[60] L. F. Zhu, J. C. She, J. Y. Luo, S. Z. Deng, J. Chen, and N. S. Xu, "Study of physical and chemical processes of H2 sensing of Pt-coated WO3 nanowire films," *The Journal of Physical Chemistry C,* vol. 114, pp. 15504-15509, 2010.
[61] C. Zhang, A. Boudiba, C. Navio, C. Bittencourt, M.-G. Olivier, R. Snyders, *et al.,* "Highly sensitive hydrogen sensors based on co-sputtered platinum-activated tungsten oxide films," *international journal of hydrogen energy,* vol. 36, pp. 1107-1114, 2011.

[62] J. Wright, W. Lim, D. Norton, S. Pearton, F. Ren, J. L. Johnson, *et al.*, "Nitride and oxide semiconductor nanostructured hydrogen gas sensors," *Semiconductor Science and Technology,* vol. 25, p. 024002, 2010.
[63] S. N. Das, J. P. Kar, J.-H. Choi, T. I. Lee, K.-J. Moon, and J.-M. Myoung, "Fabrication and characterization of ZnO single nanowire-based hydrogen sensor," *The Journal of Physical Chemistry C,* vol. 114, pp. 1689-1693, 2010.
[64] E. Şennik, Z. Colak, N. Kılınç, and Z. Z. Öztürk, "Synthesis of highly-ordered TiO 2 nanotubes for a hydrogen sensor," *International Journal of Hydrogen Energy,* vol. 35, pp. 4420-4427, 2010.
[65] X. Zeng, M. Latimer, Z. Xiao, S. Panuganti, U. Welp, W. Kwok, *et al.*, "Hydrogen gas sensing with networks of ultrasmall palladium nanowires formed on filtration membranes," *Nano letters,* vol. 11, pp. 262-268, 2010.
[66] M. G. Chung, D.-H. Kim, D. K. Seo, T. Kim, H. U. Im, H. M. Lee, *et al.*, "Flexible hydrogen sensors using graphene with palladium nanoparticle decoration," *Sensors and Actuators B: Chemical,* vol. 169, pp. 387-392, 2012.
[67] Z. Wang, Z. Li, T. Jiang, X. Xu, and C. Wang, "Ultrasensitive hydrogen sensor based on Pd0-loaded SnO2 electrospun nanofibers at room temperature," *ACS applied materials & interfaces,* vol. 5, pp. 2013-2021, 2013.
[68] K. Skucha, Z. Fan, K. Jeon, A. Javey, and B. Boser, "Palladium/silicon nanowire Schottky barrier-based hydrogen sensors," *Sensors and Actuators B: Chemical,* vol. 145, pp. 232-238, 2010.
[69] G. Timp, "Nanotechnology, 1999," ed: Springer, New York.
[70] A. Mnyusiwalla, A. S. Daar, and P. A. Singer, "'Mind the gap': science and ethics in nanotechnology," *Nanotechnology,* vol. 14, p. R9, 2003.
[71] C. P. Poole Jr and F. J. Owens, *Introduction to nanotechnology*: John Wiley & Sons, 2003.
[72] B. Bhushan, *Springer handbook of nanotechnology*: Springer Science & Business Media, 2010.
[73] G. Skandan, A. Singhal, C. Contescu, and K. Putyera, *Dekker encyclopedia of nanoscience and nanotechnology*: Taylor & Francis, 2009.
[74] R. C. Merkle, "Computational nanotechnology," *Nanotechnology,* vol. 2, p. 134, 1991.
[75] H. Kind, H. Yan, B. Messer, M. Law, and P. Yang, "Nanowire ultraviolet photodetectors and optical switches," *Advanced materials,* vol. 14, p. 158, 2002.
[76] Y. Li, G. Meng, L. Zhang, and F. Phillipp, "Ordered semiconductor ZnO nanowire arrays and their photoluminescence properties," *Applied Physics Letters,* vol. 76, pp. 2011-2013, 2000.
[77] C. Soci, A. Zhang, B. Xiang, S. A. Dayeh, D. Aplin, J. Park, *et al.*, "ZnO nanowire UV photodetectors with high internal gain," *Nano letters,* vol. 7, pp. 1003-1009, 2007.
[78] M. S. Gudiksen, L. J. Lauhon, J. Wang, D. C. Smith, and C. M. Lieber, "Growth of nanowire superlattice structures for nanoscale photonics and electronics," *Nature,* vol. 415, pp. 617-620, 2002.
[79] E. Garnett and P. Yang, "Light trapping in silicon nanowire solar cells," *Nano letters,* vol. 10, pp. 1082-1087, 2010.

[80] Y. Li, F. Qian, J. Xiang, and C. M. Lieber, "Nanowire electronic and optoelectronic devices," *Materials today,* vol. 9, pp. 18-27, 2006.
[81] M. H. Huang, S. Mao, H. Feick, H. Yan, Y. Wu, H. Kind, *et al.*, "Room-temperature ultraviolet nanowire nanolasers," *science,* vol. 292, pp. 1897-1899, 2001.
[82] X. Duan, Y. Huang, R. Agarwal, and C. M. Lieber, "Single-nanowire electrically driven lasers," *Nature,* vol. 421, pp. 241-245, 2003.
[83] J. C. Johnson, H.-J. Choi, K. P. Knutsen, R. D. Schaller, P. Yang, and R. J. Saykally, "Single gallium nitride nanowire lasers," *Nature materials,* vol. 1, pp. 106-110, 2002.
[84] Y. Cui, Q. Wei, H. Park, and C. M. Lieber, "Nanowire nanosensors for highly sensitive and selective detection of biological and chemical species," *Science,* vol. 293, pp. 1289-1292, 2001.
[85] G. Zheng, F. Patolsky, Y. Cui, W. U. Wang, and C. M. Lieber, "Multiplexed electrical detection of cancer markers with nanowire sensor arrays," *Nature biotechnology,* vol. 23, pp. 1294-1301, 2005.
[86] J.-i. Hahm and C. M. Lieber, "Direct ultrasensitive electrical detection of DNA and DNA sequence variations using nanowire nanosensors," *Nano letters,* vol. 4, pp. 51-54, 2004.
[87] Q. Wan, Q. Li, Y. Chen, T.-H. Wang, X. He, J. Li, *et al.*, "Fabrication and ethanol sensing characteristics of ZnO nanowire gas sensors," *Applied Physics Letters,* vol. 84, pp. 3654-3656, 2004.
[88] A. Kolmakov, Y. Zhang, G. Cheng, and M. Moskovits, "Detection of CO and O2 using tin oxide nanowire sensors," *Advanced Materials,* vol. 15, pp. 997-1000, 2003.
[89] Z. Fan, D. Wang, P.-C. Chang, W.-Y. Tseng, and J. G. Lu, "ZnO nanowire field-effect transistor and oxygen sensing property," *Applied Physics Letters,* vol. 85, pp. 5923-5925, 2004.
[90] M. Law, L. E. Greene, J. C. Johnson, R. Saykally, and P. Yang, "Nanowire dye-sensitized solar cells," *Nature materials,* vol. 4, pp. 455-459, 2005.
[91] J. B. Baxter and E. S. Aydil, "Nanowire-based dye-sensitized solar cells," *Applied Physics Letters,* vol. 86, p. 053114, 2005.
[92] L. Tsakalakos, J. Balch, J. Fronheiser, B. Korevaar, O. Sulima, and J. Rand, "Silicon nanowire solar cells," *Applied Physics Letters,* vol. 91, p. 233117, 2007.
[93] E. C. Garnett and P. Yang, "Silicon nanowire radial p− n junction solar cells," *Journal of the American Chemical Society,* vol. 130, pp. 9224-9225, 2008.
[94] P. G. Collins, K. Bradley, M. Ishigami, and A. Zettl, "Extreme oxygen sensitivity of electronic properties of carbon nanotubes," *science,* vol. 287, pp. 1801-1804, 2000.
[95] A. Star, J.-C. P. Gabriel, K. Bradley, and G. Grüner, "Electronic detection of specific protein binding using nanotube FET devices," *Nano Letters,* vol. 3, pp. 459-463, 2003.
[96] O. Varghese, P. Kichambre, D. Gong, K. Ong, E. Dickey, and C. Grimes, "Gas sensing characteristics of multi-wall carbon nanotubes," *Sensors and Actuators B: Chemical,* vol. 81, pp. 32-41, 2001.

[97] G. Shen, P.-C. Chen, K. Ryu, and C. Zhou, "Devices and chemical sensing applications of metal oxide nanowires," *Journal of Materials Chemistry,* vol. 19, pp. 828-839, 2009.
[98] C. A. Mirkin, R. L. Letsinger, R. C. Mucic, and J. J. Storhoff, "A DNA-based method for rationally assembling nanoparticles into macroscopic materials," *Nature,* vol. 382, pp. 607-609, 1996.
[99] M.-C. Daniel and D. Astruc, "Gold nanoparticles: assembly, supramolecular chemistry, quantum-size-related properties, and applications toward biology, catalysis, and nanotechnology," *Chemical reviews,* vol. 104, pp. 293-346, 2004.
[100] I. Sondi and B. Salopek-Sondi, "Silver nanoparticles as antimicrobial agent: a case study on E. coli as a model for Gram-negative bacteria," *Journal of colloid and interface science,* vol. 275, pp. 177-182, 2004.
[101] J. R. Morones, J. L. Elechiguerra, A. Camacho, K. Holt, J. B. Kouri, J. T. Ram ́ırez, *et al.*, "The bactericidal effect of silver nanoparticles," *Nanotechnology,* vol. 16, p. 2346, 2005.
[102] R. Elghanian, J. J. Storhoff, R. C. Mucic, R. L. Letsinger, and C. A. Mirkin, "Selective colorimetric detection of polynucleotides based on the distance-dependent optical properties of gold nanoparticles," *Science,* vol. 277, pp. 1078-1081, 1997.
[103] K. L. Kelly, E. Coronado, L. L. Zhao, and G. C. Schatz, "The optical properties of metal nanoparticles: the influence of size, shape, and dielectric environment," *The Journal of Physical Chemistry B,* vol. 107, pp. 668-677, 2003.
[104] K. Saha, S. S. Agasti, C. Kim, X. Li, and V. M. Rotello, "Gold nanoparticles in chemical and biological sensing," *Chemical reviews,* vol. 112, pp. 2739-2779, 2012.
[105] L. Wang, Z.-c. Hao, L. Dai, Y. Li, and H. Zhou, "A planar, impedancemetric NO 2 sensor based on NiO nanoparticles sensing electrode," *Materials Letters,* vol. 87, pp. 24-27, 2012.
[106] C. C. Huang, Z. Yang, K. H. Lee, and H. T. Chang, "Synthesis of highly fluorescent gold nanoparticles for sensing mercury (II)," *Angewandte Chemie,* vol. 119, pp. 6948-6952, 2007.
[107] C. L. DeCastro and B. S. Mitchell, "Nanoparticles from mechanical attrition," *Synthesis, Functionalization, and Surface Treatment of Nanoparticles,* pp. 1-15, 2002.
[108] M. Willard, L. Kurihara, E. Carpenter, S. Calvin, and V. Harris, "Chemically prepared magnetic nanoparticles," *International Materials Reviews,* vol. 49, pp. 125-170, 2004.
[109] Y. Sun and Y. Xia, "Shape-controlled synthesis of gold and silver nanoparticles," *Science,* vol. 298, pp. 2176-2179, 2002.
[110] A. H. Lu, E. e. L. Salabas, and F. Schüth, "Magnetic nanoparticles: synthesis, protection, functionalization, and application," *Angewandte Chemie International Edition,* vol. 46, pp. 1222-1244, 2007.
[111] S. Tsai, Y. Song, C. Tsai, C. Yang, W. Chiu, and H. Lin, "Ultrasonic spray pyrolysis for nanoparticles synthesis," *Journal of materials science,* vol. 39, pp. 3647-3657, 2004.

[112] H. Song, R. M. Rioux, J. D. Hoefelmeyer, R. Komor, K. Niesz, M. Grass, *et al.*, "Hydrothermal growth of mesoporous SBA-15 silica in the presence of PVP-stabilized Pt nanoparticles: Synthesis, characterization, and catalytic properties," *Journal of the American Chemical Society*, vol. 128, pp. 3027-3037, 2006.
[113] R. Cakan, "Hydrothermal carbon spheres containing silicon nanoparticles: synthesis and lithium storage performance," *Chemical Communications*, pp. 3759-3761, 2008.
[114] T. Daou, G. Pourroy, S. Begin-Colin, J. Greneche, C. Ulhaq-Bouillet, P. Legaré, *et al.*, "Hydrothermal synthesis of monodisperse magnetite nanoparticles," *Chemistry of Materials*, vol. 18, pp. 4399-4404, 2006.
[115] D.-H. Chen and X.-R. He, "Synthesis of nickel ferrite nanoparticles by sol-gel method," *Materials Research Bulletin*, vol. 36, pp. 1369-1377, 2001.
[116] M. Epifani, C. Giannini, L. Tapfer, and L. Vasanelli, "Sol–gel synthesis and characterization of Ag and Au nanoparticles in SiO2, TiO2, and ZrO2 thin films," *Journal of the American Ceramic Society*, vol. 83, pp. 2385-2393, 2000.
[117] Y. Lu, Y. Yin, B. T. Mayers, and Y. Xia, "Modifying the surface properties of superparamagnetic iron oxide nanoparticles through a sol-gel approach," *Nano letters*, vol. 2, pp. 183-186, 2002.
[118] M. Vafaee and M. S. Ghamsari, "Preparation and characterization of ZnO nanoparticles by a novel sol–gel route," *Materials Letters*, vol. 61, pp. 3265-3268, 2007.
[119] M. C. McAlpine, H. Ahmad, D. Wang, and J. R. Heath, "Highly ordered nanowire arrays on plastic substrates for ultrasensitive flexible chemical sensors," *Nature materials*, vol. 6, pp. 379-384, 2007.
[120] O. Elibol, D. Morisette, D. Akin, J. Denton, and R. Bashir, "Integrated nanoscale silicon sensors using top-down fabrication," *Applied Physics Letters*, vol. 83, pp. 4613-4615, 2003.
[121] R. B. Sadeghian and M. Kahrizi, "A novel miniature gas ionization sensor based on freestanding gold nanowires," *Sensors and Actuators A: Physical*, vol. 137, pp. 248-255, 2007.
[122] Y. Im, C. Lee, R. P. Vasquez, M. A. Bangar, N. V. Myung, E. J. Menke, *et al.*, "Investigation of a single Pd nanowire for use as a hydrogen sensor," *Small*, vol. 2, pp. 356-358, 2006.
[123] C. Li, D. Zhang, B. Lei, S. Han, X. Liu, and C. Zhou, "Surface treatment and doping dependence of In2O3 nanowires as ammonia sensors," *The Journal of Physical Chemistry B*, vol. 107, pp. 12451-12455, 2003.
[124] I. Raible, M. Burghard, U. Schlecht, A. Yasuda, and T. Vossmeyer, "V 2 O 5 nanofibres: novel gas sensors with extremely high sensitivity and selectivity to amines," *Sensors and Actuators B: Chemical*, vol. 106, pp. 730-735, 2005.
[125] J. Huang, S. Virji, B. H. Weiller, and R. B. Kaner, "Polyaniline nanofibers: facile synthesis and chemical sensors," *Journal of the American Chemical Society*, vol. 125, pp. 314-315, 2003.
[126] Y. Dan, Y. Cao, T. E. Mallouk, A. T. Johnson, and S. Evoy, "Dielectrophoretically assembled polymer nanowires for gas sensing," *Sensors and Actuators B: Chemical*, vol. 125, pp. 55-59, 2007.

[127] S.-J. Chang, T.-J. Hsueh, I.-C. Chen, and B.-R. Huang, "Highly sensitive ZnO nanowire CO sensors with the adsorption of Au nanoparticles," *Nanotechnology,* vol. 19, p. 175502, 2008.
[128] E. Formo, E. Lee, D. Campbell, and Y. Xia, "Functionalization of electrospun TiO2 nanofibers with Pt nanoparticles and nanowires for catalytic applications," *Nano Letters,* vol. 8, pp. 668-672, 2008.
[129] A. Kolmakov, D. Klenov, Y. Lilach, S. Stemmer, and M. Moskovits, "Enhanced gas sensing by individual SnO2 nanowires and nanobelts functionalized with Pd catalyst particles," *Nano Letters,* vol. 5, pp. 667-673, 2005.
[130] H. Morkoç, "Handbook of Nitride Semiconductors and Devices," ed: Wiley, 2009.
[131] P. Ruterana, M. Albrecht, and J. Neugebauer, *Nitride semiconductors: handbook on materials and devices*: John Wiley & Sons, 2006.
[132] S. Nakamura and S. F. Chichibu, *Introduction to nitride semiconductor blue lasers and light emitting diodes*: CRC Press, 2000.
[133] C. Van de Walle, J. Neugebauer, and C. Stampfl, *of Book: Properties, processing and applications of gallium nitride and related semiconductors* vol. 23: Inspec, 1999.
[134] P. J. Harris and P. J. F. Harris, *Carbon nanotubes and related structures: new materials for the twenty-first century*: Cambridge university press, 2001.
[135] A. Jorio, G. Dresselhaus, and M. S. Dresselhaus, *Carbon nanotubes: advanced topics in the synthesis, structure, properties and applications* vol. 111: Springer Science & Business Media, 2007.
[136] K. Bertness, N. Sanford, J. Barker, J. Schlager, A. Roshko, A. Davydov, *et al.*, "Catalyst-free growth of GaN nanowires," *Journal of electronic materials,* vol. 35, pp. 576-580, 2006.
[137] T. Stoica, E. Sutter, R. J. Meijers, R. K. Debnath, R. Calarco, H. Lüth, *et al.*, "Interface and Wetting Layer Effect on the Catalyst‐Free Nucleation and Growth of GaN Nanowires," *Small,* vol. 4, pp. 751-754, 2008.
[138] C. Chèze, L. Geelhaar, O. Brandt, W. M. Weber, H. Riechert, S. Münch, *et al.*, "Direct comparison of catalyst-free and catalyst-induced GaN nanowires," *Nano Research,* vol. 3, pp. 528-536, 2010.
[139] S. Strite and H. Morkoç, "GaN, AlN, and InN: a review," *Journal of Vacuum Science & Technology B,* vol. 10, pp. 1237-1266, 1992.
[140] W. Hughes, W. Rowland Jr, M. Johnson, S. Fujita, J. Cook Jr, J. Schetzina, *et al.*, "Molecular beam epitaxy growth and properties of GaN films on GaN/SiC substrates," *Journal of Vacuum Science & Technology B,* vol. 13, pp. 1571-1577, 1995.
[141] D. Kohl, "Function and applications of gas sensors," *Journal of Physics D: Applied Physics,* vol. 34, p. R125, 2001.
[142] G. Korotcenkov, "Metal oxides for solid-state gas sensors: What determines our choice?," *Materials Science and Engineering: B,* vol. 139, pp. 1-23, 2007.
[143] H. Meixner and U. Lampe, "Metal oxide sensors," *Sensors and Actuators B: Chemical,* vol. 33, pp. 198-202, 1996.
[144] N. Yamazoe, G. Sakai, and K. Shimanoe, "Oxide semiconductor gas sensors," *Catalysis Surveys from Asia,* vol. 7, pp. 63-75, 2003.

[145] J. A. Rodriguez, "Orbital-band interactions and the reactivity of molecules on oxide surfaces: from explanations to predictions," *Theoretical Chemistry Accounts,* vol. 107, pp. 117-129, 2002.
[146] T. A. Albright, J. K. Burdett, and M.-H. Whangbo, *Orbital interactions in chemistry*: John Wiley & Sons, 2013.
[147] R. Hoffman, "Solids and surfaces: a chemist's view of bonding in extended structures," DTIC Document1988.
[148] E. Joselevich, "Electronic structure and chemical reactivity of carbon nanotubes: a chemist's view," *ChemPhysChem,* vol. 5, pp. 619-624, 2004.
[149] R. W. Siegel, "Nanostructured materials-mind over matter," *Nanostructured Materials,* vol. 3, pp. 1-18, 1993.
[150] P. Moriarty, "Nanostructured materials," *Reports on Progress in Physics,* vol. 64, p. 297, 2001.
[151] A. Tseung and K. Chen, "Hydrogen spill-over effect on Pt/WO 3 anode catalysts," *Catalysis Today,* vol. 38, pp. 439-443, 1997.
[152] P. Sermon and G. Bond, "Hydrogen spillover," *Catalysis Reviews,* vol. 8, pp. 211-239, 1974.
[153] W. C. Conner, G. Pajonk, and S. Teichner, "Spillover of sorbed species," *Adv. Catal,* vol. 34, pp. 1-79, 1986.
[154] S. R. Morrison, "Semiconductor gas sensors," *Sensors and Actuators,* vol. 2, pp. 329-341, 1982.
[155] N. Yamazoe, Y. Kurokawa, and T. Seiyama, "Effects of additives on semiconductor gas sensors," *Sensors and Actuators,* vol. 4, pp. 283-289, 1983.
[156] C. Xu, J. Tamaki, N. Miura, and N. Yamazoe, "Grain size effects on gas sensitivity of porous SnO 2-based elements," *Sensors and Actuators B: Chemical,* vol. 3, pp. 147-155, 1991.
[157] P. Moseley and B. Tofield, "Semiconductor gas sensors," *Materials science and technology,* vol. 1, pp. 505-509, 1985.
[158] R. Leghrib, R. Pavelko, A. Felten, A. Vasiliev, C. Cané, I. Gràcia, *et al.*, "Gas sensors based on multiwall carbon nanotubes decorated with tin oxide nanoclusters," *Sensors and Actuators B: Chemical,* vol. 145, pp. 411-416, 2010.
[159] N. V. Hieu, N. V. Duy, P. T. Huy, and N. D. Chien, "Inclusion of SWCNTs in Nb/Pt co-doped TiO 2 thin-film sensor for ethanol vapor detection," *Physica E Low-Dimensional Systems and Nanostructures,* vol. 40, pp. 2950-2958, 2008.
[160] C. Balázsi, K. Sedlácková, E. Llobet, and R. Ionescu, "Novel hexagonal WO 3 nanopowder with metal decorated carbon nanotubes as NO 2 gas sensor," *Sensors and Actuators B: Chemical,* vol. 133, pp. 151-155, 2008.
[161] Q. Kuang, C.-S. Lao, Z. Li, Y.-Z. Liu, Z.-X. Xie, L.-S. Zheng, *et al.*, "Enhancing the photon-and gas-sensing properties of a single SnO 2 nanowire based nanodevice by nanoparticle surface functionalization," *The Journal of Physical Chemistry C,* vol. 112, pp. 11539-11544, 2008.
[162] Y. Zhang, J. Xu, P. Xu, Y. Zhu, X. Chen, and W. Yu, "Decoration of ZnO nanowires with Pt nanoparticles and their improved gas sensing and photocatalytic performance," *Nanotechnology,* vol. 21, p. 285501, 2010.

[163] V. Dobrokhotov, D. McIlroy, M. G. Norton, A. Abuzir, W. Yeh, I. Stevenson, *et al.*, "Principles and mechanisms of gas sensing by GaN nanowires functionalized with gold nanoparticles," *Journal of applied physics*, vol. 99, p. 104302, 2006.
[164] B. Gil, *Group III nitride semiconductor compounds: physics and applications*: Clarendon Press, 1998.
[165] W. Lim, J. Wright, B. Gila, J. L. Johnson, A. Ural, T. Anderson, *et al.*, "Room temperature hydrogen detection using Pd-coated GaN nanowires," *Applied Physics Letters*, vol. 93, p. 72109, 2008.
[166] J. Wright, W. Lim, B. Gila, S. Pearton, J. L. Johnson, A. Ural, *et al.*, "Hydrogen sensing with Pt-functionalized GaN nanowires," *Sensors and Actuators B: Chemical*, vol. 140, pp. 196-199, 2009.
[167] A. A. Talin, G. T. Wang, E. Lai, and R. J. Anderson, "Correlation of growth temperature, photoluminescence, and resistivity in GaN nanowires," *Applied Physics Letters*, vol. 92, p. 093105, 2008.
[168] Y. Sun, R. A. Graff, M. S. Strano, and J. A. Rogers, "Top‐Down Fabrication of Semiconductor Nanowires with Alternating Structures along their Longitudinal and Transverse Axes," *Small*, vol. 1, pp. 1052-1057, 2005.
[169] X. T. Vu, J. F. Eschermann, R. Stockmann, R. GhoshMoulick, A. Offenhäusser, and S. Ingebrandt, "Top‐down processed silicon nanowire transistor arrays for biosensing," *physica status solidi (a)*, vol. 206, pp. 426-434, 2009.
[170] Q. Li, K. R. Westlake, M. H. Crawford, S. R. Lee, D. D. Koleske, J. J. Figiel, *et al.*, "Optical performance of top-down fabricated InGaN/GaN nanorod light emitting diode arrays," *Optics express*, vol. 19, pp. 25528-25534, 2011.
[171] Q. Li, J. B. Wright, W. W. Chow, T. S. Luk, I. Brener, L. F. Lester, *et al.*, "Single-mode GaN nanowire lasers," *Optics express*, vol. 20, pp. 17873-17879, 2012.
[172] P. Offermans, M. Crego-Calama, and S. H. Brongersma, "Gas detection with vertical InAs nanowire arrays," *Nano letters*, vol. 10, pp. 2412-2415, 2010.
[173] G. Sberveglieri, C. Baratto, E. Comini, G. Faglia, M. Ferroni, A. Ponzoni, *et al.*, "Synthesis and characterization of semiconducting nanowires for gas sensing," *Sensors and Actuators B: Chemical*, vol. 121, pp. 208-213, 2007.
[174] C.-Y. Wang, L.-Y. Chen, C.-P. Chen, Y.-W. Cheng, M.-Y. Ke, M.-Y. Hsieh, *et al.*, "GaN nanorod light emitting diode arrays with a nearly constant electroluminescent peak wavelength," *Optics Express*, vol. 16, pp. 10549-10556, 2008.
[175] C.-P. Chen, A. Ganguly, C.-Y. Lu, T.-Y. Chen, C.-C. Kuo, R.-S. Chen, *et al.*, "Ultrasensitive in situ label-free DNA detection using a GaN nanowire-based extended-gate field-effect-transistor sensor," *Analytical chemistry*, vol. 83, pp. 1938-1943, 2011.
[176] R. Chen, C. Lu, K. Chen, and L. Chen, "Molecule-modulated photoconductivity and gain-amplified selective gas sensing in polar GaN nanowires," *Applied Physics Letters*, vol. 95, p. 233119, 2009.
[177] J. L. Johnson, Y. Choi, A. Ural, W. Lim, J. Wright, B. Gila, *et al.*, "Growth and characterization of GaN nanowires for hydrogen sensors," *Journal of electronic materials*, vol. 38, pp. 490-494, 2009.

[178] G. Liu, D. A. Lowy, A. Kahrim, C. Wang, Z. Dilli, N. Kratzmeier, *et al.*, "A low cost micro-heater for aerosol generation applications," *Microelectronic Engineering,* vol. 129, pp. 46-52, 2014.
[179] J. E. Northrup and J. Neugebauer, "Theory of GaN (10 1¯0) and (11 2¯0) surfaces," *Physical Review B,* vol. 53, p. R10477, 1996.
[180] Q. Sun, C. D. Yerino, B. Leung, J. Han, and M. E. Coltrin, "Understanding and controlling heteroepitaxy with the kinetic Wulff plot: A case study with GaN," *Journal of Applied Physics,* vol. 110, p. 053517, 2011.
[181] I. Zubel, I. Barycka, K. Kotowska, and M. Kramkowska, "Silicon anisotropic etching in alkaline solutions IV: the effect of organic and inorganic agents on silicon anisotropic etching process," *Sensors and Actuators A: Physical,* vol. 87, pp. 163-171, 2001.
[182] I. Zubel and M. Kramkowska, "The effect of isopropyl alcohol on etching rate and roughness of (1 0 0) Si surface etched in KOH and TMAH solutions," *Sensors and Actuators A: Physical,* vol. 93, pp. 138-147, 2001.
[183] D.-F. Wang, F. Shiwei, C. Lu, A. Motayed, M. Jah, S. N. Mohammad, *et al.*, "Low-resistance Ti/Al/Ti/Au multilayer ohmic contact to n-GaN," *Journal of Applied Physics,* vol. 89, pp. 6214-6217, 2001.
[184] A. Motayed, R. Bathe, M. C. Wood, O. S. Diouf, R. Vispute, and S. N. Mohammad, "Electrical, thermal, and microstructural characteristics of Ti/Al/Ti/Au multilayer Ohmic contacts to n-type GaN," *Journal of applied physics,* vol. 93, pp. 1087-1094, 2003.
[185] A. Motayed, M. Jah, A. Sharma, W. T. Anderson, C. W. Litton, and S. N. Mohammad, "Two-step surface treatment technique: Realization of nonalloyed low-resistance Ti/Al/Ti/Au ohmic contact to n-GaN," *Journal of Vacuum Science & Technology B,* vol. 22, pp. 663-667, 2004.
[186] Z. Zou, J. Ye, K. Sayama, and H. Arakawa, "Direct splitting of water under visible light irradiation with an oxide semiconductor photocatalyst," *Nature,* vol. 414, pp. 625-627, 2001.
[187] V. Aroutiounian, V. Arakelyan, and G. Shahnazaryan, "Metal oxide photoelectrodes for hydrogen generation using solar radiation-driven water splitting," *Solar Energy,* vol. 78, pp. 581-592, 2005.
[188] J. H. Park, S. Kim, and A. J. Bard, "Novel carbon-doped TiO2 nanotube arrays with high aspect ratios for efficient solar water splitting," *Nano letters,* vol. 6, pp. 24-28, 2006.
[189] E. Ruckenstein and Y. H. Hu, "Carbon dioxide reforming of methane over nickel/alkaline earth metal oxide catalysts," *Applied Catalysis A: General,* vol. 133, pp. 149-161, 1995.
[190] B. M. Bhanage, S.-i. Fujita, Y. Ikushima, and M. Arai, "Synthesis of dimethyl carbonate and glycols from carbon dioxide, epoxides, and methanol using heterogeneous basic metal oxide catalysts with high activity and selectivity," *Applied Catalysis A: General,* vol. 219, pp. 259-266, 2001.
[191] H. Hamada, "Selective reduction of NO by hydrocarbons and oxygenated hydrocarbons over metal oxide catalysts," *Catalysis today,* vol. 22, pp. 21-40, 1994.

[192] D. A. Pena, B. S. Uphade, and P. G. Smirniotis, "TiO 2-supported metal oxide catalysts for low-temperature selective catalytic reduction of NO with NH 3: I. Evaluation and characterization of first row transition metals," *Journal of catalysis*, vol. 221, pp. 421-431, 2004.
[193] M. Shelef, K. Otto, and H. Gandhi, "The oxidation of CO by O 2 and by NO on supported chromium oxide and other metal oxide catalysts," *Journal of Catalysis*, vol. 12, pp. 361-375, 1968.
[194] F. Auret, S. Goodman, M. Hayes, M. Legodi, H. Van Laarhoven, and D. C. Look, "Electrical characterization of 1.8 MeV proton-bombarded ZnO," *Applied Physics Letters*, vol. 79, pp. 3074-3076, 2001.
[195] S. Das, S. Chakrabarti, and S. Chaudhuri, "Optical transmission and photoluminescence studies of ZnO? MgO nanocomposite thin films," *Journal of Physics D: Applied Physics*, vol. 38, p. 4021, 2005.
[196] S. Paik, S. Shak, G. Tang, C. Kim, J. Baker, M. Cronin, *et al.*, "A multigene assay to predict recurrence of tamoxifen-treated, node-negative breast cancer," *New England Journal of Medicine*, vol. 351, pp. 2817-2826, 2004.
[197] Y. Shen, X. Yan, Z. Bai, X. Zheng, Y. Sun, Y. Liu, *et al.*, "A self-powered ultraviolet photodetector based on solution-processed p-NiO/n-ZnO nanorod array heterojunction," *RSC Advances*, vol. 5, pp. 5976-5981, 2015.
[198] Y. Q. Bie, Z. M. Liao, H. Z. Zhang, G. R. Li, Y. Ye, Y. B. Zhou, *et al.*, "Self‐Powered, Ultrafast, Visible‐Blind UV Detection and Optical Logical Operation based on ZnO/GaN Nanoscale p‐n Junctions," *Advanced Materials*, vol. 23, pp. 649-653, 2011.
[199] S. M. Hatch, J. Briscoe, and S. Dunn, "A Self‐Powered ZnO‐Nanorod/CuSCN UV Photodetector Exhibiting Rapid Response," *Advanced Materials*, vol. 25, pp. 867-871, 2013.
[200] T. Xie, G. Liu, B. Wen, J. Y. Ha, N. V. Nguyen, A. Motayed, *et al.*, "Tunable ultraviolet photoresponse in solution-processed pn junction photodiodes based on transition metal oxides," *ACS applied materials & interfaces*, 2015.
[201] D. Y. Kim, J. Ryu, J. Manders, J. Lee, and F. So, "Air-stable, solution-processed oxide p–n heterojunction ultraviolet photodetector," *ACS applied materials & interfaces*, vol. 6, pp. 1370-1374, 2014.
[202] Y. Vygranenko, K. Wang, and A. Nathan, "Low leakage p-NiO/i-ZnO/n-ITO heterostructure ultraviolet sensor," *Applied physics letters*, vol. 89, p. 2105, 2006.
[203] H. Ohta, M. Hirano, K. Nakahara, H. Maruta, T. Tanabe, M. Kamiya, *et al.*, "Fabrication and photoresponse of a pn-heterojunction diode composed of transparent oxide semiconductors, p-NiO and n-ZnO," *Applied physics letters*, vol. 83, pp. 1029-1031, 2003.
[204] R. t. Shannon, "Revised effective ionic radii and systematic studies of interatomic distances in halides and chalcogenides," *Acta Crystallographica Section A: Crystal Physics, Diffraction, Theoretical and General Crystallography*, vol. 32, pp. 751-767, 1976.
[205] J. Sarver, F. L. Katnack, and F. Hummel, "Phase Equilibria and Manganese‐Activated Fluorescence in the System Zn3 (PO 4) 2‐Mg3 (PO 4) 2," *Journal of The Electrochemical Society*, vol. 106, pp. 960-963, 1959.

[206] A. Ohtomo, M. Kawasaki, T. Koida, K. Masubuchi, H. Koinuma, Y. Sakurai, *et al.*, "Mg x Zn 1-x O as a II-VI widegap semiconductor alloy," *Applied Physics Letters*, vol. 72, pp. 2466-2468, 1998.
[207] K. Koike, K. Hama, I. Nakashima, G.-y. Takada, K.-i. Ogata, S. Sasa, *et al.*, "Molecular beam epitaxial growth of wide bandgap ZnMgO alloy films on (111)-oriented Si substrate toward UV-detector applications," *Journal of crystal growth*, vol. 278, pp. 288-292, 2005.
[208] R. Ghosh and D. Basak, "Composition dependent ultraviolet photoresponse in MgxZn1− xO thin films," *Journal of applied physics*, vol. 101, p. 113111, 2007.
[209] R. Ghosh and D. Basak, "Composition dependence of electrical and optical properties in sol-gel MgxZn1− xO thin films," *Journal of applied physics*, vol. 101, p. 023507, 2007.
[210] R. Ghosh and D. Basak, "Optical studies on Mg x Zn1− x O wide band gap semiconductor in the perspective of phase equilibrium," *Journal of Materials Science: Materials in Electronics*, vol. 18, pp. 141-144, 2007.
[211] A. Singh, A. Vij, D. Kumar, P. Khanna, M. Kumar, S. Gautam, *et al.*, "Investigation of phase segregation in sol–gel derived ZnMgO thin films," *Semiconductor Science and Technology*, vol. 28, p. 025004, 2013.
[212] Z. Yin, Q. Zheng, S. C. Chen, D. Cai, L. Zhou, and J. Zhang, "Bandgap Tunable Zn1 ‐ xMgxO Thin Films as Highly Transparent Cathode Buffer Layers for High ‐ Performance Inverted Polymer Solar Cells," *Advanced Energy Materials*, vol. 4, 2014.
[213] S. Fujihara, C. Sasaki, and T. Kimura, "Effects of Li and Mg doping on microstructure and properties of sol-gel ZnO thin films," *Journal of the European Ceramic Society*, vol. 21, pp. 2109-2112, 2001.
[214] A. Hierro, G. Tabares, J. Ulloa, E. Munoz, A. Nakamura, T. Hayashi, *et al.*, "Carrier compensation by deep levels in Zn1-xMgxO/sapphire," *Applied Physics Letters*, vol. 94, p. 2101, 2009.
[215] T. Xie, N. Sullivan, K. Steffens, B. Wen, G. Liu, R. Debnath, *et al.*, "UV-assisted room-temperature chemiresistive NO 2 sensor based on TiO 2 thin film," *Journal of Alloys and Compounds*, vol. 653, pp. 255-259, 2015.
[216] M. R. Hasan, T. Xie, S. C. Barron, G. Liu, N. V. Nguyen, A. Motayed, *et al.*, "Self-powered p-NiO/n-ZnO heterojunction ultraviolet photodetectors fabricated on plastic substrates," *APL Materials*, vol. 3, p. 106101, 2015.
[217] E. Sichel and J. Pankove, "Thermal conductivity of GaN, 25–360 K," *Journal of physics and chemistry of solids*, vol. 38, p. 330, 1977.
[218] C. Mion, J. Muth, E. A. Preble, and D. Hanser, "Thermal conductivity, dislocation density and GaN device design," *Superlattices and Microstructures*, vol. 40, pp. 338-342, 2006.
[219] J. Zou, D. Kotchetkov, A. Balandin, D. Florescu, and F. H. Pollak, "Thermal conductivity of GaN films: Effects of impurities and dislocations," *Journal of applied physics*, vol. 92, pp. 2534-2539, 2002.
[220] A. Jeżowski, B. Danilchenko, M. Boćkowski, I. Grzegory, S. Krukowski, T. Suski, *et al.*, "Thermal conductivity of GaN crystals in 4.2–300 K range," *Solid state communications*, vol. 128, pp. 69-73, 2003.

[221] W. Liu and A. A. Balandin, "Thermal conduction in AlxGa1-xN alloys and thin films," *Journal of Applied Physics,* vol. 97, pp. 73710-73710, 2005.
[222] W. Liu and A. A. Balandin, "Temperature dependence of thermal conductivity of AlxGa1− xN thin films measured by the differential 3ω technique," *Applied physics letters,* vol. 85, pp. 5230-5232, 2004.
[223] B. Daly, H. Maris, A. Nurmikko, M. Kuball, and J. Han, "Optical pump-and-probe measurement of the thermal conductivity of nitride thin films," *Journal of applied physics,* vol. 92, pp. 3820-3824, 2002.
[224] D. G. Archer, "Thermodynamic Properties of Synthetic Sapphire (α - Al2O3), Standard Reference Material 720 and the Effect of Temperature - Scale Differences on Thermodynamic Properties," *Journal of physical and chemical reference data,* vol. 22, pp. 1441-1453, 1993.
[225] D. G. Cahill, S. Lee, and T. I. Selinder, "Thermal conductivity of j-Al2O3 and a-Al2O3 wear-resistant coatings," *J. Appl. Phys,* vol. 83, pp. 5783-5786, 1998.
[226] D. G. Cahill and T. H. Allen, "Thermal conductivity of sputtered and evaporated SiO2 and TiO2 optical coatings," *Applied Physics Letters,* vol. 65, pp. 309-311, 1994.
[227] F. Brotzen, P. Loos, and D. Brady, "Thermal conductivity of thin SiO 2 films," *Thin Solid Films,* vol. 207, pp. 197-201, 1992.
[228] D. O. Scanlon, C. W. Dunnill, J. Buckeridge, S. A. Shevlin, A. J. Logsdail, S. M. Woodley, *et al.*, "Band alignment of rutile and anatase TiO2," *Nature materials,* vol. 12, pp. 798-801, 2013.
[229] B. Sexton, K. Rendulic, and A. Huges, "Decomposition pathways of C 1 C 4 alcohols adsorbed on platinum (111)," *Surface Science,* vol. 121, pp. 181-198, 1982.
[230] M. M. Islam, M. Calatayud, and G. Pacchioni, "Hydrogen adsorption and diffusion on the anatase TiO2 (101) surface: A first-principles investigation," *The Journal of Physical Chemistry C,* vol. 115, pp. 6809-6814, 2011.
[231] M. Paulose, O. K. Varghese, G. K. Mor, C. A. Grimes, and K. G. Ong, "Unprecedented ultra-high hydrogen gas sensitivity in undoped titania nanotubes," *Nanotechnology,* vol. 17, p. 398, 2006.
[232] O. K. Varghese, D. Gong, M. Paulose, K. G. Ong, and C. A. Grimes, "Hydrogen sensing using titania nanotubes," *Sensors and Actuators B: Chemical,* vol. 93, pp. 338-344, 2003.
[233] X. Du, Y. Wang, Y. Mu, L. Gui, P. Wang, and Y. Tang, "A new highly selective H2 sensor based on TiO2/PtO-Pt dual-layer films," *Chemistry of materials,* vol. 14, pp. 3953-3957, 2002.
[234] U. Roland, T. Braunschweig, and F. Roessner, "On the nature of spilt-over hydrogen," *Journal of Molecular Catalysis A: Chemical,* vol. 127, pp. 61-84, 1997.
[235] A. Maiti, J. A. Rodriguez, M. Law, P. Kung, J. R. McKinney, and P. Yang, "SnO2 nanoribbons as NO2 sensors: insights from first principles calculations," *Nano Letters,* vol. 3, pp. 1025-1028, 2003.
[236] J. S. Dalton, P. A. Janes, N. Jones, J. A. Nicholson, K. R. Hallam, and G. C. Allen, "Photocatalytic oxidation of NO x gases using TiO 2: a surface spectroscopic approach," *Environmental Pollution,* vol. 120, pp. 415-422, 2002.

[237] M. Law, H. Kind, B. Messer, F. Kim, and P. Yang, "Photochemical sensing of NO2 with SnO2 nanoribbon nanosensors at room temperature," *Angewandte Chemie,* vol. 114, pp. 2511-2514, 2002.